Titre: Title:	Dielectric THz Waveguides
Auteur: Author:	Alexandre Dupuis
Date:	2010
Type:	Mémoire ou thèse / Dissertation or Thesis
Référence: Citation:	Dupuis, A. (2010). Dielectric THz Waveguides [Ph.D. thesis, École Polytechnique de Montréal]. PolyPublie. https://publications.polymtl.ca/447/

UNIVERSITÉ DE MONTRÉAL

DIELECTRIC THz WAVEGUIDES

ALEXANDRE DUPUIS
DÉPARTEMENT DE GÉNIE PHYSIQUE
ÉCOLE POLYTECHNIQUE DE MONTRÉAL

THÈSE PRÉSENTÉE EN VUE DE L'OBTENTION DU DIPLÔME DE
PHILOSOPHIÆ DOCTOR
(GÉNIE PHYSIQUE)
NOVEMBRE 2010

UNIVERSITÉ DE MONTRÉAL

ÉCOLE POLYTECHNIQUE DE MONTRÉAL

Cette thèse intitulée :

DIELECTRIC THz WAVEGUIDES

présentée par : M. DUPUIS Alexandre.
en vue de l'obtention du diplôme de : Philosophiæ Doctor
a été dûment acceptée par le jury d'examen constitué de :

M. MASUT Remo A., Ph.D., président.
M. SKOROBOGATIY Maksim A., Ph.D., membre et directeur de recherche.
Mme. LACROIX Suzanne, D.Sc., membre et codirectrice de recherche.
M. GODBOUT Nicolas, Ph.D., membre et codirecteur de recherche.
M. FRANCOEUR Sébastien, Ph.D., membre.
M. SAEEDKIA Daryoosh, Ph.D., membre.

To my parents, Réjean and Diane,
may they share with me the
pleasure of a completed thesis.

Acknowledgements

Long gone are the days when a lonely patent clerk could change the science of physics in his free time. Today science is an immense collaborative effort and there are a lot of people to thank. I would like to begin by thanking my supervisors. I would like to thank Maksim for welcoming me into his group, for pushing me along when I needed it, and for giving me so many wonderful opportunities. I would like to thank Suzanne for always believing in me, starting way back in the old undergrad days, and for continuing to support me even if all of our projects and ambitions didn't pan out.

I would like to thank all of my colleagues with whom I have worked and collaborated with. Especially, fellow THz enthusiast Jean-François Allard, who made my trips to the University of Sherbrooke memorable, and the expert polymer chemist Karen Stoeffler, for all her help with the processing of the polymers used in this thesis. I would also like to thank professor Denis Morris, at the University of Sherbrooke, who welcomed us into his impressive lab for a fruitful collaboration at a time when our own setup was still an idea on paper; I thank Alireza Hassani for his theoretical work on porous subwavelength fibers; Anna Mazhorova, Frédéric Désévédavy, and Mathieu Rozé for fabricating some of the porous fiber samples; professor Charles Dubois for giving us some polyethylene and letting us press and extrude polymers in his lab; M. Robert Lemieux at the Industrial Materials Institute for his help in extruding some doped-polymer film; and Bora Ung for helping with some numerical calculations and proof-reading some papers.

I must thank the National Sciences and Engineering Research Council of Canada for their repeated and very generous financial support of my work.

I thank my friends and family for their love and support... over so many years.

Finally I would like to give a special acknowledgement to our technician Francis Boismenu. The praise of technicians cannot go unsung. His meticulously good work and jovial nature offered not only excellent technical assistance but also much appreciated moral support. He was often the sounding board of my ideas and would offer suggestions and words of encouragement after lending an ear to my frustrations. My heartfelt thanks to him, and to everyone.

Résumé

Dans cette thèse nous avons exploré une grande variété de guides d'onde diélectriques pour guider la lumière THz (infrarouge lointain). Nous avons exploré théoriquement et expérimentalement un grand nombre de designs, basés sur plusieurs mécanismes de guidage différents, dans le but de réduire les pertes de propagation et les pertes par rayon de courbure élevées qui limitent les guides d'onde actuels. Les différents guides d'onde peuvent être classés selon deux stratégies fondamentalement différentes pour réduire les pertes de propagation : soit une fibre optique monomode dont le petit coeur guide un champ évanescent ou soit un tube creux multimode guidant la lumière à l'intérieur d'un trou d'air.

Au delà du design et de la fabrication de nouveaux guides d'onde THz, les résultats présentés dans cette thèse sont basés sur une mesure adéquate des spectres de transmission THz des guides. Un montage innovateur de spectoscopie THz dans le domaine temporel a dû être conçu et réalisé afin de mesurer la propagation de la lumière THz à travers les guides d'onde. Un montage ajustable de spectroscopie THz a été implémenté en fixant des miroirs sur des rails de translation, afin de pouvoir déplacer les miroirs pour accomoder des guides d'onde d'une longueur pouvant atteindre 50 cm. Avec ce montage, nous avons mesuré avec succès des échantillons plans (≤ 3.25 mm) ainsi qu'une variété de guides d'onde THz, allant jusqu'à 40 cm de longueur.

Nos efforts ont d'abord été concentrés sur la stratégie de réduction de pertes de propagation qui repose sur le guidage d'un champ évanescent par une fibre optique dont la taille du coeur est plus petite que la taille de longueur d'onde (lambda) de la lumière guidée. Cette fibre optique est dite de diamètre infra-lambda. Suite à des travaux théoriques par notre groupe sur le potentiel de ces fibres, nous avons entrepris la fabrication et la mesure d'une variété particulaire de fibres de diamètre infra-lambda dont le coeur est *poreux* afin de réduire davantage les pertes de propagation. La fabrication des fibres poreuses est un défi qui a nécessité le dévelopement de plusieurs nouvelles méthodes d'étirage de fibre afin d'éviter l'effondrement des trous à l'intérieur des fibres poreuses. La première méthode consistait à emprisonner de l'air dans un assemblage de tubes de polymère en les scellant avec de la colle. La réduction de la taille des trous lors de l'étirage donne lieu à des fibres ayant une faible porosité

(∼25% d'air à l'intérieur du coeur). La seconde méthode est une technique novatrice basée sur l'utilisation d'un polymère sacrificiel. Deux polymères sont utilisés pour former une préforme solide, contenant aucun trou, qui peut facilement être étirée en fibre. Par la suite, la fibre est placée dans un solvant afin de dissoudre le polymère sacrificiel et révéler les trous d'air à l'intérieur de la fibre. Une troisième méthode consiste à mouler une préforme de polymère et ensuite de l'étirer en injectant de l'air sous pression dans les trous. Cette méthode a menée à des fibres ayant une porosité record (86% d'air à l'intérieur du coeur).

La mesure de ces fibres poreuses a commencé par une collaboration avec un groupe de spectroscopie THz à l'université de Sherbrooke. À l'époque, le seul détecteur disponible était un bolomètre (puissance-mètre) refroidi à l'hélium liquide et qui intégrait en fréquence la puissance. Une méthode novatrice, basée sur un coupleur à champ évanescent, a été développée pour mesurer les pertes de propagation des fibres de diamètre infra-lambda. Un coupleur est formé en plaçant une fibre sonde à proximité d'une fibre échantillon. En translatant la fibre sonde le long de la fibre échantillon les pertes de propagation ont pu être mesurées de façon non-destructive. Étant donné que le coupleur agit comme un filtre fréquentiel passe-bas et que le détecteur intégrait toutes les fréquences, nous avons estimé que l'information spectrale était limitée à une fréquence moyenne autour de 0.2 THz. Par la suite, des mesures spectrales plus précises avec le montage ajustable de spectroscopie THz dans le domaine temporel ont permis la détermination des pertes de propagation à toutes les fréquences. Nous avons confirmé que les fibres à diamètre infra-lambda ont de faible pertes (< 0.02 cm^{-1} @ f=0.25 THz), parmi les plus faibles pertes mesurées à date. De plus, ces mesures ont démontrées que l'addition de la porosité a translaté les pertes d'absorption à des plus hautes fréquences, ce qui a permis la transmission à des fréquences plus élevées que ne le permet les fibres infra-lambda non-poreuses.

Par ailleurs, beaucoup d'efforts ont été concentrés sur l'exploration de la stratégie de guidage par un tube creux avec le dévelopement de fibres de Bragg THz, où un réflecteur Bragg sur la paroi interne d'un tube confine la lumière dans le trou d'air du tube. Étant donné la similitude des indices de réfraction des polymères dans le régime THz, deux techniques différentes ont été proposées et implémentées pour augmenter le contraste d'indice entre les couches des réflecteurs Bragg. La première méthode consistait à rouler des particles de poudre avec un film de polymère afin de former des couches d'air. La deuxième méthode consistait à rouler un film de polyéthylène pur

avec un film de polyéthylène dopé avec une poudre de TiO_2. Malgré l'augmentation considérable du contraste d'indice entre les couches dopées et non-dopées, les pertes de propagation totales de la fibre de Bragg résultante furent plus élevées que dans le cas de la fibre de Bragg air-polymère étant donné les pertes d'absorption très élevées du film dopé au TiO_2. Bien qu'il y avait beaucoup de travaux antérieurs par d'autres chercheurs sur les réflecteurs Bragg THz planaires, nous avons fait la première démonstration de fibres de Bragg THz. Toutefois, il reste des problèmes de fabrication et dans leur état actuel ces fibres ont des pertes de propagation plusieurs ordres de grandeur plus élevées que les prédictions théoriques.

Finalement, une panoplie d'idées ont été proposées pour des travaux futurs sur les guides d'onde THz diélectriques et des études préliminaires ont été faites sur chacune de ces idées. Pour l'amélioration des fibres de Bragg THz de polymère dopé, des matériaux qui absorbent moins de lumière THz ont été considérés pour le dopage. Les pertes par rayon de courbure ont été étudiées, ainsi que le potentiel pour un régime monomode basé sur le guidage du mode TE_{01} et l'élimination des autres modes guidables. Par ailleurs, les guides d'onde reposants sur la réflection totale interne ce sont révélés prometteurs. Les copolymères de fluorure de polyvinylidène (PVDF-TrFE) ont été proposés comme matériaux pour des guide d'onde reposants sur la réflection totale interne atténuée. Cette solution est très intéressante puisqu'elle repose sur l'utilisation d'un simple tube de plastique. En dernier lieu, nous avons exploré le design d'une fibre de mousse de polymère, guidant par réflection totale interne. Ce guide d'onde offre la possibilité d'être réellement flexible ainsi que d'avoir de faibles pertes de propagation et de faibles pertes par rayon de courbure. De plus, le guidage confiné à l'intérieur de la mousse offre une solution au problème d'absorption THz par la vapeur d'eau en éliminant le contact avec l'air humide environnant.

Abstract

In this thesis we have explored a wide variety of dielectric waveguides that rely on many different waveguiding mechanisms to guide THz (far-infrared) radiation. We have explored both theoretically and experimentally a large number of waveguide designs with the aim of reducing propagation and bending losses. The different waveguides can be classified into two fundamentally different strategies for reducing the propagation loss: small-core single-mode evanescent-field fibers or large hollow-core multi-mode tubes.

Beyond the design and fabrication of new THz waveguides, the results of this thesis hinged on the proper measurement of waveguide transmission spectra. This required the development of a novel THz time-domain spectroscopy (THz-TDS) setup specifically designed for measuring THz propagation through waveguides. By placing mirror assemblies on a translation rail we implemented a versatile THz-TDS setup with an easily adjustable path length capable of accommodating waveguides up to 50 cm in length. With this setup we successfully measured both thin planar samples ($\leq$ 3.25 mm) as well as a variety of THz waveguides, some 40 cm in length.

Our focus was first set on exploring the small-core evanescent-field fiber strategy for reducing propagation losses. Following initial theoretical work in our group, much effort was spent on the fabrication and measurement of evanescent *porous* subwavelength diameter plastic fibers, in an attempt to further reduce the propagation losses. The fabrication of such fibers is a challenge and many novel techniques were devised to enable fiber drawing without hole collapse. The first method sealed the holes of an assembly of polymer tubes and lead to fibers of relatively low porosity ($\sim$25% air within the core) due to reduction in hole size during fiber drawing. The second method was a novel sacrificial polymer technique whereby drawing a completely solid fiber prevented any hole collapse and the subsequent dissolution of the sacrificial polymer revealed the holes in the fiber. The third method was a combination of preform casting using glass molds and drawing with pressurized air within the holes. This led to fibers of record porosity (86% air).

The measurement of these porous fibers began with a collaboration with a group from the university of Sherbrooke. At the time, the only available detector was a

frequency integrating liquid-helium-cooled bolometer (powermeter). A novel directional coupler method for measuring the losses of subwavelength fibers was developed whereby an evanescent coupler is formed by bringing a probe fiber in proximity to the sample fiber. By translating the coupling probe fiber along the length of the sample the propagation loss could be estimated in a non-destructive way. Because of the low-pass frequency filtering of the probe fiber and the frequency integration of the detector, the results required careful interpretation and spectral information was limited to the vicinity of 0.2 THz. Subsequent transmission experiments using the adjustable THz-TDS setup enabled the measurement of the full loss spectrum and confirmed the very low propagation loss (< 0.02 cm^{-1}) of the porous subwavelength fibers, among some of the lowest reported losses to date. These measurements further demonstrated that the addition of porosity blue-shifted absorption losses, by virtue of increasing the fraction of power guided in air, thus enabling transmission at higher frequencies and with a wider transmission peak than non-porous subwavelength fibers.

Much effort was also spent on exploring the hollow-core waveguide strategy with the development of large hollow-core Bragg fibers. Owing to the similarities in the refractive indices of polymers in the THz regime, two different methods were proposed and implemented for increasing the refractive index contrast between the layers of the Bragg reflector. The first method consisted of co-rolling a polymer film with powder particles in order to create air layers. The second method consisted in rolling a bi-layer of a TiO_2 doped polyethylene film and a pure polyethylene film. Despite the increased index contrast between the doped and undoped layers, the overall propagation loss was larger than that of the air-polymer Bragg fiber due to the high absorption loss of the TiO_2 doped film. Although much prior work had been done by others on planar THz Bragg reflectors this is the first implementation of a THz Bragg fiber. Unfortunately, in their current implementation the fibers are either too lossy or mechanically unstable.

Finally, many new ideas were proposed for future work on dielectric THz waveguides and initial theoretical investigations were given. For the improvement of THz Bragg fibers, less absorbing dopant materials were considered for doped-polymer Bragg fibers. The effects of bending losses were also investigated as well as the potential for an effectively single-TE_{01}-mode regime. On the other hand, total internal reflection waveguides were seen to be very promising. Polyvinylidene fluoride copolymers (PVDF-TrFE) were proposed as new materials for Attenuated Total In-

ternal Reflection waveguides and this solution is very attractive because the fabrication process reduces to the sheer simplicity of forming a polymer tube. Finally, we theoretically investigated the design of a Total Internal Reflection foam fiber. This waveguide offers the possibility of a truly flexible, low propagation loss, low bending loss fiber that also solves the problem of THz absorption from water vapor by completely encapsulating the THz radiation.

Condensé en Français

Chapitre 1 : Introduction

Cette thèse traite d'une multitude de guides d'ondes diélectriques pour guider la lumière dite térahertz (THz). Cette désignation fait référence à la plage du spectre électromagnétique où la fréquence de la lumière est de l'ordre de 10^{12} (téra) Hertz. La bande THz s'étend d'environ 0,1 THz à 4 THz, c'est-à-dire aux longueurs d'onde allant respectivement de 3000 μm à 75 μm, ce qui correspond à l'infrarouge lointain.

Il y a eu un grand engouement pour la lumière THz dans les dernières années car elle offre beaucoup de potentiel en terme de spectroscopie et d'imagerie. En terme de spectroscopie, les hautes fréquences de l'infrarouge proche permetent d'identifier la signature spectrale spécifique aux vibrations des liaisons chimiques, tandis que les basses fréquences THz permettent d'étudier les vibrations des macro-molécules. Plusieurs études ont démontré : la détection de l'ADN sans marqueurs fluorescents, l'étude de la dynamique des protéines et des acides aminés, ainsi que la détection d'explosifs.

Peut-être plus intéressants encore sont les applications en termes d'imagerie. Puisque les grandes longueurs d'onde réduisent les effets de diffusion Rayleigh, la lumière THz pénètre davantage à travers certains matériaux. De plus, la lumière THz est non-ionisante (contrairement au rayons X), offre une meilleure résolution spatiale que l'imagerie micro-onde (car $\lambda_{\mathrm{THz}} < \lambda_{\mathrm{micro-onde}}$) et offre des contrastes spectraux qui ne sont pas disponibles autrement. Parmi les nombreuses démonstrations d'imagerie soulignons, entre autres : la détection de cellules cancéreuses grâce à un contraste d'absorption d'eau, l'inspection des matériaux pour la détection de défauts de fabrication et l'inspection des colis pour des fins de sécurité.

Malgré la grande utilité de la lumière THz il reste encore de nombreux défis technologiques pour amener la technologie THz au grand public. Parmi les multiples problèmes, on compte l'efficacité faible et le coût élevé des sources THz, l'absorption de lumière THz par la vapeur d'eau dans l'air ambiant, ainsi que les longs temps d'acquisition pour mesurer les échantillons. Un des plus grands obstacles est le *guidage* de la lumière THz. Les applications industrielles nécessitent une distance entre la source THz et l'échantillon à mesurer. Toutefois, le guidage THz se fait actuellement

par la *propagation en espace libre* dans l'air à l'aide de miroirs métalliques. Idéalement, un guide d'onde flexible, avec de faibles pertes de propagation et de faibles pertes par rayon de courbure permettrait de manipuler la lumière THz d'une façon analogue à la lumière infrarouge proche qui est guidée par les fibres optiques.

Cependant, l'absorption matérielle est un obstacle majeur qui freine le développement d'un tel guide. Dans la bande THz, les métaux souffrent de pertes ohmiques considérables et les diélectriques ont des pertes d'absorption très élevées. Seuls les gaz ont des pertes négligeables (d'où la propagation dans l'air) et le développement de guides d'onde THz repose sur des techniques de guidage particulières qui augmentent la fraction de la puissance guidée dans l'air. Les deux stratégies de base pour réduire les pertes de propagation, tant pour les guides métalliques que diélectriques, sont :

1. le guidage unimodal par un champ évanescent sur une fibre dont le cœur est de petite taille et le champ guidé s'étend très loin dans l'air ambiant autour de la fibre.

2. le guidage multimodal par le confinement d'un champ dans un gros tube à cœur creux où une multitude de mécanismes servent à confiner la lumière par la réflection sur les parois du tube.

Dans cette thèse, nous avons choisi l'étude des guide diélectriques car ils offrent une plus grande flexibilité de design. Nous avons exploré les deux stratégies mentionnées ci-dessus. De nouvelles techniques de fabrication et de nouveaux montages de caractérisation ont été développés pour arriver à mesurer les nouveaux types de guides d'onde proposés. Finalement, une analyse approfondie nous a mené à proposer de nouveaux designs mieux adaptés pour remédier au problème persistant de pertes par rayon de courbure.

Chapitre 2

Afin de caractériser les spectres de transmission des guides d'onde fabriqués, nous avons développé et réalisé un montage innovateur de spectroscopie THz dans le domaine temporel. Pour la mesure des spectres THz, la spectroscopie par transformée de Fourier a été supplantée par la spectroscopie dans le domaine temporel, étant donné la plus grande luminosité des sources, la détection à la température ambiante, la plus grande résolution spectrale et la mesure de l'information de phase. Contrairement au montage standard qui mesure des échantillons ponctuels (généralement

des échantillons minces et plans), nous avons développé un montage qui a une longueur de chemin variable afin de recevoir des échantillons longs (des guides d'ondes) et de longueur variable. Un collimateur, comprenant des miroirs montés sur un rail de translation, peut facilement être déplacé pour introduire des guides d'ondes d'une longueur maximale de 50 cm.

Certains détails permettent de mieux saisir la complexité du montage. La source et le détecteur sont des antennes photo-conductrices identiques, qui consistent d'électrodes métalliques imprimées sur un substrat semi-conducteur. L'opération des antennes repose sur la focalisation d'une impulsion laser fs sur l'espace de 5 μm séparant les deux électrodes. L'absorption de l'impulsion laser génère des charges pendant un bref instant. Dans le cas de l'émetteur, une différence de potentiel est appliquée aux bornes de l'antenne et l'accélération des charges provoque un rayonnement THz large-bande. Dans le cas du détecteur, c'est le champ THz incident qui crée la différence de potentiel et le courant engendré est proportionnel au champ THz.

La particularité fondamentale est que le détecteur mesure le *champ électrique* et non la puissance. Donc, la détection se fait par un échantillonnage point par point du champ THz dans le domaine temporel. Ceci implique l'utilisation d'une ligne à délai pour faire varier le délai entre l'arrivée de l'impulsion THz sur le détecteur et le déclenchement du détecteur (pour l'échantillonnage d'un point). L'alignement optique doit être précis afin de focaliser correctement sur l'antenne et empêcher une déviation du faisceau lorsque la ligne à délai se déplace. De plus, toute l'optique THz doit être alignée soigneusement pour maximiser le signal qui se rend au détecteur, surtout dans le cas de notre montage car le collimateur peut être translaté. Finalement, tout le montage est enfermé dans une cage purgée à l'azote afin d'éliminer l'absorption par l'humidité dans l'air.

Une longue section est dédiée à l'énumération des problèmes d'alignement du montage. Les solutions qui ont été trouvées sont également énumérées car peu ou pas d'information à cet égard n'est disponible dans la littérature.

Chapitre 3

Nous avons commencé par l'étude de la première stratégie pour la réduction des pertes d'absorption en développant un guide d'onde de diamètre inférieur à la longueur d'onde guidée. L'exemple le plus simple, proposé par un groupe de l'Université Nationale de Taiwan, est simplement un fil de plastique suspendu dans l'air. Cette

fibre à deux couches comprend un cœur solide de diamètre (d_{coeur}) inférieur à la longueur d'onde guidée ($\lambda \leq d_{\text{coeur}}$) et l'air environnant qui agit comme gaine optique. La fibre est unimodale et le couplage dans la fibre est efficace puisque le mode est linéairement polarisé. Le mode guidé a un champ évanescent qui s'étend très loin dans l'air, ce qui entraîne de faibles pertes de propagation de l'ordre de $\sim 0,01$ cm^{-1}.

Dans le but de réduire davantage les pertes d'absorption, nous avons proposé d'ajouter des trous à la fibre. L'ajout des trous crée une porosité qui augmente la fraction de puissance guidée dans l'air. Des simulations démontrent que la diminution du diamètre et l'augmentation de la porosité augmentent la fraction de puissance guidée dans l'air et réduisent les pertes de propagation. L'inconvénient est que le mode est moins confiné dans le coeur et par le fait même plus susceptible aux pertes par diffusion, sur les défauts de fabrication, ou aux pertes par courbure.

Des fibres de polymère ont été fabriquées par un processus d'étirage. Une version macroscopique de la fibre, dite préforme, est préparée avec la géométrie désirée. La préforme est ensuite chauffée et étirée en forme de fibre à l'aide d'une tour d'étirage. La technique standard pour la fabrication des fibres poreuses, empruntée aux travaux sur les fibres à cristaux photoniques, consiste à empiler des tubes pour former une préforme. Un problème réside dans le fait que, sans aide extérieure, les trous de la fibre poreuse ont tendance à se fermer lors de l'étirage. Trois nouvelles méthodes de fabrication ont été développées pour remédier à ce problème.

La première méthode consiste à emprisonner de l'air à l'intérieur de la préforme en scellant les tubes empilés avec de la colle. Lors de l'étirage, l'air emprisonné crée une pression qui contre-balance les forces de rétreint des trous. Bien que les trous restent ouverts, ils ont tendance à rétrécir quand même, et après plusieurs essais et erreurs nous obtenons une fibre avec 25% de porosité.

La deuxième technique est basée sur l'utilisation d'un polymère sacrificiel. Des tiges de polymère B sont enveloppées de polymère A de façon à former une préforme *entièrement solide*. L'étirage d'une préforme solide élimine complètement les problèmes de rétrient des trous. Par la suite, les tiges de polymère B à l'intérieur de la fibre sont sélectivement dissoutes dans un solvant afin de révéler des trous d'air. Cette technique a donné des fibres ayant une porosité de 35% mais elle est limitée par la longueur de fibre pour laquelle le polymère sacrificiel peut être complètement dissous.

La dernière technique consiste à mouler la préforme de polymère et à étirer la fibre en injectant de l'air sous pression dans les trous. Bien que nous ayons atteint

une porosité élevée de 86%, la technique d'étirage sous pression reste capricieuse et il est difficile d'empêcher la déformation de la fibre.

Afin de comparer les pertes de propagation des fibres poreuses et non-poreuses, nous avons collaboré avec un groupe de l'université de Sherbrooke pour faire des mesures de transmission. Suite à des problèmes techniques, nous avons développé une nouvelle méthode pour mesurer les pertes de propagation. Cette méthode consiste à placer une fibre *sonde* à proximité de la fibre *échantillon* de façon à former un coupleur évanescent. En translatant le coupleur le long de la fibre échantillon, le signal couplé dans la fibre sonde et acheminé vers le détecteur est atténué. La mesure de cette atténuation permet d'estimer les pertes de propagation. La méthode est non-destructive et permet en principe une plus grande précision dans la détermination des pertes par un plus grand échantillonnage de l'atténuation en fonction de la distance de propagation. Toutefois, il n'en résulte qu'une valeur moyenne de l'atténuation puisque le détecteur intégrait toutes les fréquences. Nous avons déterminé que la fibre sonde agissait comme un filtre de fréquences passe-bas et nous estimons que la fréquence moyenne de la mesure était d'environ 0,2 THz.

Une meilleure comparaison a été faite en mesurant les spectres de transmission des fibres poreuses et non-poreuses par la spectroscopie dans le domaine temporel. Les pertes d'absorption à hautes fréquences et les pertes par diffusion à basses fréquences engendrent un minimum dans les pertes de propagation. La porosité des fibres réduit les pertes d'absorption, mais le confinement plus faible de la lumière augmente les pertes par diffusion. Expérimentalement, nous mesurons des pertes similaires pour les fibres poreuses et non poreuses, de l'ordre de $0,02$ cm^{-1}. Les spectres de transmission révèlent plutôt que l'avantage des fibres poreuses est la capacité de guider la lumière à des plus hautes fréquences et avec des pics de transmission plus larges.

Pour ces guides, les pertes par courbure sont extrêmement élevées étant donné le faible confinement du mode guidé. Néanmoins, les fibres peuvent tolérer des déflexions de petits angles ($\sim 2^\circ$) autour d'un point et il y a déjà eu des démonstrations d'imagerie à l'aide des fibres à cœur solide.

Chapitre 4

La deuxième stratégie pour réduire les pertes de propagation repose sur le confinement de la lumière à l'intérieur d'un gros tube creux. Nous avons exploré cette stratégie en considérant deux mécanismes différents pour confiner la lumière à l'intérieur du

tube : la réflexion anti-résonante d'un résonateur Fabry-Pérot et la réflexion Bragg d'un miroir multicouches. Une caractéristique fondamentale des guides creux est que les pertes de propagation suivent une loi d'échelle $1/(f^2d^3)$, où f est la fréquence guidée et d est le diamètre du cœur. On note qu'une réduction substantielle des pertes peut être réalisée en augmentant le diamètre du cœur mais le guide devient hautement multimodal.

Le premier type de guide creux consiste tout simplement en un tube de polymère. Les réflexions sur les parois internes et externes du tube créent un résonateur Fabry-Perot. Les réflexions multiples à l'intérieur de la paroi créent de l'interférence constructive ou destructive selon l'épaisseur du tube et la fréquence. La réflectivité résultante est périodique en fréquence et la période est inversement proportionnelle à l'épaisseur de la paroi. D'un point de vue technologique il est plus intéressant d'augmenter la largeur des pics de transmission du tube (pics de réflexion de la paroi) en diminuant l'épaisseur de la paroi du tube.

La mesure des spectres de transmission de tubes à parois minces et épaisses confirment la résonance Fabry-Pérot comme mécanisme de guidage. Toutefois, le régime multimodal rend le couplage extrêmement sensible à l'alignement et la mesure des pertes de propagation s'est avérée impraticable par manque de reproductibilité. De plus, la déformation des tubes engendre des variations spectrales et les tubes à parois minces sont plus susceptibles d'être déformés étant donné leur moins bonne rigidité mécanique. Un calcul simple, basé sur une méthode de rayons optiques, permet d'estimer les pertes par rayon de courbure. La réflectivité du résonateur Fabry-Perot baisse rapidement lorsque l'angle d'incidence d'un rayon décroît et conséquemment les pertes par courbures sont très élevées ($\geq 0,1$ cm^{-1}). L'utilité de simples tubes est donc très limitée.

Le deuxième type de guide creux considéré est la fibre de Bragg. Il s'agit d'un tube dont la paroi est constituée d'un empilement de couches à symétrie circulaire, où il y a une alternance de couches d'indice de réfraction élevé et faible. Les réflexions multiples à l'intérieur du système multicouches créent des bandes de fréquences interdites (dites *bandgaps*) où l'interférence constructive donne lieu à une réflexion efficace. L'empilement forme donc un miroir diélectrique confinant la lumière dans le cœur creux.

Puisque le contraste d'indice entre les polymères est faible dans la bande THz, deux nouvelles techniques ont été essayées pour augmenter le contraste d'indice des

fibres de Bragg. La première comprend des couches d'air pour diminuer l'indice des couches de faible indice. Tandis que la deuxième comprend des couches de polymère dopé avec de la poudre de TiO_2 afin d'augmenter l'indice des couches d'indice élevé. Pour les fibres air-polymère, nous avons déposé de la poudre sur un film et roulé le tout autour d'un cylindre. La nouvelle fibre est entourée d'un mince film de téflon pour empêcher qu'elle ne se déroule lorsque le cylindre est retiré. Les particules de poudre agissent comme des blocs séparateurs pour forcer une couche d'air entre les couches de polymère. Pour les fibres de polymère dopé, nous avons mélangé 80% m/m (46% vol./vol.) de poudre de TiO_2 (diamètre $\sim 0,22$ μm) dans du polyéthylène à l'aide d'une extrudeuse. Une deuxième extrudeuse a été utilisée pour fabriquer un film de polymère dopé. Le film dopé a été écrasé dans une presse pour l'amincir. Des bandes de film aminci ont été pressées contre un film de polyéthylène pur pour former une bi-couche et cette bi-couche a été roulée et solidifiée pour former la fibre de Bragg.

Les mesures de spectres de transmission et les simulations des guides d'onde ont révélé qu'il n'y a pas vraiment de réflexions Bragg dans le cas des modes HE de la fibre de polymère dopé car les pertes d'absorption de ce polymère étaient trop élevées. Dans le cas de la fibre air-polymère les simulations de pertes révèlent des modes HE avec des pertes très faibles. Une mesure expérimentale des pertes de propagation s'est avérée impossible étant donnée la sensibilité du couplage à l'alignement. Les simulations de la transmission ne concordent pas très bien avec les résultats expérimentaux car de nombreux défauts de fabrication ne sont pas inclus dans le modèle et, expérimentalement, un couplage décentré (en dehors de l'axe optique) peut être mis en cause.

Malgré les problèmes de fabrication actuels, les fibres de Bragg offrent des régimes de transmission intéressants. Plusieurs calculs ont été faits pour élucider et mieux comprendre les deux régimes d'opération fondamentalement différents des deux fibres de Bragg fabriquées. Dans un régime, un angle de Brewster existe à l'intérieur de l'empilement multicouches, tandis que dans l'autre régime les indices de réfraction sont tels qu'un angle de Brewster n'existe pas. L'angle de Brewster affecte grandement les pertes de propagation des modes TM et HE. Nous avons prédit qu'avec des couches d'air et un *faible contraste* d'indice les modes HE ont des pertes très faibles. De plus, un nouveau design ayant des couches d'air et un *grand contraste* d'indice est proposé. Dans ce cas l'angle de Brewster approche l'indice rasante, soit les angles d'opération des fibres de Bragg, et les pertes des modes HE et TM deviennent très

élevées. En contrepartie, les pertes de modes TE demeurent très faibles.

Chapitre 5

Il y avait tellement d'idées pour les perspectives futures des guides d'onde diélectriques dans les THz que des investigations préliminaires méritaient un chapitre en soi. Nous avons d'abord révisé les fibres de Bragg pour trouver de meilleurs dopants. Ensuite, nous avons évalué les pertes par courbure et étudié la faisabilité d'un régime unimodal pour les fibres de Bragg. Finalement, nous avons proposé deux nouveaux types de guides d'onde qui fonctionnement par réflexion totale interne.

Dans un premier cas, nous avons vu que le choix de la poudre TiO_2 pour doper le polymère engendrait des pertes d'absorption trop élevées. Des calculs de l'indice de réfraction moyen des mélanges polymère-dopant révèlent des alternatives intéressantes. Pour la diminution d'indice, nous avons considéré les mousses de polymères qui peuvent être traitées en considérant un dopage par des bulles d'air. Les mousses sont des matériaux prometteurs car les pertes d'absorption peuvent être réduites significativement. Pour l'augmentation d'indice nous avons considéré le silicium et les métaux. Même si on s'attend que le dopage avec des particules de silicium *réduise* les pertes, l'augmentation d'indice qui peut être atteinte n'est pas suffisamment grande pour être intéressante. Une alternative plus prometteuse est le dopage avec des particules de métal, juste en dessous du seuil de percolation où le mélange se comporte encore comme un diélectrique avec des faibles pertes. Un dopage de 25% vol./vol. de poudre de cuivre dans du polyéthylène donnerait un indice de 3,0 avec des pertes $< 0,5\ \mathrm{cm}^{-1}$.

Des simulations de fibres de Bragg incorporant ces nouveaux mélanges ont été effectuées. Les pertes de propagation des modes TE des fibres dopées au métal sont extrêmement faibles. Nous avons également démontré qu'en utilisant des couches de mousse pour les couches d'indice faible, il est possible de s'approcher d'un design idéal où l'angle de Brewster à l'intérieur de l'empilement multicouche atteint l'incidence rasante de 90°. Par conséquence, il n'y a plus de réflexion Bragg pour les modes HE et TM, qui sont plutôt guidés inefficacement par une réflectivité de type Fabry-Pérot. Nous avons également étudié les pertes par courbure des différentes fibres de Bragg. Nous arrivons à la conclusion que les pertes des modes TE sont très faibles et que les pertes par courbure peuvent être utilisées comme mécanisme pour éliminer les modes HE et TM.

Bien que l'augmentation du diamètre du coeur d'une fibre à cœur creux permette de diminuer significativement les pertes, la fibre guide dans un régime hautement multimodal qui engendre des problèmes de couplage où il est difficile d'exciter uniquement le mode fondamental. Pour clore le sujet des fibres de Bragg nous avons étudié le potentiel d'un régime unimodal. La technique la plus simple pour diminuer le nombre de modes guidés est de réduire le diamètre du cœur. Toutefois, des simulations démontrent que dans la bande THz les pertes d'absorption deviennent trop élevées pour permettre un régime unimodal dans une fibre avec un coeur de faible taille. Une alternative consiste à exploiter la différence entre les pertes de propagation des différents modes afin d'éliminer tous les modes sauf un. Si la fibre est assez longue, tous les modes sauf le mode de plus faible perte sont éliminés et la fibre devient unimodale *de facto*. Un design de fibre de Bragg avec l'angle de Brewster à incidence rasante ainsi que les pertes par courbure peuvent aider à éliminer les modes HE et TM. Toutefois il faut trouver le diamètre optimal pour le coeur afin d'éliminer le mode TE_{02} sans encourir de trop grosses pertes pour le mode TE_{01}. Seul le mode TE_{01} permettrait un régime unimodal donc un convertisseur de mode simple est proposé afin d'augmenter l'efficacité de couplage dans le mode TE_{01}.

Par ailleurs, une démonstration importante d'un guide d'onde multimodal de polyfluorure de vinylidène (PVDF) a révélé qu'un simple tube pouvait guider la lumière THz avec de faibles pertes de propagation et d'assez faibles pertes par rayon de courbure. Dans ce cas-ci la lumière est guidée par réflexion totale interne atténuée, car il y a une bande de fréquences (1 à 2 THz) où le polymère est dans un régime de dispersion anormale et l'indice de réfraction est < 1. Par conséquence, le cœur creux d'un tube devient le milieu d'indice *élevé* qui confine la lumière par réflexion totale interne. Le régime est dit atténué car la bande de fréquences propices se trouve à proximité d'un pic d'absorption. Néanmoins, avec la taille du cœur les pertes de propagation peuvent être très faibles. Le problème c'est que le PVDF est un polymère semi-cystallin et il doit être "pôlé" électriquement afin d'induire la bonne phase cristalline ayant le régime $n < 1$. Cette étape de "poling" est très difficile et rend ce type de guide peu attrayant. Toutefois, suite à de nombreuses recherches, nous avons trouvé des indices qui laissent croire que d'autres matériaux, les copolymères P(VDF-TrFE), pourraient remédier aux problèmes de fabrication. Les copolymères P(VDF-TrFE) cristallisent *automatiquement* dans la bonne phase et l'orientation nécessaire des cristaux dans le sens de la longueur du tube devrait se faire automatiquement lors du processus de

fabrication (étirage ou extrusion). Ce type de guide est fort prometteur car la technique de fabrication est très simple (il ne s'agit que d'un tube) et ne nécessite pas de "poling" électrique.

Pour le dernier design nous étudions le potentiel d'utiliser des mousses de polymère pour guider la lumière par réflexion totale interne. Nous proposons une fibre à deux couches où le cœur et la gaine optiques sont des mousses de porosité différentes. L'objectif principal est de faire le design d'une fibre dont les pertes par courbure sont *négligeables*. Il faut donc un grand confinement de la lumière dans le coeur et des simulations démontrent que les pertes de propagation du mode tendront vers la perte d'absorption matérielle du cœur. De faibles pertes de l'ordre de $0,02$ cm^{-1} devraient être atteignables grâce à la porosité de la mousse. De plus, nous avons examiné les bandes de transmission de fibres de différentes tailles. L'exigence d'un régime unimodal impose une fréquence maximale. Par ailleurs, une fréquence minimale est imposée par la condition d'avoir des pertes par courbure négligeables. Une augmentation du diamètre du cœur de la fibre permet de guider des fréquences plus faibles mais la largeur de bande est rétrécie. Finalement, l'encadrement de la fibre de mousse par un gros tube de polymère permet d'augmenter la rigidité mécanique, de réduire les pertes de couplage avec l'environnement et d'isoler la lumière THz de l'humidité dans l'air, empêchant ainsi les pertes d'absorption par la vapeur d'eau.

Chapitre 6 : Conclusion

Au cours de cette thèse, nous avons développé une multitude de nouveaux guides d'ondes, ainsi qu'un nouveau montage de spectroscopie dans le domaine temporel spécifiquement adapté pour la mesure des guides. Toutefois, il reste place à de nombreuses améliorations.

Quant au montage de caractérisation, nous avons réussi à mesurer des pertes de propagation sur des guides droits mais nous sommes mal équipés pour mesurer les pertes par rayon de courbure. Même si une fibre pouvait être enroulée sur elle-même il serait préférable d'avoir un détecteur qui suit le bout de la fibre courbée. Ceci nécessiterait un détecteur amovible tel une antenne photo-conductrice couplée à une fibre optique. De plus, nous avons encore des problèmes à purger correctement la cage entourant le montage. Les temps de purge sont longs et il y a des pics résiduels d'absorption d'eau dans les spectres mesurés. Une purge sous vide serait peut-être préférable. Finalement, le temps d'acquisition d'un spectre pourrait être réduit en

modulant le voltage de l'émetteur ou en utilisant le taux de répétition du laser comme fréquence de référence.

Quant aux guides d'onde, un des problèmes majeurs qui persiste est l'absorption d'eau. Dans un cadre de recherche, toutes les mesures sont faites dans un environnement contrôlé, mais dans un cadre pratique le guide d'onde baignerait dans l'humidité ambiante. Pour remédier à cette situation il serait nécessaire de sceller de l'air sec à l'intérieur d'un guide d'onde creux. Ce problème est rarement mentionné dans la littérature et nous avons proposé un type de guide d'onde qui isole automatiquement la lumière THz de l'air ambiant. Par ailleurs, la dispersion dans les guides d'onde est souvent reprochée comme une propriété néfaste. En fait, la dispersion est néfaste car la spectroscopie dans le domaine temporel utilise des impulsions fs (engendrant des impulsions THz ps). Si, toutefois, la spectroscopie était faite dans le domaine des fréquences avec une source à fréquence balayée (soit des sources continues ou à impulsions longues), alors la dispersion ne serait pas un problème. Il est à noter que de telles sources existent, mais que le temps de balayage actuel est trop lent. En fait, il y a une raison fondamentale pour promouvoir le développement de sources balayées. Pour les applications industrielles, le laser de pompe de la source THz devra être séparé de plusieurs dizaines de mètres de l'échantillon. Il est peu probable qu'un guide d'onde THz puisse atteindre une propagation sur 100 m. Donc il est plus réaliste d'envisager une génération THz à distance et pour ce faire les sources laser balayées sont plus avantageuses que les lasers fs. Dans l'optique où la génération THz se fait à distance, il n'est pas nécessaire d'avoir un long guide d'onde THz pour manipuler la lumière. Un guide d'onde d'un mètre serait suffisant pourvu que les pertes par courbure soient suffisamment faibles. Ce sont ainsi les pertes par courbure qui vont départager les différents types de guide d'onde.

Pour les perspectives de recherches futures, il est recommandé de travailler sur des sources ou des convertisseurs de modes afin de générer un mode TE qui faciliterait le développement d'une fibre de Bragg unimodal TE_{01}. De plus, l'extrême simplicité d'un tube pour guider la lumière motive une étude approfondie des copolymères P(VDF-TrFE). Finalement, les fibres en mousse de polymère méritent une attention particulière étant donné l'élimination du problème d'absorption d'eau, les pertes par courbure négligeables et des bandes de transmission potentiellement plus larges que celle des fibres de Bragg.

Contents

List of Tables

List of Figures

List of Appendices

List of Symbols and Abbreviations

α	Propagation loss coefficient
α_{eff}	Effective propagation loss of mode (includes absorption and radiation losses)
ABS	Poly(acrylonitrile-butadiens-styrene)
ARR	Anti-Resonant Reflection
ATIR	Attenuated Total Internal Reflection
BWO	Backwards Wave Oscillator
c	Speed of light in the vacuum
CW	Continuous-Wave
DFG	Difference Frequency Generation
EO	Electro-Optic
ESMR	Effectively Single-Mode Regime
ϵ_c	Permittivity of composite material
ϵ_C	Permittivity of waveguide core
ϵ_d	Permittivity of dopant material
ϵ_h	Permittivity of host material
ϵ_H	Permittivity of high refractive index layer
ϵ_L	Permittivity of low refractive layer
f	Frequency of light
f_V	Volume fraction of a dopant within a host material
FEL	Free Electron Laser
FWHM	Full-Width Half-Maximum
HDPE	High density poly(ethylene)
HE	Hybrid mode with magnetic (H_z) field dominating electric (E_z) field
ID	Inner Diameter
λ	Wavelength of light, field decay rate (eigenvalue)
	in the case of Bragg reflectors
Λ	Hole-to-hole pitch between air holes of porous fibers
LLDPE	Linear low density poly(ethylene)
n	Index of refraction
n_{eff}	Effective index of mode

NIR	Near Infra-Red ($\sim \lambda = 0.8 - 3.0$ μm)
OR	Optical rectification
PA 6	Poly(amide nylon-6)
PC	Poly(carbonate)
PC	Photo-Conductive
PE	Poly(ethylene)
PET	Poly(ethylene terephthalate), (polyester, mylar)
PMMA	Poly(methyl methacrylate)
PP	Poly(propylene)
PS	Poly(styrene)
PTFE	Poly(tetrafluoroethylene)
PVDF	Poly(vinylidene fluoride)
QCL	Quantum Cascade Laser
SCFH	Standard Cubic Foot per Hour
TDS	Time-Domain Spectroscopy
TE	Transverse Electric
THz	Terahertz (frequencies)
TM	Transverse magnetic
TOPAS	TOPAS® Cyclic Olefin Copolymer (ethylene, norbornene)
TrFE	Tri-fluoroethylene
VDF	Vinylidene fluoride
WT	Wall Thickness

Chapter 1

INTRODUCTION

The adjective *THz* (10^{12} Hz) has become synonymous with the far infra-red region of the electromagnetic spectrum, with frequencies, f, ranging approximately from 0.1 to 4 THz (wavelengths, λ, ranging from 3000 μm to 75 μm, respectively). Unfortunately the study of THz radiation has been plagued by serious technological challenges in generating and detecting THz light. Despite the potential for many interesting applications, THz technology has remained "in reach within the next 5 years" for the past three decades.

Thanks to recent advances in detection and generation (notably cheaper fs lasers and commercially available photo-conductive antennae), there has finally been an explosion of research on THz applications. It has gotten to the point where entire books are devoted to THz applications [1, 2]. The two main applications are spectroscopy and imaging. In terms of spectroscopy, near-infrared vibration bands only yield signatures of chemical bonds and small molecules, whereas the relatively low THz frequencies now give insight into the vibration bands of macro-molecules. Among a wide range of spectroscopic studies, we find demonstrations of the label-free detection of DNA and proteins [3, 4], the study of the vibrational dynamics of proteins and amino acids [5, 6], the detection of explosives [7], as well as optical-pump/THz-probe experiments to study the carrier dynamics of semiconductors and superconductors [8]. In terms of imaging, the longer wavelengths penetrate more deeply into a wide variety of dielectrics due to the reduced Rayleigh scattering ($\sim \frac{1}{\lambda^4}$), offer a higher spatial resolution than microwaves (of even longer wavelengths), and contrary to X-Rays the THz-rays are non-ionizing. A wide range of imaging modalities have been developed including: transmission [9], reflection [10], time-of-flight [11], near-field [12], computed tomography [13], and synthetic aperture imaging [14]. Among the more important imaging applications we find: cancer detection [15, 16] due to the water retention of cancer cells, non-destructive material inspection for the detection of mechanical defects [17], process control (such as monitoring polymer extrusion [18] or the forma-

tion of pharmaceutical tablets [19]), security screening/package inspection [20, 21], and Laser-THz -Emission imaging for inspecting faults in semiconductor circuits [22]. A few examples of these applications are presented in Fig. 1.1.

Despite many proof of concept demonstrations, THz technology still remains largely confined to laboratory experiments. This is due in part to the few products that are commercially available (less than a handful of companies offer THz products) and in part to many technological hurdles that still remain. Among these obstacles we count the low power of THz sources (due to low generation efficiencies), the relatively expensive fs pump lasers (typically $> 50\,000$\$), and the long signal acquisition times (due to long detector integration times and slow delay line speeds). Moreover, one of the largest remaining hurdles is *THz waveguiding*. Real-world applications require a stand-off distance between the THz source and the sample. However, current THz systems rely on the use of *free-space propagation* via carefully aligned metallic mirrors. This increases the cost and complexity of the systems, not to mention the considerable amount of time that must be spent to properly align the mirrors. Ideally, this stand-off distance would be enabled by a flexible, low propagation loss, low bending loss, single-mode THz waveguide akin to the simple-to-use near-infra-red optical fibers. Unfortunately, no such THz waveguide currently exists and the main culprit is prohibitively high material absorption.

In the THz regime, the finite conductivity of metals results in ohmic losses that yield high propagation losses in metallic waveguides. Similarly, dielectric waveguides suffer from the high THz absorption of dielectrics. The lowest absorption loss occurs in gases, hence the traditional use of free-space propagation in air[1]. Thus, to lower the propagation loss of THz waveguides, methods must be devised to increase the fraction of power guided in air. The two known strategies[2] are the following:

1. a small-core fiber is used to obtain an evanescent mode, with the tail of the guided field extending far into an air cladding,

2. a large hollow core tube is used, where different tube wall reflection schemes confine the light within the hollow core.

[1] Actually there is a further constraint of using *dry* air in order to avoid the high THz absorption loss of water vapor (humidity), but this fact will be addressed in further detail in section 2.5.

[2] It should be noted that these strategies do not address the problem of water vapor absorption and it is assumed that the waveguide is in vacuum or a dry air environment. The water vapor problem for THz waveguiding is rarely addressed in the literature and a solution will be provided in section 5.5.6.

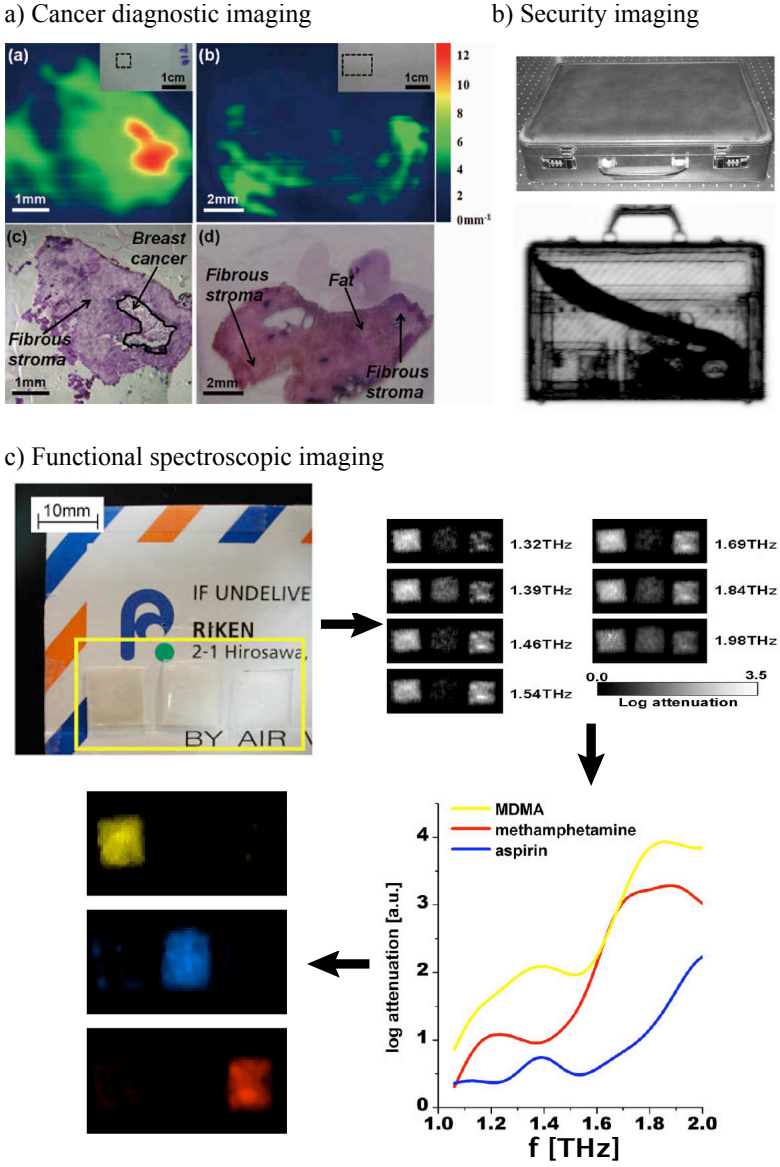

Figure 1.1 Examples of THz imaging applications. a) Medical imaging for the label-free detection of cancerous tissue (having a higher water concentration); adapted from [16]. b) Security imaging for the inspection of luggage (non-ionizing and higher resolution than microwaves). Contrast stems from differences in absorption and from reflection off metals; adapted from [20]. c) Functional imaging whereby spectroscopy gives additional information for analyzing the image (in this case identification of illicit substances in mail parcels due to differences in absorption spectra); adapted from [21].

The first strategy yields a single-mode waveguide, whereas the second strategy generally yields a highly multi-mode waveguide. It should be noted that the core size (d_{core}) of a hollow-core waveguide is of great importance since the propagation loss (α) generally scales according to $\alpha \sim \frac{1}{f^2}\frac{1}{(d_{\text{core}})^3}$ [23, 24] (see appendix A for a proof and more references).

1.1 Review of literature

In the past few years, a considerable amount of research has been devoted to exploring the development of these two waveguiding strategies and we shall now consider a review of the literature on THz waveguides to see the extent of the absorption problem and the current state of the art.

Tables 1.1 and 1.2 respectively compare the various metallic and dielectric THz waveguides in order of decreasing propagation loss. Traditionally, the power propagation loss, α, is given in units of cm^{-1} due to the high material absorptions. The following rules of thumb can be useful for understanding the tables,

$$\lambda\ [\mu\text{m}] = \frac{c}{f} \approx \frac{300\ [\text{THz}\cdot\mu\text{m}]}{f\ [\text{THz}]}, \tag{1.1}$$

$$\alpha\ [\text{dB/cm}] = 10\log_{10}(e^1)\cdot\alpha\ [\text{cm}^{-1}] \approx 4.3\cdot\alpha\ [\text{cm}^{-1}], \tag{1.2}$$

where c is the speed of light.

Also useful is the notion of absorption length, $L_\alpha \equiv \frac{1}{\alpha}$: a power loss of ~ 4.3 dB occurs over a distance of one absorption length. Considering that a typical THz setup has a power dynamic range of ~ 40 dB (limited mainly by available THz power), the absorption length can help get an appreciation for the length of waveguide that can transmit a measurable signal.

In tables 1.1 and 1.2, the first column presents a schematization of the waveguide geometry. Whenever possible a scale bar corresponding to 300 μm is shown in order to compare the relative scale of the different geometries. The subsequent columns give values of power propagation loss that were measured at a frequency f, for waveguide segments of length L.

1.1.1 Metallic waveguides

The first metal waveguides were metallic strip wires on semiconductors [25]. They were meant to be an extension of photoconductive antenna sources for compact integrated-optic THz systems, but the losses were prohibitively high. Borrowing ideas from microwave guides, circular and rectangular metal waveguides were also studied [26, 27]. However, the small core size of the tubes lead to relatively high losses.

In order to reduce the loss we see the first application of the large hollow-core waveguiding strategy with the development[3] of metallized tubes [32, 33, 34]. Since the propagation loss is proportional to $\frac{1}{d_{\text{core}}^3}$, by increasing the core size from 300 μm to 1-3 mm the loss was reduced by a few orders of magnitude. In order to have a large core metal tube that remains flexible, the solution has been the metallization of the inner surface of flexible dielectric tubes (such as polycarbonate). Only thin metal layers on the order of 100 nm are required, because the skin depths of metals at THz frequencies are in the 10-100 nm range. Such metal layers are deposited by a liquid-phase chemical deposition technique. The surface roughness of plated layers is on the order of 10 nm [32] (negligibly small compared to the THz wavelength) and a dielectric metal halide coating (such as AgI) is typically added on top of the metal to increase the reflectivity. Bending losses as low as 10 dB/m at a bending radius of 20 cm were measured [33]. It is fair to say that metallized tubes are currently the most versatile THz waveguide despite their multimode nature. However, the liquid-phase deposition technique [34] limits the fiber length to a few meters at best.

Another type of waveguide that gained favor due to its simplicity is the parallel plate waveguide [35, 36, 37, 38, 39, 40]. Two highly polished metal plates are separated by a core distance typically on the order of 100 μm. With such a small core size and with the input electric field parallel to the plates, a single TEM (Transverse Electro-Magnetic) mode is guided with a moderately high loss. It has recently been shown that the parallel plate geometry can support orders of magnitude lower propagation loss in a large-core multi-mode regime [41, 42, 43]. With an input electric field *perpendicular* to the plates, the TE_1 (Transverse Electric) mode can be excited.

[3] Interestingly, 're-developpement' would be a more accurate description. Like parallel metal plates [28] and attenuated total reflection waveguides [29], metallized hollow tubes [30, 31] are strategies that were initially developed for microwave and mid-infrared (notably CO_2 laser) waveguiding, and that have now been recycled for THz waveguiding.

Table 1.1 Comparison of metallic THz waveguides. First column presents a schematization of the waveguide geometry. Whenever possible a scale bar corresponding to 300 μm (λ at 1 THz) is shown. Values of power propagation loss α are cited at frequency f for waveguide segments of length L. The year of publication and references are given, as well as the main drawbacks of each waveguide. (n): not to scale, (h): not to scale horizontally, $*$: upper bound estimate over the entire frequency range.

Schema	Type of guide	α [cm^{-1}]	f [THz]	L [cm]	Year	Ref.	Drawbacks
 (n)	**Metal on semiconductor** (Al on sapphire)	~10-100	1	0.52	1991	[25]	High loss
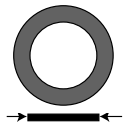	**Metal tube** circular (steel) rectangular (brass)	0.4-0.7	1	2.4	1999 2000	[26] [27]	High loss
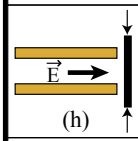 (h)	**Parallel metal plates** (Cu) (TEM mode)	~0.2*	0.5-3.5	2.5	2001	[35]	High loss No lateral confinement
(n)	**Metal sheet** (Al) (Zenneck plasmon)	0.046*	0.1-4.0	14	2006	[52]	High bending loss No lateral confinement
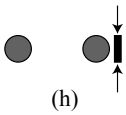 (h)	**Two-wire subwavelength guide** (stainless steel)	0.02	0.1-0.4	60	2009	[51]	No mechanical stability
 (n)	**Mettallized tube** (Ag/SiO_2) (d_{core} = 3mm) (Cu/PC) (d_{core} = 2.2mm) (Ag/PS)	0.017 0.009 0.003	1.2-1.6 1.89 2.5	60 130 80	2007 2004 2008	[32] [33] [34]	Limited length due to fabrication process
	**Subwavelength metal wire** (Cu) (Sommerfeld plasmon)	0.002	0.2	104	2004 2005 2010	[44] [48] [50]	High bending loss Coupling is difficult
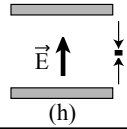 (h)	**Parallel metal plates** (Al) (TE mode) (d_{core} = 0.5mm) (d_{core} = 5mm)	6.2×10^{-3} 6×10^{-6}	1 1	2.5 2.5	2009	[42]	No lateral confinement

This mode was traditionally avoided due to the very high dispersion near its low cut-off frequency, but the increase of the core size has the double advantage of reducing the cut-off frequency and reducing the propagation loss. However, the extremely low loss of 6×10^{-6} cm^{-1} reported in Table 1.1 needs to be taken with a grain of salt since the core diameter was 1 cm. The loss of 6.2×10^{-3} cm^{-1} for a core diameter of 500 μm [42] is a better comparison to the other waveguides in the table. The disadvantage of parallel plates is that they lack lateral confinement of light and that is it difficult to make flexible waveguides of an appreciable length.

Finally, the other popular metallic waveguide is the subwavelength metal wire which supports a radially-polarized Sommerfeld plasmon mode [44, 45, 46, 47, 48]. In this case the mode has a large evanescent field that extends very far ($> 10\times$ the diameter of the wire) into the surrounding air cladding. With a large fraction of the power guided in air, this broadband waveguide has low propagation loss and low dispersion. However, the radially-polarized mode is very difficult to excite and the coupling efficiency for a typical linearly-polarized THz source is $< 1\%$. Radially-polarized radiation emitted from special radial photo-conductive antenna sources can increase the coupling efficiency to 50% [49], but such sources are not readily available. Moreover, the bending loss associated with Sommerfeld plasmons has been shown to be very high [48, 50]. Recent efforts with metallic wires have demonstrated the potential of a dual-wire waveguide suspended in air [51]. This waveguide supports a more easily excitable, lower bending loss, linearly-polarized TEM mode at the expense of a more complicated waveguide geometry that requires maintaining a constant sub-millimeter distance between the two wires.

1.1.2 Dielectric waveguides

An even greater amount of papers have been published on dielectric THz waveguides. This is perhaps due to the greater variety of available materials and to the greater flexibility in waveguide design. Although Table 1.2 offers an ensemble view of the structures tested so far, the waveguides are not all on equal footing in terms of dispersion, transmission bandwidth, and bending loss. Even the comparison of propagation loss is not a truly fair comparison because tube waveguides of different core size are being compared.

The vast majority of dielectric THz waveguides are made with polymers. Polymers

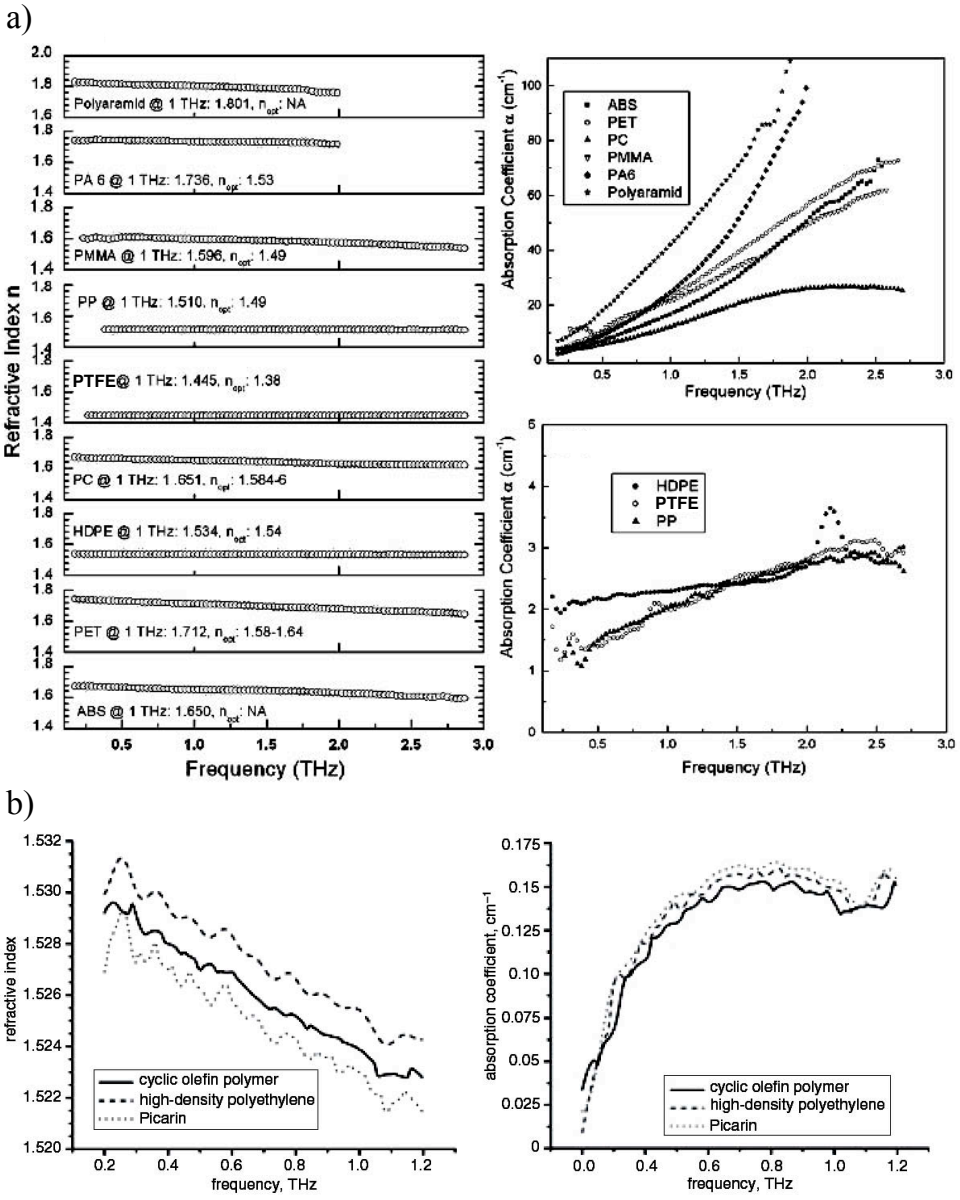

Figure 1.2 THz refractive index and absorption loss of common commercial polymers. Literature values are reproduced here for convenient reference. a) Adapted from [53], b) Adapted from [54]. See 'List of Symbols and Abbreviations' for definition of polymer acronyms. Note the order of magnitude difference in the reported losses of HDPE. A similar order of magnitude difference is reported for PTFE [55].

are easy to process and appear to be the dielectric solids that have the lowest absorption in the THz spectral region. Literature values comparing the material parameters

of the most common polymers are reproduced in Fig. 1.2. It should be noted that the reported material parameters of polymers, such as those of poly(ethylene), can vary by up to one order of magnitude. The reason is that polymers actually define a *family* of materials. The final material parameters of a polymer depend not just on the type of monomer that is repeating itself, but also on the molecular weight (or length) of the polymer chains and the amount of connections (cross-linking) between those chains. Thus a variability exists among the different grades of a given polymer. Nevertheless, the absorption loss of polymers can be as low as ~ 0.15 cm^{-1}, making them the dielectric materials of choice.

Standard total internal reflection (TIR) waveguides suffer from prohibitively high material absorption losses. In fact, from the examples of Table 1.2, it can be seen that, regardless of the guidance mechanism, the propagation loss becomes prohibitively high if too much power is guided within a solid material core (even ~ 0.15 cm^{-1} is too high to be directly useful). Thus dielectric waveguides have also converged towards the two previously mentioned loss reduction strategies.

On one hand, we have the development of small-core single-mode subwavelength-diameter fibers [56, 57, 58, 59, 60, 61, 62]. The small core leads to an evanescent field extending far beyond the fiber core into the surrounding air cladding. Contrary to metal wire Sommerfeld plasmon waveguides, the fundamental mode supported by these dielectric fibers is the linearly polarized HE_{11} mode. Thus it is considerably easier to excite the fundamental mode and coupling efficiencies can exceed 90% (as will be shown in Fig. 3.2 of Chapter 3). Such fibers are currently among the waveguides that have the lowest propagation loss and the addition of an air hole within the core was recently proposed as a means of reducing the loss even further [60]. The compromise is that the bending loss is high in subwavelength diameter fibers due to the weak guidance of the evanescent mode. Nevertheless, it has been demonstrated that small-angle deflection loss, i.e. bending of a straight fiber about a fixed point by an angle $< 2°$, can be negligibly small. Thus, despite their limitations, subwavelength plastic fibers have been successfully integrated into a raster scanning imaging system [63, 64] and a near-field microscope [16]. Fig.1.1.a) is an example of an image taken from that near-field microscope.

Table 1.2: Comparison of dielectric THz waveguides. First column presents a schematization of the waveguide geometry. Whenever possible a scale bar corresponding to 300 μm (λ at 1 THz) is shown. Values of power propagation loss α are cited at frequency f for waveguide segments of length L. The year of publication and references are given, as well as the main drawbacks of each waveguide. (n): not to scale, (h): not to scale horizontally, $*$: upper bound estimate over the entire frequency range.

Schema	Type of guide	α [cm^{-1}]	f [THz]	L [cm]	Year	Ref.	Drawbacks
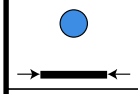	**Subwavelength rod** (sapphire)	~1.0	1	0.8	2000	[56]	High loss
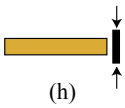 (h)	**Subwavelength film** (PE)	<1.0*	0.1-4.0	1	2000	[57]	High loss
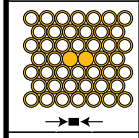	**Photonic Crystal Fiber** (PE)	0.92	1	2	2008	[65]	High loss
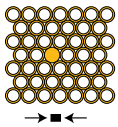	**Photonic Crystal Fiber** (PE)	<0.5*	0.1-4.0	2	2002	[66]	High loss
	**Microstructured fiber** (PMMA) ($d_{holes} << \lambda$)	~0.44	1	1.5	2008	[68]	High loss
	**1-hole subwavelength fiber** (SiO_2)	~0.41	0.5	4	2006	[60]	High loss
	**Photonic Crystal Fiber** (PTFE)	0.12*	0.1-4.0	15	2004	[55]	High loss

Continued . . .

Table 1.2 – Continued

Schema	Type of guide	α [cm^{-1}]	f [THz]	L [cm]	Year	Ref.	Drawbacks
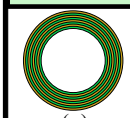 (n)	Doped-polymer Bragg Fiber	~0.042	0.69	22.5	2010	[76]	(see Chapter 4) Fabrication difficulties
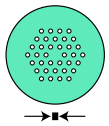	Photonic Crystal Fiber (TOPAS)	~0.035	0.5-0.6	4.6	2009	[69]	High dispersion Not flexible
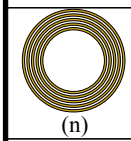 (n)	Air-polymer Bragg Fiber	~0.028	0.82	21.4	2010	[76]	(see Chapter 4) Fabrication difficulties
 (n)	n_{clad}<1 fiber (Poled PVDF)	~0.017	1-2	50	2005	[72]	Poling of PVDF is difficult
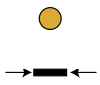	Subwavelength fiber (PE)	~0.01 ~0.04	0.3 0.12	17.5 38.4	2006 2010	[58] [62]	High bending loss (see Chapter 3)
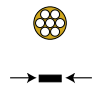	Porous subwavelength fiber (PE)	~0.012	0.25	38.5	2009 2010	[61] [62]	(see Chapter 3) (see Chapter 3) High bending loss
	Anti-resonant reflecting tube (PTFE)	~0.005	0.38	300	2009	[73]	High bending loss
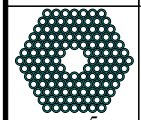 5mm	Photonic Crystal Fiber (PTFE)	~0.002	0.77	20	2008	[75]	Large Not flexible

On the other hand, there is the development of large hollow-core multi-mode tube waveguides. Confinement of light within hollow-core dielectric tubes has either been theorized or experimentally demonstrated using a wide variety of cladding reflection schemes that fall into four categories (see Fig. 1.3): photonic crystal reflection [65, 66, 55, 67, 68, 69, 70, 71], attenuated total internal reflection ($n_{\text{clad}} < 1$ using PVDF) [72], anti-resonant Fabry-Perot reflection [73, 74, 75], or Bragg reflection [76, 77, 78].

Firstly, photonic crystal reflection is the constructive interference between the multiple reflections of light scattering off a periodic array of scatterers. The interference is only constructive within a relatively narrow frequency window (known as the

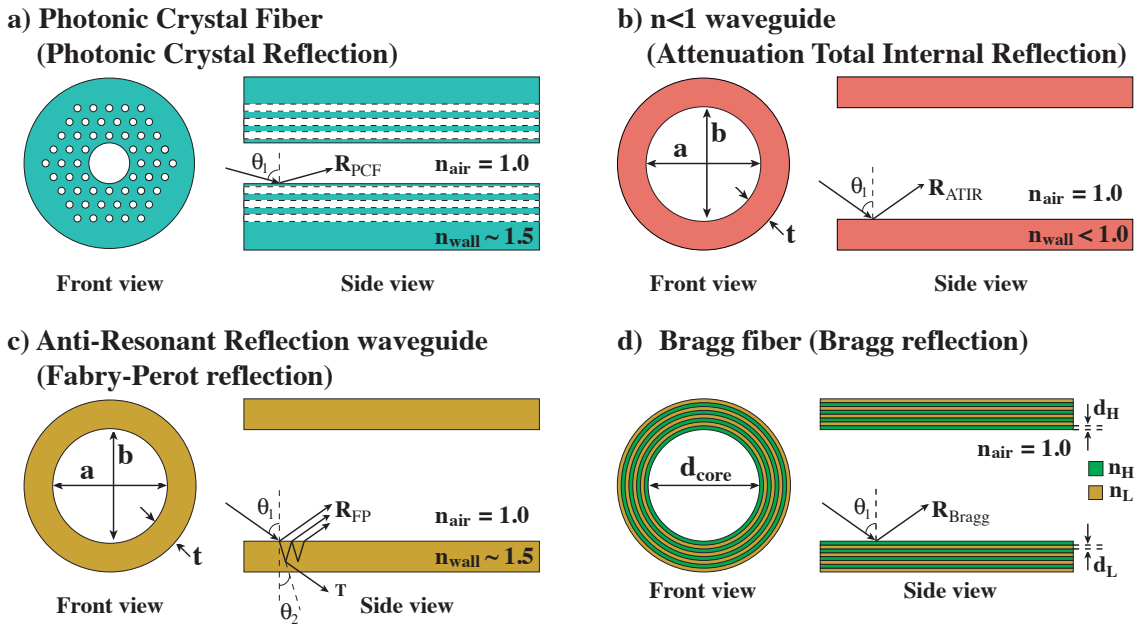

Figure 1.3 Schematization of hollow-core waveguide cladding reflection schemes.

bandgap of the reflector), and the scatterers are generally air holes having a diameter and separation (pitch) comparable to the wavelengths within the bandgap window. Since the wavelengths of interest are in the $300-3000$ μm range at THz frequencies, THz photonic crystals require rather large hole sizes. Moreover, the efficiency of the reflection increases with the number of periods in the photonic crystals. Therefore the total size of photonic crystal waveguides can become very large. The lowest loss reported for a photonic crystal waveguide is $\sim 2\times10^{-3}$ cm^{-1} for a 5 mm core diameter PTFE waveguide [75]. However, such a waveguide is impractical because of its size ($\sim$ 3.3 cm) and is probably inflexible as a result.

Secondly, the anomalous dispersion (decrease of the refractive index) on the high frequency side of an absorption peak can lead to a frequency region where $n_{\text{material}} < 1$. Curiously, a tube of such a material will guide the light within the air core by attenuated TIR. The reflection is said to be attenuated because the frequency band where $n_{\text{material}} < 1$ is in the vicinity of a strong absorption peak. Nevertheless, this guidance mechanism was actually shown to give one of the lowest reported propagation losses (~ 0.017 cm^{-1}). The bending losses were also shown to be ~ 0.023 cm^{-1} for a bending radius of 35 cm [72]. However, the problem is that the tube material, poly(vinylidene

fluoride) [4], must be electrically poled to align the chain into the proper crystal phase for the anomalous dispersion to occur. This makes the fabrication of this attenuated TIR waveguide exceedingly difficult.

Thirdly, anti-resonant reflection waveguides are simply single-layer tubes where the reflection stems from the tube wall acting as a Fabry-Perot resonator. The multiple reflections within the tube wall interfere to give a constructive resonator reflection or transmission at specific frequencies. 'Anti-resonant' is a somewhat confusing term meant to emphasize the use of the reflection of the Fabry-Perot resonator. Such a waveguide was proposed a long time ago [79] and was recently investigated experimentally [73]. It is easy to show that such a waveguide has a periodic transmission as a function of frequency and that the width (also the period) of the transmission peaks are inversely proportional to the tube wall thickness. The authors claim a record low loss for a *straight* dielectric waveguide [73], but 0.005 cm^{-1} is a little generous given the spread of their experimental points. More importantly, such a waveguide is of questionable use because of the high bending losses that result from the very strong incidence angle dependence of the Fabry-Perot wall reflectivity.

Fourthly, Bragg fibers are a special class of photonic crystal fibers where the geometry is circularly symmetric, and the Bragg reflector is a one dimensional photonic crystal that is periodic in the radial direction. The Bragg reflector consists of a periodic alternation of high and low refractive layers, where indices and thicknesses of the layers help determine the frequency region where the reflection will be most efficient (the reflector bandgap). The reflection will also be more efficient if the optical thickness of both the high and low index layers are the same (the maximum efficiency is for quarter wavelength thickness layers), and if the number of layers is increased. An important difference with respect to the two dimensional photonic crystals mentioned above is that the geometric thickness of the high refractive index layers of a Bragg reflector is shorter than the thickness of a ring of air holes in the photonic crystal. This can lead to more compact waveguides with a smaller outer diameter.

A comparison of theoretical simulations of hollow-core THz waveguides is also shown in Table 1.3. Very low losses are predicted with a sufficiently large core size, but the choice of materials and the very thin material bridges in some of the geometries makes these structures difficult to fabricate. It is also unfortunate that no simulations

[4]The monomer vinylidene fluoride is $C_2H_2F_2$, which is similar to ethylene (C_2H_4) and tetrafluoroethylene (C_2F_4, the precursor to Teflon^{TM}).

of bending losses have been provided.

Table 1.3 Comparison of simulations of hollow-core dielectric waveguides. Values of power propagation loss, α, are cited at frequency, f. Core size, d_{core}, is indicated because $\alpha \sim (d_{\text{core}})^{-3}$. The year of publication and references are also given.

Type of PCF	α [cm^{-1}]	f [THz]	d_{core} [m]	Year	Ref.
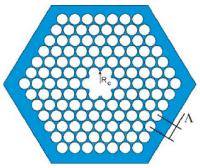 (PE)	~0.014 to 0.023	1.55 to 1.8	584	2008	[70]
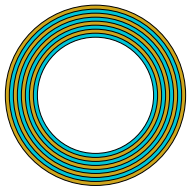 (Poled β-phase PVDF)	<0.023	1.0-2.0	2000	2007	[77]
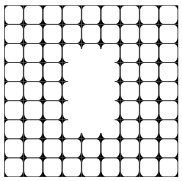 (PTFE)	<0.006	1.0-1.3	1125 x1875	2009	[71]
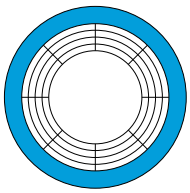 (HDPE)	<1.8x10^{-5}	1.5-4.3	16000	2007	[78]

The references in tables 1.1, 1.2, and 1.3 indicate the year of publication. A majority of the cited papers were published within the past four years, indicating that THz waveguiding is an active field of research and that these developments are concurrent with the work presented in this thesis. Furthermore, it can be seen that the current state of the art for α is in the $10^{-2} - 10^{-3}$ cm^{-1} range. The results of this thesis were also added to Table 1.2 for completeness, and they are seen to compare favorably with the literature.

1.2 Scope of this thesis

The goal of this thesis was to explore different types of dielectric structures in an attempt to guide THz radiation more efficiently. We therefore fabricated and characterized a variety of polymer waveguides, exploring both small-core single-mode and large-core multi-mode waveguiding strategies. In particular, porous subwavelength fibers, as well as air/polymer and doped/undoped polymer Bragg fibers were considered. For each type of waveguide, multiple fabrication methods were developed. Finally, in order to measure the transmission properties and propagation losses of these waveguides, two new measurement setups were developed. Specifically, a clever non-destructive technique using an evanescent directional coupler and a novel THz-TDS (Time-Domain Spectrocopy) setup that has an easily adjustable optical path length.

To better understand the characterization challenge, Chapter 2 begins by a brief introduction to far-infrared spectroscopy and THz sources and detectors. The standard THz-TDS setup is then explained in order to subsequently highlight the innovative design of the adjustable-path waveguide measurement setup. Some alignment difficulties are discussed, notably the alignment of parabolic mirrors, and the issue of water vapor absorption is addressed.

Chapter 3 begins with an overview of theoretical work on subwavelength dielectric fibers and the improved design of porous subwavelength fibers that was proposed by our group. We then discuss fabrication techniques, a novel Directional Coupler Method [61] for measuring the fiber propagation loss, and the clearer comparison between the transmission properties of porous and non-porous fibers that was obtained by using the adaptive THz-TDS setup described in Chapter 2 [62].

Chapter 4 presents the study of hollow-core waveguides. Initial investigations of single-walled dielectric tubes (anti-resonant reflection tubes) demonstrate the limitations of such waveguides. Hollow-core Bragg fibers were subsequently investigated in an attempt to increase the width of the transmission peaks and reduce the bending losses. Two strategies are presented for increasing the index contrast between the layers of the periodic Bragg reflector, in order to increase the efficiency of the Bragg reflection [76]. Methods of fabricating such fibers are discussed. Finally, the THz transmission experiments are analyzed.

Chapter 5 presents an overview of future design possibilities as many structures

remain to be tested. Topics range from better doping materials, single-mode Bragg fibers, attenuated TIR waveguides ($n_{\text{clad}} < 1$), and porous total-internal-reflection foam fibers.

Finally, chapter 6 concludes with a general discussion on THz waveguides, dispersion effects, and encapsulation to avoid water vapor absorption.

Chapter 2

Waveguide THz-TDS setup

In order to measure the transmission properties of THz waveguides, we require a setup that can accurately measure the THz spectrum of waveguides of different lengths. This seemingly simple task is far from trivial. Spectroscopy setups generally measure *point* samples and a conventional setup must be adapted to accommodate samples of variable length. Moreover, care must be taken to insure proper coupling of light into and out of the waveguide. In this chapter we discuss far-infrared spectroscopy and the design we implemented for a waveguide measurement setup.

We begin by discussing the fundamental differences between Fourier-Transform Infra-Red (FTIR) spectroscopy and Time-Domain Spectroscopy (TDS); explaining why TDS is preferable at THz frequencies. We then describe some generation and detection techniques, limiting ourselves to those generally used in TDS setups. This sets the stage for a detailed description of the standard THz-TDS setup, which is then contrasted with our design for a new adaptable-path-length setup. A special section is devoted to alignment issues and their solutions. Finally, we present a typical reference spectrum of the THz source and discuss the effects of water vapor absorption.

2.1 FTIR vs. THz-TDS

2.1.1 FTIR

Far-infrared (THz) spectroscopy was traditionally done with a Fourier-Transform Infra-Red spectrometer [80]. The output of a Michelson interferometer, measured with a *power* detector, is used to resolve frequency information. One arm is scanned such that the delay gives an interferogram and a Fourier cosine transform of the interferogram recovers the corresponding power spectrum, as illustrated in Fig. 2.1.

There are three reasons justifying the choice of interferometry to measure the THz spectrum: low source power, low detector sensitivity, and the high energy throughput

of a Michelson interferometer.

The simplest broadband source is an arc lamp, which behaves like a black-body source with a typical temperature $\sim$ 1000 K. From Planck's law it is well known that infra-red power of a black-body source decreases rapidly with decreasing emission frequency and less than 1 part in 10^4 of the total black body radiation is emitted at frequencies below 3 THz [80]. Thus, a lamp is not only a low power source, there is also a substantial amount of light at higher frequencies that has to be eliminated to prevent detection by the broadband detector.

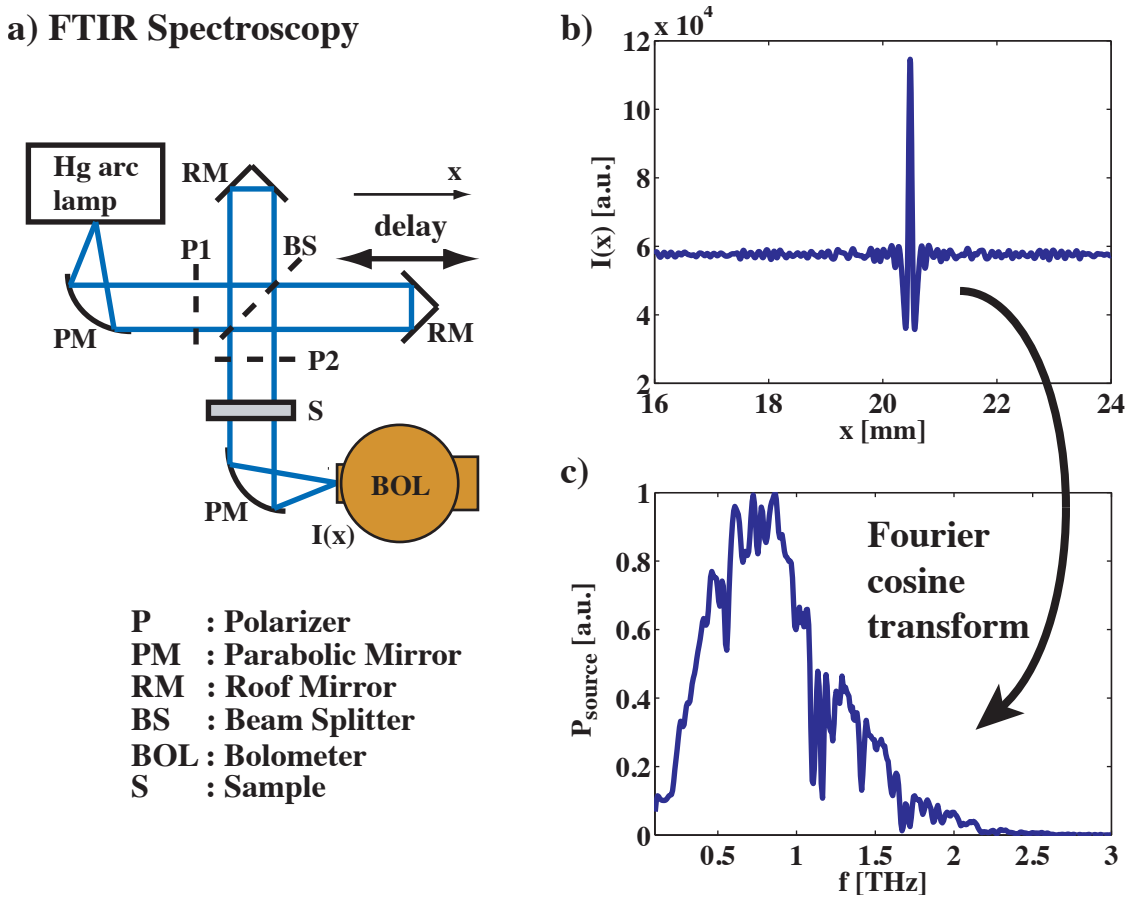

Figure 2.1 Illustration of the operating principle of Fourier Transform Infra-Red (FITR) spectroscopy. a) Schematization of Martin-Puplett (Michelson polarization) interferometer. b) Example of delay scan and the corresponding power spectrum obtained by Fourier cosine transform.

Although different THz power detectors exist, such as Golay cells and pyrometers,

they have rather low sensitivities resulting in part from the high thermal noise at THz frequencies. The power detector with the highest sensitivity is a bolometer detector, which measures heat from absorbed radiation. However, in terms of energy, room temperature (300 K) corresponds to a frequency of about 6 THz, so if a THz photon is to have a much larger energy than the electrons in the detecting material (in order to heat that material) then those electrons must be cooled to a much lower temperature. Thus, to obtain the desired sensitivity, bolometers must be placed in a cryostat and cooled with liquid helium. This incurs a considerable cost, because helium is an expensive gas and a complicated infrastructure including a liquefactor is required to produce liquid helium.

Moreover, with a broadband source and a broadband detector we require a means of differentiating the frequencies. Prism and grating spectrometers are simple because they spatially separate the frequencies, however they are wasteful of energy and prone to inadvertent observation of stray light (from different orders of diffraction for instance). While prism and grating spectrometers are commonly used in the visible and near-infrared, their low energy throughput for a given resolving power make them a poor choice for use with the low power THz sources. Two-beam interferometers, such as the Michelson interferometer, have a higher energy throughput and have been favored in this case [80]. Furthermore, a higher contrast interferogram is obtained if a 50/50 beam splitter is used. A wire-grid polarizer at 45° makes an efficient, broadband, 50/50 beam-splitter for linearly polarized light, but the beams are separated in polarization and care must be taken to properly re-align the polarization of the beams such that the reflected beam is subsequently transmitted and vice versa. This more complicated polarization Michelson interferometer is the Martin-Puplett interferometer [81].

The main limitations of FTIR are the low brightness of the source, the use of expensive bolometer detectors, and the fact that a power measurement implies loss of the phase information. As a result we can only obtain information about the sample absorption.

2.1.2 THz-TDS

Time-domain spectroscopy relies on a fundamentally different principle. In this case the detector is sensitive to the actual *electric field* E_{THz}. A typical pulse ($E_{\mathrm{THz}}(t)$)

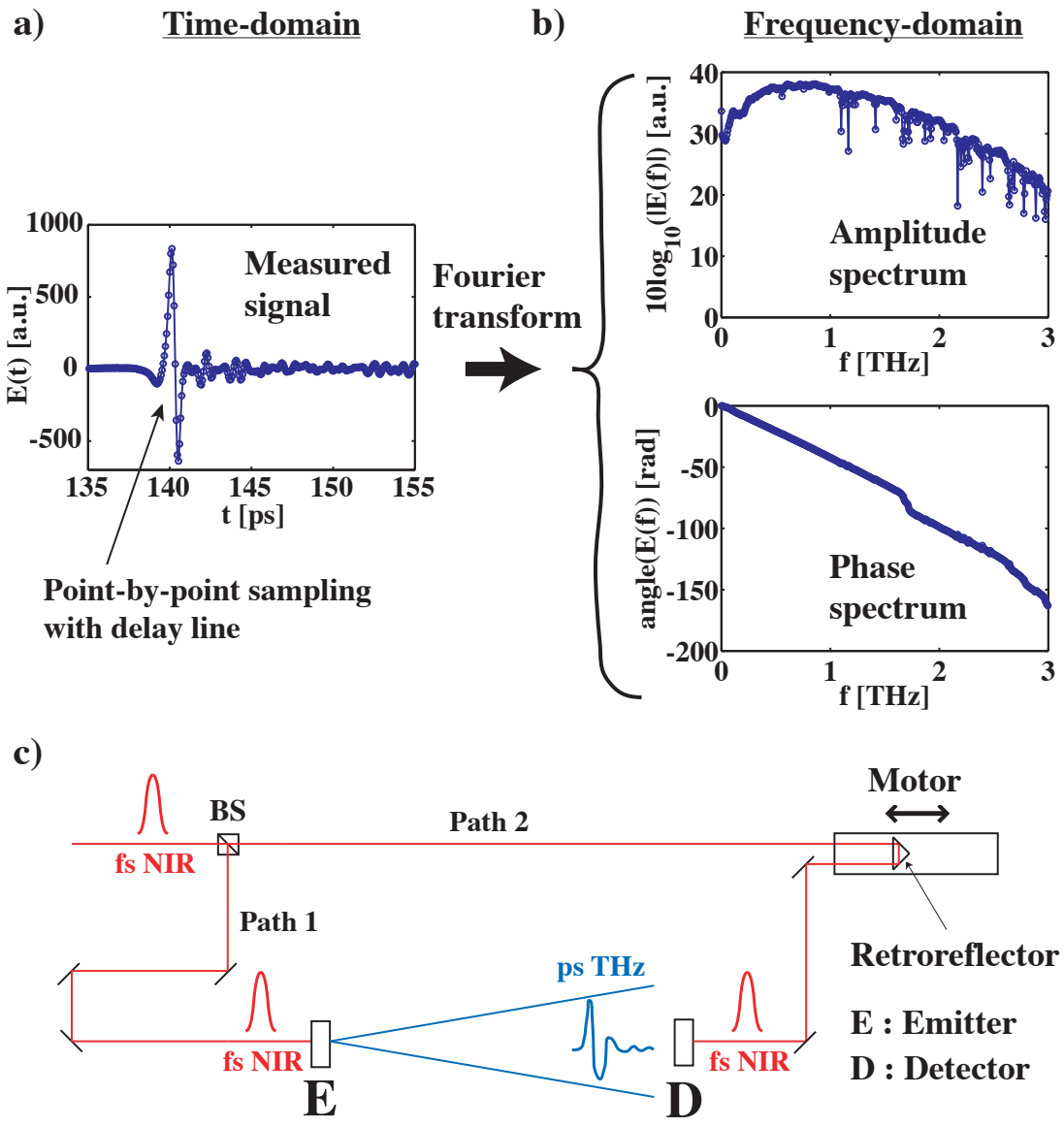

Figure 2.2 Sampling in time-domain gives amplitude and phase frequency spectra. a) The THz electric field is measured point-by-point in the time-domain ($E_{\mathrm{THz}}(t)$) by using a field detector. b) The Fourier transform of the time signal gives a complex valued frequency spectrum yielding amplitude ($|\tilde{E}_{\mathrm{THz}}(f)|$) and phase ($angle(\tilde{E}_{\mathrm{THz}}(f))$) information. Note the presence of water vapor absorption peaks in the amplitude spectrum. c) Point sampling of time signal is enabled by short activation time of detector and the use of a delay line to change the delay of the detector trigger pulse with respect to the THz signal pulse (change of activation time).

generated by a pulsed broadband THz source is illustrated in Fig. 2.2.a). Point by point sampling of the electric field with a time resolved measurement yields $E_{\mathrm{THz}}(t)$. Contrary to FTIR, the Fourier transform of $E_{\mathrm{THz}}(t)$ now gives amplitude *and* phase information (see Fig. 2.2.b)). The amplitude yields information about absorption whereas the phase gives important information about the refractive index.

The point sampling relies on the fact that the detector only measures a signal when activated by an optical trigger pulse. For simplicity, assume that the detector is only turned on for the duration of the near infrared (NIR) optical pulse[1]. If a fs laser pulse is used as the trigger then the response of the detector is essentially a Dirac delta function. The actual measured signal is a convolution between the THz electric field and the response function of the detector. So in the case of a delta function response, the convolution reduces to the sampling of a single point. Thus the signal is proportional to the instantaneous value $E_{\mathrm{THz}}(t = \tau)$ measured at a delay time τ between the THz pulse and the detector trigger pulse.

Fig. 2.2.c) illustrates the basic measurement procedure. An optical pulse is also used to trigger the generation of a THz pulse from the THz emitter. A beam-splitter separates a fs laser pulse into the emitter and detector branches and ensures synchronicity between the two trigger pulses. For a given optical path difference between the emitter and detector branches, the delay between the emitted THz pulse and the detector trigger pulse remains constant. By scanning a delay line in one of the two branches the delay time between the signal and probe pulses is varied and the entire THz pulse can be sampled. An example is provided in Fig. 2.2.a) where the THz pulse length is > 5 ps, the optical pulse width is ~ 100 fs, and the separation between the point samples is 67 fs.

A general consequence of the Fourier transformation of the measured time-domain signal is that the frequency range (Δf) and frequency resolution (df) are inversely proportional to the time resolution (dt) and time range (Δt) of the sampling, respectively. Moreover, the equation $2x = c \cdot t$, where c is the speed of light, relates the

[1] As will be explained in the next section, the response of the detector also depends on the carrier lifetime in the case of photo-conductive antennae.

delay line displacement x to the delay time t. Thus,

$$f_{\max}\ [\mathrm{THz}] = \frac{1}{dt} = \frac{c}{2 \cdot dx} \approx \frac{300\ [\mathrm{THz} \cdot \mu\mathrm{m}]}{2 \cdot dx\ [\mu\mathrm{m}]}, \tag{2.1}$$

$$df\ [\mathrm{GHz}] = \frac{1}{t_{\max} - t_{\min}} = \frac{c}{2 \cdot \Delta x} \approx \frac{300\ [\mathrm{GHz} \cdot \mathrm{mm}]}{2 \cdot \Delta x\ [\mathrm{mm}]}, \tag{2.2}$$

where dx is the stepsize of the delay line motor and Δx is the total motor displacement. Thus, for a typical source spectrum that extends from 0 to 3 THz, we require $f_{\max} > 5$ THz and $dx < 30$ μm to avoid spectral artifacts. Furthermore, a frequency resolution of 10 GHz requires a delay line displacement of $\Delta x = 15$ mm ($\Delta t = 100$ ps), and a resolution of 1 GHz requires $\Delta x = 15$ cm ($\Delta t = 1$ ns). It is worth noting that the measurement noise can limit the achievable resolution because the THz signal decreases rapidly with increasing delay (Fig. 2.2.a)) and there is no increase of resolution if the signal is below the noise. Moreover, it should be noted that advancing the motor step by step is slow because of the acceleration and deceleration time of the motor. A considerable decrease of scan time can be achieved with a continuous motor scan, but care must be taken to maintain the spatial resolution. The detector integration time for the measurement of a point (t_{point}) is generally fixed, so the scan speed must be set to $v_{\mathrm{motor}} = \frac{dx}{t_{\mathrm{point}}}$ to insure that points are measured at dx intervals.

Measurement with and without a sample allows for the measurement of the complex transmission spectrum. Details of the calculation of the propagation loss and refractive index from the complex transmission spectrum of a planar sample or waveguide are deferred to Appendix B.

Finally, we note that an excellent and more detailed introduction to TDS can be found in [82], including a detailed comparison between FTIR and TDS. For the measurement of THz spectra, FTIR has been superseded by THz-TDS because of brighter sources, higher signal/noise ratios, and a higher frequency resolution. The higher brightness of sources such as photo-conductive antennae and the higher frequency resolution achievable with the delay line are two important reasons that make THz-TDS more appropriate than FTIR for the transmission measurements of waveguides.

2.2 THz generation and detection

Although a multitude of generation methods exist[2] (PC antenna, DFG, OR, CW photomixing, QCL, FEL, Gunn diode, BWO, Smith-Purcell effect, Semiconductor surface emission, plasma OR) and a variety of detection methods exist (PC antenna, EO, bolometer, pyrometer, Golay cell), a thorough discussion is beyond the scope of this thesis. The interested reader is referred to books [83, 1] and review papers [84, 85] on the subject. Here we shall limit our discussion to sources and detectors that are generally used in THz-TDS setups. The two most common techniques are generation and detection using Photo-Conductive antennae, as well as generation via Optical Rectification and detection using Electro-Optic sampling. Both methods rely on the ultrafast pulses of a fs laser and their widespread use stems from the broadness of the THz spectrum that is generated.

2.2.1 Optical Rectification and Electro-Optic sampling

Optical Rectification (OR) is a somewhat non-descriptive term that refers to intra-pulse Difference Frequency Generation (DFG). THz radiation is generated in the following way. An ultrashort near-infrared pulse has a relatively broad spectrum and the frequency separation between the highest and lowest frequency components of the pulse spectrum can be a few THz. For instance, a mode-locked laser with a peak emission wavelength of 800 nm and a peak width of $\sim$ 21 nm emits a 100 fs pulse with a full-width-half-maximum frequency separation of 10 THz between the spectral components of the pulse. Thus the OR corresponds to DFG between the different instantaneous frequency components inherent to the optical pump pulse and a continuum of frequencies are generated in the THz band. It is easy to understand that the bandwidth of THz emission is inversely proportional to the pulsewidth of the pump and that emitted THz power decreases at higher frequencies. Due to the second order nonlinear optical process of DFG, a crystal with a lack of inversion symmetry is used. To insure phase-matching over the broad spectrum of frequencies the crystal is generally quite thin. For diffraction limited efficiency, the pump pulse is focused (Fig. 2.3.a)) to the size of the average wavelength, say 300 μm [86]. However, the current energy conversion efficiencies are on the order of 10^{-5} [87] to 10^{-4} [88]. This is due in part to the Manley-Rowe conversion limit [89], to differences in material

[2]Please refer to 'List of Symbols and Abbreviations' for the definitions of the acronyms.

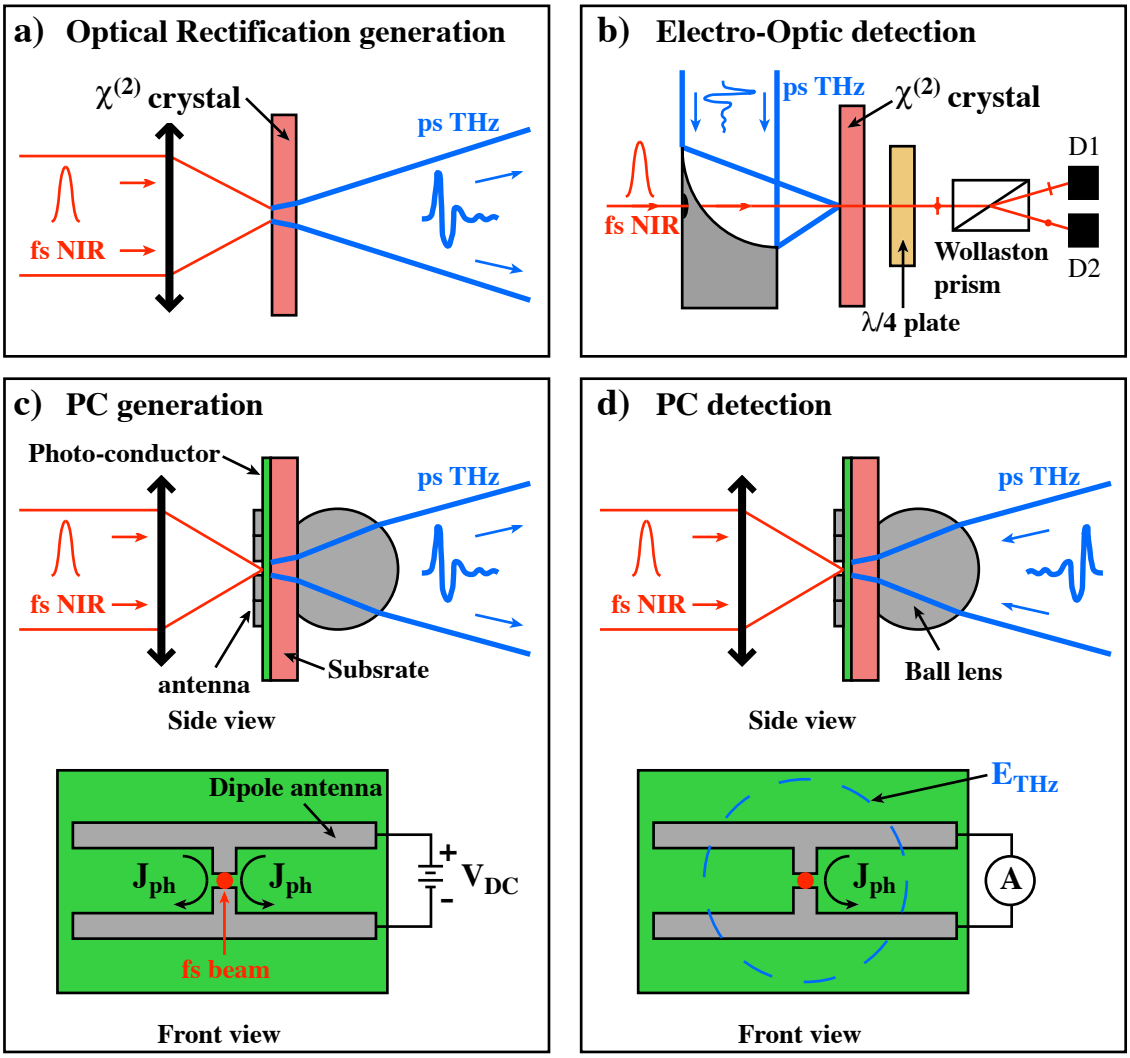

Figure 2.3 The most common techniques for generation and detection of THz radiation for THz-TDS. a) Optical Rectification: difference frequency mixing between the frequency components of a near-infrared (NIR) pulse. b) Electro-Optic detection: polarization rotation of NIR beam is proportional to $E_{\mathrm{THz}}(t)$ and measured with balanced photodectors (D1 and D2). c) Photoconductive antenna generation: photocarriers are accelerated by voltage bias. d) Photoconductive antenna detection: photocurrent is proportional to $E_{\mathrm{THz}}(t)$.

parameters and phase-matching conditions [90], as well as to the onset of saturation effects such as two-photon absorption [91].

A new method that has gained a considerable amount of interest recently is plasma OR [92]. Focusing of an intense fs pulse can ionize a gas, such as nitrogen in the air,

and create a plasma. This plasma can act as a nonlinear medium, replacing the crystals. The disadvantage is that more powerful and more expensive laser sources are required.

Another alternative is large area reflection OR on a semiconductor surface [93]. A surface effect creates the polarization required for the DFG and the larger area allows for larger pump intensities while avoiding the damage threshold of the semiconductor. Again this requires amplified fs lasers.

As for detection, Electro-Optic (EO) sampling [94] exploits the electro-optic effect (also known as the Pockels effect). In the presence of an electric field (THz field), a detector probe pulse (near infrared) undergoes a polarization rotation that is proportional to the strength and direction of the electric field. By using a polarization sensitive device, the polarization information is transformed into amplitude information. A typical setup uses a Wollaston prism for polarization separation and balanced photodetectors to more accurately measure the difference between the orthogonal polarizations. One requirement, however, is that the probe beam must be colinear with the THz beam. A common method is to pass the optical probe beam through a small hole drilled into a parabolic mirror, as illustrated in Fig. 2.3.b).

2.2.2 Photo-conductive antennae

A Photo-Conductive (PC) antenna emitter relies on the generation of photo-carriers which are then accelerated by a DC bias field. The carrier dynamics on a time scale of ps result in radiation of light at THz frequencies. An antenna structure is used to spatially orient the generated current [96, 97] and to help direct the radiation of THz light. The most common antenna is a dipole structure [96] that generates linearly polarized light aligned in the direction of current flow. This dipole structure consists of two long metallic electrodes that are separated by a small gap (see Fig. 2.3.c)) A pump pulse is focused onto the small gap between the electrodes. With a photon energy larger than the bandgap energy of the semiconductor, photo-carriers are excited by the pump pulse. Under the effect of the DC voltage bias applied to the electrodes the charges are accelerated and form a current which flows between the electrodes. The electric field of the emitted THz radiation is proportional to the time derivative of this current [95], as can be seen in Fig. 2.4.a) Note that the THz radiation is emitted in all directions but, because the dipole is situated at the air/semiconductor interface,

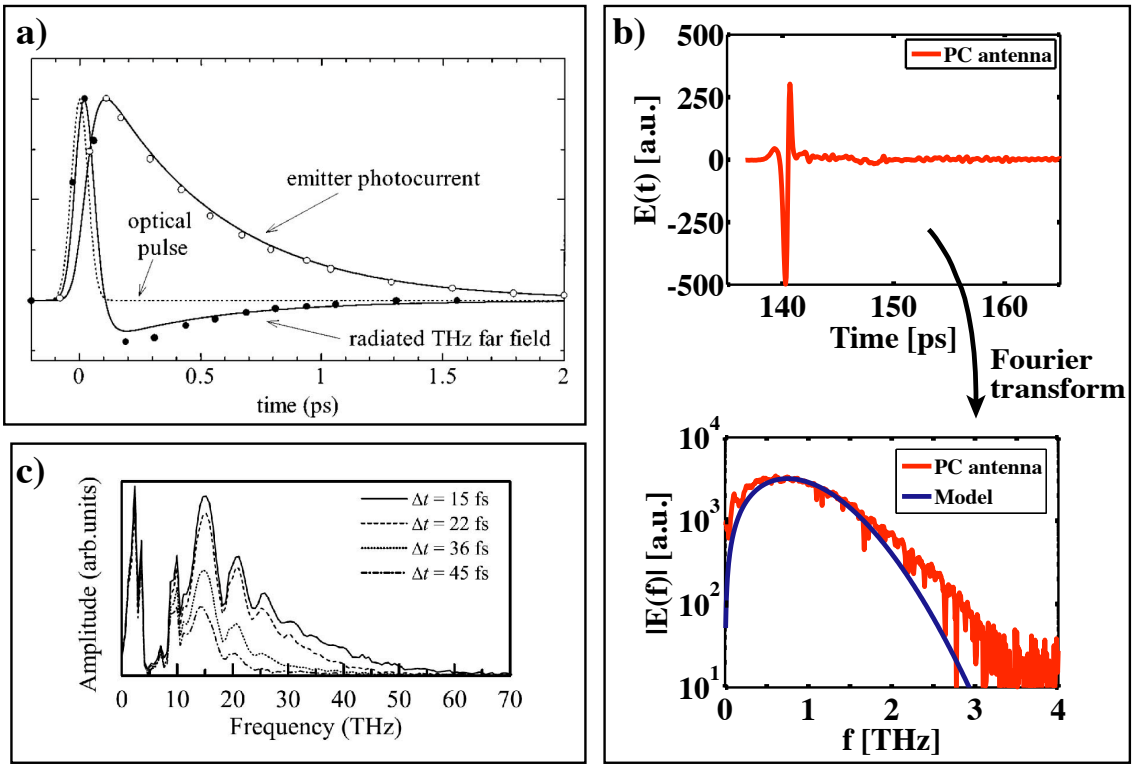

Figure 2.4 Theory of PC antenna THz generation and optical pulsewidth dependence. a) Optical pulse generates photo-carriers that are accelerated by the bias voltage and eventually recombine due to finite carrier lifetime. Variation of the photo-current over ps (sub-ps) time scales leads to emission of THz radiation. (adapted from [95]) b) Example of an experimental PC dipole antenna emission spectrum, well approximated by the simple model of equation (2.5) using $\tau_{\text{laser}} = 100$ fs, $C = 7035$, and $D = 9.43$. c) Frequency spectrum of PC antenna emission for different optical pulse durations. Note that spectral deformations, especially in the 5-9 THz range, result from absorption bands of the crystal used for electro-optic detection of the THz light. Nevertheless, shorter fs pulses lead to emission/detection at higher THz frequencies. (adapted from [83])

there is a greater amount of power radiated into the semiconductor than radiated out into the air [83]. A hyperhemispherical Si lens (truncated ball lens) is generally used to help extract the THz radiation and make it more directional. However, the emitted beam is still divergent and lenses or parabolic mirrors must be used to collimate the beam.

Photo-conductive emission can be accurately explained using the Drude model [95]. Although the exact model depends on many parameters such as the power and du-

ration of the incident pump laser pulse, as well as the lifetime and the effective mass of the free-carriers within the photo-conductor, the underlying physics can be understood by the following simplified model. The incident pump laser pulse can be assumed to be gaussian (Fig. 2.4.a)). The photocurrent generated within the semiconductor gap between the antenna electrodes is proportional to the incident laser power [95]. Although the actual emitter current is asymmetrical (Fig. 2.4.a)) due to the lifetime of the carriers, for simplicity the photocurrent can be approximated by a gaussian,

$$j_{\text{emit}}(t) \sim P_{\text{laser}}(t) \sim A \exp(-B^2(\frac{t}{\tau_{\text{laser}}})^2), \tag{2.3}$$

where A and B are constants and τ_{laser} is the laser pulse duration. In the far-field, the THz electric field emitted by the dipole antenna will be proportional to the time-derivative of the photocurrent [95],

$$E_{\text{THz}}(t) \propto \frac{\partial j_{\text{emit}}(t)}{\partial t}. \tag{2.4}$$

From the above assumptions we therefore obtain,

$$\begin{aligned} E_{\text{THz}}(t) &\propto \frac{\partial j_{\text{emit}}(t)}{\partial t} \sim -\left(\frac{2AB^2}{\tau_{\text{laser}}^2}\right) t \cdot \exp(-B^2(\frac{t}{\tau_{\text{laser}}})^2), \\ E_{\text{THz}}(f) &= FT\{\ E_{\text{THz}}(t)\ \} \sim \left(\frac{-iA\tau_{\text{laser}}}{\sqrt{2}B}\right) \omega \cdot \exp(-(\frac{\omega\tau_{\text{laser}}}{2B})^2) \\ E_{\text{THz}}(f) &= C \cdot f \cdot \exp(-D^2(f \cdot \tau_{\text{laser}})^2), \end{aligned} \tag{2.5}$$

where $FT\{\cdot\}$ denotes the Fourier transform, $\omega = 2\pi f$, and C and D are constants. In Fig. 2.4.b) this simple model is compared to an experimentally measured PC antenna emission spectrum. A more accurate antenna model, taking into account the Drude model for the photo-carriers [95], can give a more accurate fit at high frequencies. Nevertheless, from equation (2.5) it is easy to understand that the emission and detection bandwidth are inversely proportional to the optical pulse duration. This bandwidth dependence on the optical pulse duration has been verified experimentally by many groups [83]. One example is given in Fig. 2.4.c), where a PC antenna was used as an emitter and electro-optic sampling was used for detection. Although the bandwidth of the generated THz pulse is around 3 THz for $\tau_{\text{laser}} \sim 100$ fs pulses, much

broader THz generation was achieved with shorter fs pulses. An obvious consequence is that the energy density of broader spectra decreases. It should be noted that the spectral deformations in Fig. 2.4.c), especially in the 5-9 THz range, are due to absorption bands within the crystal used for electro-optic detection.

For detection with a PC antenna, no bias voltage is applied. Instead it is $E_{\mathrm{THz}}(t)$ that accelerates the photo-carriers, so the detected signal is proportional to $E_{\mathrm{THz}}(t)$. It should be noted that the measured signal is actually a time convolution between $E_{\mathrm{THz}}(t)$ and the response function of the detector, $N(t)$. If the carrier lifetime τ_{carrier} is very short ($\tau_{\mathrm{carrier}} \ll E_{\mathrm{THz}}(t)$) then the detector will respond like a delta function ($N(t) \sim \delta(t)$). The measured signal then gives $E_{\mathrm{THz}}(t)$ directly. However, if the carrier lifetime is long ($\tau_{\mathrm{carrier}} \gg E_{\mathrm{THz}}(t)$) then the detector will respond like a Heaviside step function ($N(t) \sim \mathrm{Heaviside}(t)$). In this case, it is the derivative of the convolution (derivative of the measured signal) that will give $E_{\mathrm{THz}}(t)$ [82].

Finally, we note that dipole antennae have only recently become commercially available and that they generate linearly polarized THz radiation. There have also been recent experimental demonstrations of novel antenna structures that emit TM-like radially-polarized [49] and TE-like azimuthally-polarized [97] THz radiation.

2.3 Design of an adaptable-path-length THz-TDS setup

To emphasize the difference between the standard setup and the adjustable-path setup, we begin by giving a detailed description of the standard geometry. This description is given with some implementation details that are specific to the equipment that we have used. We subsequently describe how the geometry is changed to accommodate waveguides and how waveguide transmission is measured.

2.3.1 Standard geometry

A standard THz-TDS setup is illustrated in Fig. 2.5. In this case, identical GaAs PC antennae are used for both the emitter and the detector. The dimensions and operating parameters of the photo-conductive antenna are given in Table 2.1. Furthermore, the pump source, purchased from Menlo Systems GmbH, is a fs C-fiber laser operating around $\lambda = 1560$ nm. The 1560 nm emission is frequency doubled

(Second Harmonic Generation) to 780 nm in order to be below the bandgap of the GaAs semiconductor (868 nm). The optical path begins with a periscope that is used to increase the height of the beam. A filtering iris blocks the higher harmonics (third harmonic at 520 nm and forth harmonic at 390 nm) that were also generated during the frequency doubling process. The source beam is then split into an emitter beam (path 1) and a detector beam (path 2). These two paths ultimately terminate on the detector.

Table 2.1 Dimensions and operating parameters of dipole photo-conductive antennae used as emitter and detector

Schematization of dipole antenna	Antenna parameters	
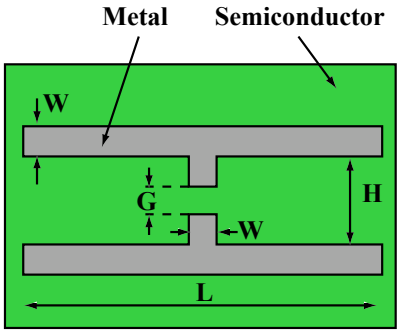 Not to scale	Material	LT-GaAs
	H [µm]	20
	L [µm]	20 000
	W [µm]	10
	G [µm]	5
	P_{avg} [mW]	$\leqslant$ 10
	V_{bias} [V]	$\leqslant$ 45

Let us now consider the THz generation. The photo-conductive material of the antennae is Low-Temperature (LT) grown GaAs. The low growth temperature creates a higher amount of crystal defects and lowers the carrier lifetime. LT-GaAs has a carrier lifetime of $\sim$ 300 fs so the detector has a Dirac delta function response. The antennae, also from Menlo Systems GmbH, are mounted in special alignment modules. We have (x, y, z) alignment of a pump beam focusing lens, used to focus the optical pulse onto the gap of the antennae. Furthermore, there are actually 6 dipole antennae of different sizes on a LT-GaAs chip. So we also have an (x, y) alignment of the antenna chip to choose one antenna among the six on a chip. A final (x, y) alignment of a Si truncated ball lens is possible in order to properly orient the emitted THz beam. A voltage source applies a 39 V bias to the emitter antenna and the emitter pump beam is focused onto the 5 μm gap of the emitter antenna. Understandably, this alignment is critical for efficient THz generation.

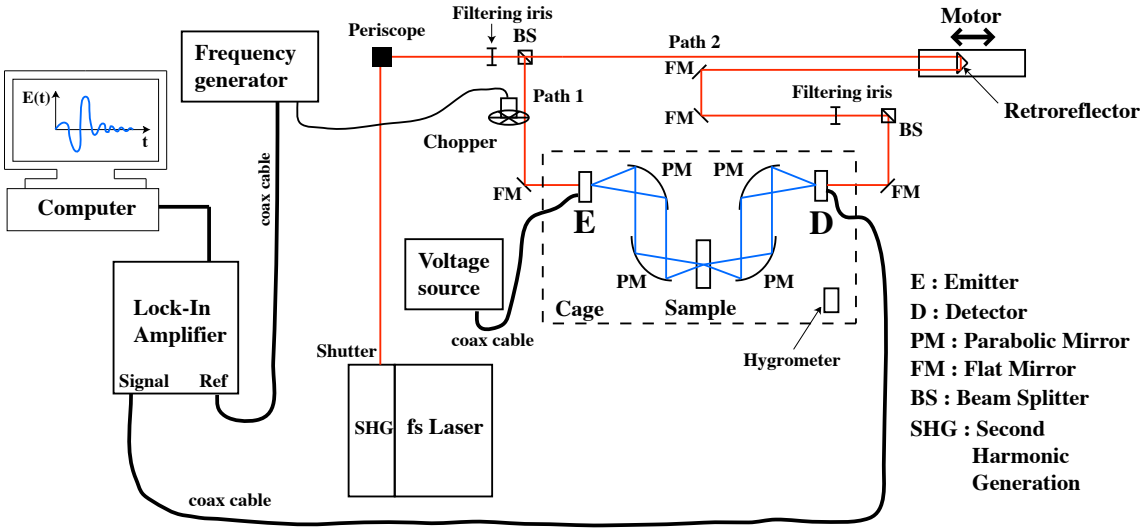

Figure 2.5 Schema of standard THz-TDS setup for measuring point samples. Four static parabolic mirrors are used to collimate the emitted THz radiation, form an intermediate focus on the sample, and focus the transmitted light onto the detector. The fs laser pulse is in red and the ps THz pulse is in blue.

Despite the truncated Si ball lens, the emitted THz beam is still divergent. The THz beam is generally collimated and brought to an intermediate focus through a point sample before being focused onto the detector. Plastic lenses can be used for the THz optics, however, they suffer from absorption losses, frequency dependent beam size (in certain configurations), and the fact that the power throughput is highly sensitive to the spacing between the optics of a lens system [1]. These problems are avoided through the use of metallic parabolic mirrors. These mirrors generally conjugate a collimated parallel beam with a 90° off-axis focal point. In the standard THz-TDS geometry, four parabolic mirrors are typically arranged to form an intermediate focus through a point sample, as shown in Fig. 2.5. All of the THz optics are placed inside a cage in order to purge the humidity from the air[3].

As mentioned in the previous section, the time-resolved point-sampling detection requires a precise control of the THz pulse and trigger pulse arrival times on the detector. Path 1 is generally of fixed length such that it always takes the same amount of time for the THz pulse to arrive to the detector. Instead, it is typically the detector trigger pulse which is delayed to vary the arrival time between the trigger

[3]Purging will be discussed thoroughly in the final section.

pulse and the THz signal pulse. Note that this requires path 2 to be slightly shorter than path 1, and for the missing optical distance to be compensated by the delay line. A retro-reflector is mounted on a high precision translation stage ($dx_{\text{min}} = 1$ μm) to create a delay line. A maximum motor displacement of 30 cm offers a considerable delay of up to 2 ns. The delay line is computer controlled and the delay can be scanned to sample the entire THz waveform.

Finally, an important detail is the modulation of the source. Given the weakness of the detected signal, the emitter beam is modulated with a mechanical beam chopper and both the detected and reference signals are analyzed using a Lock-In Amplifier. The principle of operation of the amplifier is explained elsewhere [98], but the essential feature is that filtering the detected signal at the reference frequency (f_{ref}) allows amplification of weak signals without an extraneous increase of noise. There is however a waiting time associated with the noise filtering, generally $\sim 10\tau_{\text{RC}}$ where τ_{RC} is the time constant of the RC filter being used to extract the signal. In addition to white thermal noise, there is a $1/f_{\text{ref}}$ electronic noise that makes it advantageous to increase f_{ref}. Moreover, the THz scan speed is limited by the acquisition time of points, which is in turn limited by the choice of time constant τ_{RC}. The limiting factor is the requirement that $\tau_{\text{RC}} > \frac{1}{f_{\text{ref}}}$ in order for the signal to be filtered properly. Thus faster scans can be achieved either by reducing the filtering (at the expense of higher noise) or by increasing the modulation frequency. Note that there is a limit to mechanical chopping speeds; higher modulations ($f_{\text{ref}} > 10$ kHz) can be achieved by modulating the bias voltage of the antenna with a square wave instead.

2.3.2 Adjustable-path-length geometry

Fig. 2.6 illustrates how we further modified the TDS setup to accommodate waveguides. The details of operation remain the same as the previously described setup except that the four static parabolic mirrors were replaced by more complicated THz optics featuring two translation rails. The first parabolic mirror still collimates the emitted THz radiation and the final parabolic mirror still focuses the THz beam onto the detector, however the intermediate optics are replaced with a system that can be dynamically reconfigured. Each rail displaces a mirror assembly that allows a convenient adjustment of the total THz optical path length (rail 2), and allows the easy insertion of a THz waveguide (rail 1).

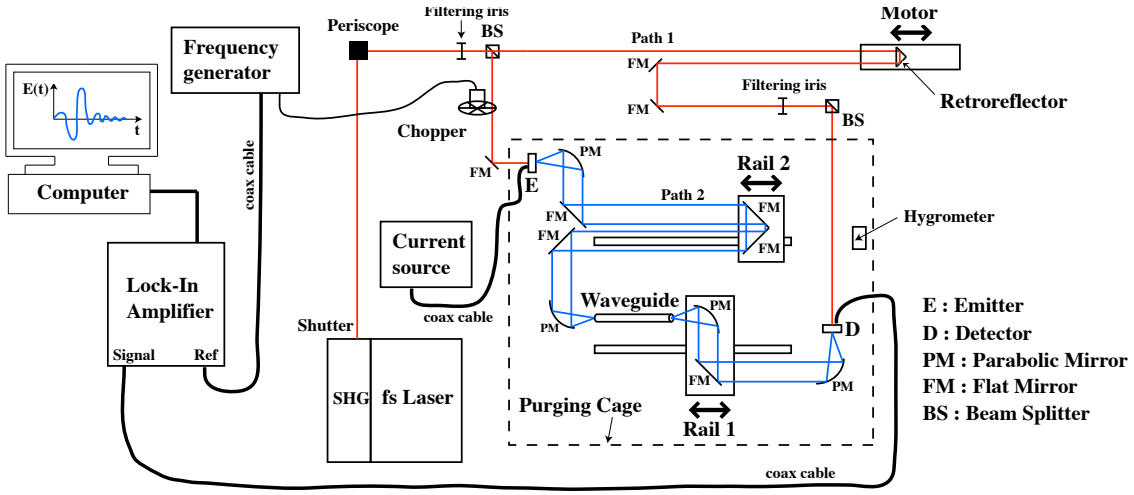

Figure 2.6 Schema of an adaptable-path-length THz-TDS setup for measuring the transmission of THz waveguides. A mirror assembly (rail 1) can translate the output focal plane to accommodate waveguides up to 50 cm in length. The fs laser pulse is in red and the ps THz pulse is in blue.

Let us begin by considering the accommodation of a waveguide. A fixed parabolic mirror focuses the THz radiation into the waveguide; the input coupling plane is therefore fixed. The output of a waveguide is placed at the focal point of another parabolic mirror, which can be displaced along rail 1 together with a flat mirror. Light collected and collimated by the parabolic mirror is then redirected towards the fixed detector via the flat mirror. In the absence of a waveguide, the mirror assembly is translated to the far left such that the focal points of the input and output parabolic mirrors are super-imposed, see Fig. 2.7.a). In that case, we return to the standard intermediate focus where a point sample can be measured. In our setup, waveguides up to 50 cm in length can be measured by simply translating the position of these two mirrors along the rail 1, as illustrated in Fig. 2.7.b). The various waveguides are held in place with 3-axis positioning mounts, and the entire assembly of THz optics was housed in a much larger cage for nitrogen purging.

Note that rail 2 is an additional delay line used to compensate for the change in the optical path length generally introduced by the addition of a waveguide. The rail 2 assembly is especially important when measuring long waveguides that support modes of refractive indices which are significantly different from 1.0. In such a case, the difference in THz path lengths between a setup with a fiber in it and an empty

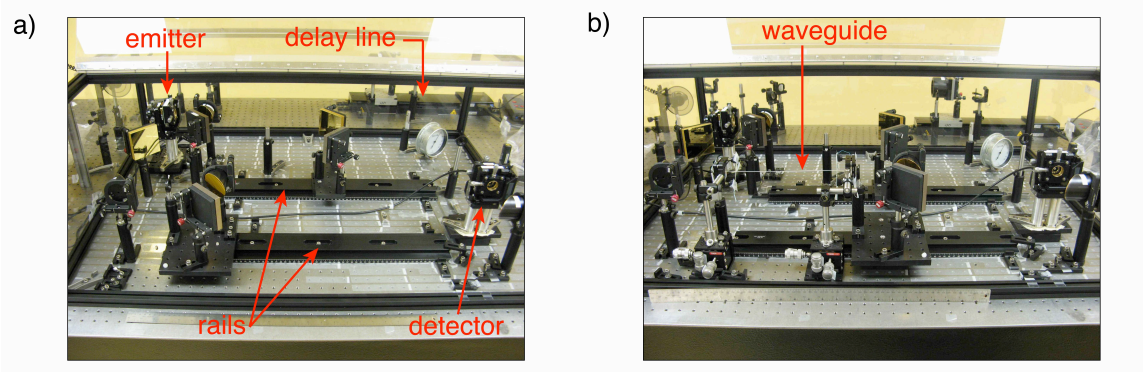

Figure 2.7 Pictures of the adaptable-path-length THz-TDS setup for measuring the transmission of THz waveguides. a) Without a waveguide, b) With a waveguide.

setup (reference) could become so large that the maximal pulse delay of the variable delay line would be insufficient to compensate it.

Interestingly, the requirement that THz waveguides principally guide in air, in order to reduce the absorption loss, also has the effect of lowering the effective refractive index of the guided mode to a value that is very close to 1.0. Therefore, the additional pulse delay introduced by the waveguide (as compared to an empty setup) is easily compensated by the variable delay line. In all the measurements reported in this thesis the mirrors on rail 2 were fixed, and thus, the physical length between the source and the detector (denoted as L_{path2}) was fixed. Following a standard modeling procedure [35] the waveguide transmission T can be described as:

$$E_{\mathrm{waveguide}}(\omega) = E_{\mathrm{source}}(\omega) \cdot \eta \cdot C_{\mathrm{in}} \cdot C_{\mathrm{out}} \cdot e^{i[\frac{\omega}{c}(n_{\mathrm{eff}} L_{\mathrm{w}}) + \frac{\omega}{c}(L_{\mathrm{path2}} - L_{\mathrm{w}})]} e^{-\frac{\alpha L_{\mathrm{w}}}{2}}, \tag{2.6}$$

$$E_{\mathrm{reference}}(\omega) = E_{\mathrm{source}}(\omega) \cdot \eta \cdot e^{i\frac{\omega}{c} L_{\mathrm{path2}}}, \tag{2.7}$$

$$T(\omega, L_{\mathrm{w}}) = \frac{E_{\mathrm{waveguide}}(\omega)}{E_{\mathrm{reference}}(\omega)} = C_{\mathrm{in}} \cdot C_{\mathrm{out}} \cdot e^{i(n_{\mathrm{eff}} - 1)(\frac{\omega}{c}) L_{\mathrm{w}}} e^{-\frac{\alpha L_{\mathrm{w}}}{2}}, \tag{2.8}$$

where $E_{\mathrm{waveguide}}(\omega)$ is the modal field coming out of a waveguide of length L_{w}, and $E_{\mathrm{reference}}(\omega)$ is the reference signal measured[4] in the absence of the waveguide at the position of the coupling plane. $E_{\mathrm{source}}(\omega)$ is the spectrum of the source, whereas η is the transfer function describing transmission through the setup in the absence of a

[4]It is common parlance to state that the spectrum is measured. Obviously, because of the time-domain measurement, it is acutally the time-scan ($E(t)$) that is measured and Fourier transformed to yield the spectrum ($E(\omega)$).

waveguide. α and n_{eff} are the power propagation loss and effective index of the mode guided by the waveguide. C_{in} and C_{out} are respectively the input and output coupling coefficients with respect to the waveguide, which are calculated by the following ratio of field overlap integrals,

$$C = \frac{\int \left(E^*_{\text{mode}} \times H_{\text{beam}} + E_{\text{beam}} \times H^*_{\text{mode}}\right) dA}{\sqrt{\int 2Re\left(E_{\text{mode}} \times H^*_{\text{mode}}\right) dA}\sqrt{\int 2Re\left(E_{\text{beam}} \times H^*_{\text{beam}}\right) dA}}, \tag{2.9}$$

where $E_{\text{mode}}, H_{\text{mode}}$ are the fields of the waveguide mode and $E_{\text{beam}}, H_{\text{beam}}$ are the fields of the input or output THz beam.

Note that the transmission through the waveguide induces a time delay of $\frac{(n_{\text{eff}}-1)L_{\text{w}}}{c}$ with respect to a reference THz pulse propagating through an empty setup. This result is a consequence of the *taxicab geometry* [99] of the adjustable-path-length setup. Consider the free-space THz propagation in the absence of a waveguide. The total geometrical length of path 2 remains *constant* no matter where the mirror assembly is positioned along rail 1. By inserting a waveguide, we induce a differential delay due to a change in *optical length* not a change in geometrical length, hence the $\frac{(n_{\text{eff}}-1)L_{\text{w}}}{c}$ delay. The differential delay is an added bonus of this setup design, because it reduces the delay offset that must be compensated by the delay line (or by rail 2). In fact, the total pulse delay becomes negligibly small for waveguides that have $n_{\text{eff}} \sim 1$.

Finally, the *power* attenuation coefficient α can be calculated by comparing the *amplitude* transmission of waveguide segments of different length (cutback method),

$$\frac{|T(\omega, L_2)|}{|T(\omega, L_1)|} = \frac{|E_{\text{waveguide}}(\omega, L_2)|}{|E^{(2)}_{\text{reference}}(\omega)|} \cdot \frac{|E^{(1)}_{\text{reference}}(\omega)|}{|E_{\text{waveguide}}(\omega, L_1)|} = e^{-\frac{\alpha(L_2-L_1)}{2}}, \tag{2.10}$$

where the superscript (j) of $E^{(j)}_{\text{reference}}(\omega)$ is used to indicate that the reference spectrum for segment L_j is measured immediately after the measurement of $E_{\text{waveguide}}(\omega, L_j)$. Note that because of the power fluctuations of the source and the long time required to cut and re-align the waveguide segments, $|E^{(2)}_{\text{source}}(\omega)| \neq |E^{(1)}_{\text{source}}(\omega)|$ in general. Thus, using the ratio of transmission amplitudes takes into account any fluctuations in $|E_{\text{source}}(\omega)|$ which may occur between the times when segments L_1 and L_2 are measured.

2.4 Alignment of the setup

The optical components described in the previous section require careful alignment. In this section, we describe in detail some of the alignment problems that were encountered and how they were resolved. There are two reasons for this special section. First, some of the problems concerning THz optics highlight the alignment benefit that flexible, easy to couple, THz waveguides would bring. Second, there is little or no information concerning these aspects in either the literature or the manufacturer documentation. A considerable amount of time was spent perfecting the alignment so it is hoped that the tips outlined in this section will benefit others.

2.4.1 Optical alignment of rails and mirrors

All mirror alignment was done with a He-Ne laser before insertion of the fs-laser and the PC antennae.

Given the length of the optical paths within the setup and the importance of an accurate alignment, care was taken to insure that the alignment was as precise as possible. One problem that was encountered was the ambiguous alignment of a gaussian profiled laser beam. Due to the corrugations in the metal irises the reflection of a simple gaussian laser beam can lead to an ambiguous determination of its position. This is schematized in Fig. 2.8.a). In order to get a greater alignment precision a "bull's eye" technique was used, where diffraction from a pinhole, precisely aligned on the optical axis, created a circularly symmetric Bessel diffraction pattern. The alternance of minima and maxima in the Bessel function forms a pattern that resembles a "bull's eye" pattern. This pattern made a precise alignment target, where proper alignment was easy to verify by varying the size of the iris and insuring that the pattern remained centered. The alignment ambiguity was thus eliminated, as illustrated in Fig. 2.8.a).

Another, unexpected, problem that was encountered was the distortion of the high-precision optical rails upon screwing them into the optical table. Alignment of the rails was verified by translating a mirror that retro-reflected a He-Ne laser beam aligned onto the optical axis. Proper alignment would be insured if the beam retro-reflected correctly for all positions of the mirror along the rail. This was especially important in our setup in order to eliminate signal distortions that would result from uneven alignment. Without taking care, merely screwing the rails into place

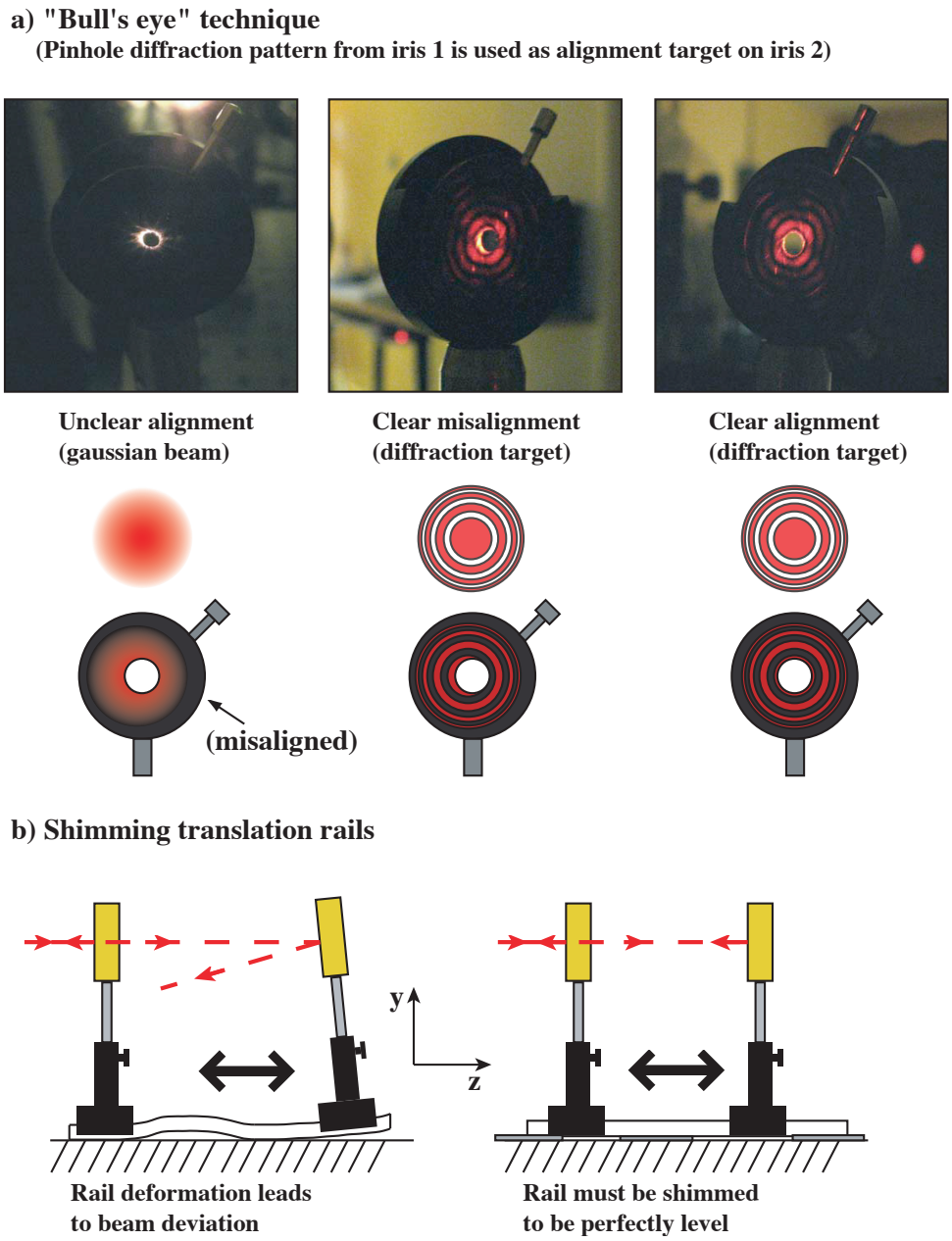

Figure 2.8 Precise optical alignment techniques. a) "Bull's eye technique" consisting of using the pinhole diffraction pattern of one iris as an alignment target on subsequent irises. This method was deemed more precise than the alignment of a gaussian profile beam. b) Screwing the optical rail into the table led to distortion that would deviate the beam significantly. Distortion needed to be compensated by shimming the rails.

would distort the shape of the 60 cm long rails. The distortion is exaggerated in the schema of Fig. 2.8.b), but the point is that even a mild distortion provoked a considerable deviation of the retro-reflected beam upon translation of the mirror; > 1 mm transverse deviation over a propagation distance of 50 cm gives $> 1°$ angular deviation. To insure proper alignment, shimming of the rails (with sheets of paper) was required to insure that the rail was not deformed once screwed into the table. After proper shimming, the retro-reflected beam remained level across the entire length of the rail, as illustrated in Fig. 2.8.b).

2.4.2 Parabolic mirrors

Proper alignment of the parabolic mirrors was critical in our case. In the compact 4-mirror arrangement shown in Fig. 2.5, the mirrors are static and a misalignment can be tolerated as it merely reduces the throughput of the system. In our case, one of the parabolic mirrors is mounted on a translation rail and any misalignment would lead to a deviation of the THz beam and a severe loss of signal.

Unfortunately, the alignment of parabolic mirrors is not trivial and very little, if any, information about alignment is available in the literature. One reference [100] explains the alignment of large parabolic mirrors, but this is not directly useful for the alignment of off-axis parabolic mirrors.

Fig. 2.9 describes the alignment procedures that were found through trial and error. The alignment relies on the use of a reference beam, from a visible laser such as a He-Ne laser, that has been pre-aligned to be parallel to the optical table. The parabolic mirror is then translated such that this alignment beam remains parallel to the optical axis of the mirror (axis of the cylinder). Let the axes be defined by the frame of reference in Figures 2.9.a) and 2.9.b). For any given z position, the height of the mirror will be correct if the beam remains in a plane of reflection that is parallel to the table (beam A). If the mirror is too low, the beam will reflect downwards (beam B), and contrariwise if the mirror is too high the beam will reflect upwards (beam C). Furthermore, the inclination of the parabolic mirror must be adjusted to insure that incident beams that are parallel to the optical axis (for all z positions) remain in the same plane of reflection parallel to the table. If the mirror is tilted, then beam E could reflect upwards while beam F reflects downwards, or vice-versa. The height of the reflection can easily be verified by translating an iris that has been set at a fixed

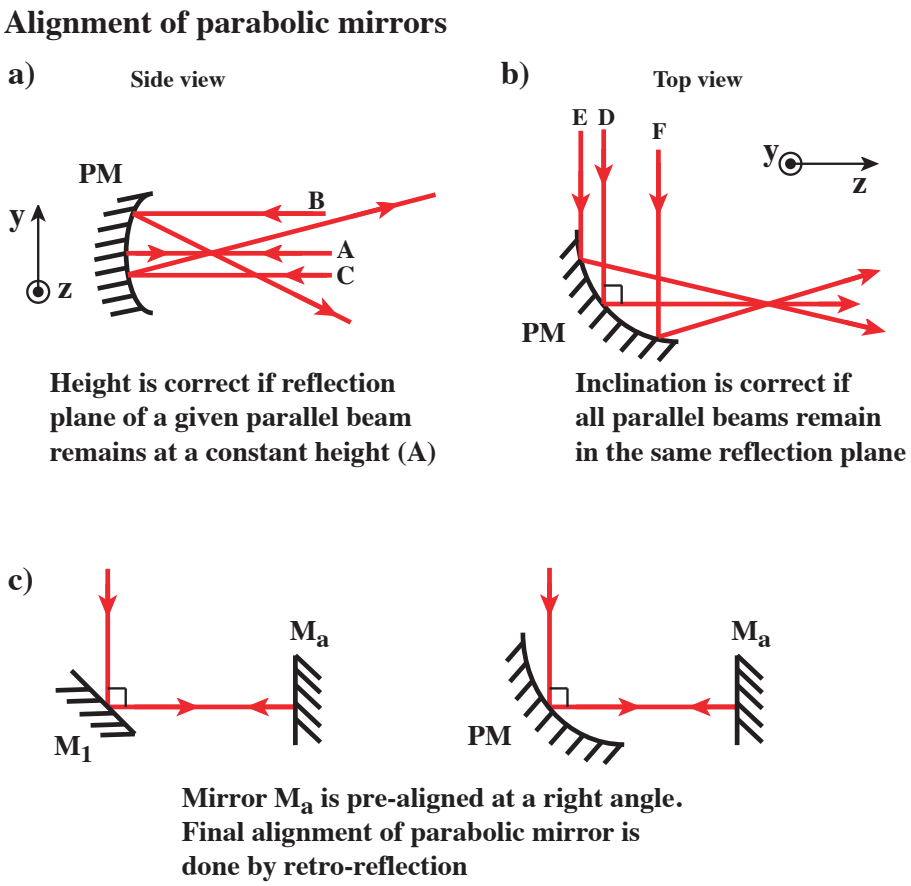

Figure 2.9 Techniques for the proper alignment of off-axis parabolic mirrors. a) Height is adjusted such that parallel beams at the same z reflect in the same plane. b) Tilt is adjusted such that parallel beams at different z reflect in the same plane. c) Final alignment is done by retro-reflection of the visible laser beam (He-Ne laser) using a pre-aligned temporary mirror M_a, that was pre-set at the off-axis angle of the parabolic mirror (in this case 90°).

height. The above steps can be repeated until the height and tilt of the parabolic mirror are correct and that all reflections remains in a plane parallel to the optical table.

Finally, once this pre-alignment has been done the parabolic mirror can be inserted into the setup. The most convenient and precise way to do this is to rely upon retro-reflection. Exploiting the fact that we have 90° off-axis parabolic mirrors, a temporary retro-reflection mirror M_a is pre-aligned at a 90° degree angle. The parabolic mirror can then be translated and rotated (around the y-axis) until a proper retro-reflection

is achieved. Note that mirror M_a need not be placed at the focus of the parabolic mirror. There is generally enough light on the optical axis to insure a visible retro-reflection.

2.4.3 Antenna alignment

Another critical alignment step is the proper alignment of the THz antennae. This alignment is two-fold. Firstly, there is the proper focusing of the optical pump beam on the photo-conductive gaps of the dipole antennae. Secondly, there is the proper optimization of the alignment of the hyperhemispherical Si lens (truncated ball lens).

The alignment of the pump beam lens for proper excitation of the antennae implies optimization of the focus and optimization of the (x, y) position such that the focused beam illuminates only the small gap between the electrodes. The focus can easily be adjusted by verifying the retro-reflection of the optical beam on the surface of the non-metallized regions of the antenna. Note however that the optimal focus is not the focal distance of the lens as a slightly larger beam that fills the entire gap region is more efficient. Given the small dimensions, a visual inspection of the alignment is difficult. Instead a very accurate alignment can be achieved indirectly by optimization of the generated photo-current. Because of the applied voltage, the creation of photo-carriers results in the creation of a photo-current. The photo-current of the emitter is typically in the $20 - 40$ μA range. This photo-current is *extremely* sensitive to alignment. Fig. 2.10.a) illustrates how the maximization of the THz emission is achieved through the maximization of the photo-current. Recall that no voltage bias is applied to the detector. However, for the purposes of alignment, the detector antenna can be temporarily operated as an emitter (by applying a voltage bias) and the above procedure can be used to insure the proper alignment of the detector too.

The other major alignment procedure involves the optimization of the position of the truncated ball lens. Visual alignment is difficult because of the diffuse reflection of an optical beam. Generally speaking, optimization is achieved by maximizing the value of a given signal such as the peak amplitude of the emitted THz field. However, in the case of Time-Domain measurements special care must be taken due to the possible time delay of the signal that is being optimized. The major point, which has not been addressed in the literature nor in the documentation of the manufacturer, is that the signal cannot be optimized at a fixed delay time because the variation of the

position of the ball lens changes the overall length of the THz beam path and causes a delay in the arrival of the THz pulse. Thus, optimization should be carried by making *short time scans* ($\Delta t \sim 2$ ps) to track the displacement of the THz amplitude peak.

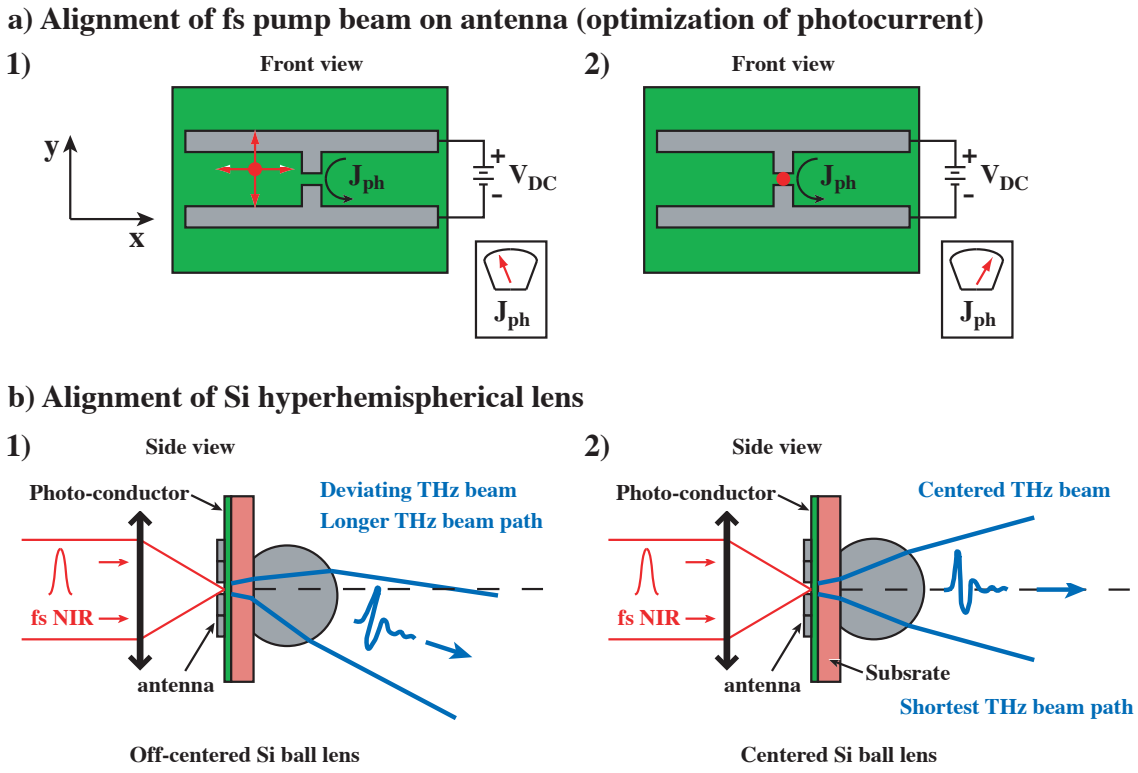

Figure 2.10 Techniques for the alignment of photoconductive antenna and ball lens. a) Precise alignment of the NIR fs pump beam on the photoconductive gap between the antenna branches can be achieved by optimizing the emission photocurrent ($\sim \mu$A). b) Optimization of the ball lens alignment can be carried out be maximization of the measured THz peak amplitude. The key point is that short time scans must be used to track the change in the peak arrival time due to the change in optical path length when the THz beam is deviated.

2.4.4 THz beam profiling

Finally, another tool to verify the proper alignment is THz beam profiling using the knife-edge technique. Since the far-infrared radiation is not visible and no scopes exist for the visualization of the THz beam, an indirect means must be taken to measure the characteristics of the THz beam.

The knife-edge technique is routinely used to measure the gaussian beam profile of optical and near-infrared pulses. In such a case, a screen is progressively translated across the optical axis to block the beam. A *power* meter measures the change in power, which takes the shape on an $erf(x)$[5]. In the case of a THz-TDS setup we have an *amplitude* meter instead of a power meter. So instead of a direct measurement of power at a given frequency, we measure the electric field in the time domain ($E_{\mathrm{THz}}(t)$) and then calculate the amplitude spectrum ($|E_{\mathrm{THz}}(f)|$) and the power spectrum ($|E_{\mathrm{THz}}(f)|^2$) for all frequencies.

Fig. 2.11.a) illustrates the knife-edge measurement technique in the specific case where the beam size is measured at the focal point of the parabolic mirrors, i.e. in the THz waveguide input coupling plane. The screen is displaced along the x axis in the direction perpendicular to the THz beam axis. Fig. 2.11.b) shows a typical result, where for each screen position x a time-scan yields the power spectrum in the frequency domain. For each frequency (Fig. 2.11.c)), the variation of power as a function of screen position x is then plotted. In Fig. 2.11.d) we consider a particular example of the curve measured for $f = 1$ THz. The power $P(x)$ is seen to decrease. If we assume that the THz beam profile is gaussian, $P(x)$ can be modeled by an complimentary error function $erfc(x)$, and the derivative of this function gives us a model for the corresponding gaussian distribution of the beam. The full-width at $1/e$ (2σ) of the gaussian distribution is indicated in the figure. Fitting of the $erfc(x)$ model can be repeated at all frequencies and from the corresponding gaussian functions (Fig. 2.11.e)) we can extract the characteristics of the beam such as the full-width at half-maximum (FWHM) and the center position of the gaussian distributions. Fig. 2.11.f) presents the FWHM of the power gaussian profiles as a function of frequency. Note that certain artifacts can be seen in the vicinity of water absorption peaks (0.56, 1.11, 1.41, and 1.92 THz [101]) due to the fact that the measurement was carried out at ambient humidity. It should also be noted that thee screen was positioned manually. This

[5]Or a complimentary error function $erfc(x)$, depending on which direction the screen is scanned. Or some other function if the beam profile is not gaussian.

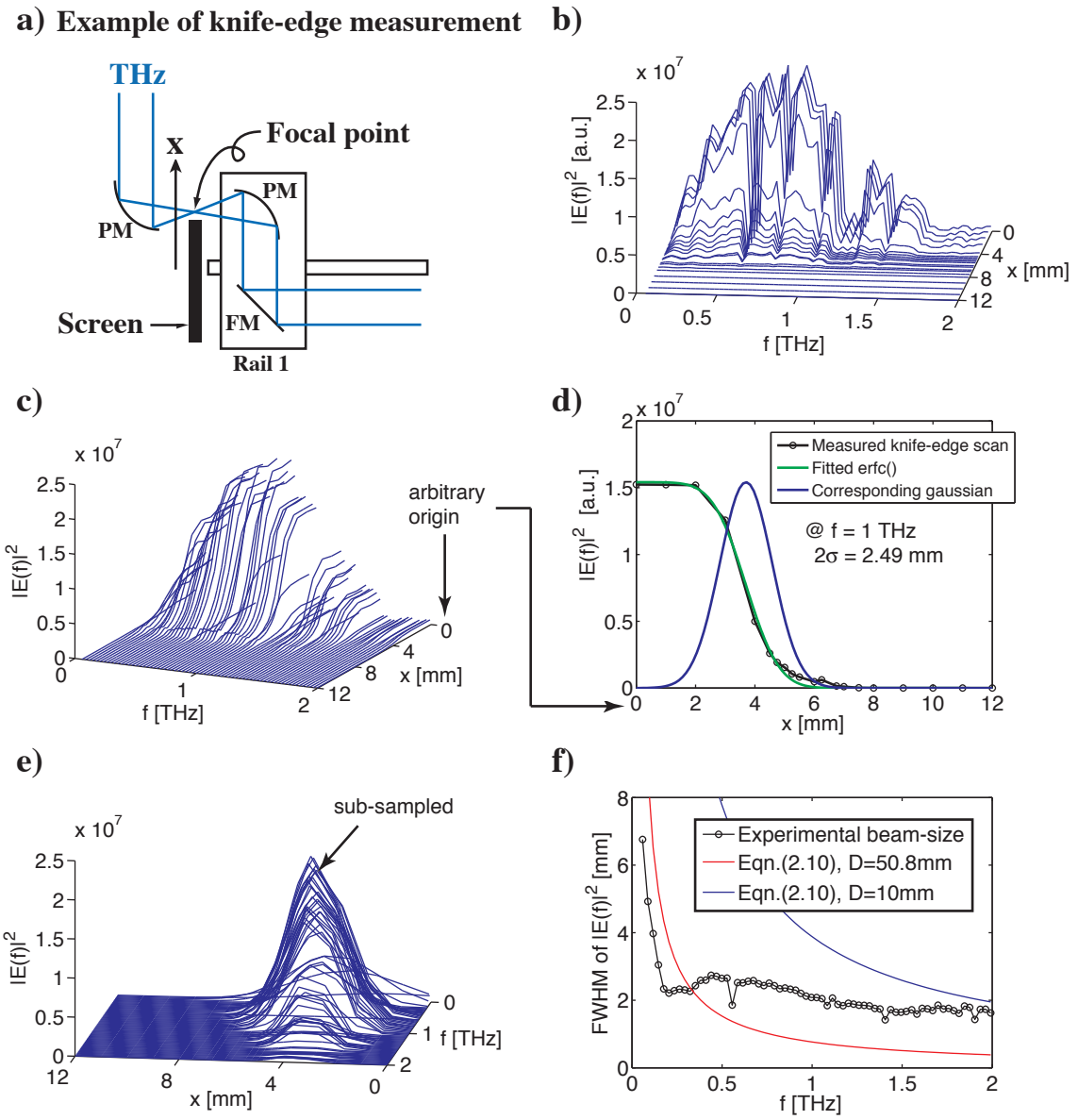

Figure 2.11 THz beam profiling using the knife-edge technique. a) Example illustrates the measurement of the beam size at the focal point of a parabolic mirror. b) Juxtaposition of power spectra measured at different screen positions (x). c) Transformation into knife-edge scans at individual frequencies. d) Example of erfc() fit at $f = 1$ THz, with corresponding Gaussian profiles and beam size. e) Gaussian functions fitted at each frequency (note the slight sub-sampling along x-axis). f) Full-Width-Half-Maximum (FWHM) of power distribution as a function of frequency, for the THz beam at the focal point of the parabolic mirror.

means that the smallest stepsize in the x-direction was $dx \sim 0.5$ mm. Such a coarse resolution limits the amount of screen positions that could be measured and hence affects the accuracy of the $erfc(x)$ fitting. Finally, manual displacement of the screen prevented a beam profiling measurement in the absence of humidity because of the difficulty of manipulating the screen with the purging cage closed (see section 2.5).

The frequency-dependent size of the THz beam in the input coupling plane is important for calculating coupling efficiency of a waveguide. For the knife-edge technique we tacitly assumed a gaussian profile for the THz beam. The focusing of a gaussian beam leads to a frequency-dependent beam size that is approximately given by [102],

$$w_0 \cdot w(\hat{f}) \approx \frac{\hat{f}\lambda}{\pi}, \tag{2.11}$$

where $w(\hat{f})$ is the initial waist of the beam, w_0 is the waist of the beam at the focal point, λ is the wavelength, and $\hat{f}$ is the focal length of the lens, or in this case the parabolic mirror. Alternatively, we can use D and d_0 to respectively designate the initial and focal point diameters of the gaussian beam. However, the diameter of a gaussian beam is an ambiguous notion. A common definition uses,

$$D = 2w(\hat{f}), \tag{2.12}$$

$$d_0 = 2w_0, \tag{2.13}$$

which leads to [102],

$$d_0 \approx \frac{4\hat{f}\lambda}{D\pi}. \tag{2.14}$$

An initial estimate of D is the aperture size of the parabolic mirror. In our setup the off-axis parabolic mirrors have a focal length of 101.2 mm (4 in.) and an aperture of 50.4 mm (2 in.). However, knife-edge measurements before the parabolic mirror reveal that the THz beam does *not* fill the entire mirror aperture and that $D \sim 10$ mm is a better approximation. In Fig. 2.11.f) the experimental focal point beam size is compared to the prediction of equation (2.14). It can be seen that there is considerable discrepancy between the experimental result and the theoretical prediction for a focused gaussian beam. It should be noted that more precise beam

profiling experiments have demonstrated that the THz beam of a PC antenna does *not* behave like a TEM_{00} gaussian [103]. A sum of multiple Laguerre-Gauss modes are required to accurately describe the true THz beam and a TEM_{00} gaussian can only be considered as an approximation. Unfortunately, we lack the fiber-coupled THz detectors that would be required for a more accurate measurement of the THz beam profile. Moreover, the spatially integrated knife-edge measurement is not sufficient for accurately estimating parameters of the Laguerre-Gauss modes.

The THz beam profile is also important for the calculation of the coupling efficiencies between the input THz beam and the modes of a waveguide. In the subsequent chapters, the gaussian approximation for THz beam profile is assumed but the experimentally measured beam size is used.

2.5 The humidity problem

In this final section we discuss one of the largest challenges of far-infrared spectroscopy. Ambient water vapor (humidity) has very strong absorption lines at THz frequencies. A detailed list of the frequency positions and strengths of the absorption lines can be found in the literature [104, 101].

To illustrate the adverse effects of water vapor absorption, Fig. 2.12 compares the typical source spectra measured with and "without" humidity in the ambient air. Actually, we compare high and low humidity levels because we are unable to completely remove the water vapor in our setup. The positions of the water absorption lines are indicated by red lines in the spectra. Also note that the spectrum is on a log scale. At high humidity levels absorption is clearly seen to burn holes in the spectrum. The signal to noise ratio in these absorption bands severely decreases. At low humidity levels we approach the ideal smooth decrease of amplitude expected for the THz emission from a PC antenna [95]. At 8.5% humidity, despite certain small absorption peaks that are still present at higher frequencies the spectrum is relatively smooth. The exact value of the humidity level is not important provided that it is low enough to give a decent signal to noise ratio ($\geq$20 dB) across the entire spectrum and that it remains constant over the course of the experiment. Note that from 0 to 2 THz the *amplitude* dynamic range is on the order of 20 dB, i.e. an amplitude signal/noise ratio of 100 and a power signal/noise ratio of 10 000.

The main problem is the difficulty of removing the humidity. There are two

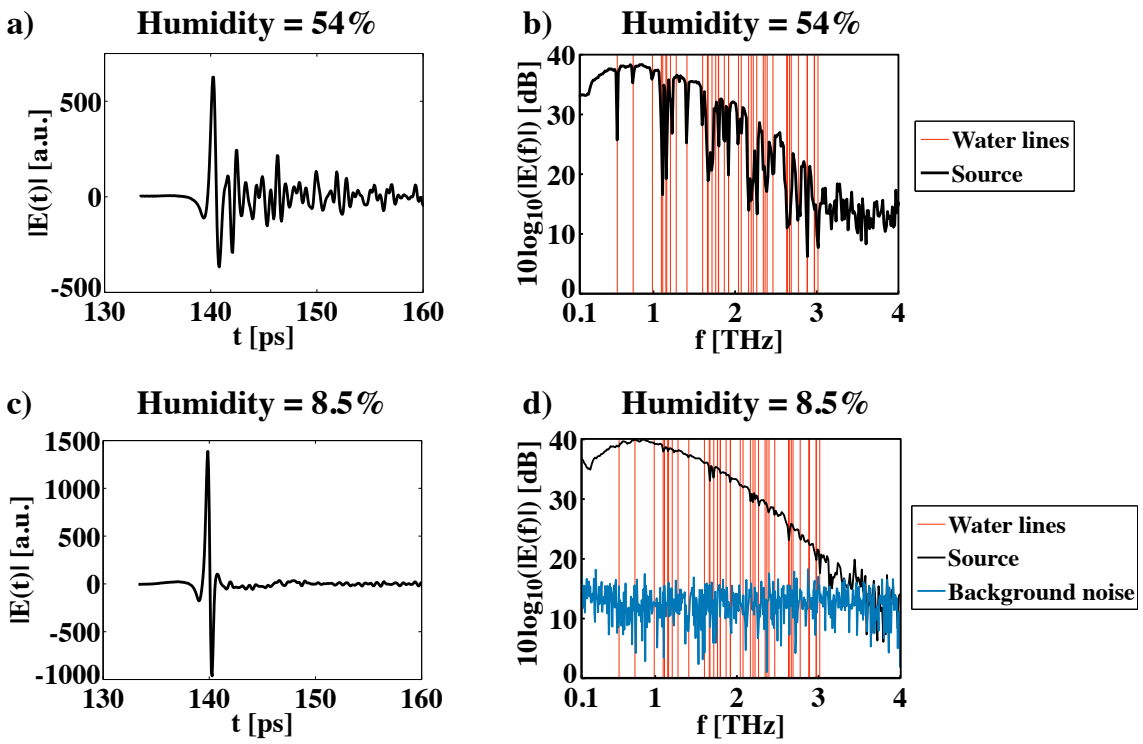

Figure 2.12 Effects of water vapor absorption on the source spectrum. a) Time scan measured at a humidity level of 54%, b) corresponding spectrum. c) Time scan measured at a humidity level of 8.5%. d) corresponding spectrum. Note the slight residual water absorption above 1.5 THz at 8.5% humidity.

basic approaches: vacuum purging [105, 106] or nitrogen purging [107, 108, 109]. Both techniques have their advantages and disadvantages. On one hand, vacuum purging requires a metallic cage surrounding the setup in order to support the pressure differential with the ambient atmosphere. This further implies that the optics are mounted on a breadboard that can be set within the cage. Finally, a proper seal is required to insure the air-tightness of the cage. On the other hand, nitrogen purging can be done with a simpler plexiglass cage and out-gassing from positive pressure eliminates the strict requirement of air-tightness.

For our setup we opted for nitrogen purging. A large plexiglass cage was set atop the THz optics, see Fig. 2.13.a). The front and top of the cage opens with a double hinged flap. When the cage is closed dry nitrogen is pumped through a small hole on the side of the cage. The humid air can then escape from the open holes left for the fs-laser beams, the holes in the imperfectly sealed flap, and through the unsealed

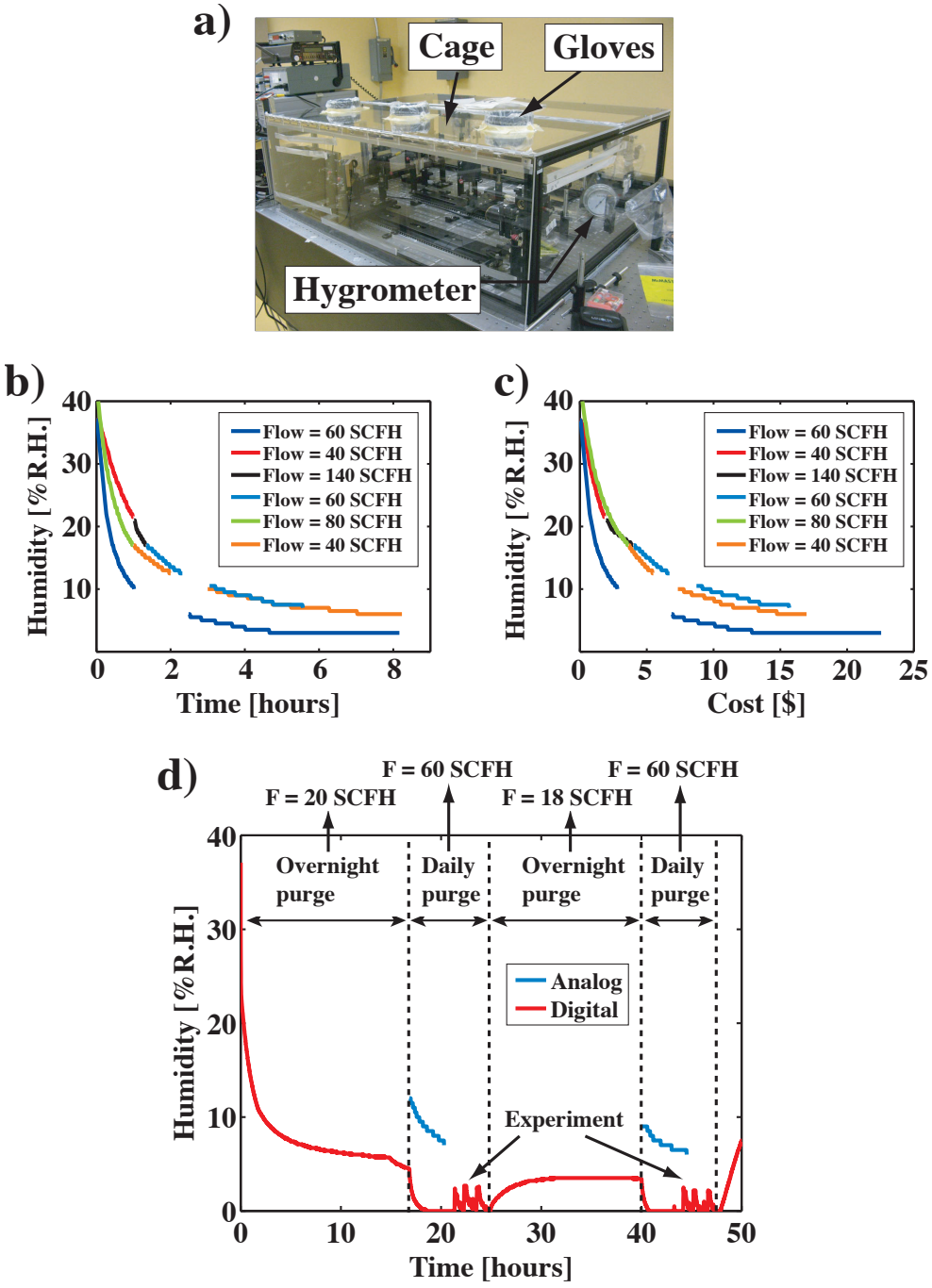

Figure 2.13 Assessment of purging time and cost. a) Photo of purging cage. b) Purging time tests. c) Purging cost. d) Comparison of the humidity measured by an analog and a digital hygrometer during the purging before waveguide transmission measurements.

holes of the optical table. An added difficulty in our case is the considerable volume of the cage ($V_{\text{cage}} = 323\ \ell$), which is much larger than those in conventional setups.

Different trial runs of purging were made in an attempt to optimize the purging time. The results of different purging attempts using different nitrogen flow rates are presented in Fig. 2.13.b). Note that the flow is measured in Standard Cubic Feet per Hour (SCFH), where 1 SCFH = 28.3 ℓ/hour at standard pressure and temperature (1 atm., 0°C). A common feature in Fig. 2.13.b) is that many *hours* are required to reduce the humidity to an acceptable level and that after several hours the humidity level appears to saturate at some sort of equilibrium. The first purge (navy blue curve) was carried out at a moderate flow of 60 SCFH and without any special attention paid to the cage. The subsequent purges, at different flow rates, where carried out after attempting to seal all possible air holes with tape. Trying to seal the cage hermetically actually made the purging worse and the purging rate was also found to be relatively independent of the nitrogen flow rate. Fig. 2.13.c) presents the humidity level achieved as a function of total purging cost. The final point of each series indicates the total cost of that purge. Due to the long purging times the cost in terms of gas becomes non negligible. In an attempt to maximize the number of experiments carried out under a given purge, we have installed gloves on top of the cage (Fig. 2.13.a)) to manipulate objects in the cage without opening the flap and losing the purged environment.

Both an analog and a digital hygrometer are set in the cage to monitor the humidity level. The digital hygrometer is useful because it can be programmed to take periodic measurements for days at a time, however the analog hygrometer is more accurate. Hygrometers are notoriously difficult to calibrate and must be re-calibrated often. An example of this can be seen in Fig. 2.13.d), where the humidity is measured over the course of multiple purging runs and experiments. The digital hygrometer is seen to be incorrectly calibrated as the humidity it measures appears to saturate at 0% while the analog hygrometer is still measuring a decrease in humidity. Thus it is difficult to confirm the actual values of humidity and the values of 8.5% and 54% reported in Fig. 2.12 should be interpreted with care.

Furthermore, Fig. 2.13.d) illustrates a typical purging run that must be carried out in order to do experiments at low humidity levels. First a slow purge was carried out overnight to start reducing the humidity. During the day, the purge flow was increased to bring the humidity down to a value acceptable for measurements. Note

the fluctuations in the humidity level of the digital hygrometer when the gloves are used to change samples. The gloves are not hermetically sealed to the cage and it is possible that humid air is seeping into cage when manipulating the gloves. This is difficult to confirm however, since the response time of the analog hygrometer appears to be slower and no change in humidity was measured on the analog instrument. After a day's worth of experiments were completed a low flow was left overnight to maintain a relatively low humidity level without wasting too much gas. At the end of the second series of experiments, the flow of nitrogen was stopped and the humidity level is seen to quickly rise despite *not* opening the cage. This example further illustrates that a purging flow must be maintained for a long time and at great expense.

More work is required to perfect the purging in our setup. A significant improvement would be eliminating rail 2 (see Fig. 2.6) from the setup. As previously mentioned, this manual delay line turns out not to be necessary for the THz measurements. Although it would require a complete re-alignment of the THz optics, removing rail 2 would simplify the setup layout and the size of the cage could be considerably reduced. A smaller cage would reduce the purging time.

Chapter 3

Single-mode porous subwavelength fibers

In this chapter we explore the first propagation loss reduction strategy, i.e. a small-core single-mode fiber that has low propagation loss resulting from an evanescent mode. These evanescent fields occur when the diameter of the fiber is smaller than the wavelength being guided. Therefore, these fibers are called subwavelength diameter fibers, or subwavelength fibers for short.

The simplest subwavelength fiber is merely a solid wire. Following work done on subwavelength holes in visible and near-infrared regions, Nagel *et al.* proposed the use of a single subwavelength hole to lower the loss of a waveguide by increasing the fraction of power guided in air [60]. A natural extension of this idea was to increase the number holes in the fiber to further decrease the propagation loss. After some initial theoretical work by my colleague Alireza Hassani, these porous subwavelength fibers were fabricated and characterized. This forms the basis of the work outlined in this chapter.

In the first section, we describe the guidance mechanism, the effect of the subwavelength holes, and consider simulations that illustrate what can be expected of these fibers in terms of propagation and coupling loss. In the second section, we describe in detail the multiple fabrication techniques that were developed to make the porous fibers. In the third section, we describe initial propagation loss measurements using a novel Directional Coupler Method technique. In the forth section, we describe the more accurate transmission and propagation loss spectra measured with the THz-TDS setup described in Chapter 2. Finally, in the last section, we discuss the limitations of this type of waveguide.

3.1 Waveguiding principle and design simulations

To illustrate the difference between the different types of subwavelength fibers Fig. 3.1 presents the power distribution of the modes guided by the different fiber geometries.

The simplest subwavelength dielectric fiber consists of a solid dielectric wire acting as a fiber core, surrounded by a low refractive index low loss cladding such as dry air (see Fig. 3.1.a). Light is guided by total internal reflection resulting from the step-index refractive index profile. At wavelengths larger than the fiber diameter, this simple fiber supports modes that extend into the air cladding, over distances that can be many times larger than the fiber diameter. It is the significant fraction of power guided in the air cladding ($\eta_{\text{clad}} \geq 50\%$) that reduces the propagation loss of the fiber. At large wavelengths (low frequencies), the mode size[1] increases and the effective modal loss due to material absorption can be reduced by a factor of 10 or more (see Fig. 3.2) when compared to the bulk absorption of the fiber material.

As an improvement to this design, Nagel *et al.* proposed adding a subwavelength hole to a THz subwavelength fiber [60]. As can be seen in Fig. 3.1.b), in this design the fraction of power guided in the air increases because of the higher field concentration within the hole. Thus the gain comes not only from the presence of power within the air hole but also from the fact that the concentration of power is higher in the air hole than in the adjacent material regions. This effect is due to the continuity of the electric flux density normal to the dielectric interfaces. Particularly, the electric field at the dielectric/air interface shows a discontinuous jump to *higher* values inside of the air hole because the hole has a much lower refractive index compared to that of a fiber material [110].

As a further improvement, our group proposed adding more holes within the subwavelength fiber core, see Fig. 3.1.c), as a means of further reducing the fiber absorption loss by forcing a greater portion of light to guide in the dry low-loss gas regions within the porous fiber core. A theoretical investigation of this design demonstrated that the propagation loss of porous fibers was indeed expected to be lower than their non-porous counterparts [111, 112]. This is due not only to a higher fraction of power in the air cladding but is also due to a significant fraction of power within the air holes of the core. These simulations were also confirmed by another group [113]. Moreover,

[1] Consider the mode size to be the full width at 1/10 of the maximum height as we are interested in gauging the extent of the evanescent tail in the outer air cladding.

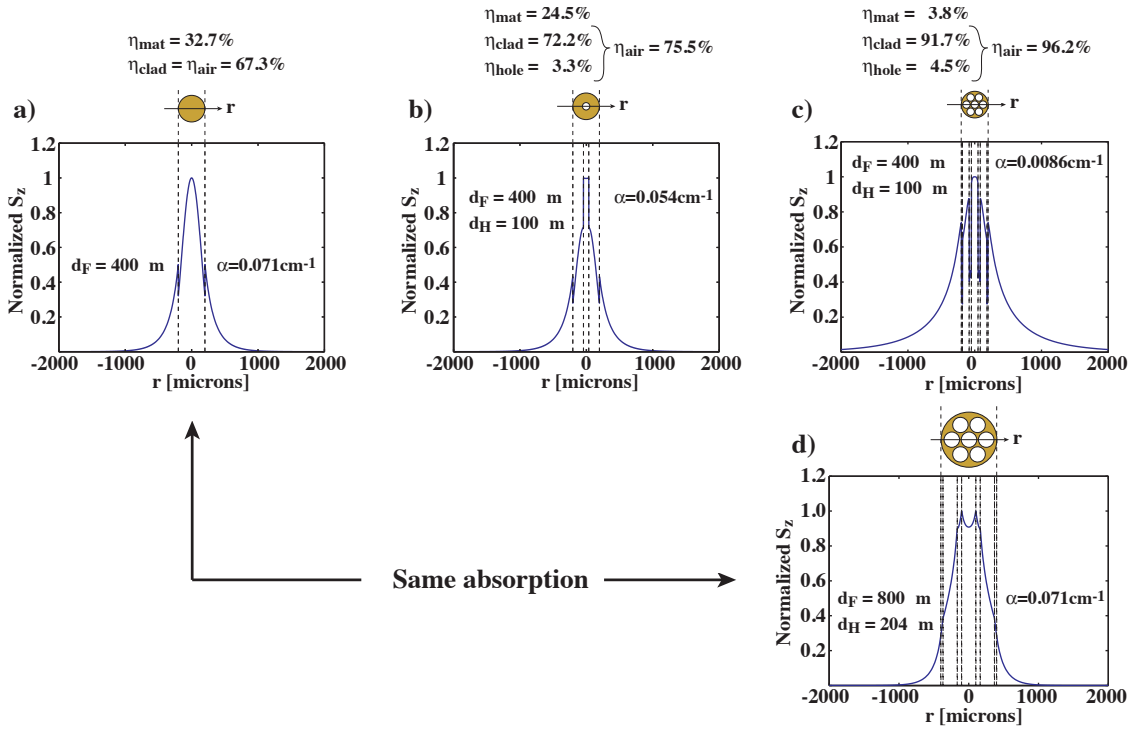

Figure 3.1 Comparison between the power distributions of the porous and non-porous subwavelength fiber modes. Spatial power distribution given by the z-direction Poynting vector, where z is the direction of propagation, is plotted for subwavelength diameter fibers that contain no holes (a), one hole (b), and seven holes (c,d). The dashed lines indicate the dielectric interfaces and the fiber geometries are schematized above the graphs. The simulation frequency is 0.3 THz ($\lambda = 1000\mu$m) and the fiber dimensions (and modal propagation losses) are given in the graphs. Note the discontinuous *increase* of the power within the subwavelength air holes.

since the holes are subwavelength it is straightforward to understand that the porous fiber acts as an effective medium with a lower index contrast than the non-porous fiber. Thus, when comparing fibers of same diameter and modes of same frequency (Figs. 3.1.a) and 3.1.c)), it can be seen that the evanescent field of the porous fiber extends farther into the air cladding than that of the non-porous fiber. This lower field confinement leads to a lower effective propagation index, a higher bending loss, and a greater susceptibility to scattering off fiber defects. Thus the tradeoff of porous fibers is lower absorption loss at the expense of lower mode confinement.

An interesting corollary is the comparison of fibers of *same absorption*. Fig. 3.1.d) presents a *large diameter* porous fiber that has the same absorption loss as the smaller

non-porous fiber shown in Fig. 3.1.a). The higher absorption due to the greater amount of material in the larger diameter fiber has been compensated by the addition of porosity. In this case, it is possible to show that the effective refractive index of the porous fiber mode is higher than that of the non-porous fiber [112]. The resulting mode confinement is stronger in the porous fiber and it is thus the larger diameter porous fiber that has lower bending loss in this case [112].

In order to appreciate the differences between these subwavelength fibers we now consider a quantitative comparison. Fig. 3.2 presents vectorial simulations of the optical properties of the fundamental mode propagating in subwavelength fibers having no holes (first row), seven holes (second row), and one hole (third) row. To model a non-porous rod fiber (first row) and a single-hole porous fiber (third row) we have used a transfer matrix code, see Appendix C, to find the fundamental HE_{11} mode of both circularly-symmetric fibers. In the case of a seven hole porous fiber we have used a vectorial finite element code to find the fiber mode, see Appendix D. A fiber mode is a solution to Maxwell's equations and is characterized by a complex-valued propagation constant,

$$\widetilde{\beta} = \frac{2\pi f}{c}\widetilde{n}, \tag{3.1}$$

where $\widetilde{n} = n_{\text{eff}} + i\kappa_{\text{eff}}$. The real part, n_{eff}, is the effective propagation index of the mode as it propagates along the waveguide, and the imaginary part, κ_{eff}, is related to the power propagation loss coefficient, $\kappa_{\text{eff}} = \alpha_{\text{eff}} \frac{c}{4\pi f}$. Thus,

$$\widetilde{n} = n_{\text{eff}} + i\alpha_{\text{eff}} \frac{c}{4\pi f}, \tag{3.2}$$

where n_{eff} and α_{eff} are real-valued.

The $\widetilde{\beta}$ mode solutions are found numerically using the above mentioned Transfer Matrix or Finite Element methods. However, since $\widetilde{\beta}$ values are not very descriptive it is more intuitive to present the results in terms of n_{eff} and α_{eff}. It should be noted that throughout this thesis the calculations are carried out with complex-valued refractive indices, however the mode solutions are characterized by the real-valued n_{eff} and α_{eff}, which are presented separately.

The calculations assume poly(ethylene) (PE) as the fiber material and further assume frequency independent values $n_{\text{PE}} = 1.56$ and $\alpha_{\text{PE}} = 0.2$ cm^{-1}. It should be noted that in the literature there are several widely different values reported for the bulk absorption loss of PE, ranging from ~ 0.1 cm^{-1} in Ref. [54] to ~ 2 cm^{-1}

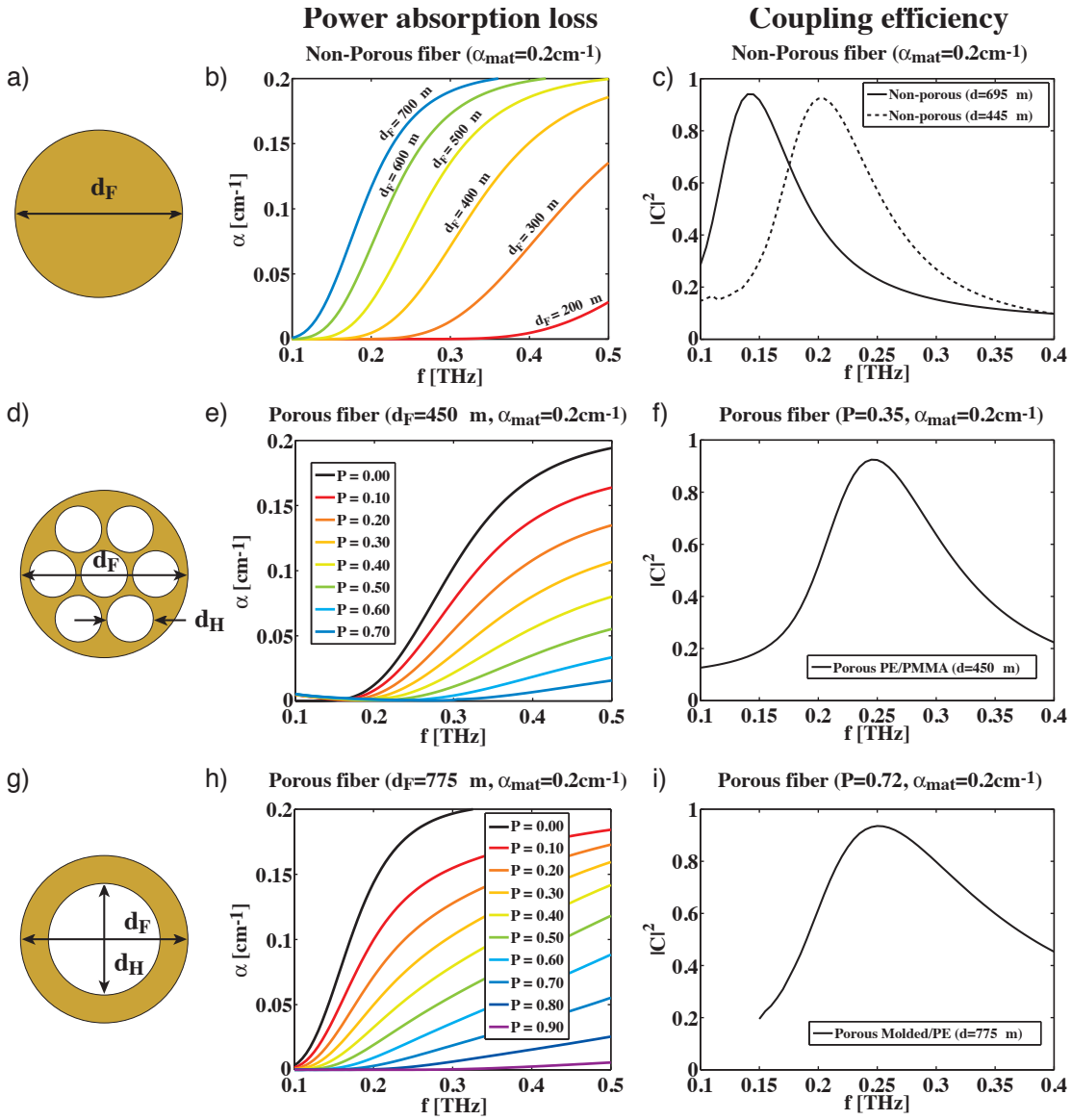

Figure 3.2 Modal losses of porous and non-porous subwavelength fibers as a function of the fiber geometry parameters (d_{F} = fiber diameter, P = porosity). First row: non-porous subwavelength fiber; second row: subwavelength fiber with seven identical air holes; third row: subwavelength fiber with one air hole. First column: schematics of the fiber geometries; second column: attenuation loss of the fundamental HE_{11} mode as a function of frequency; third column: power coupling coefficient between a gaussian beam (with frequency independent FWHM=2.3 mm) and the fundamental mode.

in Ref. [53] at frequencies around 0.2 THz. The exact value depends greatly on the fabrication process of the polymer. In our case, the exact values for the PE we used (see Fig.3.4.d)) were measured using THz-TDS *after* the calculations of Fig. 3.2 were completed. Nevertheless, the frequency independent values cited above are an excellent approximation at the frequencies of interest ($f < 0.5$ THz).

Fig. 3.2 presents the simulation results for each of the three geometries. The first column presents schematics of the fiber geometries. The second column presents the power absorption loss, α, of the fundamental mode as a function of frequency. Fig. 3.2.b) presents absorption loss of the fundamental mode of a non-porous fiber; in the figure, different curves correspond to the different fiber diameters. Figs. 3.2.e) and 3.2.h) present the modal losses for porous fibers of given diameter; in the figures, different curves correspond to the different values of the fiber porosity. Porosity is defined as the ratio of the total area of the air holes to the total area of the fiber core. To vary fiber porosity, the size of the air holes is varied. For simplicity, all the holes are assumed to have the same diameter.

Behavior of the loss curves for various values of the fiber geometry parameters is easy to understand in terms of the normalized (dimensionless) frequency,

$$V = \frac{2\pi}{c} \cdot f \cdot d_{\text{core}} \sqrt{n_{\text{core}}^2 - n_{\text{clad}}^2}. \tag{3.3}$$

It is well known that the fields of a two-layer step-index fiber can be described in terms of V and that the extent of the fundamental mode increases when V decreases [114, 115]. Consider, for example, Figure 3.2.b). At a given frequency, choosing fibers of smaller diameters results in a fundamental mode with a lower V value. Hence this mode is strongly delocalized, extending beyond the lossy fiber core into the low-loss cladding. Therefore, at a fixed frequency, fibers of smaller diameters will exhibit smaller absorption loss due to a larger fraction of power guided in the low-loss cladding. Inversely, for a fiber of fixed diameter, decreasing the frequency of operation also decreases the value of V and leads to a more delocalized mode. Thus lower effective modal refractive index and lower modal absorption loss are also seen at lower frequencies. Consider now Figures 3.2.e) and 3.2.h). There, one observes a decrease in the fiber absorption loss for higher fiber porosities. This is easy to rationalize by noting that higher fiber porosities lead to a lower refractive index contrast between the porous fiber core and a gaseous cladding. A lower refractive

index contrast, in turn, means lower effective V values and higher modal presence in the air cladding. In addition to the fraction of power guided within the air holes, this delocalization once again contributes to the lower absorption losses of fibers featuring higher porosities.

Consider now the coupling losses from the gaussian-like THz beam into the fundamental mode of porous and non-porous fibers. The third column of Figure 3.2 presents the power coupling efficiency ($|C|^2$) between the linearly-polarized gaussian beam of a THz source and the fundamental mode of fibers under consideration, calculated using equation (2.9). For simplicity, a frequency independent full-width-half-maximum (FWHM) of 2.3 mm was assumed for the gaussian power distribution of the input beam in the focal plane of the parabolic mirror. This is a reasonable approximation of the measured beam size in the $f = 0.1 - 0.4$ THz frequency range (see Fig. 2.11.f)). Note that the calculated coupling coefficients are strongly frequency dependent due to the strong frequency dependence of the mode size. In fact, for all the fibers there exists a frequency of optimal coupling where the size of the gaussian beam and the size of the fundamental fiber mode are matched. Moreover, the frequency of optimal coupling into porous fibers is always higher than that of the non-porous fibers of the *same diameter*, which is due to stronger modal delocalization in the porous fibers compared to non-porous fibers of same diameter.

Finally, it is worth mentioning that although periodic arrays of holes were simulated theoretically and fabricated experimentally, the subwavelength fibers presented in this chapter are not photonic crystal fibers. Although bandgap guidance in holey fibers has been attempted for guiding THz radiation [69], the small size of the holes in the subwavelength fibers are such that the guidance mechanism remains total internal reflection.

3.2 Fabrication techniques

Fibers were fabricated using the standard fiber drawing technique. A macroscopic version of the desired fiber geometry, known as the preform, is prepared for drawing in a draw tower. It is mounted in a fiber holder, heated in the furnace of the draw tower and the molten preform is pulled into a fiber by a tractor assembly. Adjusting the drawing temperature and pulling speed controls the final diameter of the fiber.

There are two main challenges associated with drawing porous fibers. The first

is preparing the porous preform and the second is preventing the air holes from collapsing during the drawing process. Three different fabrication techniques were developed to address these problems: a hole-sealing technique, a sacrificial-polymer technique, and a preform-molding/fiber-inflation technique.

3.2.1 Hole-sealing technique

The standard technique for making holey fibers is the tube stacking technique [116]. To achieve a fiber with a high porosity it is preferable to stack thin-walled tubes when making the fiber preform. Since such tubes were not available commercially, we fabricated thin-walled tubes (straws) by rolling 100 μm thick PE film within a 5 mm inner diameter metal tube followed by solidification and annealing in the oven. The resulting tubes (Fig. 3.3.a)) had inner and outer diameters of 4.25 and 5 mm, respectively. Thus fabricated tubes were subsequently stacked and an outer layer of PE film was rolled around the stack. This outer film helps keep the tubes together and rounds out the hexagonal geometry that results from hexagonal stacking. The problem with drawing this type of preform is that without any compensation mechanism the air holes tend to collapse due to surface tension during the drawing process (examples can be seen in Fig. 3.4).

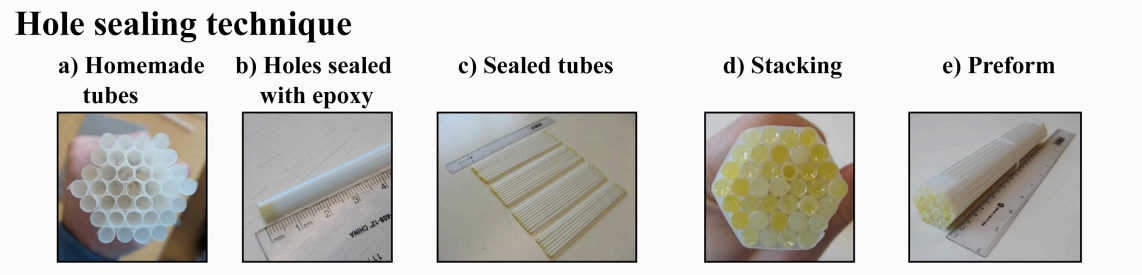

Figure 3.3 Illustration of the hole sealing technique. Air is trapped within plastic tubes by sealing both ends with epoxy glue. The sealed tubes are then stacked into a preform and drawn into a fiber.

The first method for preventing hole collapse is to trap some air within the tubes by sealing the ends shut. The trapped air builds pressure within the tubes which prevents the tube walls from shrinking too much. Thus both ends of each thin-walled tube were sealed with epoxy glue (Fig. 3.3.b)). Sealed tubes are then stacked into a preform (Fig. 3.3). While the trapping of air within the tubes generally prevents

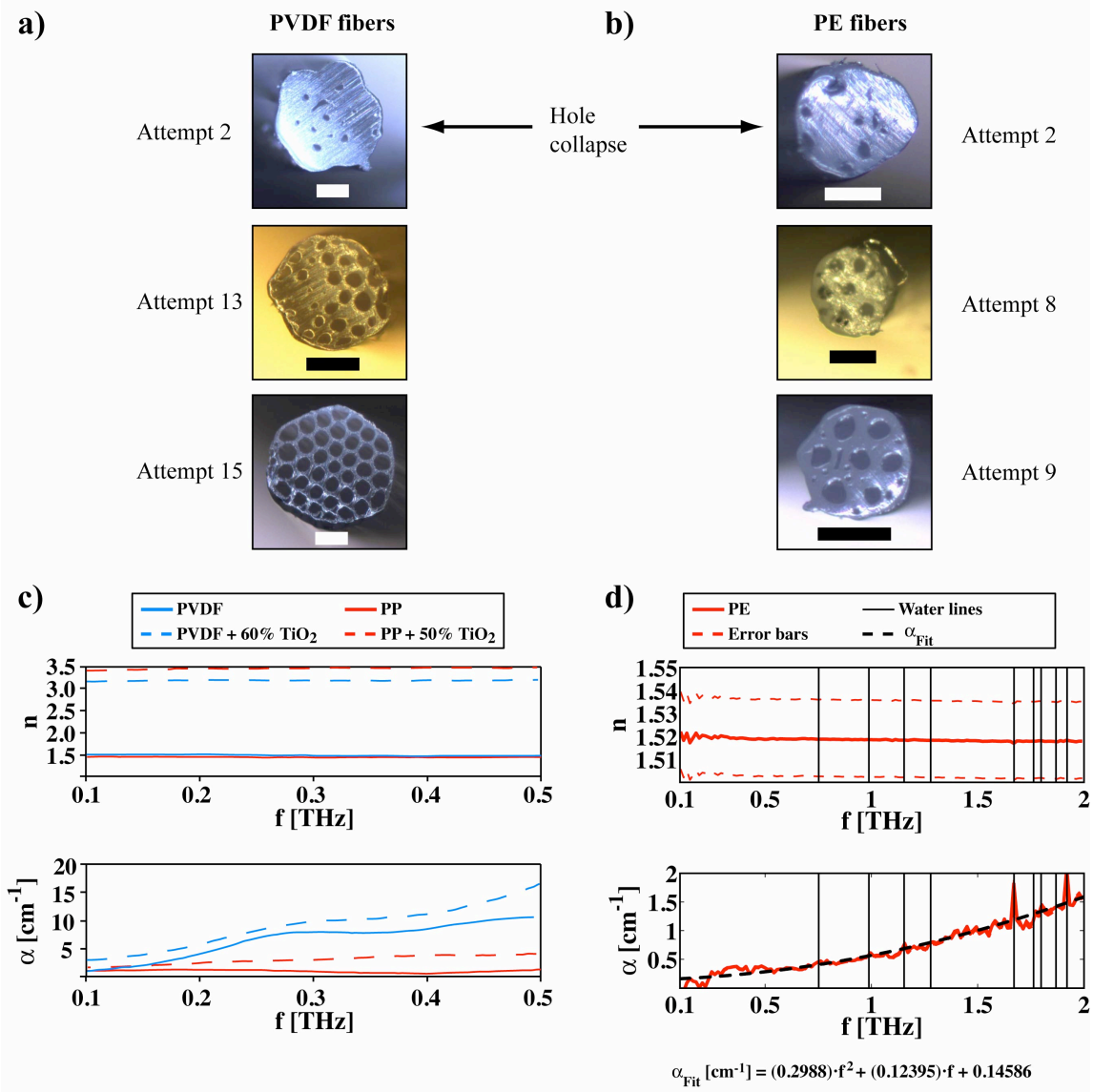

Figure 3.4 PVDF and PE fibers made by the hole-sealing technique. Many iterations are required to perfect the fiber drawing process and prevent hole collapse. Much effort was invested in PVDF fibers (a) before discovering that the PVDF absorption loss was prohibitively high (b). Efforts were repeated with PE fibers (c) because PE is one of the lowest loss polymers (d). Note that b) is adapted from [117]. All scale bars correspond to 200 μm.

complete hole collapse, it does not prevent hole reduction (partial collapse) which is an inherent consequence of the drawing process. Thus the fabrication of a proper porous fiber requires multiple iterations involving the verification that the tubes are properly

sealed and an optimization of the fiber drawing parameters. For example, the PE preform was drawn into fiber at 145°C with a drawing speed of 0.5 m/min. Whereas PE becomes soft at $T_g \sim 110$°C, it only melts and becomes drawable at higher temperatures. However, this type of fiber was drawn at a rather low temperature (145°C) in an attempt to reduce the effect of hole reduction.

Fig. 3.4 illustrates the importance of knowing the transmission properties of the fiber material and testifies to the large amount of iterations that are required for optimizing the fiber drawing process. Poly(vinylidene fluoride) (PVDF) was initially used as the fiber material and much effort was spent in perfecting PVDF subwavelength fibers. Because of a prior demonstration of a PVDF THz waveguide [72] and because of the similarity with respect to the molecular structure of PE it was naively *assumed* that the absorption loss of PVDF was acceptably low. Work on PVDF fibers began before any values of PVDF loss had been reported in the literature and before we had constructed our own THz-TDS setup to verify the material properties. It was only *after* that it was discovered that the loss of α-phase PVDF was prohibitively high for waveguiding (see Fig. 3.4.b)). Optimization efforts were consequently repeated using low loss PE (Fig. 3.4.d)) as the fiber material.

While a porous microstructure was clearly achieved with this technique, the fabrication process requires many optimization iterations. Furthermore, it was found that hole reduction is difficult to prevent and that the final porosity is somewhat low ($P \sim 25\%$ in Fig. 3.4.c)).

3.2.2 Sacrifical-polymer technique

The second method for fabricating porous PE fibers is a subtraction technique whereby sacrificial polymer regions within a drawn *all-solid* fiber are dissolved in order to form air holes. We chose poly(methyl methacrylate) (PMMA) as a sacrificial polymer as it can be easily dissolved in a solvent while leaving the PE plastic intact. Schematics of the fabrication steps are presented in Fig. 3.5.a). First, seven PMMA rods (6.35 mm diameter), purchased from McMaster-CARR, were placed without touching in a hexagonal array within a poly(tetrafluoroethylene) (PTFE) tube (2.54 cm inner diameter). The interstitial regions of the preform were then filled with polyethylene (PE) granules, more specifically Grade Sclair FP120A linear low density poly(ethylene) purchased from Nova Chemicals. An added benefit was that the sacrificial material

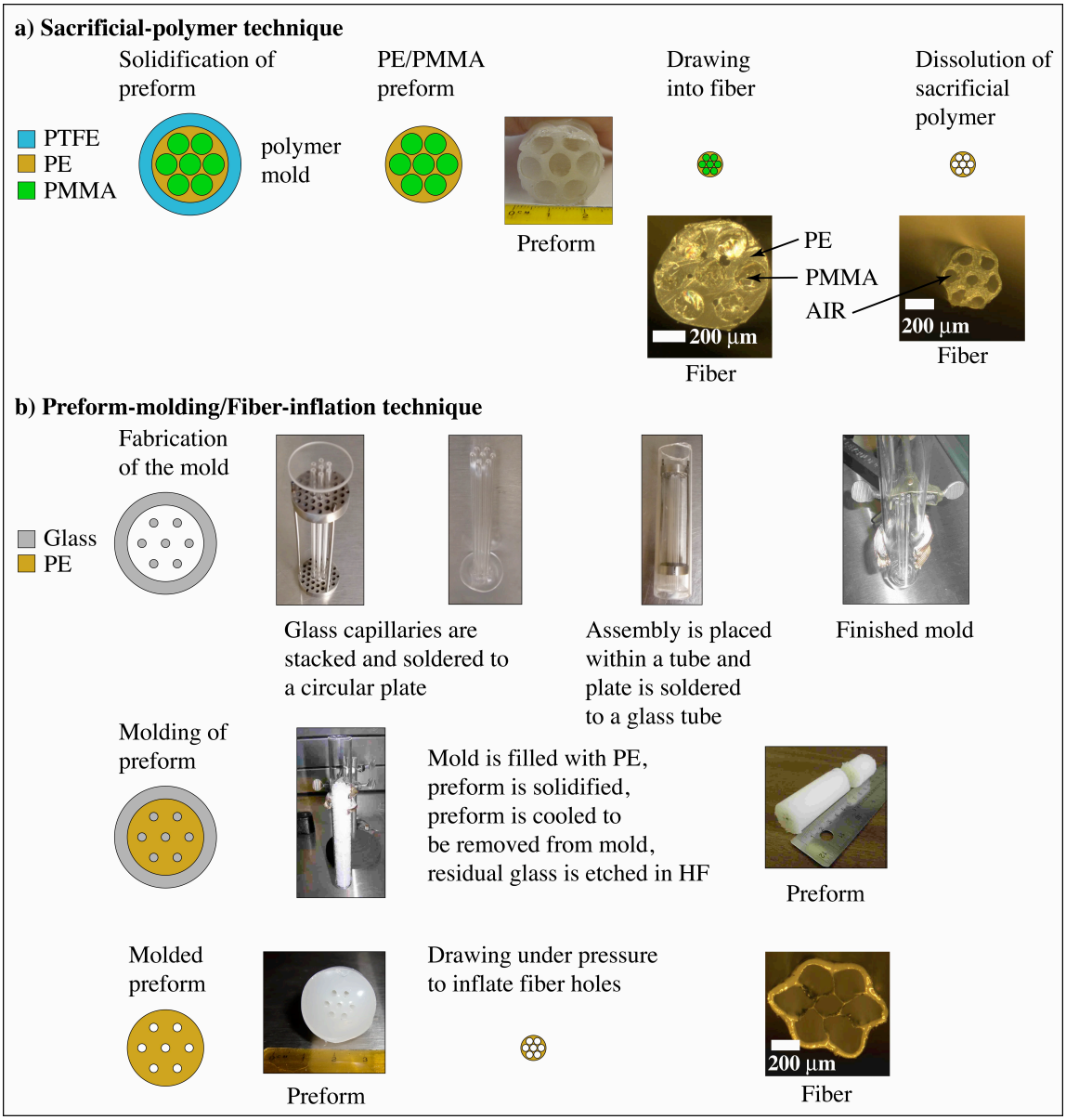

Figure 3.5 Schematics illustrating the sacrificial-polymer and molded-preform/fiber-inflation fabrication techniques. a) Fabrication steps of the sacrificial-polymer technique. b) Fabrication steps of the molded-preform/fiber-inflation technique.

had a significantly higher glass transition temperature. This allowed melting of the low viscosity PE polymer granules that consequently filled out the space between the sacrificial rods without any substantial mixing between the two polymers. The resulting preform was subsequently drawn into fiber at 210°C with a drawing speed

of 0.8 m/min. Note that this arbitrarily high temperature (210°C) was much higher than necessary (PMMA melts around 180°C) in order to insure that both polymers were melted enough to draw readily. Fiber segments of different lengths and diameters were then submerged into the solvent tetrahydrafuran (THF) for several days to etch away the PMMA inclusions. The fiber segments were subsequently left to dry for several days to allow the solvent within the fibers to evaporate. The resulting fibers showed clear porous microstructure with a porosity $\sim 35\%$.

The presence of PMMA prevents the collapse of the holes that would otherwise have occurred if they were left empty. The main advantage of the sacrificial polymer technique is that drawing of porous structures is greatly facilitated as hole collapse is completely prevented during fabrication. It should also be noted that decent fiber samples were obtained on the *first* try. The main disadvantage of this method is that a postprocessing step of removing the sacrificial polymer is required. While tens of meters of fiber are readily drawn from a preform, the dissolution process can ultimately limit the length of etched fiber. Although we present a fiber with 35% porosity by area, it should be noted that this technique is very versatile and that much higher porosities can easily be achieved by incorporating more sacrificial polymer into the preform (with larger PMMA rods, for instance).

There are some non-uniformities in the resulting fibers (see the second column of Fig. 3.9). However, these defects arise during the drawing process, not during the etching process, as can be seen by extra holes in the non-etched fiber cross-section in Fig. 3.5.a). These extra holes are attributed to non-uniform cooling of the fiber due to the vastly different melting temperatures of PMMA and PE. Further optimization of the fabrication process would be required to minimize these defects.

3.2.3 Preform-molding/fiber-inflation technique

Another method that was developed for the fabrication of porous (and, in general, microstructured) fibers uses casting of a fiber preform in a microstructured mold. The resultant preform features air holes which have to be pressurized during drawing to prevent hole collapse.

Schematics of the fabrication steps are presented in Fig. 3.5.b). A porous cylindrical preform, featuring seven holes running its entire length, was fabricated by melting PE granules and solidifying the melt within a microstructured glass mold. The glass

mold was prepared by first aligning thin-walled quartz capillaries in a hexagonal arrangement using special alignment rigs, followed by the fusion of the aligned capillaries to a circular quartz plate with the aid of a propane torch. The ends of the capillaries were sealed to prevent PE from filling the capillaries during the molding process. The assembly of glass capillaries was then inserted in and fused to the bottom of a large diameter quartz tube. The other end of the tube is left open to allow placement of the polymer granules on top of the microstructured mold. The tube was then filled with granules and placed into a furnace. After melting the polymer, the polymer melt was transferred by gravity into the mold region. Upon cooling, most of the glass mold could be removed by simply pulling it from the polymer preform. Any residual glass was dissolved in hydrofluoric acid, which had no effect on the PE preform. A porous fiber was subsequently drawn while pressurizing the preform holes. In addition to preventing hole collapse during drawing, a sufficiently large air pressure could *inflate* the holes and greatly increase the fiber porosity. The resulting fibers had a porosity as high as 86%.

In principle, the molding technique can yield a faster more repeatable production of preforms. Another advantage is that molding produces preforms that do not have the interstitial holes[2] which are present in preforms fabricated by tube stacking. The pressurization step is thus greatly facilitated. A disadvantage is that it is difficult to balance the effects of pressurization and hole collapse during the drawing process. Without dynamic control of the pressure the fiber easily inflates to the point of deformation and rupture.

3.2.4 Non-porous fiber

A non porous fiber was fabricated using the same PE granules as in the previous sections. Granules were melted in a PTFE tube and compacted to remove air bubbles. The preform was subsequently drawn into fiber at 160°C with a drawing speed of 0.6 m/min. The resulting non-porous fibers of different diameter were used as a benchmark for comparison with the porous fibers.

[2]Hexagonal stacking of tubes leaves small triangular interstices between the touching tubes.

3.2.5 Process control

Further optimization needs to be done to truly demonstrate process control. The fabricated fibers still have multiple defects including dust, impurities trapped in the polymer, non-uniformities in the fiber cross-section, occasional variation of the porous microstructure along the length of the fiber, and fluctuations in the fiber diameter. Although we have fabricated short segments ($\sim$ 30 cm) of fibers with few defects, these defects accumulate over longer fiber lengths, notably with large fluctuations in the fiber diameter. Proper control of the fiber diameter would require fine tuning of the preform heating profile and feedback control of the tractor assembly, as well as the possible addition of a jet of cold air to quench the temperature of the fiber. Finally, it should be mentioned that in order to compare the various fiber fabrication techniques a comparison would ideally be made with fibers of the exact same diameter. However, beyond the diameter fluctuations (Δd_{F}), difficulties with the feedback control made it experimentally difficult to obtain fibers with the same average diameter ($[d_{\mathrm{F}}]_{\mathrm{avg}}$). Hence, fibers of slightly different average diameters are compared in the following sections.

3.3 Loss measurements using Directional Coupler Method

Initial characterization of the transmission properties of porous and non-porous subwavelength fibers was carried out in collaboration with Denis Morris's THz spectroscopy group at the University of Sherbrooke. The experiments were carried out using a broadband PC antenna source and a liquid-helium-cooled frequency integrating bolometer.

To circumvent the difficulties associated with cutback measurements when using a bolometer detector (section 3.3.1) we devised a novel loss measurement method that is both reliable and non-destructive. The method consists in using a second subwavelength fiber to form a directional coupler with the test fiber. This directional coupler is then translated along the length of the test fiber in order to probe its power attenuation (see Fig. 3.6.a)). The power coupled to the second fiber (and the subsequent detector) will decrease as the coupler is translated towards the output end of the test fiber because of the test fiber propagation loss. This method is similar in

spirit to an evanescent prism coupling technique that had been used by Boudrioua *et al.* to measure the transmission loss of planar waveguides [118]. It should also be mentioned that a directional coupler featuring two touching subwavelength fibers had previously been demonstrated in a THz imaging setup [63], but that the coupler geometry was fixed in that case.

The setup for this Directional Coupler Method (DCM), the cross-sections of the measured fibers, and the measured fiber attenuation losses are discussed in the following sub-sections. Also discussed are fiber holding techniques and the careful interpretation of the experimental results due to frequency averaging and low-pass filtering effects.

3.3.1 Cutback measurement with a bolometer

A standard technique for measuring fiber transmission loss is a cutback method. Within this method the direct power transmission through fibers of different lengths is measured. The input end of the test fiber is fixed during the procedure, and the output end is repeatedly cut to shorten the length of the fiber. The shortest waveguide can be used as a reference point to calculate the power reduction. The advantage of this procedure is that it eliminates the need to estimate the input coupling efficiency into the waveguide. While being a very powerful method for measuring losses in telecommunication fibers, the use of the cutback method is limited in the case of short subwavelength fibers and bolometer detectors. The two main problems are the difficulty in filtering the background noise and the sensitivity to detector alignment.

First of all, the cutback method hinges on measuring power originating only from fiber transmission. However, the input aperture of the bolometer is large and the small diameter fibers led to a high level of stray light reaching the detector. To obtain the sole contribution of the fiber the reference signal, measured in the absence of a test fiber, must be subtracted from the total signal, measured with the fiber in place. In many situations this reference (background) signal corresponds to the noise floor of the detector and is negligible. However, in the case of the short length ($\sim$ 25 cm) subwavelength fibers that we sought to measure, the background signal was not negligible because of a large amount of light that was not coupled into the waveguide could reach the large aperture of the detector. On one hand, the effects of stray light can be eliminated by a time-resolved measurement, because light following

different paths will have different arrival times on the detector and time-windowing can extract the desired signal. Of course, such time-windowing is not possible with a bolometer because it only measures a time-averaged signal. On the other hand, the background signal can also be eliminated by screening (with irises, for instance), but this was found to interfere with the evanescent field of the waveguide and attenuate the fiber transmission. Proper measurement and subtraction of the background signal was therefore required.

Secondly, the cutback technique is a destructive method and is prone to errors because of variations in the cleave quality and the realignment of the fiber output end. The realignment problem is especially pronounced when working with a THz bolometer. This is due in part to the large input aperture of the instrument and to the sensitivity to detector alignment. Because of its internal optics, the amount of light sent onto the actual detector head is highly dependent on the distance and angle of the fiber with respect to the input aperture.

Despite efforts in following a careful and systematic procedure, these effects exacerbated any human errors made in the realignment and led to non-reproducible bolometer measurements. After a great deal of trial and error the cutback technique was found to be impractical in this case.

3.3.2 Directional coupler method setup

Fig. 3.6.a) presents a schematization of the DCM setup developed to circumvent the difficulties associated with the cutback measurements. A Ti:sapphire laser beam is focused onto a photoconductive antenna to emit THz light. The THz emission spectrum was relatively broad (inset in Fig. 3.6.b)), extending from 0.25 THz to 2.15 THz (10% of the maximum power) with an emission peak at 0.75 THz. The THz radiation is collimated and refocused by the parabolic mirrors in order to couple light into a test fiber. The two ends of a test fiber are positioned individually with micrometer accuracy using 3-axis mounts. Moreover, the fiber can be accurately aligned with the focal point of the THz beam with the help of a Ti:sapphire laser beam, which passes through a small hole in the PM2 parabolic mirror.

The coupler fiber and the bolometer are both mounted on a rail, which can be translated along the length of the test fiber with an accuracy of 0.5 mm. The coupler fiber is a 29 cm long non-porous PE fiber with an average diameter of 380 μm. The

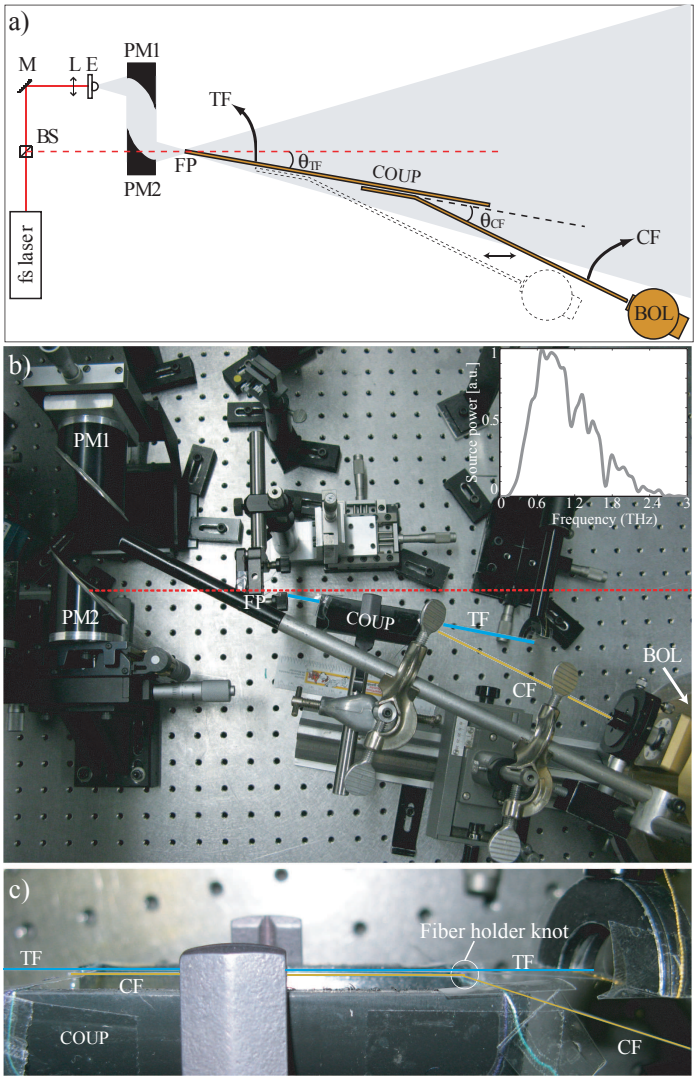

Figure 3.6 Experimental setup for measuring fiber transmission losses using the directional coupler method. a) Sketch of a setup. The directional coupler (COUP) detector, consisting of a coupling fiber (CF) and a bolometer (BOL), is translated along the length of the test fiber (TF). Test fiber is placed at a θ_{TF} angle with respect to the axes of a focusing parabolic mirror (PM2), while coupling fiber is placed at θ_{CF} angle with respect to the test fiber. Such placement of the fibers is done to reduce background noise by insuring that the bolometer is placed outside of the THz light cone generated by the PM2 parabolic mirror. Also in the sketch - E: emitter, L: lens, M: mirror, BS: beam splitter. b), c) Photos of the experimental setup. Images of fibers are enhanced for visibility. Inset: THz source spectrum.

coupler region consists of a 7 cm long straight segment which was brought parallel to and almost touching the test fiber. The distance between the fibers in the coupler region is dictated by the size of the knots holding the coupler fiber (see section 3.3.6). Measuring the size of the knots in photographs of the fiber coupler we estimate the distance between the fibers in the coupling region to be $\sim$400 μm in all the experiments. Outside of the coupler region, the coupler fiber is angled off by $\theta_{\mathrm{CF}} = 16^{\circ}$ towards the bolometer (see Fig. 3.6). Furthermore, the test fiber was placed at an angle of $\theta_{\mathrm{TF}} = 10^{\circ}$ with respect to the optical axis. These two angles were chosen as to insure that the bolometer remained outside of the divergence cone of the THz light, while there was still enough light passing through the bend in the coupler fiber to reach the detector. As was confirmed by the calibration experiments, only the light guided by the coupler fiber could reach the detector, since the bolometer was registering the normal noise level when the coupling fiber was removed. This approach eliminated all the background signal problems encountered with the standard cutback technique. As an example, when both the coupler and test fibers were removed, the bolometer measured 6 μV as the noise level. When only the coupler fiber was used, the bolometer measured $\sim$100 μV as the reference signal. Finally, when both the coupler and the test fibers were used, the bolometer measured $\sim$800 μV.

3.3.3 Measurement example

To understand how to interpret the data let us begin by considering the case of a fixed frequency. Denoting $P_{CF}(z)$ to be the power measured at the end of the coupler fiber translated by the distance z along the test fiber, and under the assumption of constant coupling efficiency η between the two fibers along the whole length of the test fiber, the test fiber attenuation coefficient, α_{TF}, in principle, can be calculated from the measurement of only two points:

$$\begin{aligned} P_{CF}(z_1) &= \eta \cdot P^0_{TF} \cdot e^{-\alpha_{TF} \cdot z_1 - \alpha_{CF} \cdot z_{CF}} \\ P_{CF}(z_2) &= \eta \cdot P^0_{TF} \cdot e^{-\alpha_{TF} \cdot z_2 - \alpha_{CF} \cdot z_{CF}} \\ \alpha_{TF} &= \frac{1}{z_2 - z_1} \ln\left(\frac{P_{CF}(z_1)}{P_{CF}(z_2)}\right), \end{aligned} \tag{3.4}$$

where α_{CF} is the loss of a coupler fiber, z_{CF} is its length between the coupler and bolometer, and P^0_{TF} is the power injected into the test fiber. First of all, let us

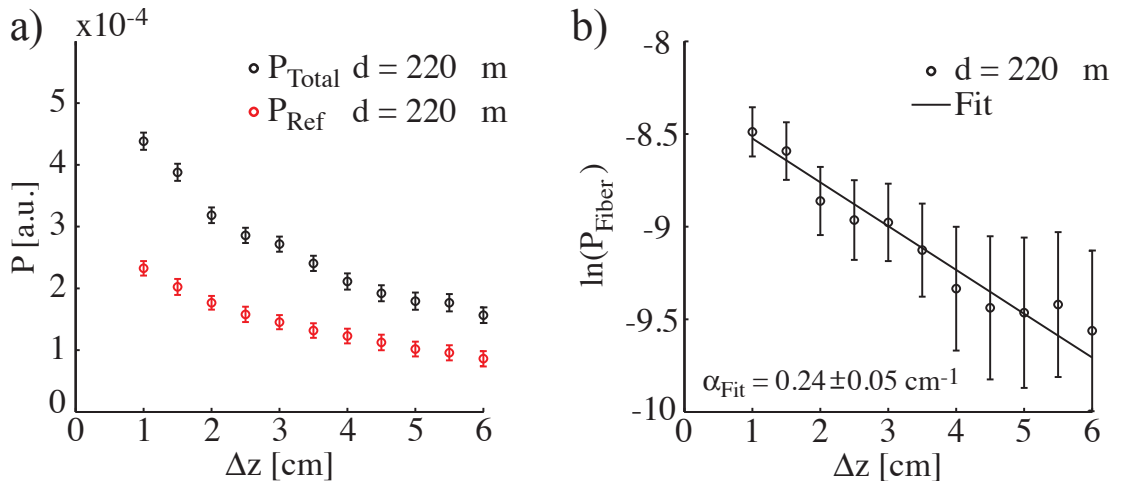

Figure 3.7 Example of the fiber attenuation measurement for a 220 μm average diameter non-porous fiber using the directional coupler method. a) Variation of power as a function of relative displacement (Δz) along the test fiber. Total and reference signals are measured with and without the test fiber, respectively. b) Fit of the fiber attenuation data ($P_{\text{Fiber}} = P_{\text{Total}} - P_{\text{Ref}}$).

remark that equation (3.4) is a simple scaling law that describes a linear response on a semilog scale. While the strict minimum for fitting a line is two points, such a fit will be more accurate on multiple experimental points. The main advantage of the directional coupler method (DCM) is that it is straightforward to measure many data points by simply displacing the coupler fiber along the test fiber (no cleaving or realignment is required). This is an important part of the validation process as one can easily measure as many points as deemed necessary for a satisfactory fit. Secondly, it should be noted that the use of a linear least squares fit yields maximum likelihood limits for the fitted slopes, which give a more accurate evaluation of the attenuation constant error bounds. These facts lead us to believe that the directional coupler method increases the accuracy and reliability of the loss estimates in comparison to the propagation losses of subwavelength fibers previously determined by the cutback method [58].

Fig. 3.7 presents an example of the power attenuation measurement with the directional coupler. Fig. 3.7.a) shows the variation of power as a function of the displacement (Δz) along the length of the test fiber. Note that the measurement did not start at the beginning of the test fiber. The reference signal (red circles),

measured by translating the coupler in the absence of a test fiber, is due to direct coupling of the THz light, from the divergent cone produced by the parabolic mirror PM2, into the coupler fiber. The bolometer signal is modulated at 300 Hz and is sent to a lock-in amplifier. The values and error bars correspond to the average and standard deviation of 500 bolometer measurements sampled over a ~ 3 minute time span. The fiber transmission is obtained by subtracting the reference signal from the signal measured with the test fiber ($P_{\text{Fiber}} = P_{\text{Total}} - P_{\text{Ref}}$). Fig. 3.7.b) shows the power attenuation in the test fiber as a function of the displacement (Δz) on a semi-logarithmic scale. The slope of the fit ($P_{\text{Fiber}}(\Delta z) \sim e^{-\alpha_{TF}\Delta z}$) gives an estimate of the attenuation coefficient, in this case 0.24 ± 0.05 cm^{-1}. A least squares linear fit was used on a semilog scale, taking into account the standard deviation of the ordinate values.

3.3.4 Interpretation of the measurement

Strictly speaking, the data interpretation method expressed by equation (3.4) is only valid for a frequency resolved measurement. In our case we used a bolometer as a detector, therefore we could only register the spectral average of the power attenuation. This consideration is modified by the fact that the coupler we used acted effectively as a low pass frequency filter. Indeed, theoretical simulations indicate that two subwavelength fibers of 380 μm diameter separated by a 380 μm air gap couple strongly only at frequencies smaller than ~ 0.35 THz, due to the otherwise strong confinement of the modal fields within the fiber core. We demonstrate this point by comparing numerically simulated distributions of the x-components of the coupler supermode electric fields at frequencies 0.36 THz and 0.5 THz. From Fig. 3.8.a) it is clear that at 0.36 THz the coupler x-polarized supermodes become strongly hybridized. Such modes extend well over the two fibers (especially supermode 1), thus indicating an onset of a broadband directional coupling regime. In contrast, at 0.5 THz (see Fig. 3.8.b)) the coupler supermodes resemble eigen modes of the individual fibers. From these considerations we conclude that the coupler acts as a low-pass filter, operating as a broadband coupler at low frequencies ($\simeq 0.35$ THz) and with negligible coupling at higher frequencies. Considering that the THz emission spectrum falls off rapidly below 0.25 THz, the evanescent coupling regime leads to a narrow band response for the coupler. Therefore, the directional coupler method

data can be considered as a measurement of the average fiber transmission losses in the immediate vicinity of 0.3 THz.

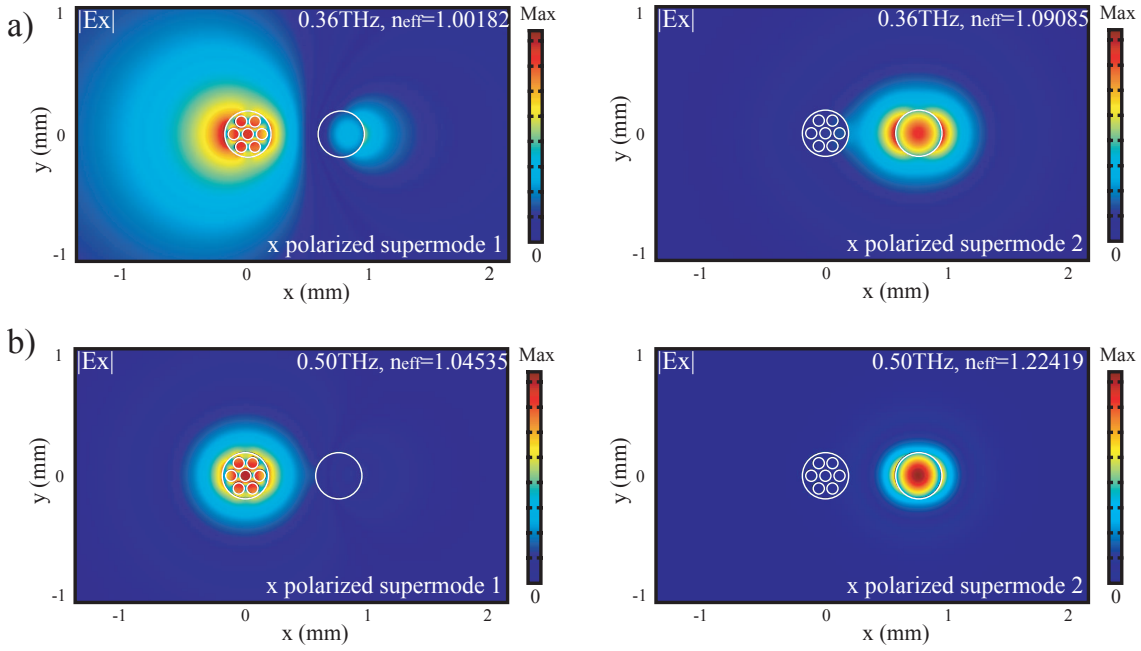

Figure 3.8 Numerical simulations of x-polarized supermodes of a subwavelength fiber directional coupler consisting of a 380 μm diameter porous fiber and a 380 μm diameter non-porous fiber separated by an air gap of 380 μm. The fiber interfaces are indicated in white. a) Strong coupling regime at 0.36 THz. b) Weak coupling regime at 0.50 THz.

3.3.5 Fibers

Using this characterization method we proceeded in measuring the attenuation loss of different series of fabricated fibers. Fig. 3.9 presents the cross-sections of the porous and non-porous fibers measured. The first column presents fibers made by the hole-sealing technique (labeled *PE Tubes*), with average diameters of 180, 240, and 325 μm respectively. The second column presents fibers made by the sacrificial-polymer technique (labeled *PE/PMMA*), with average diameters of 285, 310, 380 μm, respectively. The third column presents non-porous fibers (labeled *Non-Porous*), with average diameters of 220, 245, 410 μm, respectively.

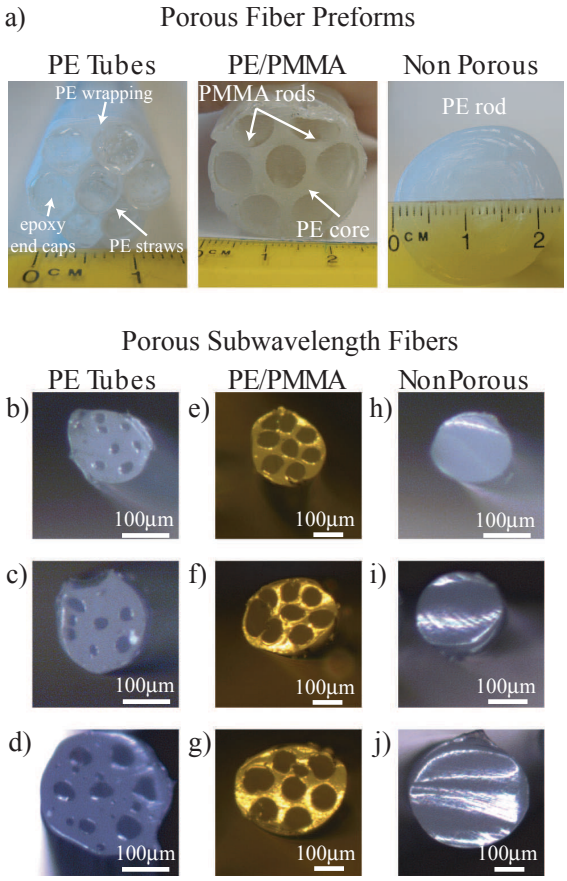

Figure 3.9 Pictures of preform and fiber cross-sections of the porous and non-porous subwavelength PE fibers measured with the directional coupler method. Top: Images of preform cross-sections. Bottom: Images of the fiber cross-sections. First column: Fibers made by the hole-sealing technique (labeled *PE Tubes*). Second column: Fibers made by the sacrificial-polymer technique (labeled *PE/PMMA*). Third column: Non-Porous fibers made by densification of PE granules into a rod (labeled *Non Porous*).

3.3.6 Fiber holders

During the course of the experiment we have discovered that it is critical for the evanescent fibers to be held straight in order to avoid strong bending losses. Design of fiber holders in the case of subwavelength fibers is challenging as such holders must insure low interference with the delocalized modal fields, while still holding the fiber strongly enough so that enough tension can be applied to keep the fibers straight. Some papers have proposed using small holes in a sheet of paper or a PE film to pinch an inserted fiber in place [58, 63]. However, it is difficult to find just the right hole

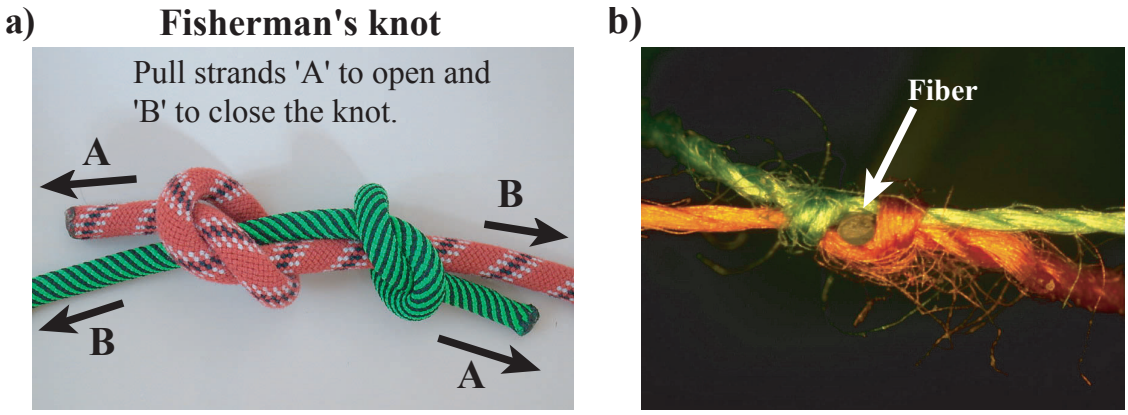

Figure 3.10 Pictures illustrating the Fisherman's knot used as fiber holder for the subwavelength fibers. a) Picture of knot adapted from Wikipedia [119]. b) Picture of fiber held tightly by the knot.

size to be able to insert the fiber into the hole, while also holding the fiber tightly. Moreover, fibers of different diameter require different holders.

After experimenting with different fiber holders we believe a better solution is to tie a knot on the fiber using thin sewing thread. A knot holds the fiber tightly, remains low loss because of the small diameter of the thread, and easily accommodates fibers of different diameter. Note, however, that asymmetrical knots can apply torsion and bend the fiber tip. We therefore used a symmetrical Fisherman's Knot and inserted the fiber between its two constituent simple knots (see Fig. 3.10). This technique was used for holding all the subwavelength fibers. Finally, two knots were used as separators between the test and coupler fibers to make sure that the distance between the fibers in the coupler remained constant even when the coupler fiber was displaced along the test fiber. The setup was aligned to ensure that during translations of the coupler the test fiber was always just-touching the knots on the coupler fiber (see Fig. 3.6.c)).

3.3.7 Loss measurement of porous and non-porous fibers

The power attenuation of porous and non-porous subwavelength THz fibers of different diameter were measured using the directional coupler method. Each test fiber was first aligned with the focal point of the PM2 parabolic mirror for input coupling and then brought parallel to the 7 cm straight segment of the coupler. After the at-

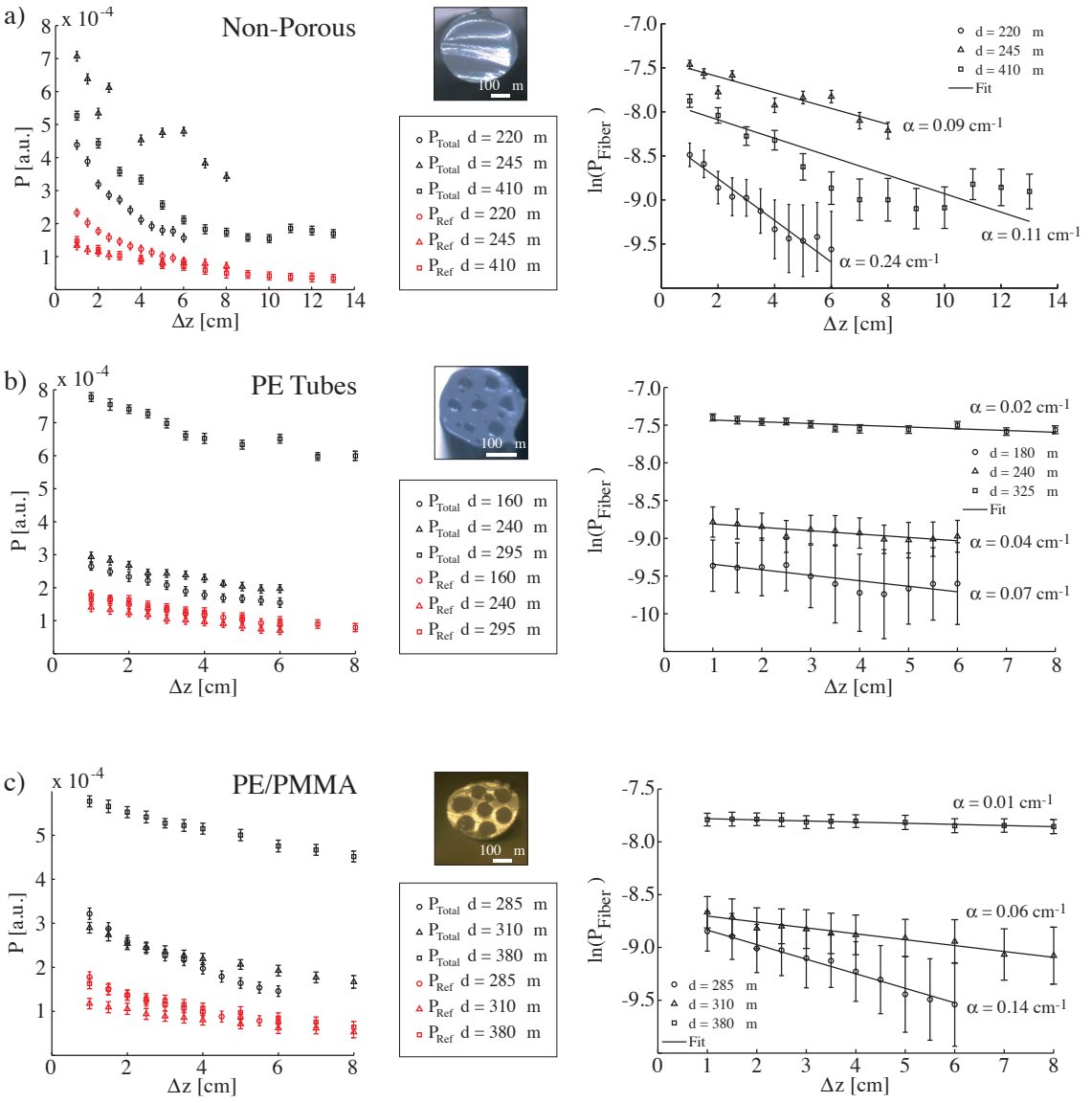

Figure 3.11 Directional coupler fiber loss measurements of various porous and non porous fibers of different diameters. Plots on the left show the Total and Reference signals measured with and without the test fiber, respectively. Plots on the right show fits of the fiber attenuation data ($P_{\text{Fiber}} = P_{\text{Total}} - P_{\text{Ref}}$). a) Non Porous PE fibers. b) Porous PE/Tube fibers produced by the hole-sealing technique. c) Porous PE/PMMA fibers produced by the sacrificial-polymer technique.

tenuation measurement was performed the test fiber was removed and the reference signal was acquired by displacing the coupler setup. Fig. 3.11 presents the measured

power attenuation as well as the data fits for each fiber type. Note slight variation in the intensity of the reference signal from one measurement to another. We attribute such variations to the minor displacements of the coupler fiber, as well as to small changes in the knot structure after they were mechanically brought in contact with the test fiber.

Fig. 3.12 compiles the results presented in Fig. 3.11 by showing the measured attenuation coefficient for fibers of different types as a function of the fiber diameter. Error bars correspond to maximum likelihood limits of the fitted slopes considering the errors bars on the points of Fig. 3.11 as standard deviations of normal distributions. Recall that the results are assumed to correspond to a frequency response in the vicinity of $f \sim 0.35$ THz. Also shown in Fig. 3.12 is a non-porous fiber of 563 μm diameter with an attenuation loss of $\alpha = 0.88 \pm 0.18$ cm^{-1}. For purposes of clarity, this larger diameter fiber was omitted from Fig. 3.11 because of the much steeper slope resulting from much larger attenuation. The measured non-porous fiber points are linked with solid lines to give some indication of the overall behavior of attenuation as a function of fiber diameter, despite the limited amount of points.

First of all, let us stress that the attenuation coefficients presented in Fig. 3.12 include both absorption and scattering losses. The non-porous fiber points in Fig. 3.12 illustrate that, for a constant frequency, there exists a minimum in subwavelength diameter fiber transmission loss as function of fiber diameter. Similarly, Chen *et al.* have demonstrated that, for a constant diameter, there exists a minimum in subwavelength diameter fiber transmission loss as a function of frequency [59]. Both absorption and scattering losses can be understood in terms of mode confinement within the fiber, and this confinement is a function of the normalized frequency V. Therefore there is a good correspondence between our results and those of Chen, because an increase of diameter at constant frequency or an increase of frequency at constant diameter equivalently increase the value of V (see equation (3.3)) and increase the mode confinement. Consider the increased mode confinement at constant frequency when the fiber diameter progressively increases. At large fiber diameters, transmission is dominated by absorption loss because of the higher mode confinement within the highly absorbent solid core. However, at small fiber diameters the transmission loss becomes dominated by scattering loss because the guided mode becomes delocalized (more loosely confined) and more prone to radiation losses on fiber defects. We therefore expect a transmission loss minimum at an optimum fiber diameter, due to

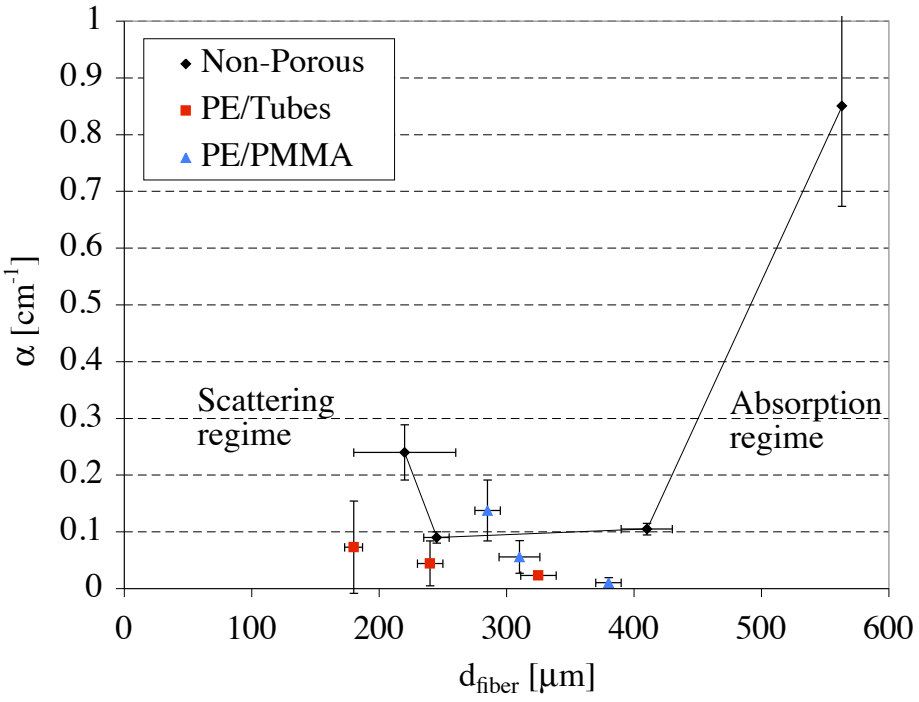

Figure 3.12 Attenuation coefficient as a function of fiber diameter for various porous and non-porous PE subwavelength THz fibers. The results are assumed to correspond to a frequency response in the vicinity of $f_{\text{avg}} \sim 0.35$ THz.

the increase in absorption loss at large fiber diameters and the increase of scattering loss at small fiber diameters. For the non-porous fibers in Fig. 3.12 we observe this transition from the radiation dominated regime to the absorption dominated regime for fiber diameters around $300 - 350$ μm.

Secondly, the increase in the fiber transmission loss as the fiber diameter decreases is an interesting albeit somewhat counterintuitive result. Although one expects the material absorption loss to decrease when reducing the fiber diameter, this is over-compensated by an increase in the fiber radiation losses. Such losses are due to modal scattering at various fiber defects: *i)* dust on the fiber surface, *ii)* material impurities within the fiber, *iii)* fiber diameter fluctuations, *iv)* fiber holders, and *v)* variations in the porosity microstructure. Scattering at these fiber defects becomes *more* pronounced as the fiber diameter gets smaller because the subwavelength fiber mode becomes less confined. It is difficult to quantify the relative contribution of each defect type to the total scattering loss. On one hand, the effects of dust and impu-

rities can be minimized with proper cleanliness. On the other hand, the large effect of fiber diameter fluctuations on the losses of non-porous subwavelength THz fibers has previously been documented by Chen *et al.* [59]. In their paper, they claim that diameter fluctuations are the *dominant* scattering mechanism. Diameter fluctuations are certainly present in our experimental fiber and in Fig. 3.12 it can be seen that the fiber diameter fluctuations are on the order of $\frac{\Delta d_{\mathrm{F}}}{d_{\mathrm{F}}} \sim 3-18\%$. It should be noted that the error bars on fiber diameter correspond to measured diameter extrema but do not testify to the frequency of diameter fluctuations along the length of the fiber. Obviously, a greater number of diameter oscillations translates into a greater number of scattering points and a higher scattering loss. Note that by better controlling the fabrication process of the fibers it should be possible to reduce diameter fluctuations and, thus, partially reduce the scattering loss. However, there will always remain a contribution to scattering loss from the fiber holders. This contribution is higher in polymer fibers (compared to glass fibers for instance) because the tight knots required for holding the fibers tend to squish the soft polymer fibers, thereby increasing the fiber deformation and the scattering.

Thirdly, from Fig. 3.12 we observe that all but one of the porous fibers exhibits smaller transmission losses than the non-porous fibers. We also find that losses of porous fibers increase as their diameter decreases. In our earlier work [111] we showed that fiber porosity leads to additional reduction in the subwavelength fiber absorption losses. As for the scattering losses, all the fibers were made with a similar fabrication process and presumably have comparable scattering losses due to similar fiber defects. The fibers notably have similar diameter fluctuations, as seen by the diameter error bars in Fig. 3.12, and diameter fluctuations are probably the dominant scattering mechanism [59]. Therefore, when comparing fibers of the same outer diameters, and under the assumption of comparable scattering from comparable diameter fluctuations, we expect both porous fiber types to demonstrate losses smaller than those of the non-porous fibers. This tendency is indeed confirmed in Fig. 3.12. However, from the absence of increased loss at larger diameters, we conclude that all our measurements for the porous fibers are done in the regime where radiation losses dominate. A larger sampling of fiber diameters would have given a more complete assessment of the porous fiber transmission loss behavior.

Finally, we define d_{H} to be the hole diameter and Λ to be the hole-to-hole pitch[3].

[3]The d_{H}/Λ ratios are useful for comparison to our previously published simulations [111]

From the fiber cross-sections we estimate $d_H/\Lambda \sim 0.32 - 0.48$ or porosity $\sim 8 - 18\%$ for the PE/Tube fibers, and $d_H/\Lambda \sim 0.61 - 0.76$ or porosity $\sim 29 - 45\%$ for the PE/PMMA fibers. The higher porosity leads us to expect lower absorption loss from the PE/PMMA fibers. However, because these porosities are still rather low we only expect an absorption loss reduction by a factor of $\sim 2-4$ compared to the non porous fibers [111]. Moreover, Fig. 3.12 indicates that the attenuation loss of the PE/PMMA fibers is generally higher than that of the PE/Tube fibers. We attribute this to a higher scattering loss due to a higher amount of fiber defects resulting from this new fiber fabrication technique and from the possibly higher fiber holder scattering upon squishing high porosity fibers. It should be possible to reduce the scattering loss by better controlling the fabrication process.

3.4 Loss measurements using THz-TDS

In this section, we present a more comprehensive comparison of the transmission properties of porous and non-porous subwavelength fibers by comparing the spectrally resolved loss measurements obtained by THz-TDS. We begin by presenting the bell-shaped transmission spectra and the cutback loss measurements. Although both porous and non-porous fibers of the same diameter show very low propagation losses below 0.02 cm^{-1}, the porous fiber attenuation loss is not lower than that of the non-porous fiber. Instead, we find that the porous fibers exhibit a much wider spectral transmission window and enable transmission at higher frequencies compared to the non-porous fibers. We then provide a theoretical justification for these results.

3.4.1 Cutback measurement with THz-TDS

The transmission spectra of porous and non-porous subwavelength fibers were measured using the THz-TDS setup described in chapter 2. The cutback method was used to evaluate modal propagation loss. There are two main differences with respect to the difficulties reported in section 3.3.1 that allow the cutback method to be used in this case. First, the entire output of the waveguide is collimated and properly re-focused onto the PC antenna detector. This eliminates the alignment problem previously encountered with the bolometer. Second, the time-resolved measurement automatically helps to eliminate stray light problems as stray light will have different

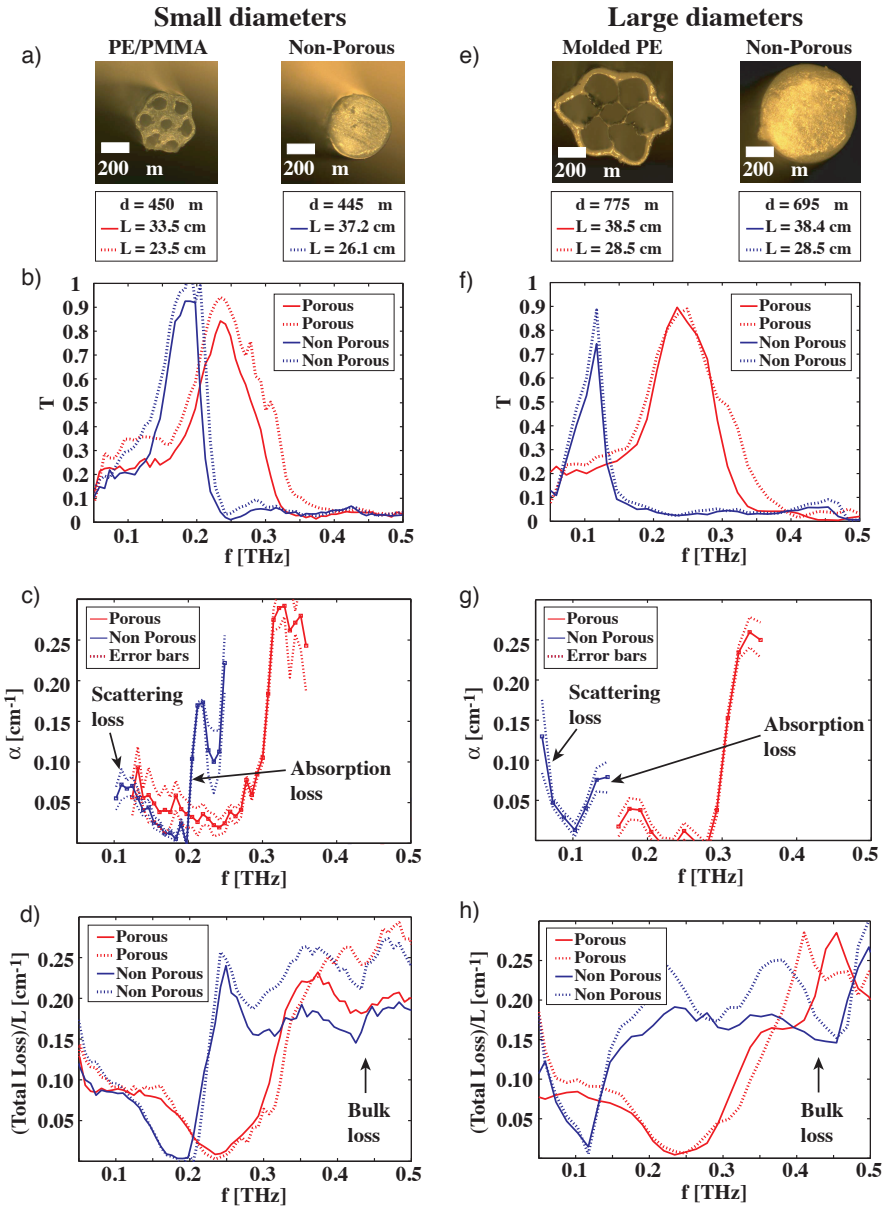

Figure 3.13 THz-TDS transmission and loss measurements of porous and non-porous subwavelength PE fibers. Left column: small diameter fibers, Right column: large diameter fibers. The data for the porous fibers is in red and data for the non-porous fibers is in blue. Fiber diameters and measured segments lengths are indicated in the legends. Photos a) and e) show measured fiber cross-sections; b) and f) Normalized amplitude transmission; c) and g) Power propagation loss calculated from the transmission spectra using cutback technique; d) and h) Upper bound on propagation loss given by total loss normalized (per unit of length).

optical paths and may arrive at the detector when it is not active. During measurements the fibers were held straight by knotted threads and the fiber ends were aligned with respect to pre-installed aligning apertures using 3-axis mounts. These apertures marked the locations of focal points of the input and output off-axis parabolic mirrors. Proper alignment with respect to these apertures insured consistent coupling into and out of the fibers.

Figs. 3.13.a) and 3.13.e) present cross-sections of the measured subwavelength fibers. A porous fiber made using the sacrificial-polymer technique (designated as *PE/PMMA* fiber in Fig. 3.13.a)) features 35% porosity, has an outer diameter of $d_F = 450$ μm, hole size $d_H = 100$ μm, and a hole diameter to the hole-to-hole pitch ratio d_H/Λ =0 .60. In turn, a porous fiber made with the preform-molding/fiber-inflation technique (designated as *molded PE* fiber in Fig. 3.13.e)) features an outer diameter $d_F = 775$ μm and 86% porosity (equivalent to the hole diameter to pitch ratio d_H/Λ =0 .93). To our knowledge, this is currently the highest reported porosity for a subwavelength fiber. Diameters of the corresponding non-porous fibers are 445 μm and 695 μm, respectively.

In Figs. 3.13.b) and 3.13.f) we present the measured amplitude transmission spectra of the porous and non-porous fiber segments, up to 38.5 cm in length. For each fiber diameter, two segments of different length are presented. The lengths of the corresponding fiber segments are indicated in the figure legends. In Figs. 3.13.c) and 3.13.g) we present the power propagation loss of the subwavelengths fibers, as calculated using equation (2.10) and the transmission spectra shown in Fig. 3.13.b) and 3.13.f). We would like to note that due to the short lengths of the studied fibers it was difficult to cut them while keeping the input end fixed. Therefore, during cutback measurements we had to remove the fibers segments, cut them, and then place them back and re-align them for every measurement, thus incurring small alignment errors [120]. The dotted curves in Figs. 3.13.c) and 3.13.g) indicate the error bars associated with our cutback loss measurements. These error bars on α originate from error bars on the transmission that were obtained by the measurement of multiple transmission spectra for each fiber length (not shown for clarity) to take into account fluctuations of the THz source. Tests were also done on the multiple re-alignment of a fiber segment and indicated good reproducibility.

Figs. 3.13.c) and 3.13.g) indicate that, at constant diameters, both porous and non-porous subwavelength diameter fibers have an attenuation loss minimum as a

function of frequency. Similarly to the previously studied case of an attenuation minimum as a function of fiber diameter, the loss minimum at an optimum frequency results from increased absorption loss at high frequencies and increased scattering losses at low frequencies. These results are in good agreement with the non-porous subwavelength diameter attenuation loss minima observed by Chen *et al.* [59]. From Figs. 3.13.c) and 3.13.g) we find that the propagation loss minima of the ~ 450 μm diameter fibers are $[\alpha_{\text{min}}]_{\text{non-porous}} = 0.024 \pm 0.004$ cm^{-1} at 0.190 THz for the non-porous fiber, and $[\alpha_{\text{min}}]_{\text{porous}} = 0.022 \pm 0.014$ cm^{-1} at 0.234 THz for the porous fiber; for the ~ 700 μm diameter fibers we find losses of $[\alpha_{\text{min}}]_{\text{non-porous}} = 0.040 \pm 0.008$ cm^{-1} at 0.117 THz for the non-porous fiber, and $[\alpha_{\text{min}}]_{\text{porous}} = 0.012 \pm 0.010$ cm^{-1} at 0.249 THz for the porous fiber. Hence, the minimum propagation losses of the porous and non-porous fibers are comparable within the error of the measurement. Note, however, that transmission minima of the porous fibers are located at higher frequencies than those of the non-porous fibers of the same diameter. Moreover, spectral bandwidths of the porous fibers ($\Delta f_{\text{FWHM}} \sim 0.1$ THz) are larger than those for the non-porous fibers ($\Delta f_{\text{FWHM}} \sim 0.05$ THz) of same diameter. Both of these observations are consistent with our prior theoretical work [111, 112] and will be discussed further in the next section.

Finally, in Figs.3.13.d) and 3.13.h) we take the transmission spectra of Figs. 3.13.b) and 3.13.f) and plot them in the form of *total loss* normalized with respect to the fiber segment length ($-2\ln(|T_1|)/L_1$). Here total loss includes coupling, scattering, and absorption losses. Such curves offer two interesting pieces of information. First, at high frequencies ($f \sim 0.5$ THz), where the light is highly confined within the core, we get an estimate for the bulk absorption loss of the fiber material ($\alpha_{\text{PE}} \sim 0.2$ cm^{-1}). Second, if we assume 100% coupling efficiency then the normalized total loss curve gives us an upper bound value for the propagation loss. The propagation loss cannot be higher than this upper bound, otherwise the total loss would have been higher. If the coupling efficiency is not 100%, then the coupling loss contributes to the total loss and the propagation loss (α) will actually be smaller than the total loss. Thus, if we consider the values at the normalized total loss minima, which correspond to the transmission maxima, then we deduce $\alpha \leq 0.02$ cm^{-1}. This is in good agreement with the more precise cutback measurements.

Note that although theory predicts lower losses for the porous fibers, we are unable to distinguish between the already very small losses of the porous and non-porous

fibers within the error of our experimental setup. As we demonstrate in the following sub-section, the transmission peak (bell-shaped transmission curve) results from the balance between absorption loss (at high frequencies), scattering loss (at low frequencies) [59], and frequency dependent coupling loss.

3.4.2 Interpretation of the results

In order to better understand the transmission spectra and propagation loss results presented in Fig. 3.13, we carried out vectorial simulations of the optical properties of the fundamental mode propagating in the subwavelength fibers. It should be noted that whereas the small diameter porous fiber (PE/PMMA fiber) retained a hexagonal arrangement of the holes, the large diameter porous fiber (molded PE fiber) had such a high porosity that it seems to be better approximated by a tube with a subwavelength-thick wall. To model the non porous fibers, an 86% porous fiber, and a 35% porous fiber, we therefore considered fundamental modes of a circular rod, a thin circular tube, and a 7 hole fiber, respectively. To model a non-porous rod fiber and a thin-wall-tube fiber we have used a transfer matrix code [121] to find the fundamental HE_{11} mode of both circularly-symmetric fibers. In the case of a 7 hole porous fiber we have used a vectorial finite element code to find fiber modes.

The simulation results for the absorption loss and coupling loss of these different fiber geometries were previously displayed in Fig. 3.2 and discussed in section 3.1. Except for Fig. 3.2.b), the diameters of the fibers in Fig. 3.2 correspond to the experimental diameters of the fibers measured in this section. Recall the general results that absorption loss reduces at lower frequencies, at smaller fiber diameters, and at higher porosities because the guided mode becomes more delocalized. We also saw that the coupling loss has a bell-shaped curve with an optimum when the mode size is matched to the input beam size. Consider the optimum coupling frequency of a non-porous fiber, where the mode size is matched to the input beam size. If a porous fiber of same diameter and same frequency has a more delocalized mode, then the porous fiber mode size must be decreased to match the input beam size. This optimum occurs at a higher frequency because the mode size of subwavelength fibers decreases with increasing frequency. Therefore the optimum coupling frequency of porous fibers is higher than that of non-porous fibers.

The experimentally measured transmission spectra through subwavelength fibers

all feature approximately bell-shaped profiles with frequencies of the transmission maxima defined by the competition between several loss mechanisms such as coupling, material absorption, and scattering on fiber imperfections [59, 61]. More specifically, at higher frequencies both the absorption loss and coupling loss increase substantially leading to a decrease in the fiber transmission; compare for example Figs. 3.2.b) and 3.2.c) to the non-porous fiber results in Figs. 3.13.b) and 3.13.f). At lower frequencies, it is the increased coupling loss and scattering loss that lead to a decrease in the fiber transmission. Note that scattering loss *increases* at lower frequencies because the mode is less confined.

In this thesis, no efforts were made to quantify the scattering losses because of the difficulty in modeling fiber defects and calculating the magnitude of the scattering loss. In their paper, Chen *et al.* [59] attempted to model fiber diameter fluctuations by using the simplified taper radiation loss model developed by Sumetsky [122, 123]. The calculation only gave an approximate result, because the model is limited by simplifying assumptions such as a smooth, symmetric and adiabatic (slowly varying with distance) tapering of fiber diameter. Such a model is clearly inadequate because the diameter variations in our fibers would more accurately be described by non-adiabatic swells in fiber diameter that can occur many times along the length of a fiber segment. Nevertheless, the result of Chen's study was that scattering losses increase sharply with decreasing frequency and that even diameter fluctuations smaller than 1% ($\frac{\Delta d_F}{d_F} < 1\%$) lead to scattering losses that surpass absorption losses at small enough frequencies [59]. More accurate modeling is difficult, but it is reasonable to conclude that scattering severely limits the transmission of subwavelength diameter fibers at low frequencies despite the reduced absorption loss.

To summarize, at the frequency of strongest transmission, the fiber mode size is at an equilibrium where the mode extends sufficiently into the porous regions and into the gaseous cladding to lower absorption loss, while still remaining sufficiently confined to the fiber core to avoid too much scattering losses on the fiber defects. As the onset of strong absorption and coupling losses for porous fibers happens at higher frequencies than those for the non-porous fibers of the same diameter (compare Figs. 3.2.e) and 3.2.f) to 3.2.b) and 3.2.c)), it is not surprising that experimentally measured transmission curves for the porous fibers are shifted to the higher frequencies with respect to those of the non-porous fibers (see Figs. 3.13.b) and 3.13.f)).

Finally, in Fig. 3.14 we present fits of the experimentally measured transmission

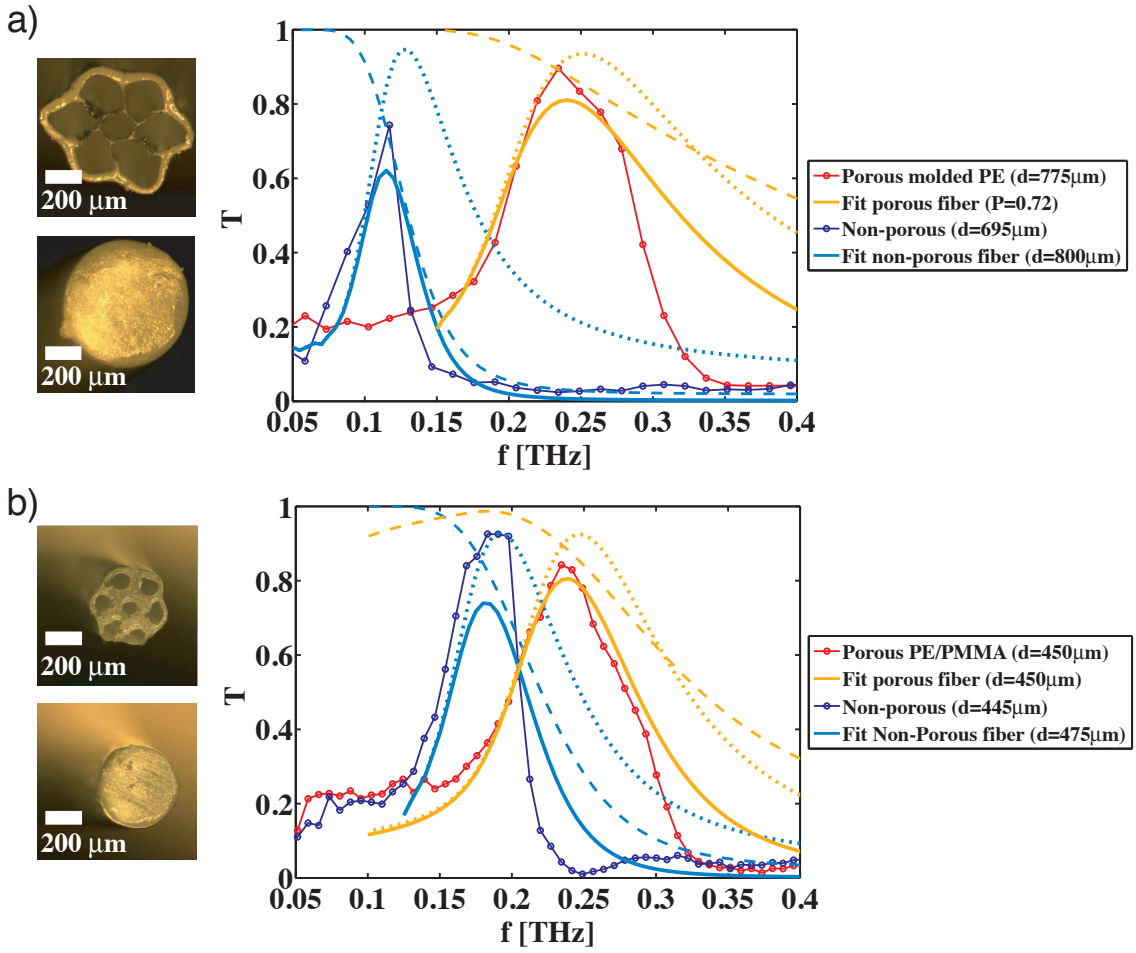

Figure 3.14 Theoretical fit of transmission spectra through large and small diameter subwavelength fibers. The theoretical fits (solid lines) take into account coupling loss (dotted lines) and absorption loss (dashed lines) contributions but neglect scattering losses. The calculations assumed $\alpha_{mat} = 0.2$ cm^{-1}, a porosity of 35% for the small diameter fiber, and a porosity of 72% for the large diameter fiber. Optimal fits for the non-porous fibers were found for diameters slightly different from the experimentally measured diameters.

curves using theoretically calculated absorption and coupling losses. The theoretical fits for the fiber transmission (solid lines) are calculated using equation (2.8) by taking into account coupling loss (dotted lines) and absorption loss (dashed lines) contributions (see Fig. 3.2). The input and output coupling coupling conditions are assumed to be identical such that $C_{\text{in}}C_{\text{out}} = |C(\omega)|^2$. Even without taking scattering loss into account we find a good correspondence between the theoretical and experi-

mental curves. Scattering losses (not considered in this work), would further narrow the transmission peaks on the low frequency side. Although the porosity of the large diameter fiber was estimated to be 86% from the photo of the fiber cross-section, we find that a porosity of 72% yielded the best fit when approximating this fiber as a thin-wall tube. The only fitting parameter for the non-porous fibers was the fiber diameter, which is reasonable considering the diameter fluctuations in the experimental fibers. The coupling coefficients were not measured experimentally and although the use of experimental values for $\alpha(\omega)$ and $|C(\omega)|^2$ in equation (2.8) could have been a self-consistency test of the cutback measurement, the decent fits obtained with certain reasonable theoretical assumptions is seen as a further validation of the theoretical simulations of the absorption and coupling losses.

In Fig. 3.14, the greater widths of the porous fiber transmission spectra are attributed in part to the slower frequency dependence of the absorption loss curves and in part to the broader coupling loss curves. The latter being due to the slower variation of the modal size as a function of frequency for the fibers with lower refractive index contrast such as porous fibers. Finally, we would like to note that although the absorption loss of a porous fiber is predicted to be much lower than that of a non-porous fiber of the same diameter, we find experimentally that the lowest measured losses of the porous and non-porous fibers are quite similar and on the order of 0.01 cm^{-1} – 0.02 cm^{-1}. We attribute this finding to the limit on the lowest obtainable loss at low frequencies, which is set by the scattering loss on various fiber imperfections such as dust on a fiber surface, bulk material impurities, fiber holders, fiber diameter fluctuations, fluctuations in the porosity microstructure, micro- and macro-bending, etc.

3.4.3 Waveguide dispersion

Let us now consider waveguide dispersion. It is well known that dispersion in solid-core THz waveguides is high ($\beta_2 \geq 1$ ps/[THz · cm] at certain frequencies) [69, 57, 124]. Waveguide dispersion can be characterized by the dispersion parameter $\beta_2 = (1/2\pi c)(f \cdot \partial^2 n_{\text{eff}}/\partial f^2 + 2 \cdot \partial n_{\text{eff}}/\partial f)$, where n_{eff} is the real-valued effective propagation index of a given mode. An order of magnitude limit for the dispersion parameter can be defined in the following manner. Dispersion can be understood in terms of the increase (or decrease) of pulse duration as a function of propaga-

tion length. From the dispersion relation for gaussian pulse [125], and assuming $\Delta t_f \gg \Delta t_0$, we have

$$\beta_2 \approx \frac{\Delta t_0 \cdot \Delta t_f}{\Delta L}, \tag{3.5}$$

where Δt_0 is the initial pulse duration, Δt_f is the final pulse duration, and ΔL is the propagation distance. From the reference time-scan of the THz source (Fig. 2.12.c)), we have full-width-half-maximum (FWHM) duration of $\Delta t_0 \sim 1.0$ ps. To be convenient to measure with the delay line we require that duration of a guided THz pulse be $\Delta t_f \leq 100$ ps. Furthermore, we consider that the measured waveguides are never longer than 100 cm, so $\Delta L \leq 100$ cm. Therefore, an order of magnitude for high waveguide dispersion can be defined as

$$\begin{aligned}(\beta_2)_{\text{limit}} &= \frac{\Delta t_0 \cdot \Delta t_f}{\Delta L} = \frac{1.0 \text{ ps} \cdot 100 \text{ ps}}{100 \text{ cm}}, \\ (\beta_2)_{\text{limit}} &= 1.0 \frac{\text{ps} \cdot \text{ps}}{\text{cm}} = 1.0 \frac{\text{ps}}{\text{THz} \cdot \text{cm}}.\end{aligned} \tag{3.6}$$

Fig. 3.15 presents some theoretical calculations of the dispersion parameter for non-porous and porous subwavelength diameter fibers. Figs. 3.15.a) and 3.15.b) respectively present effective indices of non-porous and porous fibers of different diameters. These index curves were obtained from the same simulations as the ones shown in Figs. 3.2.b) and 3.2.e). These curves are then used to calculate the dispersion β_2. Figs. 3.15.c) and 3.15.d) indicate that dispersion in subwavelength diameter fibers is high and that a reduction of the fiber diameter or an increase of the porosity decreases the fiber dispersion (in addition to the absorption) because a higher fraction of power is guided in the air. As a result of an increased fraction of power guided in air, the $n_{\text{eff}}(f)$ curve is closer to $n_{\text{air}} = 1.0$ and varies more slowly as a function of frequency.

Furthermore, a porous fiber will have lower dispersion than a non-porous fiber of the same diameter. This is corroborated by the experimental time scans shown in Fig. 3.15.e), where the transmitted THz pulses of 450 μm porous and non-porous fibers are compared to the reference scan of the source. The respective time-scans are offset vertically for clarity and normalized such that $|E(t)|_{\text{peak}} = 1.0$. The pulse duration of the reference is on the order of 1 ps. Judging from the frequency spectra of the subwavelength fibers (Fig. 3.14.b)), if we assume that the transmission is approximately gaussian with $\Delta f_{\text{FWHM}} \sim 0.1$ THz, then the Fourier-transform-limited

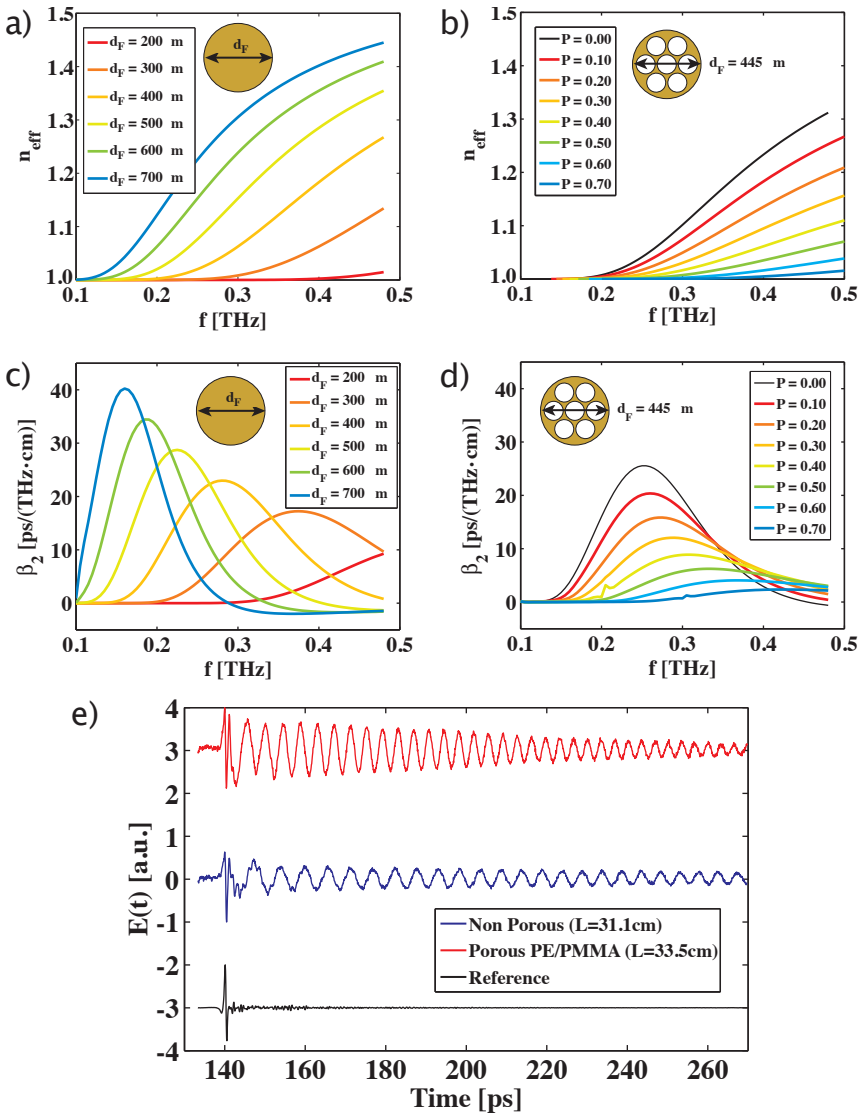

Figure 3.15 Theoretical calculations of the β_2 dispersion parameter of non-porous and porous subwavelength fibers. a), b) Effective index curves of the non-porous and porous fibers, respectively. c), d) β_2 of non-porous and porous subwavelength fibers, respectively. Decrease of the fiber diameter and increase of the porosity result in the reduction of dispersion. e) Time scans of $\sim$ 450 μm diameter porous (red curve) and non-porous (blue curve) fibers are compared to a reference pulse of the source (black curve). Dispersion is smaller in the porous fiber because the envelope is decaying faster and, therefore, the duration of the guided pulse will be shorter for a comparable length of fiber. The time-scans are offset vertically and normalized to a peak height of 1.0 for clarity.

pulse duration would be $\Delta t_{FWHM} \sim 5$ ps ($\Delta t_{FWHM} \cdot \Delta f_{FWHM} = 0.44$ for a gaussian pulse [125]). From Fig. 3.15.e) it is clear that the pulse duration of the subwavelength diameter fibers is much larger than this approximate Fourier-transform-limited pulse duration due to the presence of strong dispersion. Although the experimental values of β_2 were not calculated, it is also clear from Fig. 3.15.e) that the porous fiber has lower dispersion since the envelope of the THz pulse is decaying more rapidly than that of the non-porous fiber.

3.5 Discussion and future prospects of subwavelength fibers

This final section concludes with a general discussion on fabrication difficulties, the effect of fiber imperfections, comparisons with the literature, bending loss measurements, and the prospect of glass fibers.

In this chapter we have demonstrated low-loss THz transmission using a variety of single-mode subwavelength polyethylene fibers. Our initial goal was to demonstrate lower absorption loss in porous fibers and we devised two completely different setups to measure transmission losses. It should be noted that measuring the loss is a difficult task and that another group working on porous subwavelength fibers failed to properly measure the transmission losses [120]. Our spectrally resolved loss measurements indicated that both porous and non-porous fibers have a low minimum propagation loss on the order of 0.02 cm^{-1}. While this propagation loss is sufficiently low to enable interesting applications, the porosity was expected to give a greater advantage. The apparent discrepancy stems from the fact that experimentally we measure *propagation* loss, which has contributions from both absorption loss and scattering loss. While the porous fibers most likely *do* have lower absorption loss this is achieved at the expense of lower modal confinement. Thus the mode is more susceptible to scattering losses. The net effect appears to be that the porous fibers retain a propagation minimum at a level comparable to that of non-porous fibers, but that the propagation minimum is shifted to higher frequencies. The higher frequencies that we have observed are so far limited to 0.3 THz because of the relatively large fiber diameters (> 400 μm) that were measured using the THz-TDS setup.

A more important difference between the porous and non-porous fibers manifests

itself in the transmission spectra. Compared to non-porous fibers of same diameter, the transmission peaks of porous fibers were shown to be wider and to occur at higher frequencies. Our results are consistent with those of Chen *et al.* who demonstrated that non-porous fibers of smaller diameters have a minimum propagation loss at higher frequencies [59]. Thus the mode delocalization induces a blue-shift in the fiber propagation losses. This has a technological relevance because the useful range of subwavelength fiber transmission is currently limited to frequencies lower than ~ 0.4 THz and the imaging systems developed by Lu *et al.* have been limited to the 0.3-0.4 THz range [63, 64]. The important point is that fiber porosity is an additional design parameter that can be used in place of, or in combination with, the reduction of fiber diameter to shift the propagation loss minimum to even higher frequencies. We therefore believe that highly porous fibers will help enable single-mode transmission at higher frequencies.

Another important property is bending loss and this too is difficult to measure experimentally. Qualitatively, we find that the porous subwavelength fibers are sensitive to bending loss in a similar manner as their non-porous counterparts. Whereas theoretical simulations have shown that porosity can be exploited to reduce the bending loss [112], experimentally it is exceedingly difficult to quantify the bending loss of subwavelength fibers because of their evanescent fields. A study of bending loss as a function of bending radius would require wrapping a long, uniform length of fiber around mandrels of constant radius. However, the contact between the subwavelength fiber and the mandrel leads to prohibitively high absorption loss because of interference with the evanescent field. Bending loss measurements have been realized with metallic subwavelength fibers [40, 50], but this was facilitated by the fact that, contrary to the soft plastic fibers, the metal wires are relatively self-supporting. At this time, long and highly uniform segments of porous and non-porous fibers are unavailable and we did not explore bending loss beyond realizing that the fibers need to be held straight. Nevertheless, it has been shown that the straight fibers can be deflected to change the direction of the waveguide. Lu *et al.* have carried out a systematic study of loss as function of deflection angle for non porous subwavelength fibers [64]. It is important to note that, from a practical point of view, deflection loss is more important than bending loss as imaging systems relying on fiber deflection have successfully been implemented [64, 16].

Perhaps a more appropriate use of subwavelength fibers is sensing instead of imag-

ing. You et al. have demonstrated sensitive discrimination of refractive index changes when a sample is brought into contact with the evanescent field of a subwavelength fiber [124]. Placing an analyte in proximity of the evanescent field of a subwavelength fiber is easier than pumping an analyte within a hollow-core waveguide. This simplifies the sensing setup and the fiber can potentially increase the light-matter interaction length. Regardless of the application it is useful to increase the transmission bandwidth of subwavelength fibers. Material absorption was shown to act like a low-pass frequency filter. Although it is difficult to push the onset of absorption to higher frequencies (by reducing fiber diameter or increasing fiber porosity), it should be possible to increase the transmission at lower frequencies by reducing the scattering and coupling losses.

With regards to scattering, the scattering losses occur on fiber defects such as dust on a fiber surface, fiber material impurities, fiber diameter fluctuations, and fluctuations in the porosity microstructure. We developed three different techniques for fabricating porous fibers but they were all susceptible to fabrication defects. To summarize, the initial hole-sealing technique was supplanted by the molding/inflation technique because direct pressurization of the air holes was seen to be more effective at preventing hole collapse. Not only did the molding eliminate the interstitial holes in the preform, but the inflation of the holes under active pressurization has yielded the highest fiber porosity to date (86%). However, pressurization remains a very delicate procedure that is more prone to error than success. In contrast, the sacrificial-polymer is by far the simplest fabrication technique. The preforms are easier to prepare and the all-solid preforms are considerably easier to draw. Hole collapse problems are completely eliminated and this facilitates the optimization of drawing parameters. Despite the relatively low porosities of the fibers that we fabricated, the porosity can easily be increased by incorporating more sacrificial polymer. The main disadvantage however is that polymer dissolution limits the length of a fiber segment to a few meters. However, given the current propagation losses in the THz regime the useful length of a fiber is limited to about one meter anyway.

Although efforts can be made to remove dust and impurities, all the fabrication methods suffered from fiber diameter fluctuations. Contrary to the drawing of glass, the non linear viscosities and non-Newtonian fluid mechanics of polymers make the stabilization of polymer fiber drawing difficult [126]. An alternative polymer processing technique is extrusion, where cold water baths are typically used to quench the

temperature of the extruded fiber before the tractor assembly. Perhaps temperature quenching of the drawn fiber would help alleviate the diameter fluctuation problems encountered with our draw tower.

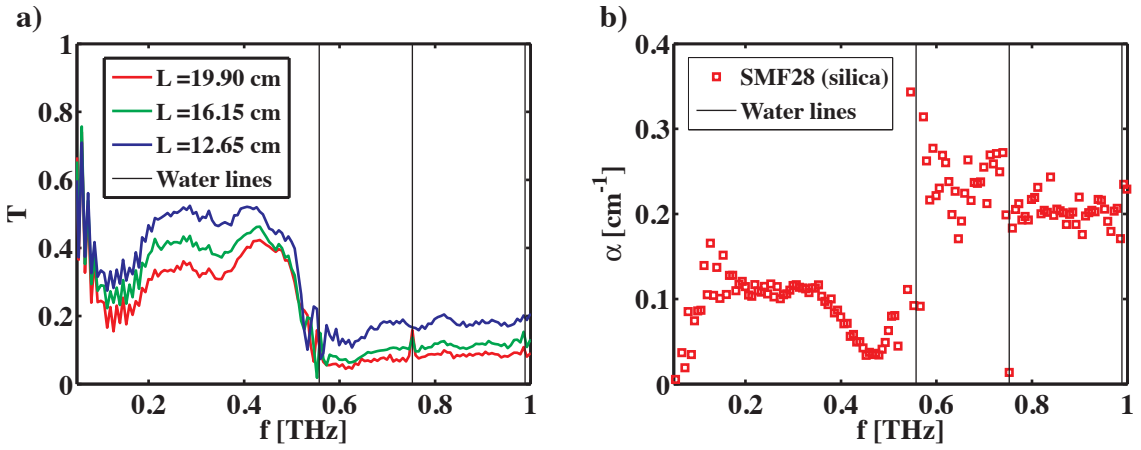

Figure 3.16 THz transmission spectrum and propagation loss measurement of an SMF28^{TM} subwavelength silica fiber (d_F = 125 μm). a) Amplitude transmission spectra of segments of different length. b) Power propagation loss, α, calculated from the spectra in a) (cutback method). Note some errors in the calculation of α in the vicinity of water vapor absorption lines due to normalization errors.

Another interesting prospect is the use of glass fibers which have negligible diameter fluctuations. To test if glass fibers effectively reduce scattering losses the propagation losses of a standard SMF28 fused silica fiber were measured. Fig. 3.16 presents a THz-TDS cutback measurement of the 125 μm diameter silica fiber with its protective plastic jacket removed. We note a broadband transmission spectrum and the onset of strong absorption at frequencies above 0.5 THz. Note that the propagation loss minimum occurs at a higher frequency than that of the polymer fibers studied in this chapter because of the much smaller fiber diameter. Despite the relatively large material losses reported for fused silica [127], the propagation loss minimum is ~ 0.04 cm^{-1} at 0.47 THz and could be made even lower with the addition of porosity. It would thus be interesting to examine holey silica fibers. Curiously, the propagation loss, and presumably the scattering loss, is seen to plateau at low frequencies. However, it is possible that slight coupling variations, due to re-alignement variations after cleaving the fiber, introduce errors in the calculated propagation loss.

Finally, with regards to coupling, the coupling loss curves were shown to have

a bell shape. While the maximum coupling efficiency is very high ($> 90\%$), the bell-shaped coupling loss forces the transmission to drop off rapidly. An assembly of polymer lenses could be used to create a frequency dependent focal-point beam size. With proper design the lens assembly could compensate the frequency dependent change in mode size, thereby increasing the coupling efficiency and flattening the bell-shaped coupling loss curve. As a result the transmission at low frequencies and the fiber transmission bandwidth could be greatly increased.

Chapter 4

Multi-mode hollow-core waveguides

In this chapter we explore the second loss reduction strategy, i.e. large hollow-core tube waveguides where light is confined in the air core. In response to the recent proposal of using simple single-walled plastic tubes as Anti-Resonant Reflection (ARR) tubes to guide THz radiation [73], we study the transmission of thick- and thin-walled polymer tubes and discuss their limitations. We then explore the potential of THz Bragg fibers for broadening the transmission windows and lowering the bending losses. Because of the relatively small differences among the THz refractive indices of common polymers [53], we report on the design and fabrication of Bragg fibers using two different schemes for achieving high index contrast Bragg layers. The first method is based on the index contrast between a polymer and air, whereas the second is based on the index contrast between a pure polymer and polymer composite doped with high-index inclusions (such as TiO_2 particles within a polyethylene host).

The first two sections present experimental results on ARR tubes and Bragg fibers, respectively. Each of these sections contains subsections describing the waveguiding principle, the fabrication methods, the experimental transmission and loss measurements, as well as modeling of the waveguide losses and theoretical explanation of the observed transmission spectra. The final section concludes with general remarks concerning the similarities and differences of the current dielectric tube waveguides. All of these waveguides have demonstrated spectral regions of fairly low propagation loss ($\alpha < 0.05$ cm^{-1}) when held straight. These losses can be decreased further by increasing the size of the core. However, we discuss fabrication difficulties, fiber imperfections, and how bending losses will ultimately be the discriminant between these various waveguiding techniques.

4.1 Anti-Resonant Reflection tubes

Recently, the group of Sun *et al.* proposed a simple waveguide where guidance in a large-core polymer tube is achieved via a Fabry-Perot anti-resonance in a low refractive index tube wall [73]. Such waveguides are similar to the planar integrated optics Anti-Resonant Reflection Optical Waveguides (ARROW) developed for the near infra-red [128]. One drawback to this anti-resonant reflecting (ARR) waveguide is that thick walls ($t_{\text{wall}} \sim 1$ mm) lead to very narrow-band THz transmission peaks. In order to increase the width of the transmission peaks the use of thin-walled tubes ($t_{\text{wall}} \sim 300$ μm) is investigated. In this section, the THz transmission spectra and loss estimates for thin and thick-walled hollow-core dielectric tubes are compared. The limitations of this simple geometry are discussed and in the following section wider transmission peaks are demonstrated using Bragg fibers.

4.1.1 Waveguiding principle

The guidance principle of the tube can easily be understood in terms of the reflectivity of a Fabry-Perot resonator. If the wavelength is much smaller than the diameter of the core (inner diameter of the tube), then the wave can be described from a ray-optic perspective. As illustrated in Fig. 4.1.b), an incoming ray will have multiple reflections off the two dielectric interfaces of the tube wall. The amount of light reflected by the wall, leading to confinement in the hollow core, will be given by the reflectivity of a Fabry-Perot resonator R_{FP} [129],

$$
\begin{aligned}
R_{\text{FP}} &= 1 - \frac{(1-R)^2}{1+R^2-2R\cos(\delta)}, \\
R_{\text{FP}} &= \frac{2R(1-\cos(\delta))}{1+R^2-2R\cos(\delta)}, \qquad (4.1) \\
R = R_{\text{TE}} &= \left(\frac{n_{\text{wall}}\cos\theta_2 - n_{\text{air}}\cos\theta_1}{n_{\text{wall}}\cos\theta_2 + n_{\text{air}}\cos\theta_1}\right)^2, \qquad (4.2) \\
\delta &= \left(\frac{2\pi f}{c}\right) 2n_{\text{wall}} \cdot t_{\text{wall}} \cdot \cos\theta_2, \qquad (4.3)
\end{aligned}
$$

where n_{wall} and n_{air} are the refractive indices of the tube wall and air core, f is the frequency, c the speed of light, t_{wall} is the thickness of the wall, and θ_2 is the refraction angle within the wall material ($n_{\text{air}}\sin\theta_1 = n_{\text{wall}}\sin\theta_2$). R_{TE} is the reflectivity of the

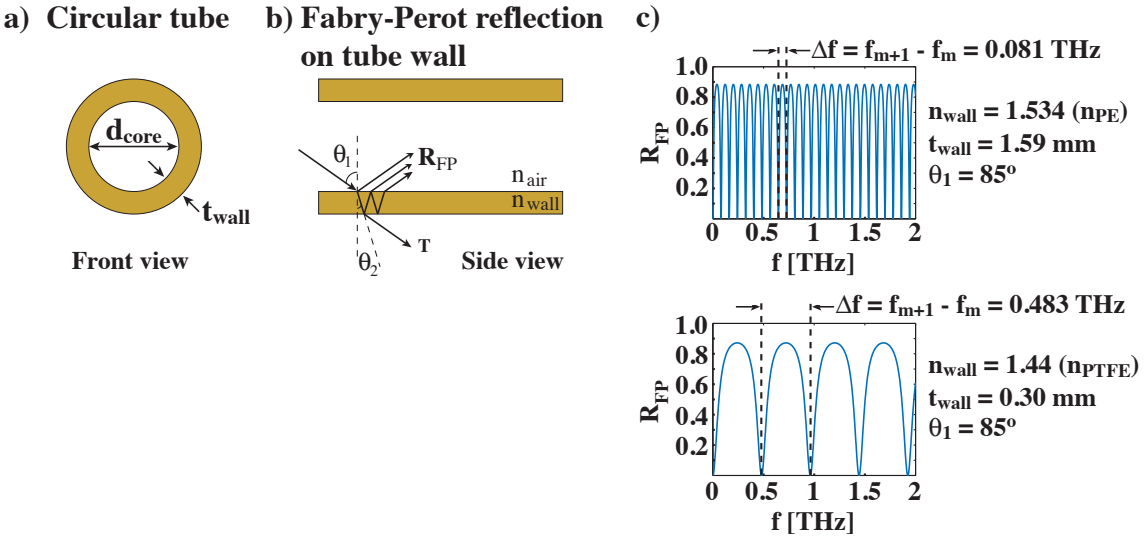

Figure 4.1 Schematization of the geometry and waveguiding principle of an ARR tube. a) Schematization of the geometry. b) Illustration of the wave confinement from a ray-optic point of view. c) Reflectivity of the tube wall for different wall thicknesses. Period of reflectivity is inversely proportional to wall thickness. Here incidence angle (θ_1) is kept constant although it is frequency dependent in a real waveguide (see appendix F).

TE polarization at the air-material interfaces; a similar expression exists for the TM polarization. R_{FP} is a periodic function of δ. With the aid of Snell's law we can express $\cos\theta_2$ in terms of the incidence angle θ_1 and assuming grazing angles of incidence ($\theta_1 \to \pi/2$) we get $\cos\theta_2 = \frac{n_{\mathrm{air}}}{n_{\mathrm{wall}}}\sqrt{(\frac{n_{\mathrm{wall}}}{n_{\mathrm{air}}})^2 - 1}$. We can then express the period in terms of frequency f_m using $\delta = m \cdot 2\pi$,

$$f_m = \frac{m \cdot c}{2n_{\mathrm{air}} \cdot t_{\mathrm{wall}} \cdot \sqrt{(\frac{n_{\mathrm{wall}}}{n_{\mathrm{air}}})^2 - 1}} \tag{4.4}$$

Thus, the reflectivity is periodic in frequency, as illustrated in Fig. 4.1.c), and the period ($\Delta f = f_{m+1} - f_m$) is inversely proportional to the thickness of the tube wall. At the peaks of the wall reflectivity we expect peaks in the tube transmission, and to obtain wider ARR transmission peaks a thinner tube wall is required.

As will be seen in section 4.1.5 and appendix F, the incidence angle dependent reflectivity ($R_{\mathrm{FP}}(\theta_1)$) can be used to calculate a very accurate estimate of the attenu-

ation losses of individual modes guided by the tube. However, this simple model does not take into account interference between the multiple modes that can be excited in this multimode waveguide. Therefore, a more elaborate model of the waveguide transmission will be discussed in section 4.1.4.

4.1.2 Fabrication technique

For the dielectric tubes we used commercially available polymer tubing. We compare a thick-walled polyethylene (PE) tube (McMaster-CARR, ID=Inner Diameter=6.35mm, WT=Wall Thickness=1.59mm) to a thin-walled polytetrafluoroethylene (PTFE) tube (Small Parts, ID=7.66mm, WT=300μm).

4.1.3 THz-TDS transmission and loss measurement

The waveguide transmission spectra were measured using the THz-TDS setup described in chapter 2. The samples were held in place with the aid of irises and the endpoints were positioned in the focal planes of parabolic mirrors. All samples were measured in a dry nitrogen environment although some residual water vapor ($< 15\%$) was present. Fig. 4.2 presents a comparison of the THz transmission characteristics of thick-walled (left column) and thin-walled (right column) dielectric tubes. The first row presents cross-sections of the measured tubes. The lengths of the thick and thin walled tubes were 16 cm and 19.4 cm, respectively. The second row presents the measured time-scans of the guided THz pulses. The reference pulse of the source is shown with a vertical offset for clarity. It is clear from the time-scans that the waveguide dispersion is low, as expected from the large fraction of power guided in the hollow air core. The third row presents the normalized amplitude transmission spectra ($|T| = |E_{\text{waveguide}}(f)|/|E_{\text{reference}}(f)|$). Note that in the case of the thin walled tube the shaded gray regions indicate a normalization error in the spectrum. This results from power fluctuations of the source in the vicinity of strong residual water vapor absorption peaks [101] (at 1.67 THz and 1.71 THz). These shaded regions are considered invalid.

In the case of the thick-walled PE tube (Fig. 4.2.e)), the transmission spectrum has a short-period frequency oscillation ($\Delta f = 0.08$ THz) but the height of the transmission peaks are modulated by a longer-period oscillation. Substituting $n_{\text{PE}} = 1.56$ and $t_{\text{wall}} = 1.59$ mm into equation (4.4) we obtain $\Delta f = 0.079$ THz, which is in good

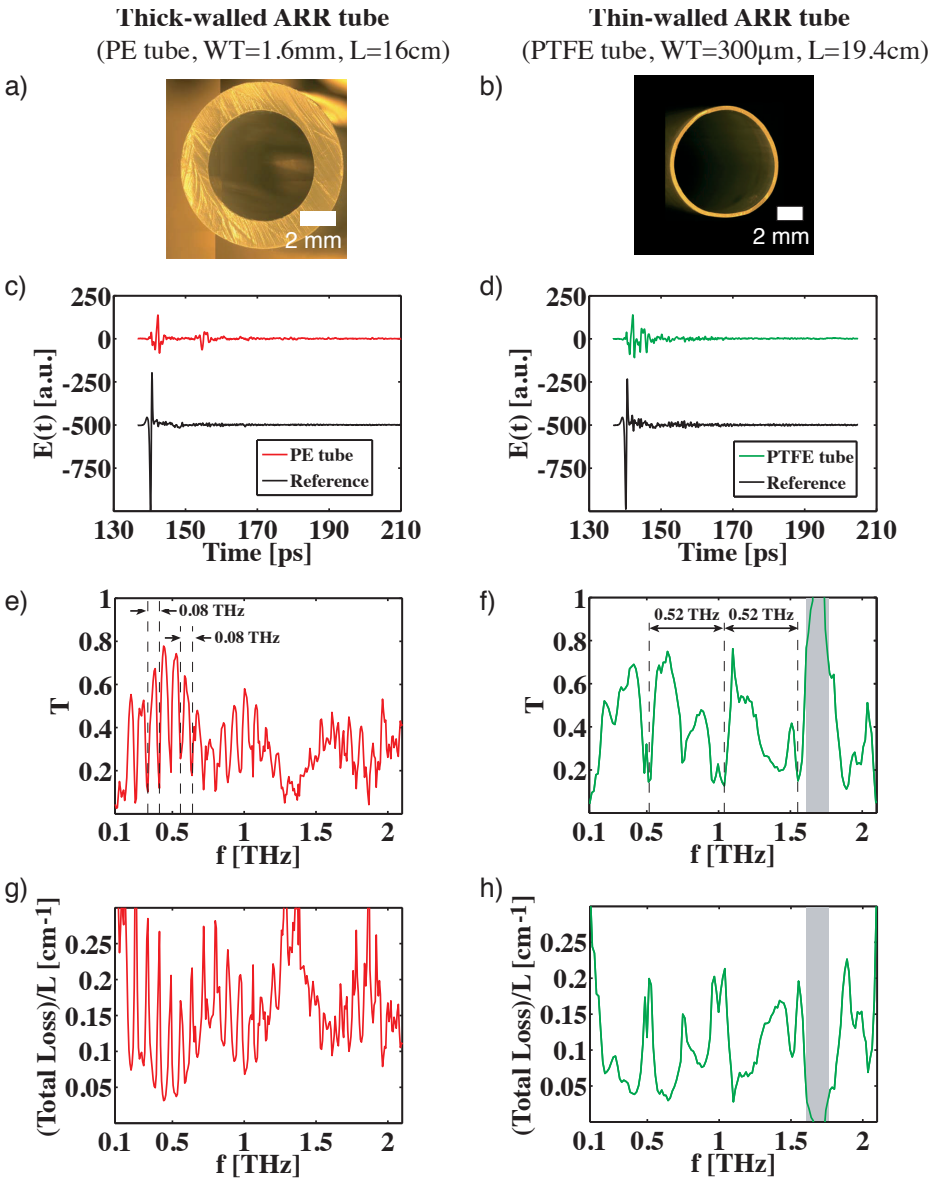

Figure 4.2 Comparison of the THz-TDS transmission characteristics of thick and thin walled dielectric ARR tubes. Left column: Thick walled PE tube, right column: Thin walled PTFE tube. a), b) Tube cross-sections. c), d) Time-domain signals of transmitted THz pulses. e), f) Normalized amplitude transmission spectra. g), h) Upper bound on propagation loss given by total loss (which includes coupling loss) normalized with respect to tube length. Note that the shaded gray regions indicate spectral normalization errors in the vicinity of residual water vapor absorption peaks (1.67 and 1.71 THz).

correspondence with the measured period. Another interesting point is that the time-domain signal (Fig. 4.2.c)) clearly exhibits two pulses. This fact is examined more closely in Fig. 4.3 because it is used to confirm the anti-resonant reflection mechanism.

Fig. 4.3.a) illustrates how the polymer tube wall is acting as a Fabry-Perot reflector. Reflections occur at the polymer/air interfaces. Here we let *Ray A* designate the initial reflection on the inner tube surface. Subsequent reflections within the tube wall (*Ray B*, etc.) are expected to give rise to echo pulses in the time-domain signal. Fig. 4.3.b) presents an enlarged view of the time-domain signal in Fig. 4.2.c). From this graph it is evident that there is a first large pulse and at least one echo pulse. The time delay between these pulses is measured to be $\Delta\tau = 12.3$ ps. Using the geometry of Fig. 4.3.a), it can be shown (see equation (E.8) in Appendix E) that the time delay between rays A and B is given by,

$$\Delta\tau = \frac{2 \cdot t_{\text{wall}} \cdot n_{\text{wall}} \cdot \cos\theta_2}{c}, \tag{4.5}$$

where c is the speed of light, t_{wall} and n_{wall} are respectively the thickness and refractive index of the tube wall, $\theta_2 = \text{asin}(\frac{n_{\text{air}} \sin\theta_1}{n_{\text{wall}}})$, and θ_1 is the incidence angle. Substituting $n_{\text{wall}} = 1.56$, $t_{\text{wall}} = 1.59$ mm, and $\theta_1 = 85°$ into equation (4.5) yields $\Delta\tau = 12.7$ ps, which is in good correspondence with the measured value (if we use the literature value $n_{\text{wall}} = n_{\text{PE}} = 1.534$ we obtain $\Delta\tau = 12.3$ ps).

Furthermore, time-windowing can be used to illustrate how the echo pulses influence the frequency spectrum. In the second row of Fig. 4.3, different time-domain signals are considered (shown as insets). In Fig. 4.3.c) we begin with the complete unmodified time-domain signal, which includes all of the echo pulses. The time-scan is Fourier transformed and normalized to the reference spectrum taken without the waveguide in order to yield a normalized transmission spectrum. Fig. 4.3.c) corresponds to Fig. 4.2.e). Next, in Fig. 4.3.d), we consider a modified time-scan where the signal has been zeroed after the first echo pulse. The corresponding spectrum is quite similar to that of Fig. 4.3.c), indicating that the short-period frequency oscillations are mainly attributed to interference effects between two time-domain pulses (two reflections). Finally, in Fig. 4.3.e) we consider the case where only the first pulse is retained, in other words all subsequent echo pulses are zeroed. The corresponding spectrum no longer has any short-period oscillations. We therefore confirm that the polymer tube is guiding by a Fabry-Perot reflection mechanism.

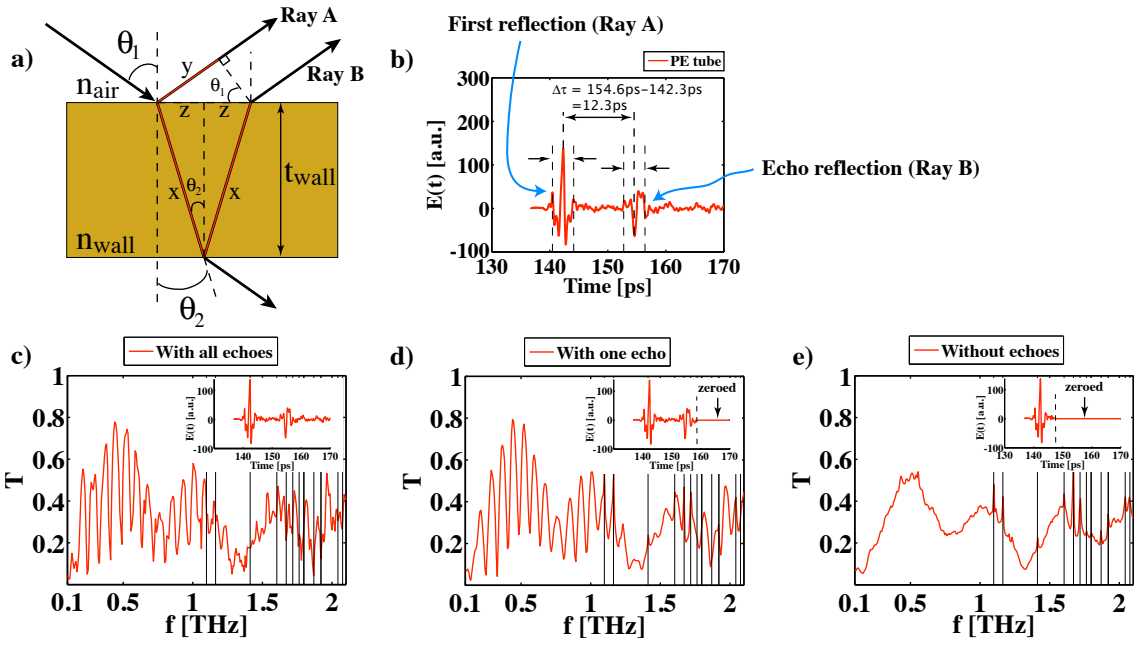

Figure 4.3 Evidence for the Anti-Resonant Reflection mechanism (Fabry-Perot reflection) in the THz transmission of polymer tubes. a) Schematization of polymer tube wall acting as a Fabry-Perot reflector. Let *Ray A* designate the initial reflection on the inner tube surface. Subsequent reflections within the tube wall (*Ray B*, etc.) are expected to give echo pulses in the time-domain signal. b) Measured THz time-domain signal transmitting through a $t_{\text{wall}} = 1.59$ mm PE tube (zoom of Fig. 4.2.c)). Note the presence of a large pulse and an echo pulse. Time delay between the pulses is $\Delta\tau = 12.3$ ps. c)-e) Measured time-domain signal (inset) is time-windowed (cropped) to retain all echoes (c), one echo (d), or no echoes (e), respectively. Fourier transform of the inset time signals (normalized to the reference signal in the absence of the PE tube) gives the corresponding transmission spectrum. The graphs indicate that short-period oscillations, due to the anti-resonant reflection, result from the interference between the multiple echo reflections of the Fabry-Perot tube wall. Vertical black lines correspond to water vapor absorption frequencies.

In the case of the thin-walled PTFE tube, echo pulses in the time-domain signal (Fig. 4.2.d)) are not readily apparent. Substituting $n_{\text{PTFE}} = 1.44$, $t_{\text{wall}} = 300$ μm, and $\theta_1 = 85°$ into equation (4.5) yields $\Delta\tau = 2.1$ ps. This means that the echo pulses overlap in the time-domain. In the frequency-domain (Fig. 4.2.f)), the expected Fabry-Perot oscillations are no longer clearly visible. In the next section, it will be argued that this is due to additional multi-mode interference that is deforming the spectrum. Nevertheless, there does appear to be a period of about $\Delta f \sim 0.52$ THz. Substituting

$n_{\mathrm{PTFE}} = 1.44$ and $t_{\mathrm{wall}} = 300$ μm into equation (4.4) we obtain a theoretical value of $\Delta f = 0.48$ THz. This value is relatively close, however an even closer correspondence is obtained by considering $t_{\mathrm{wall}} = 280$ μm, which yields $\Delta f = 0.52$ THz. This casts doubt on the uniformity of the tube wall thickness.

As will be demonstrated in the next subsection, the waveguides are multimode and the shape of the amplitude transmission curves depend on the modal interference between the excited modes. Evidence of this interference can be seen in the amplitude variations of the periodic transmission peaks. Mode coupling is very sensitive to the alignment of the large core waveguide and the interference will either be constructive or destructive depending on the phase accumulated by the modes propagating along the length of the waveguide. Cutback measurements were attempted in order to measure the propagation losses, however sample deformation during cutting and slight waveguide mis-alignment led to significant coupling variations from one segment length to the next. The resulting changes in modal interference led to complex and variable spectra making the cutback technique impracticable. Nevertheless, we obtain an upper bound estimate of the power propagation loss coefficient α by plotting (in the forth row of Fig. 4.2) the *total power loss* normalized with respect to the tube length $(-2\ln(|T|)/L)$. The total loss includes coupling loss, therefore the total loss can be considered as an upper bound on the value of propagation loss. The lowest total loss points yield $\alpha < 0.031$ cm^{-1} at 0.44 THz for the thick-walled PE tube, and $\alpha < 0.03$ cm^{-1} at 0.64 THz for the thin-walled PTFE tube. This gives a rough indication that straight waveguide propagation losses are at least as low as 0.04 cm^{-1} at certain frequencies.

4.1.4 Theoretical modeling

In order to better understand the results of Fig. 4.2, vectorial simulations of ideal circularly-symmetric structures were carried out using a transfer matrix mode solver (Appendix C). The simulations assumed material parameters taken from the literature [53]: $n_{PE} = 1.534$ and $\alpha_{PE} \sim 1$ cm^{-1} for the thick-walled PE tube, and $n_{PTFE} = 1.44$ and $\alpha_{PTFE} \sim 1$ cm^{-1} for the thin-walled PTFE tube. The dimensions of the thick walled tube were taken to be the manufacturer values ID = 6.35 mm and WT = 1.59 mm. In the case of the thin walled tube the dimensions were assumed to be ID = 7.66 mm and WT = 300 μm.

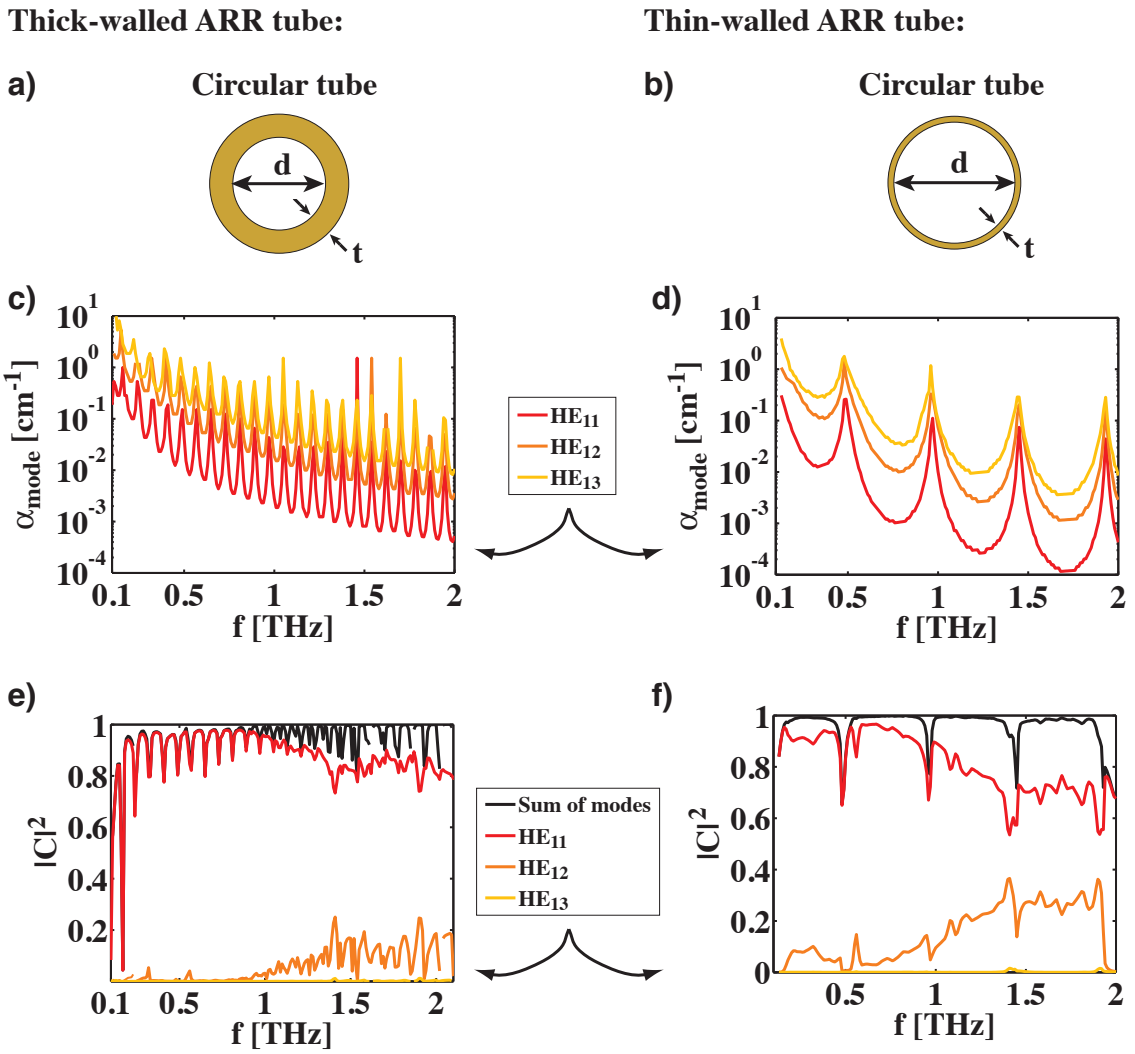

Figure 4.4 Theoretical modeling of the propagation losses and coupling coefficients of the HE modes of thick and thin walled dielectric tubes. a), b) Schematizations of the simulated geometries. The dimensions considered are d=6.35mm and t=1.59mm for the thick walled tube, as well as d=7.66mm and t=300μm for the thin walled tube. c), d) Power propagation loss coefficient α for the 3 first HE modes. e), f) Power coupling coefficients $|C|^2$ describing the coupling efficiency between the first 3 HE modes and the experimental input beam (presumed gaussian).

Figs. 4.4.c) and 4.4.d) present the calculated propagation losses (α) of the first three HE modes, for the thick and thin walled tubes respectively. Note that α includes the effects of absorption and radiation losses. The curves show periodic minima of low loss separated by discontinuous points of high loss corresponding to

the resonant frequencies given by equation (4.4). Note that all the modes share these high loss points because the reflectivity of the tube wall is zero at those resonant frequencies and the modes cease to be guided as they are radiated through the tube wall. Furthermore, the losses at the anti-resonant minima decrease with increasing frequency and with increasing tube diameter [73]. Figs. 4.4.c) and 4.4.d) also clearly demonstrate the dependence on the tube wall thickness, with wider transmission bands (wider low loss windows) for the thinner walled tube.

In order to calculate the fraction of power guided by each mode, overlap integrals (equation (2.9)) were calculated between the fields of a guided mode and the field of the input beam. The beam profile of the input beam was assumed to be gaussian and the field is approximately a plane wave in the focal plane of the parabolic mirror. The size of the gaussian input beam, shown in Fig. 2.11.f), is frequency dependent and was measured using a knife-edge technique. Figs. 4.4.e) and 4.4.f) present the calculated power coupling coefficients $|C|^2$ for the thick and thin walled tubes, respectively. The linearly polarized source favors coupling to the HE modes and at low frequencies the power is predominantly in the fundamental HE_{11} mode. This is because the mode size is larger and better matched to the input beam at low frequencies. However, at high frequencies a significant amount of power is coupled into the higher order modes. Moreover, only three modes are considered because coupling to higher order modes rapidly decreases due to mode mismatch between the input beam and the higher order modes. Nevertheless, with 20-30% of the power coupled into the second mode at frequencies above 1 THz, the interferometric beating between the modes will be significant.

The total multi-mode amplitude transmission of the waveguide can be modeled by the following equations [43],

$$E_{\mathrm{w}}(f) = |E_{\mathrm{r}}(f)| \cdot \sum_m C_m^{\mathrm{in}} \cdot C_m^{\mathrm{out}} \cdot e^{i(n_{\mathrm{eff},m}-1)\frac{2\pi f}{c}L} e^{-\frac{\alpha_m L}{2}}, \tag{4.6}$$

$$|T| = \frac{|E_{\mathrm{w}}(f)|}{|E_{\mathrm{r}}(f)|} = \left| \sum_m |C_m|^2 \cdot e^{i(n_{\mathrm{eff},m}-1)\frac{2\pi f}{c}L} e^{-\frac{\alpha_m L}{2}} \right|, \tag{4.7}$$

where $E_{\mathrm{w}}(f)$ is the modal field coming out of a waveguide of length L, and $E_{\mathrm{r}}(f)$ is the reference signal measured in the absence of the waveguide at the position of the input coupling plane. c is the speed of light and f is the frequency. The sum is taken over the number of considered modes and the subscript m refers to a given mode.

C_m^{in} and C_m^{out} are respectively the input and output amplitude coupling coefficients with respect to the waveguide, calculated with equation (2.9). Since the input and output coupling conditions are assumed to be the same we have $C_m^{\text{in}} \cdot C_m^{\text{out}} \approx |C_m|^2$, equivalent to a power coupling coefficient. α_m and $n_{\text{eff},m}$ are respectively the power propagation loss coefficient and effective propagation index of the mode guided by the waveguide. Note that the sum of complex exponentials translates into sinusoidal modal interference terms.

To illustrate the influence of coupling on the theoretical fits, we compare two simulations using two different THz input beam sizes. In Fig. 4.5, calculations are carried out with the experimentally measured beam size (same as Fig. 2.11.f)). In Fig. 4.6, calculations are carried out with a beam size corresponding to the experimentally measured beam size arbitrarily scaled down by a factor of $\sqrt{2}$. In each case, transfer matrix simulations (such as Fig. 4.4) yield the modal parameters needed for the simulations. The coupling coefficients for each mode are then calculated using the given input beam size. Finally, equation (4.7) is used to calculate the theoretical waveguide transmission.

Let us consider the case of the thick walled tube. Although there is an excellent agreement between the position of the periodic minima in the experimental transmission curves and the resonant frequencies given by equation (4.4), there is a large discrepancy in the amplitudes of the theoretical and experimental transmission peaks, as seen in Figs. 4.5.c) and 4.6.c). Beyond a simple frequency-dependent coupling variation, destructive multi-mode interference is expected to provoke large reductions in the amplitude of the transmission peaks. However, such multi-mode interference is highly sensitive to the actual amount of power coupled into the higher order modes, which is in turn sensitive to the size of the input beam. Just as an optimized coupling can maximize the amount of power in the fundamental mode, an improper beam size can couple light into multiple modes because these large core waveguides are highly *over-moded*. As a case in point, the smaller beam size in Fig. 4.6.a) leads to a significantly higher amount of power coupled into the higher order modes. Moreover, in Fig. 4.6.c) a higher amount of power in the HE_{12} mode is seen to yield a higher destructive interference contrast than in Fig. 4.5.c). Note that an input beam size variation of less than 1 mm at $f = 1$ THz has lead to a significant difference between the transmission values calculated at that frequency in Figs. 4.5.c) and 4.6.c). Although the theoretical fit in Fig. 4.6.c) still does not quantitatively agree with the

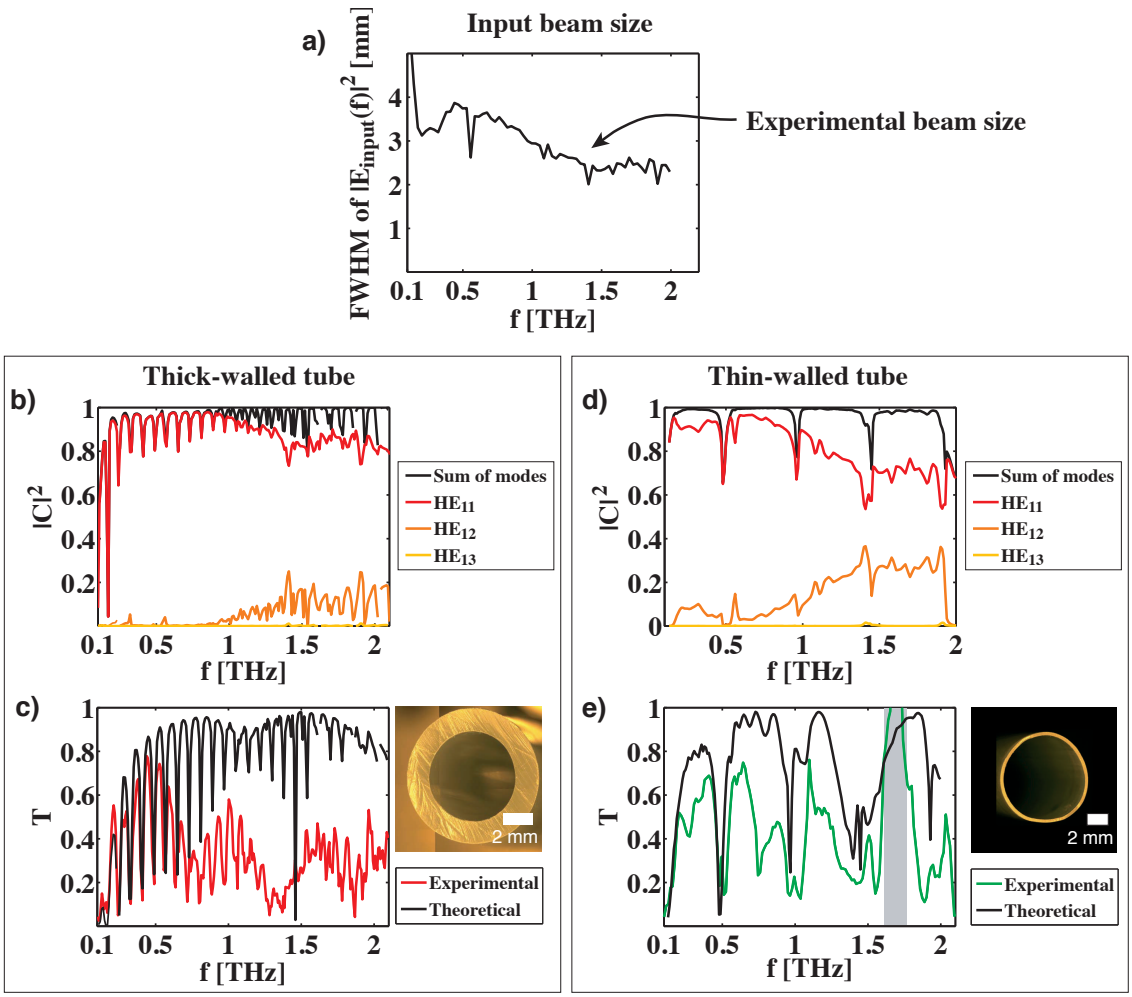

Figure 4.5 First theoretical fit of the transmission through thick and thin walled hollow-core tubes, using the experimentally measured THz beam size shown in a). Modal parameters for the fits are taken from the simulations Fig. 4.4. b) and d) show coupling coefficients calculated from beam size shown in a). c) and e) present the theoretical fits to the transmission. Complex oscillations within the spectra are explained by multi-mode interference (equation (4.7)). For the thin walled tube, the shaded gray region corresponds to a normalization error in the experimental spectrum.

nearly complete attenuation of the experimental transmission around 1.3 THz, the large influence of the coupling conditions on the final transmission spectrum has been qualitatively demonstrated. Similar results are obtained for the case of the thin-walled tube. At frequencies below 1 THz, the power in Fig. 4.5.d) is predominantly in HE_{11} and the theoretical fit largely over-estimates the waveguide transmission. In

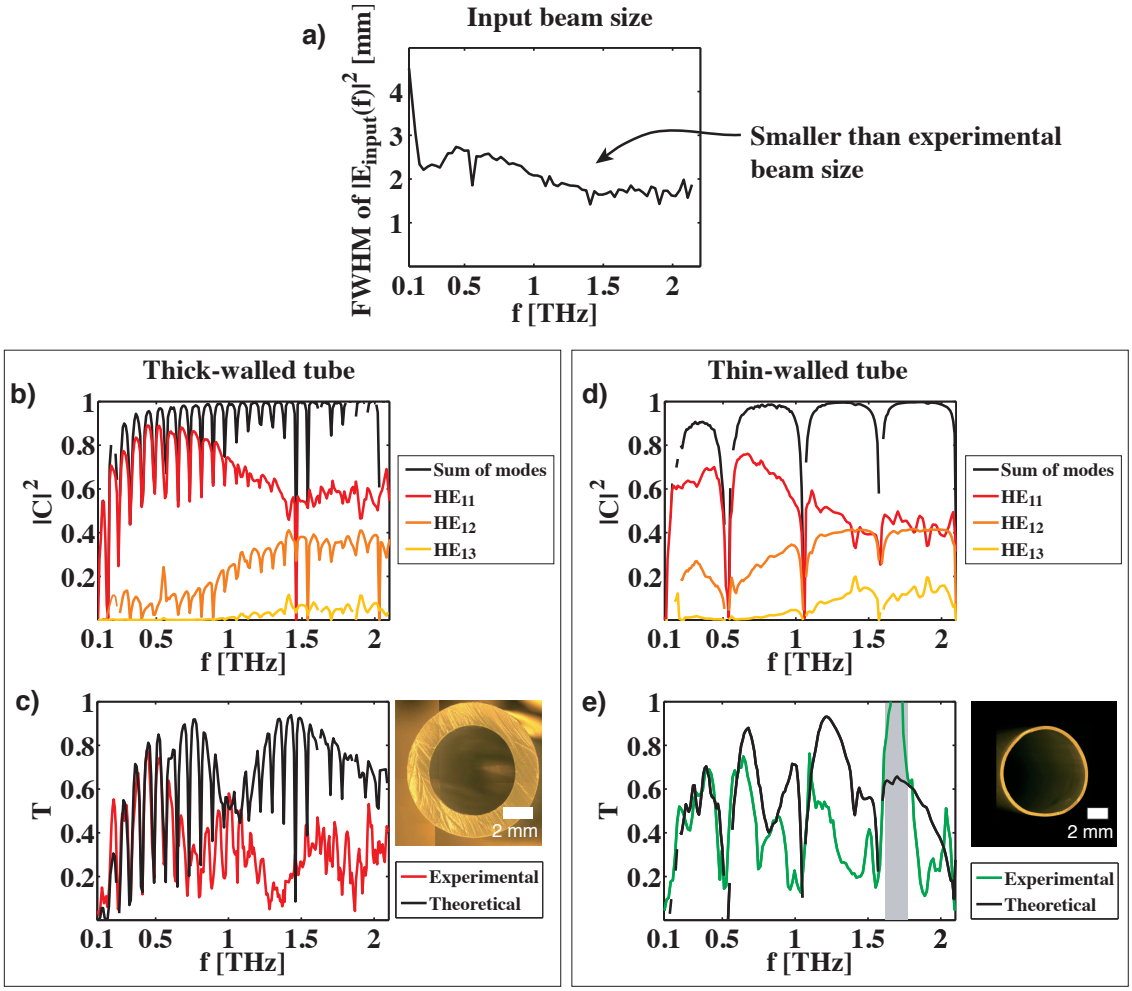

Figure 4.6 Second theoretical fit of the transmission through thick and thin walled hollow-core tubes, using a beam size that is smaller than in Fig. 4.5.a). Modal parameters for the fits are taken from transfer matrix simulations. b) and d) show coupling coefficients calculated from beam size shown in a). c) and e) present the theoretical fits to the transmission. Complex oscillations within the spectra are explained by multi-mode interference (equation (4.7)). A smaller input beam size increased the coupling into higher-order modes. For the thin walled tube, the shaded gray region corresponds to a normalization error in the experimental spectrum, and in this case a wall thickness of 275 μm was considered for the simulation.

Fig. 4.6.d) a smaller input beam size leads to a higher amount of power coupled into the HE_{12} mode and, consequently, the multi-modal destructive interference gives a substantially closer fit at frequencies below 1 THz.

These simulations lead us to question the validity of the beam size measured with

the knife-edge technique (Fig. 4.5.a)). The slightly more accurate theoretical fits of Fig. 4.6 seem to indicate that the beam-size measured by the knife-edge technique over-estimates the actual beam size and that the actual coupling conditions are different from those that have been considered. In their more precise fiber-coupled-PC-antenna measurement of the THz beam profile, Reiten *et al.* observed that Laguerre-Gauss modes better described the THz beam profile and that the gaussian beam model was an approximation that *over-estimated the experimental THz beam size* [103]. The simulations of Fig. 4.5 and 4.6 appear to be in qualitative agreement with this statement. Since we are not equipped with a fiber-coupled-PC-antenna, we are unable to precisely measure the THz beam profile and determine the Laguerre-Gauss mode parameters. Thus, we are limited to considering a gaussian approximation for the input THz beam. In light of these simulations, a more accurate knife-edge beam size measurement should be attempted in a purged environment, with a precise translation stage and a true power-meter placed immediately after the screen, because in the method described in section 2.4.4 it is unclear how diffraction off the screen affects the spatial integration of the occluded beam.

Although the general behavior in Figs. 4.6.c) and 4.6.e) is similar to the experimental transmission at low frequencies, larger discrepancies between the theory and the experiment occur at higher frequencies. Another factor that can contribute to this discrepancy is the possibility of variations in the wall thickness along the length of the tubes. Fluctuations in the thickness of the tube wall result in a frequency shifting of the Fabry-Perot reflection peaks. From a ray-optic perspective, the light reflecting though the waveguide at a given frequency would experience different reflectivities at each wall reflection. The final amplitudes participating in the modal interference would be different from those predicted from the simple invariant tube model that was considered. Moreover, recall that in the case of a tube of constant wall thickness the resonance frequencies that give a wall reflection of zero are fixed. However, in the case of wall thickness fluctuations, the frequency shifting of the resonance peaks would eliminate sharp resonance frequencies from the final waveguide transmission. We also note that wall thickness variations were also reported by Lai *et al.* [73] and that the effects of such fluctuations would be much more pronounced in thin-walled tubes. Indeed, the correspondence between the positions of the transmission minima and equation (4.4) was previously shown to be more tenuous in the case of the thin-walled tube.

Finally, upon considering the case of the thin walled tube, it is worth mentioning that the thinness of the wall leads to a poor mechanical stability making the tube more susceptible to deformations. From the cross-section picture of the thin-walled tube, it is obvious that the tube is not circularly symmetric. It is unclear how such deformations along the length of the tube affect the propagation loss. It is however evident that the mode coupling will be affected and that the induced form birefringence will lift the polarization degeneracy, leading to slight differences in the accumulated modal phase. These changes will affect the final modal interference, making the transmission of the thin-walled tube very sensitive to alignment.

4.1.5 Bending loss

ARR tubes have been touted as very low loss waveguides [73]. As can be seen in table 1.2, Lai *et al.* measured straight waveguide segments up to 3 m in length. However, since the Fabry-Perot reflection of the ARR tube wall is highly sensitive to the incidence angle we would expect a significantly large bending loss at non grazing incidence angles. In one of their papers, Lai *et al.* developed a simple ray-optic calculation to evaluate the straight waveguide propagation losses. In Appendix F this ray-optic calculation is extended to the case of bent waveguides. We now use this ray-optic method to estimate the propagation losses in a ARR tube bent with a radius $R_{\text{bend}} = 20$ cm.

As an example, we consider the above mentioned teflon tube with $d_{\text{core}} = 7.66$ mm, $t = 300$ μm, and $n_{\text{tube}} = 1.44$. To validate the ray-optic calculation, we compare the straight waveguide propagation loss calculated with the ray-optic method to the exact solution calculated using the transfer matrix method. The ray-optic method is seen to underestimate the loss, however the spectral features are well represented. From a ray-optic point of view, bending of the waveguide decreases the incidence angle of a modal ray and the mode experiences higher propagation losses because the tube wall reflectivity decreases as the incidence angle decreases. The loss minima in the bent waveguide are estimated to be on the order of ~ 0.05 cm^{-1}. Such a value is orders of magnitude higher than the straight waveguide losses. More importantly, the loss has been incremented to the point where significant spectral filtering will occur over short waveguide lengths. Consider the lobe of the loss curve in the 1.0-1.4 THz frequency range. Bending has shifted the entire loss curve to higher loss values. Although

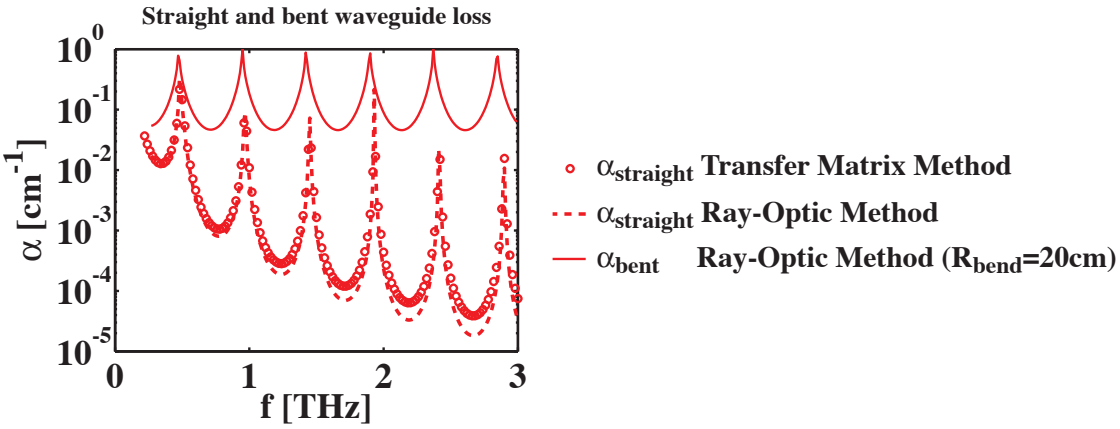

Figure 4.7 Straight and bent waveguide propagation losses of an ARR tube calculated using a ray-optic method. We consider the HE_{11} mode of an ARR tube with $d_{\text{core}} = 7.66$ mm, $t = 300$ μm, and $n_{\text{tube}} = 1.44$. The straight waveguide loss calculated by the ray-optic method is seen to underestimate the loss when compared to the exact calculation using the transfer matrix method. The bent waveguide loss is seen to be significantly higher than the straight waveguide loss.

the minimum of the lobe in the bent waveguide is ~ 0.05 cm^{-1}, the loss at most frequencies is ≥ 0.1 cm^{-1}. As a result the bending will cause a severe narrowing of the transmission peaks.

4.1.6 Summary of ARR tube results

In summary, we have measured the THz transmission spectra and loss characteristics of hollow-core dielectric tubes. Although the total loss indicates that propagation losses should be lower than 0.03 cm^{-1} at certain frequencies, cutback measurements are impracticable due to the excitation of multiple modes and spectral changes resulting from waveguide deformations and coupling variations. Thin walled dielectric tubes were shown to give larger transmission windows than the thick walled tubes, but the poorer mechanical stability results in waveguide deformations that affect transmission in an unpredictable manner. Unless the coupling conditions are optimized to maximize the amount of power coupled into the fundamental mode at all frequencies, the final waveguide transmission can suffer from destructive modal interference and will be very sensitive to waveguide alignment. Finally, the practicality of ARR tubes was seen to be limited by the prohibitively high bending losses.

4.2 Bragg fibers

An alternative solution for guiding light in hollow core waveguides relies on the multiple reflections of a Bragg reflector. Although there has been a large amount of research on planar THz Bragg reflectors [130, 131, 132, 133, 134] and a few theoretical studies proposing THz Bragg fibers [77, 78], to our knowledge, we present the first experimental realization of such fibers for guiding THz radiation. Owing to the similar refractive indices of polymers in the THz regime [53], special measures must be taken to increase the refractive index contrast between the layers of a Bragg reflector. We demonstrate two different implementations to increase the index constrast. The first structure uses air for the low refractive index layers, whereas the second structure uses a doped polymer film for the high index layers. Both fibers are shown to guide and difficulties concerning their fabrication and multi-mode regimes are discussed. Finally, we study the different Bragg fiber operating regimes in detail in order to suggest new and more efficient designs.

4.2.1 Waveguiding principle

A Bragg fiber consists of a circularly symmetric Bragg reflector (Fig. 4.8.a)) that confines light to the fiber core (Fig. 4.8.b)). Although Bragg fibers at visible and near-infrared wavelengths can have solid cores, Bragg fibers at THz frequencies require large hollow cores to avoid material absorption loss. The Bragg reflector itself consists of a periodic stack of alternating high and low refractive index layers, within which multiple reflections create constructive interference bands of high reflectivity known as (transmission) bandgaps (Fig. 4.8.c)). These reflectivity bands can be tuned arbitrarily by a suitable choice of refractive indices and thicknesses for the Bragg layers. Moreover, larger reflections (and hence lower propagation loss) as well as wider Bragg mirror reflection peaks (wider fiber transmission windows) will result from a larger index contrast between the constituent layers of the Bragg mirror. Readers should refer to the literature for more information about Bragg fiber theory [135, 24], however a main point that should be emphasized is that propagation losses are proportional to $(\frac{1}{f^2 \cdot d_{\text{core}}^3})$, where d_{core} is the diameter of the core and f is the frequency of the confined light.

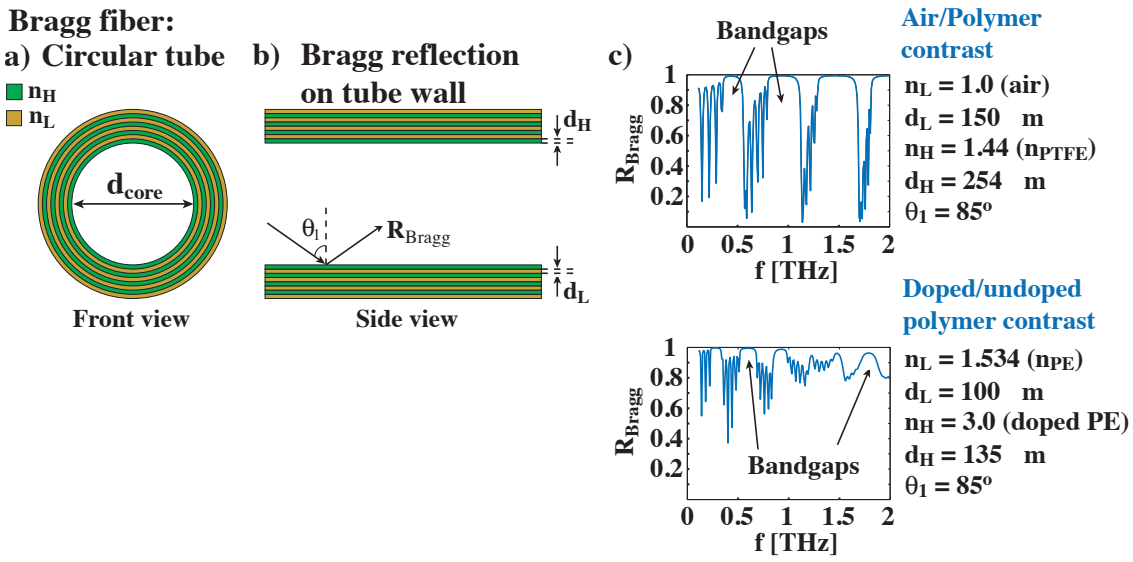

Figure 4.8 Schematization of the geometry and waveguiding principle of a Bragg fiber. a) Schematization of the geometry. b) Illustration of the wave confinement from a ray-optic point of view. c) Reflectivity of a planar Bragg reflector, similar to that of the curved wall of the Bragg fiber.

4.2.2 Fabrication technique

Air/Polymer Bragg fiber

There exist two fabrication techniques that exploit air in order to increase the refractive index contrast between the layers of a Bragg reflector. The first is a physical separation of the material layers via the use of spacers or bridges that maintain a distance between the material layers, thus creating an air gap (air layers) [131]. The second method consists of fabricating highly porous material layers, whereby porosity effectively reduces the refractive index of a layer [134] until it is close to that of air. In both cases, the size of the features (spacers or porous air bubbles) in the low index layers must be small enough to reduce the effects of scattering. Although certain polymers can be made to foam by including gas-forming additives within the polymer, processing such porous polymers into fibers is difficult. Instead, we implemented the first method by rolling a polymer film with powder particles. The process is schematized in the first row of Fig. 4.9. A polydisperse PMMA powder, with an average particle size of 150 μm, was randomly laid out on top of two touching 127 μm PTFE films. The films were subsequently rolled around a mandrel to form the Bragg fiber.

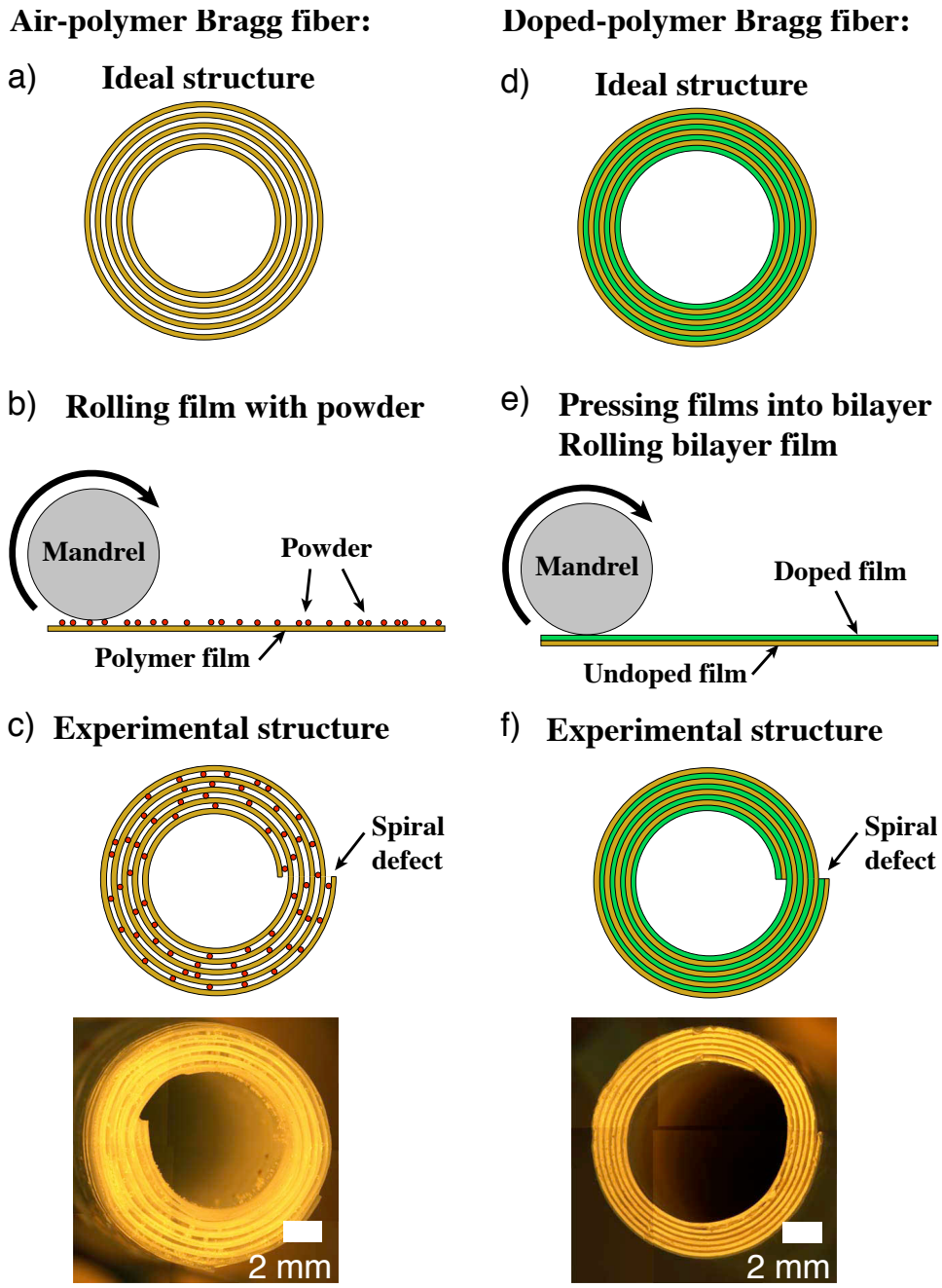

Figure 4.9 Schematization of the fabrication process of THz Bragg fibers. First row: Air/Polymer Bragg fiber. Second row: Doped/Undoped polymer Bragg fiber. The ideal geometry is circularly symmetric however the rolling of films creates a spiral defect that breaks the symmetry. Cross-section pictures of the experimental fibers are also shown.

The powder particles acted as spacers to maintain an air gap between the spiraled polymer film layers. The film was held together by wrapping it in PTFE tape and the mandrel was removed. The spiral cross-section of the fiber, shown in Fig. 4.9.c), approximates the ideal circularly symmetric structure shown in Fig. 4.9.a). The final air-polymer Bragg fiber had an inner diameter of 6.73 mm and a reflector of 5 bilayers consisting of 254 μm PTFE and roughly 150 μm air layers.

Doped/Undoped polymer Bragg fiber

The second method that we implemented was inspired by the work of Jansen *et al.* [133, 136]. They demonstrated that doping a host polymer (like polypropylene, PP) with high refractive index TiO_2 particles could significantly increase its THz refractive index. We similarly added TiO_2 particles to polyethylene. For the TiO_2 particles, we used R104 grade powder purchased from Dupont, with an average particle size of 0.22 μm. The host polymer was linear low density polyethylene (LLDPE), Grade Sclair FP120A, purchased from Nova Chemicals. Different compositions using different grades of TiO_2 powder were prepared and mixed together using a twin-screw extruder. The extrudate was cut into pellets and subsequently extruded into film using another extruder. Fig. 4.10 presents the refractive index and power absorption coefficient obtained from THz-TDS measurements of the doped and undoped polymer films. Despite some Fabry-Perot oscillations due to the thickness of the samples, the results clearly indicate a substantial increase of the refractive index at high doping concentrations; we find $n = 3$ for 80% wt. R104 grade doping[1]. Moreover, the loss is seen to increase substantially with frequency and can be modeled empirically with a quadratic function. In comparison, Jansen *et al.* reported $< 5\,\mathrm{cm}^{-1}$ absorption loss for 60% vol. rutile TiO_2 in PP [117], but for frequencies $f < 0.5$ THz.

The doped polymer Bragg fibers are fabricated by co-rolling films around a mandrel, as schematized in the second column of Fig. 4.9. In order to increase the quality of the dielectric interface between the high and low index layers of the Bragg reflector, a bilayer film is formed by pressing doped and undoped films together with a hot press. The bilayer film is subsequently rolled into a fiber and solidified in an oven.

Although processing a bilayer film into a Bragg fiber is a simple procedure, the actual fabrication of the doped polymer bilayer turned out to be a difficult task. The high concentrations of powder change not only the refractive index but also the

[1] 80% weight of TiO_2 in PE corresponds to a 46% volume fraction of TiO_2 in PE.

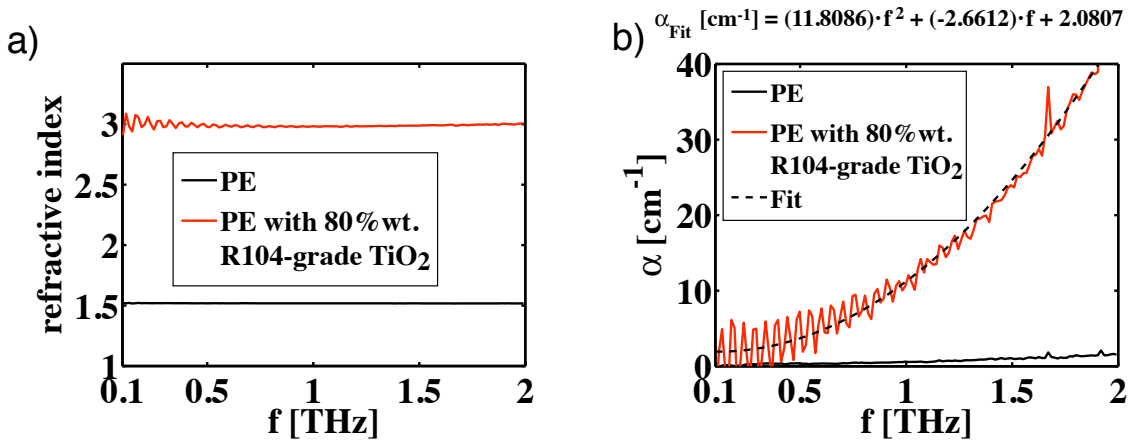

Figure 4.10 THz refractive index (a) and power absorption loss (b) of pure and TiO_2 doped poly(ethylene) films. Fabry-Perot oscillations due to the thickness of the samples can be seen. Absorption loss from the doped film can be approximated by a quadratic function.

thermo-mechanical properties of the polymer. The composite material had a higher viscosity and a much higher melting temperature than pure PE. As a result the extrusion into film was much more difficult and only thick films ($\sim$ 400 μm) were obtained. Moreover, the doped polymer film was brittle. As such the extruded film was too thick to form a Bragg reflector that would efficiently reflect at the desired frequency of 1 THz. The film therefore needed to be pressed to a smaller thickness. Without a roller press to continuously press film down to the proper thickness we had to repeatedly press small film strips using a simple hydraulic press.

The bilayer fabrication steps are illustrated in Fig. 4.11. A $\sim$400 μm thick doped PE film (80% wt. TiO_2) was cut into strips (Fig. 4.11.a)), placed between two PTFE sheets and two metal plates (Fig. 4.11.b)) and squished to a $\sim$100 μm thickness (Fig. 4.11.c)) using a hot press. The thinner doped film was again cut into strips (Fig. 4.11.d)) and a sheet of pure PE film was placed on top of the strips (Fig. 4.11.e)). The low-index undoped PE film was 101.6 μm thick commercial LDPE film, purchased from McMaster-CARR. The stack of doped/undoped polymer films was hot-pressed together (Fig. 4.11.f)) to consolidate the bilayer. Note that the pure PE film acts as a glue to stick the doped film strips together and also reduces the brittleness of the film. Although a bilayer film was successfully made, this fabrication process is far from ideal. Fig. 4.11.g) presents many bilayer film defects including density

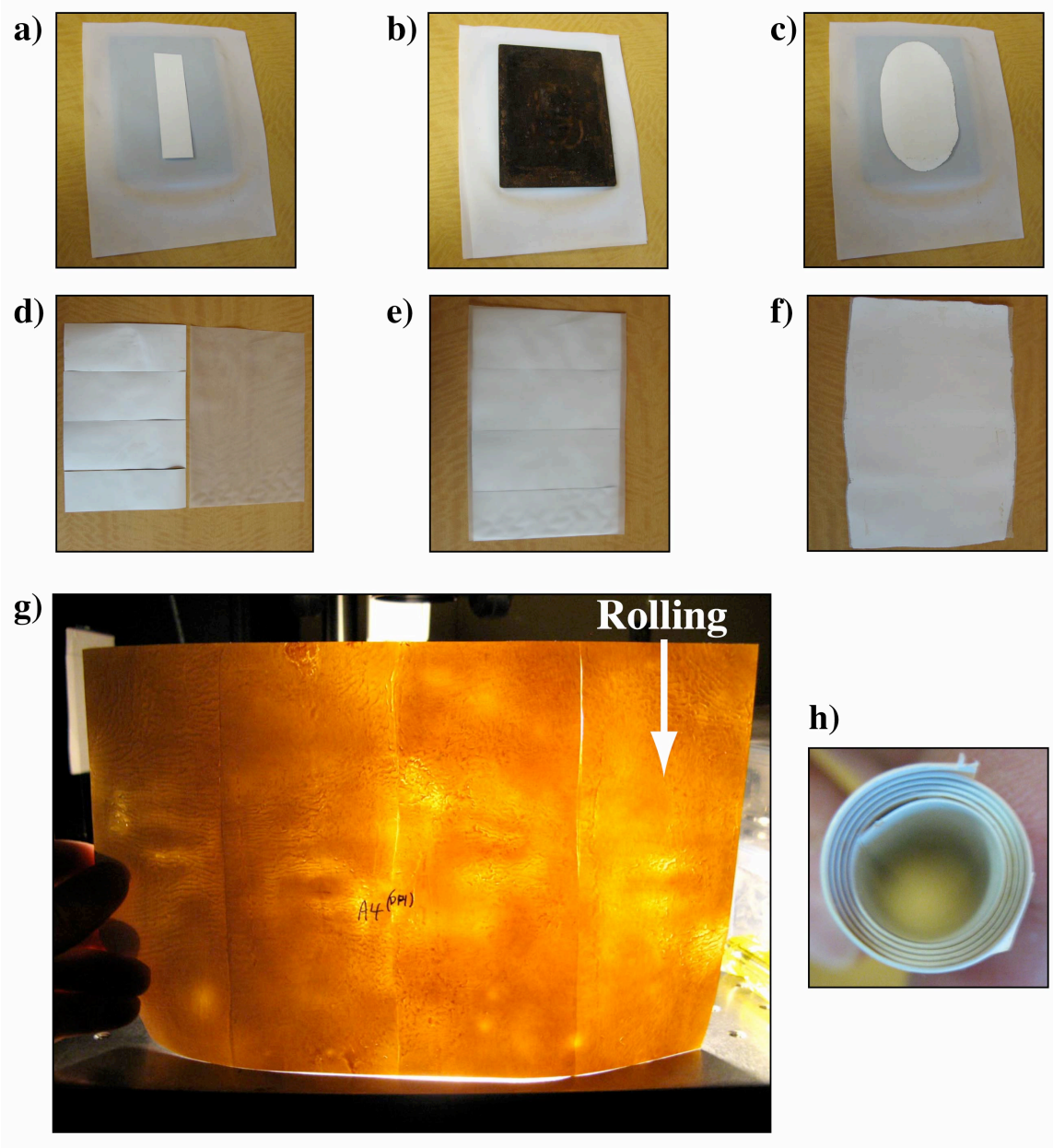

Figure 4.11 Fabrication steps of a doped polymer Bragg fiber. Thick (∼400 μm) doped PE film (80% wt. TiO_2) is cut into strips (a), placed between two PTFE sheets and two metal plates (b) and squished to a thinner thickness of (∼100 μm) (c) using a hot press. Strips of thinner doped film are prepared along with a 100 μm pure PE film (d). They are stacked to form a bilayer (e) and hot-pressed together (f) to consolidate the film. Bilayer film defects are clearly visible (g). Bilayer is rolled into a Bragg fiber (h) and heated to solidify. Arrow indicates the direction of rolling.

inhomogeneities, cracks in the film, and edge defects between the film strips.

A Bragg fiber was nevertheless fabricated from resulting bilayer. The bilayer was rolled into a Bragg fiber (Fig. 4.11.h)) and solidified in an oven at 130^{o}C. The spiral cross-section of the final fiber, shown in Fig. 4.9.f), approximates the ideal circularly symmetric structure shown in Fig. 4.9.d). The final doped-polymer Bragg fiber had an inner diameter of 6.63 mm and a reflector of 6 bilayers consisting of 135 μm high-index layers of 80% wt. TiO_2 doped PE and 100 μm low-index layers of undoped PE.

4.2.3 THz-TDS transmission and loss measurement

The fabricated Bragg fibers were measured in the same manner as the ARR tubes. Fig. 4.12 presents the measured transmission characteristics. The column on the left presents the results for the air-polymer Bragg fiber, 21.4 cm in length, and the column on the right presents the results for the doped-polymer Bragg fiber, 22.5 cm in length. Figs. 4.12.a) and 4.12.b) present the fiber cross-sections. The spiral edge defect breaking the circular symmetry can clearly be seen. Figs. 4.12.c) and 4.12.d) present the time-scans of the guided THz pulses. Once again, the dispersion is seen to be very low because of the high fraction of power guiding within the air. Figs. 4.12.e) and 4.12.f) present the measured transmission spectra. Note that both Bragg fibers display wide transmission peaks, however the transmission is lower in the case of the doped Bragg fiber. Cutback measurements were attempted and were again deemed impracticable due to the sensitivity of modal coupling with respect to waveguide alignment. We nevertheless estimate an upper bound on the power propagation loss coefficient α by plotting, in Figs. 4.12.g) and 4.12.h), the total transmission loss normalized with respect to the waveguide length $(-2ln(|T|)/L)$. The lowest total loss points yield $\alpha < 0.028$ cm^{-1} at 0.82 THz for the air-polymer Bragg fiber, and $\alpha < 0.042$ cm^{-1} at 0.69 THz for the doped-polymer Bragg fiber.

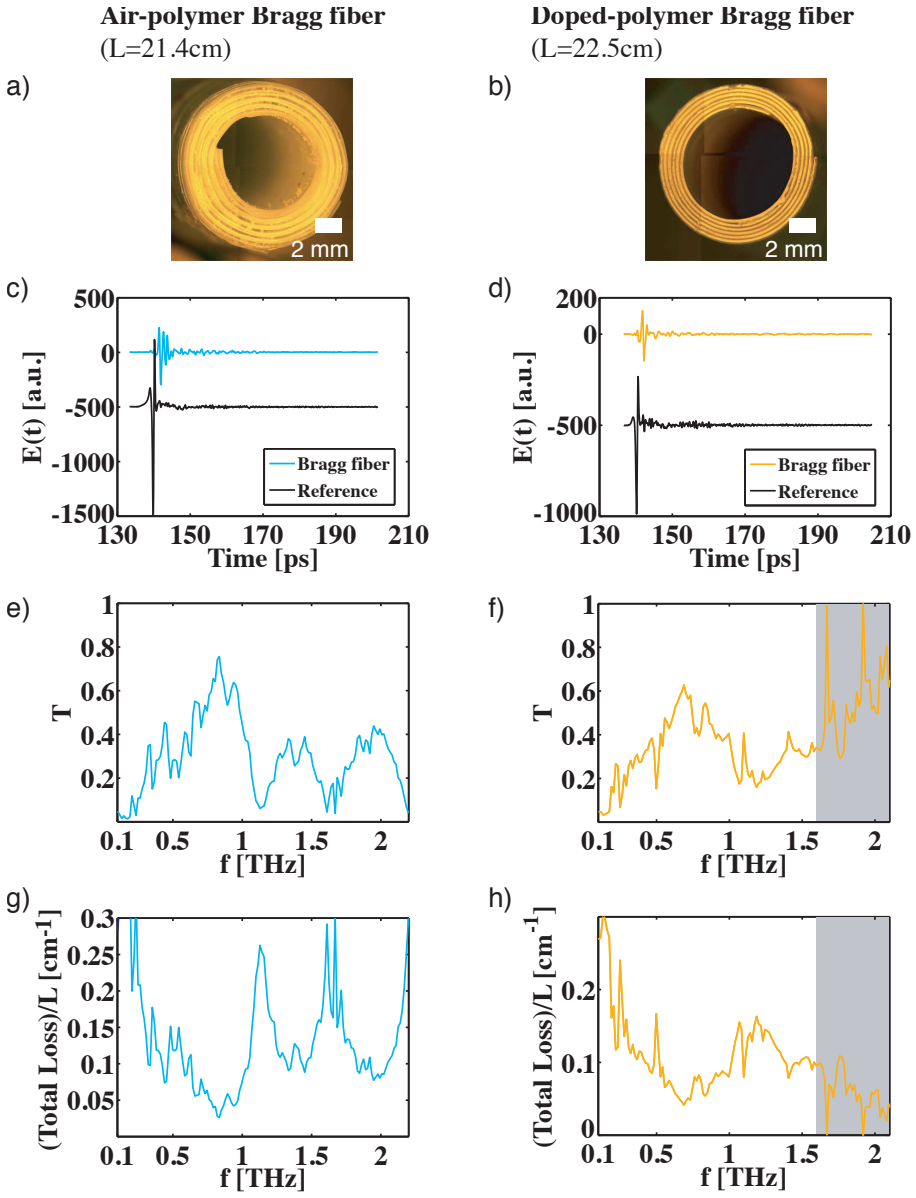

Figure 4.12 Comparison of the THz-TDS transmission characteristics of Air/Polymer and Doped/Undoped polymer Bragg fibers. Left column: Air/Polymer Bragg fiber, right column: Doped-polymer Bragg fiber. a), b) Waveguide cross-sections. c), d) Time-domain signals of transmitted THz pulses. e), f) Normalized amplitude transmission spectra. g), h) Upper bound on propagation loss given by total loss normalized with respect to waveguide length. The shaded gray region corresponds to a normalization error in the experimental spectrum due to absorption from residual water vapor.

4.2.4 Theoretical modeling

In order to better understand the results of Fig. 4.12 vectorial simulations were carried out to calculate the modal propagation losses and coupling efficiencies. The dimensions of the Bragg fibers were given in section 4.2.2. The values given in section 4.1.4 were assumed for the frequency-independent refractive index and absorption coefficients of PTFE and pure PE. Section 4.2.2 presented the THz material parameters of the TiO_2 doped PE. In Fig. 4.10, it can be seen that a constant index of $n_{\text{Doped PE}} = 3.0$ can be assumed and that the absorption coefficient of the doped polymer can be empirically fitted with a parabola: $\alpha_{\text{Doped PE}} = (11.8086) \cdot f^2 + (-2.6612) \cdot f + (2.0807)$. Where α is in cm^{-1} and f is in THz. This formula was used in the simulations for the power loss in the high refractive index layers of the doped-polymer Bragg fiber.

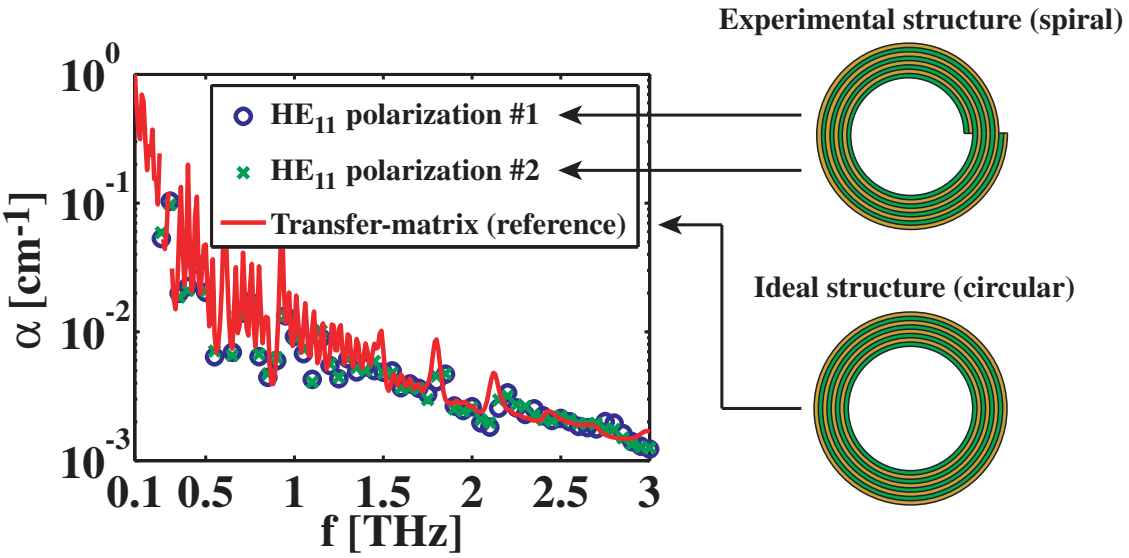

Figure 4.13 Comparison of the theoretical HE_{11} propagation losses of a doped-polymer Bragg fiber with ideal (circular) and non-ideal (spiral) geometry. Calculations for the circularly symmetric geometry were carried out with a transfer matrix mode solver. Calculations for the spiral geometry were carried out with a finite element method mode solver. There is a good agreement between the results indicating that the spiral defect does not significantly effect fiber losses.

Due to the rolling of polymer films in the fabrication process, the Bragg fibers exhibit a spiral edge defect. We began by verifying how the non-ideal spiral geometry affected the waveguide transmission. In Fig. 4.13 the propagation losses of the HE_{11} mode of an ideal circular waveguide, calculated with a transfer matrix mode solver, are

compared to the losses of a non-ideal spiral waveguide, calculated with a finite element method mode solver. There is a good agreement between the results indicating that the spiral defect does not significantly affect the mode propagation losses. This is reasonable because the edge defect is much smaller than the core diameter. The breaking of the circular symmetry does however create a form birefringence. As a result, the polarization degeneracy is lifted and there is a very slight difference between the $x-$ and $y-$polarized modes. Nevertheless, the differences are minor ($\frac{|\alpha_x-\alpha_y|}{\alpha_x} \leq 15\%$, $\frac{|n_x-n_y|}{n_x} \leq 1\%$, and $\Delta n = |n_x - n_y| \leq 8 \times 10^{-5}$) and all subsequent calculations were made assuming an idealized circular symmetry.

Fig. 4.14 presents the transfer matrix method simulations of the propagation loss and coupling efficiency for the HE modes guided by the Bragg fibers. Schematizations of the circular geometries are shown in Figs. 4.14.a) and 4.14.b). The power absorption loss coefficients of the first 4 HE modes are shown in Figs. 4.14.c) and 4.14.d). Also shown are the losses of the TE_{01} mode (in black) to more clearly illustrate the expected positions of the bandgaps. Note the qualitatively different behavior of the two types of Bragg fiber. On one hand, the doped-polymer Bragg fiber has a TE_{01} fundamental mode and the HE modes have much higher loss and do not present clear bandgaps. On the other hand, the air-polymer Bragg fiber has clearly defined low loss bandgaps and the HE_{11} mode is actually the lowest-loss fundamental mode.

Also shown in the graphs are radiation loss curves of the form B/f^2, where B is some constant. These curves describe the expected frequency scaling law of propagation loss within a Bragg fiber [24]. The B/f^2 curves in Figs. 4.14.c) and 4.14.d) were fit manually to the TE_{01} losses. On one hand, radiation loss is seen to dominate in the low absorption loss air-polymer Bragg fiber. On the other hand, the onset of strong absorption in the TiO_2-doped Bragg fiber is seen to severely affect propagation losses. Although the effects of absorption are generally seen at lower frequencies, where the field penetration into the lossy cladding is higher, in the case of the TiO_2-doped Bragg fiber even stronger absorption occurs at high frequencies because the absorption loss of the TiO_2-doped polymer increases quadratically as a function of frequency (Fig. 4.10.b)). Because of their high field penetration within the cladding, the HE modes experience such high absorption that their Bragg bandgaps are completely extinguished despite the high index contrast. Since the field penetration of the TE_{01} mode is lower than that of the HE_{11} mode, at frequencies above 1 THz the loss of the TE_{01} merely increases by one order of magnitude compared to the

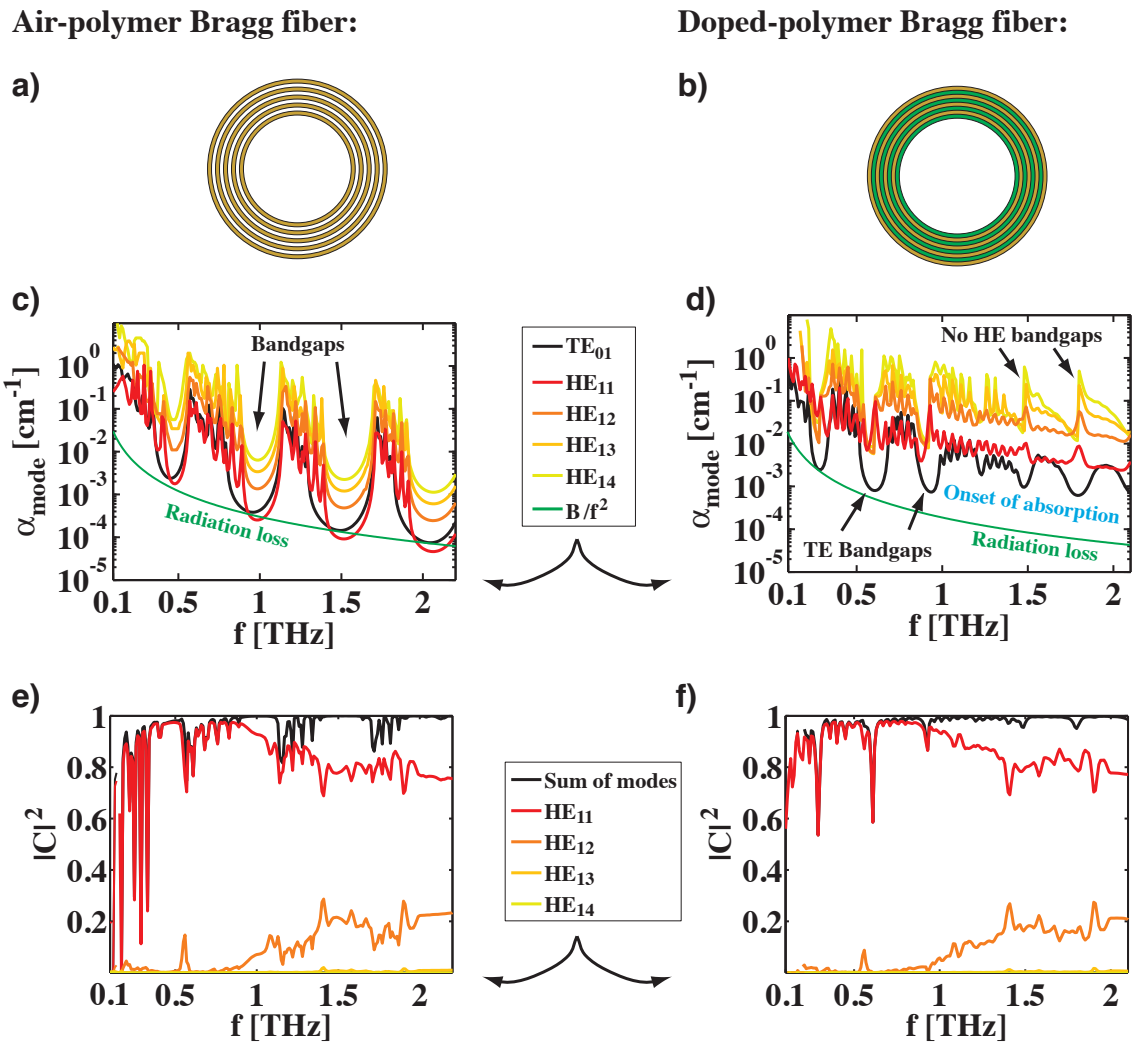

Figure 4.14 Theoretical modeling of the propagation losses and coupling coefficients of the HE modes of air-polymer and doped-polymer Bragg fibers. a), b) Schematizations of the simulated geometries. The dimensions considered are given in the text. c), d) Power propagation loss coefficient α for the 4 first HE modes. Note that α includes the effects of absorption and radiative losses. e), f) Power coupling coefficients $|C|^2$ for the first 4 HE modes.

expected radiation losses.

The frequency dependent input beam size, shown in Fig. 2.11.f), was again considered for the calculation of the power coupling coefficients of the first 4 HE modes shown in Figs. 4.14.e) and 4.14.f). Although the Bragg fibers are highly *over-moded*, coupling mismatch apparently limits the excitation to the first two modes. Never-

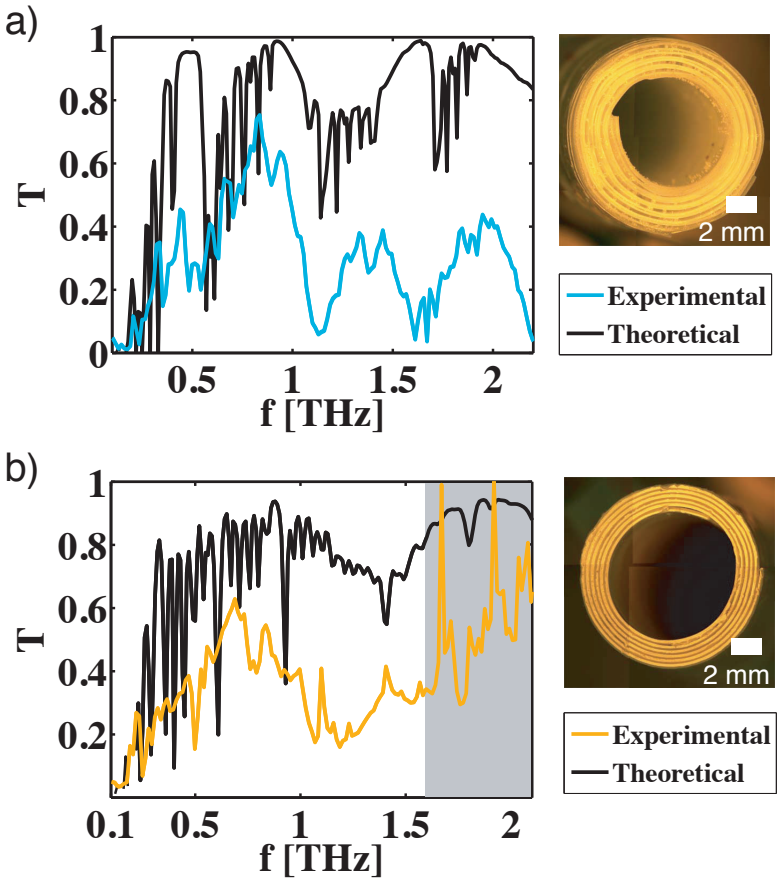

Figure 4.15 Theoretical fit of the transmission through air-polymer and doped-polymer Bragg fibers. Parameters for the fits are taken from Fig. 4.14. Complex oscillations within the spectra are explained by multi-mode interference (equation (4.7)). The shaded gray region corresponds to a normalization error in the experimental spectrum due to absorption from residual water vapor.

theless, a significant amount of power ($\sim$ 20%) is coupled into the second mode at frequencies above 1 THz.

Using the propagation losses and coupling coefficients of Fig. 4.14, we now compare the experimental transmission curves to a theoretical fit using equation (4.7). Figs. 4.15.a) and 4.15.b) compare the results of the air-polymer and doped-polymer Bragg fibers respectively. In both cases the theoretical model is seen to give a relatively poor fit. Although the theoretical curves describe the general behavior properly there are noticeable differences with respect to the experimental curves. This is due in part to the coupling coefficients that are calculated for the limited number of consid-

ered modes and in part to fiber defects and scattering losses which are not considered in the simulations.

For instance, in Fig. 4.15.a) there is a reasonable correspondence between the positions of the major Bragg peaks at low frequency, but at high frequency the peaks appear shifted. Such spectral deformations can be attributed to the imperfections seen in the fiber cross-section (other than the spiral defect). The co-rolling of two PTFE films without additional solidification has lead to regions with extra air gaps between the films of high index. These air gaps create reflections at extra interfaces and modify the thickness of the high-index layers. Furthermore, the overall transmission is lower than the theoretical prediction in part because scattering losses, notably from the powder particles in the low index layers, have been neglected. Nevertheless, clear bandgaps corresponding to the HE_{11} mode are visible in the transmission spectrum due to the lowered HE_{11} loss.

In the case of the doped-polymer Bragg fiber, there are thickness variations in the layers of the Bragg reflection due to the pressing of the films. We also suspect inhomogeneities in the dopant density (Fig. 4.11) because of the difficulty in uniformly mixing the TiO_2 powder at such high concentrations. Variations in density would result in variations of the refractive index of the Bragg layers and scattering on clusters of agglomerated dopant particles. In Fig. 4.15.b) there are no appreciable bandgaps and the shape of the spectrum is mainly dictated by coupling losses.

As a final point, we remark, once again, that the calculated coupling coefficients might not be valid. Beyond questioning the measured input beam size, we now question some underlying assumptions in the coupling coefficient calculation. The hypothesis of a negligible difference between the modal parameters of a circular and a spiral Bragg fiber appears reasonable in light of finite-element simulations. However, the implicit hypothesis that the input coupling beam is centered on the fiber might not be valid. Despite being experimentally mounted in centered circular irises, the fabricated Bragg fibers have a spiral defect with an outer edge that breaks the circular symmetry. The irises were closed onto the fibers in an attempt to insure alignment, but the edge defect actually displaces the fiber laterally in the coupling plane and provokes *off-centered* coupling. It is expected that off-centered coupling would increase the power coupled to higher order modes. Taking such effects into account could considerably increase the accuracy of the transmission model.

4.2.5 Bragg fiber design issues

Despite current fabrication difficulties, Bragg fibers hold the promise of low propagation loss and low bending loss. In the previous section we saw that the two types of Bragg fibers that were fabricated have fundamentally different operating regimes. To fully appreciate the differences between these two regimes of operation and to design better Bragg fibers we shall now compare the rate at which the fields of the TE and TM polarizations decay within the Bragg reflectors and examine how the TE, TM, and HE mode losses are affected.

To examine the field decay we consider the propagation through semi-infinite *planar* multi-layer Bragg reflectors, where a transfer matrix can be constructed to relate the fields in one layer to the fields of a subsequent layer. The planar Bragg reflection is a good approximation of the reflection within a circularly symmetric Bragg fiber provided that the core size is large enough ($d_{\text{core}} > \frac{c}{f}$) [137]. The following analysis [137] relies on the Bloch theorem, whereby translational symmetry of a wave propagating through a periodic medium implies that the eigenvalue of the transfer matrix has the form $\lambda = e^{\pm ik_z a}$, where k_z is the propagation constant in the direction of periodicity and $a = d_L + d_H$ is the period of the multilayer (see Fig. 4.16). Note that the Bloch theorem applies in the case of 1D translation symmetry such as for planar Bragg reflectors, however it does not apply in the case of circular symmetry such as Bragg fibers. Nevertheless, in the asymptotic limit of Bessel functions the transfer matrix of a Bragg fiber simplifies into a form similar to that of planar multilayers and such an approximation has been shown to be valid even in the case of relatively small diameter Bragg fibers [138]. We therefore approximate the cladding of large diameter Bragg fibers by a simpler *planar* Bragg reflector and note that for smaller diameter Bragg fibers ($d_{\text{core}} \sim \frac{c}{f}$) an analysis similar to the one presented here can be constructed using the asymptotic form of the Bragg fiber transfer matrix.

In a planar Bragg reflector the period is actually a bi-layer of alternating high (n_H) and low (n_L) refractive index layers and a transfer matrix can be constructed to describe the propagation through the bi-layer. It can be shown [137, 139] that a

quadratic equation defines the eigenvalues (λ) of such a transfer matrix,

$$\lambda^2 - \lambda\Gamma_{TE,TM} + 1 = 0, \tag{4.8}$$

$$\Gamma_{TE,TM} = 2\cos(\phi_L)\cos(\phi_H) - (r_{TE,TM} + r_{TE,TM}^{-1})\sin(\phi_L)\sin(\phi_H), \tag{4.9}$$

$$\phi_L = k_z^L d_L, \qquad \phi_H = k_z^H d_H \tag{4.10}$$

$$r_{TE} = \frac{k_z^L}{k_z^H}, \qquad r_{TM} = \frac{\epsilon_H k_z^L}{\epsilon_L k_z^H} \tag{4.11}$$

$$k_z^L = \sqrt{\left(\frac{2\pi f}{c}\right)^2 \epsilon_L - k_x^2},$$

$$k_z^H = \sqrt{\left(\frac{2\pi f}{c}\right)^2 \epsilon_H - k_x^2}, \tag{4.12}$$

$$\epsilon_L = n_L^2, \qquad \epsilon_H = n_H^2, \tag{4.13}$$

$$k_x = n_C \frac{2\pi f}{c}\sin(\theta_i) \tag{4.14}$$

where d_L and d_H are respectively the thicknesses of the low and high index layers, θ_i is the incidence angle upon the reflector, c is the speed of light, f is the frequency, and n_C is the refractive index of the ambient medium outside of the reflector (the core index in the case of a Bragg waveguide). From equation (4.8) and the Bloch theorem, we have

$$\lambda_1 = \frac{\Gamma_{TE,TM}}{2} + \sqrt{\left(\frac{\Gamma_{TE,TM}}{2}\right)^2 - 1}, \tag{4.15}$$

$$\lambda_2 = \frac{\Gamma_{TE,TM}}{2} - \sqrt{\left(\frac{\Gamma_{TE,TM}}{2}\right)^2 - 1}, \tag{4.16}$$

$$\lambda_1 = e^{ik_z a}, \qquad \lambda_2 = e^{-ik_z a} = \frac{1}{\lambda_1}, \tag{4.17}$$

$$\lambda_1 + \lambda_2 = 2\cos(k_z a), \tag{4.18}$$

$$\cos(k_z a) = \frac{\Gamma_{TE,TM}}{2}. \tag{4.19}$$

Equations (4.15), (4.16), and (4.19) completely characterize Bragg reflectors. When k_z is real, the eigenvalues (4.17) are complex exponentials and the fields propagating within the reflector are Bloch waves and are said to be delocalized as there is trans-

mission through the multilayer without change of amplitude. In other words, for such k_z values there is no reflection and the fields are radiated through the multilayer. These radiation bands can be found by plotting $|\cos(k_z a)| < 1$. When k_z is complex, instead of a delocalized state we have fields that are reflected and that decay exponentially within the multilayer at a rate λ^N, where N is the number of periods in the multilayer. These $|\cos(k_z a)| > 1$ regions define bandgaps where there is a reflection at a given frequency and incidence angle; with field decay rate given by λ^{N}.

We begin by considering the design of idealized Bragg reflectors. It is well known that the most efficient reflector is a quarter-wave stack, wherein the constituent layers have an optical thickness of a quarter-wave, i.e. $\phi_L = \phi_H = \pi/2$. In such a case, equations (4.15) and (4.16) reduce to the much simpler $|\lambda_1^{TE,TM}| = r_{TE,TM}$ and $|\lambda_2^{TE,TM}| = r_{TE,TM}^{-1}$ expressions. The solutions of interest require $|\lambda| < 1$. After some algebra we find,

$$\lambda_{TE} = r_{TE} < 1, \quad \theta_i \in [0, \pi/2]. \tag{4.20}$$

And for the TM polarization we find *two* regimes:

$$\frac{\epsilon_L \epsilon_H}{\epsilon_L + \epsilon_H} < \epsilon_C : \quad \lambda_{TM} = \begin{cases} r_{TM}^{-1} & \theta \in [0, \theta_0], \\ r_{TM} & \theta \in [\theta_0, \pi/2], \end{cases} \tag{4.21}$$

$$\frac{\epsilon_L \epsilon_H}{\epsilon_L + \epsilon_H} > \epsilon_C : \quad \lambda_{TM} = r_{TM}^{-1}, \qquad \theta \in [0, \pi/2] \tag{4.22}$$

$$\theta_0 = \arcsin\left(\sqrt{\frac{\epsilon_L \epsilon_H}{\epsilon_C(\epsilon_L + \epsilon_H)}}\right), \tag{4.23}$$

where θ_0 is the incidence angle which gives a Brewster angle *within* the multilayer stack, and $\epsilon_{\mathrm{C}} = n_{\mathrm{C}}^2$.

To get a general sense of the Bragg fiber operating regimes, it is useful to examine the efficiency of an optimal planar quarter-wave stack by plotting the field decay rate $\lambda_{TE,TM}$ as a function of an incidence angle θ_d at which the reflector is designed to operate. In others words we examine the most efficient reflection that can be achieved at a given *design angle* θ_d. From the results in Fig. 4.16, it can be seen that λ_{TE} is always smaller than λ_{TM}, i.e. the field penetration within the multilayer is always higher for the TM polarization. In the first regime ($\frac{\epsilon_L \epsilon_H}{\epsilon_L + \epsilon_H} < \epsilon_C$), the existence of a Brewster angle within the multilayer makes the TM reflection inefficient and $\lambda_{TM} = 1$ at θ_0. Furthermore, in the second regime ($\frac{\epsilon_L \epsilon_H}{\epsilon_L + \epsilon_H} > \epsilon_C$), the constituent

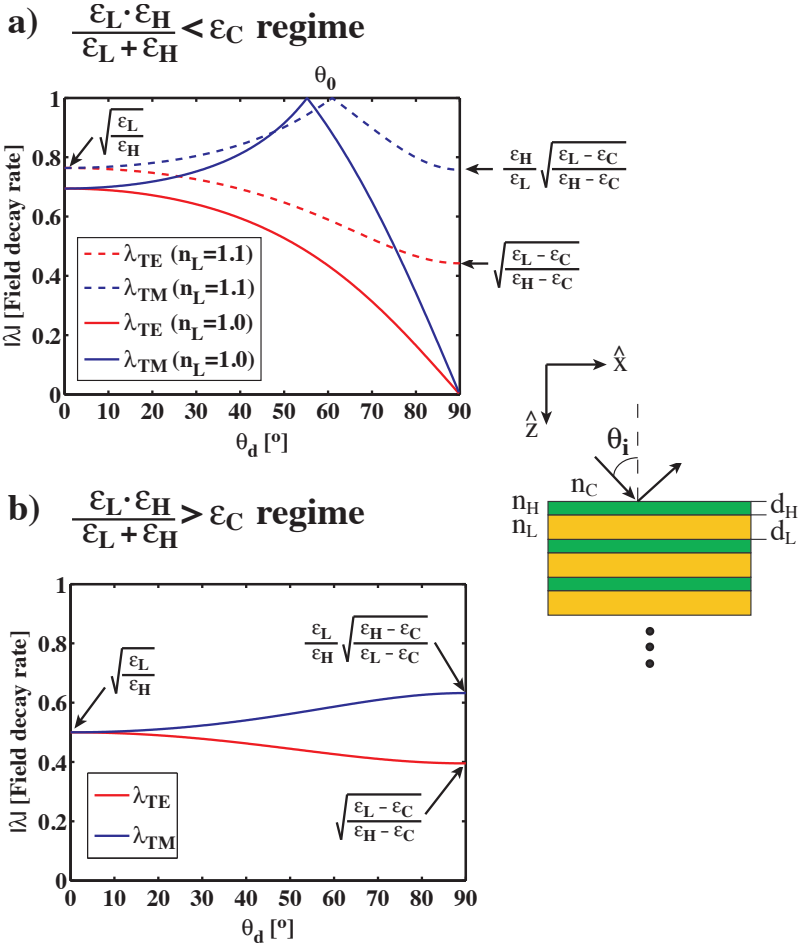

Figure 4.16 TE and TM field decay rates per bilayer for quarter-wave planar Bragg reflectors. For each incidence angle $\theta_d = \theta_i$ we consider a new Bragg reflector that is designed such that the ideal quarter-wave condition is satisfied. Shown are the decay rates in two distinct regimes of operation. a) $\frac{\epsilon_L \epsilon_H}{\epsilon_L + \epsilon_H} < \epsilon_C$, $n_C = 1.0$, $n_H = 1.5$. b) $\frac{\epsilon_L \epsilon_H}{\epsilon_L + \epsilon_H} > \epsilon_C$, $n_C = 1.0$, $n_L = 1.5$, $n_H = 3.0$.

refractive indices are such that the Brewster angle within the multilayer is avoided for all incidence angles and an omnidirectional reflection (at any incidence angle) can be achieved for both TE and TM polarizations simultaneously. Finally, an increase of the refractive index contrast ϵ_L/ϵ_H will reduce the value of $\lambda_{TE,TM}$ in both regimes of operation whereas layer thicknesses different from the quarter-wave stack will increase it.

From the above considerations it is easy to understand that the TE_{01} mode of

a Bragg fiber will always have lower loss than the TM_{01} mode. Since the hybrid mode losses can be considered as a mixture of TE and TM mode losses [74, 140], the losses of the HE modes are dominated by the contribution of the lossier TM polarization. Thus, in order to guide a low loss HE mode, the field decay of the TM polarization (λ_{TM}) must be reduced as much as possible. Whereas a planar Bragg reflector is generally designed to operate near normal incidence, a Bragg fiber is expected to operate at *grazing angles* of incidence. In Fig. 4.16 we see that there can be a substantial difference between the TM and TE field decay rates ($\lambda_{TM}^N \gg \lambda_{TE}^N$), where N is the number of periods in the multilayer reflector. Interestingly, Fig. 4.16.a) illustrates that the $\frac{\epsilon_L \epsilon_H}{\epsilon_L + \epsilon_H} > \epsilon_C$ regime can significantly reduce λ_{TM} at grazing angles of incidence ($\theta_i \to 90°$) if $\epsilon_L \to \epsilon_C$.

In practice the thicknesses of a reflector are fixed and the quarter-wave condition cannot be satisfied for all wavelengths. So we now examine the actual behavior of planar Bragg reflectors as a function of operating frequency and incidence angle, for both operating regimes.

$\frac{\epsilon_L \epsilon_H}{\epsilon_L + \epsilon_H} > \epsilon_C$ regime (doped-polymer Bragg fiber)

A conventional method for examining a Bragg reflector is to plot its band diagram. In Fig. 4.17, the first row presents the band diagrams of doped-polymer Bragg reflectors, calculated using equation (4.19) and $|\cos(k_z a)| < 1$. The first column uses the parameters of the doped-polymer Bragg fiber presented in this paper, and the second column presents a design where the quarter-wave condition is satisfied at $f = 0.49$ THz and $\theta_i = 0$. The red and blue bands are respectively the TE and TM admittance bands of the multilayer, whereas the white regions are the bandgaps where reflection occurs. Only the region above the black light-lines should be considered, as it corresponds to the physically realizable incidence angles for real k_x (recall equation (4.14)). The incidence angle increases from 0° to 90° as k_x goes from 0 to the light-line, as indicated by the incidence angle lines in Fig. 4.17.d). Since the Bragg fiber operates at grazing angles of incidence the frequency bands of interest are the bandgaps along the light-line. Note the excellent agreement between the planar Bragg reflector TE bandgaps along the light-line of Fig. 4.17.a) and the bandgap frequencies of the TE_{01} mode loss minima of the doped-polymer Bragg fiber shown in Fig. 4.14.d). Finally, the gray regions highlight frequency bands of *omnidirectional* reflection, where reflection can be achieved at any angle of incidence.

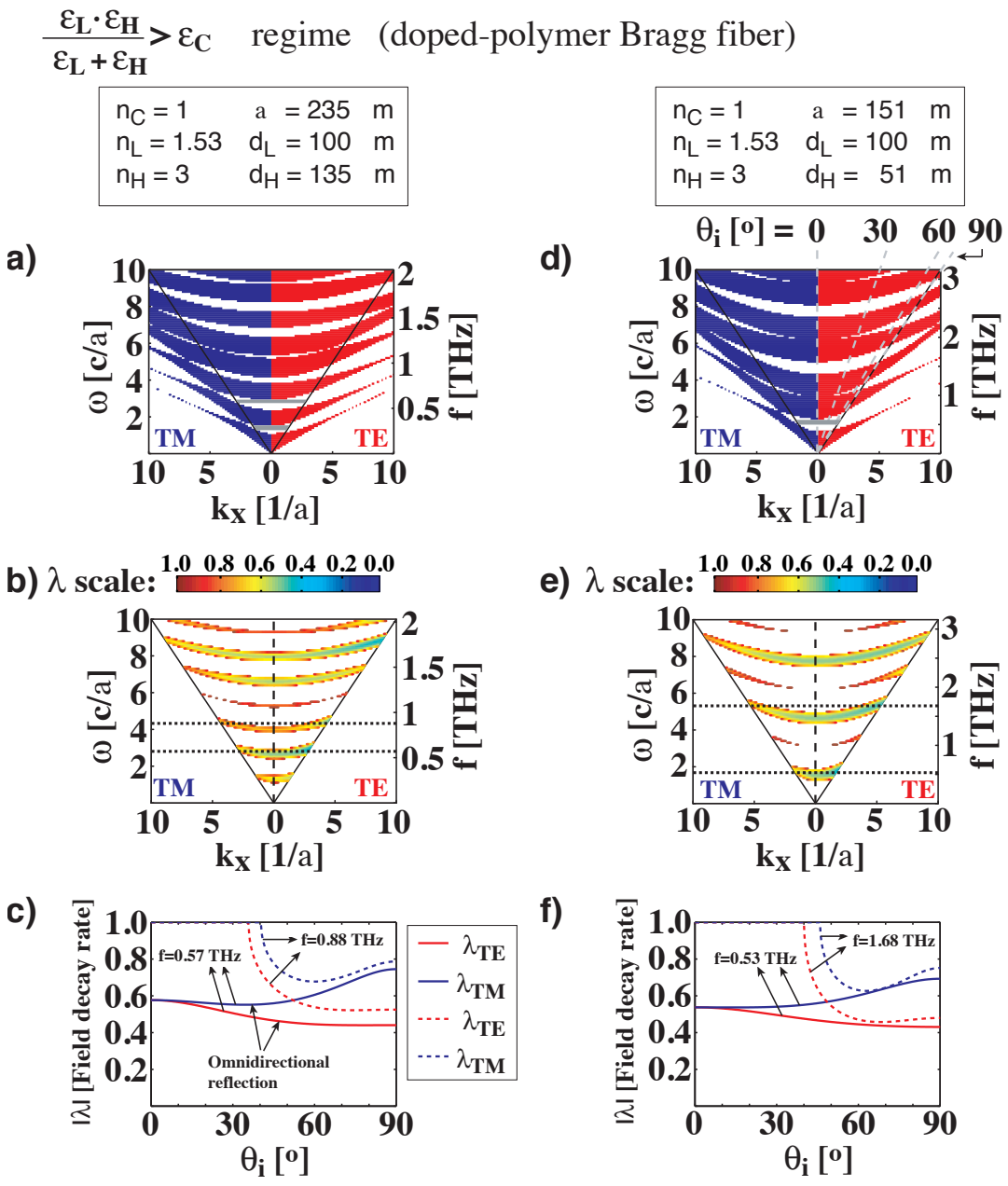

Figure 4.17 Band diagrams and field decay rates of doped-polymer planar Bragg reflectors ($\frac{\epsilon_L \epsilon_H}{\epsilon_L + \epsilon_H} > \epsilon_C$). First column uses parameters of experimental Bragg fiber, second column uses a quarter-wave design at $f = 0.49$ THz and $\theta_i = 0$. First row presents the band diagram of the reflectors. Second row presents λ-diagrams of the field decay rates within the bandgap regions. Third row presents cuts of the λ-diagrams at constant frequencies.

An interesting alternative method for examining Bragg reflectors is to plot the values of $\lambda_{TE,TM}$ within the bandgaps, in order to directly quantify the loss efficiencies of modes guided within those bandgaps. Such λ-diagrams are presented in the second row of Fig. 4.17. Note that the white regions here correspond to the admittance bands of the reflector where $|\lambda| = 1$ because of the complex exponential λ values in those regions. Once again, the left and right portions of the graph correspond to TM and TE polarizations, respectively. It is easy to see that λ_{TE} decreases and λ_{TM} increases with increasing incidence angle (increasing k_x) and that λ_{TE} is smaller than λ_{TM}, because λ_{TE} is more "blue" than λ_{TM}. This can also clearly be seen by taking a cut of the λ-diagram along a fixed frequency, as shown in the third row of Fig. 4.17. Note that for $f = 1.68$ THz in Fig. 4.17.f) the values of $\lambda_{TE,TM}$ increase with decreasing incidence angle until reaching $\lambda = 1$ and cutting off when leaving the bandgap. This is due to the curvature of the bandgaps, where a mode at such a frequency will not be able to remain within the bandgap at all angles of incidence.

$\frac{\epsilon_L \epsilon_H}{\epsilon_L + \epsilon_H} < \epsilon_C$ regime (air-polymer Bragg fiber)

Fig. 4.18 presents the band diagrams and λ-diagrams of air-polymer planar Bragg reflectors operating in the $\frac{\epsilon_L \epsilon_H}{\epsilon_L + \epsilon_H} < \epsilon_C$ regime with $\epsilon_L = \epsilon_C$. The first column shows a calculation using the parameters of the experimental air-polymer Bragg fiber. The second column shows a calculation for a design where the quarter-wave condition is satisfied at $f = 0.50$ THz and $\theta_i = 0$. In the band diagrams the closing of the TM bandgaps at the Brewster angle is seen to occur above the light line. Furthermore, in Figs. 4.18.a) and 4.18.d) the curvature of the bandgaps results in the absence of any omnidirectional reflections bands. There is very little difference between the quarter-wave and non-quarter-wave field decay rates in this case. Comparing Figs. 4.18.c) and 4.17.c) it can be seen that for grazing angles of incidence and for $f \sim 0.95$ THz that $\lambda_{TM} \sim 0.8$ for the doped-polymer reflector and $\lambda_{TM} \sim 0.6$ for the air-polymer Bragg fiber. Such a large difference in the field decay rate per bilayer leads to an order of magnitude difference in loss even with as few as $N = 5$ bilayers. This marked reduction of loss for the TM polarization helps explain why the HE mode losses are lower and more comparable to the TE mode losses in Fig. 4.14.c) than in Fig. 4.14.d).

Finally, in Fig. 4.19 we present the interesting case where $\epsilon_L = \epsilon_C$ and the index contrast is high. In the band diagram it can be seen that the Brewster angle is increased and pushed close to the light line. In this case, the proximity of the

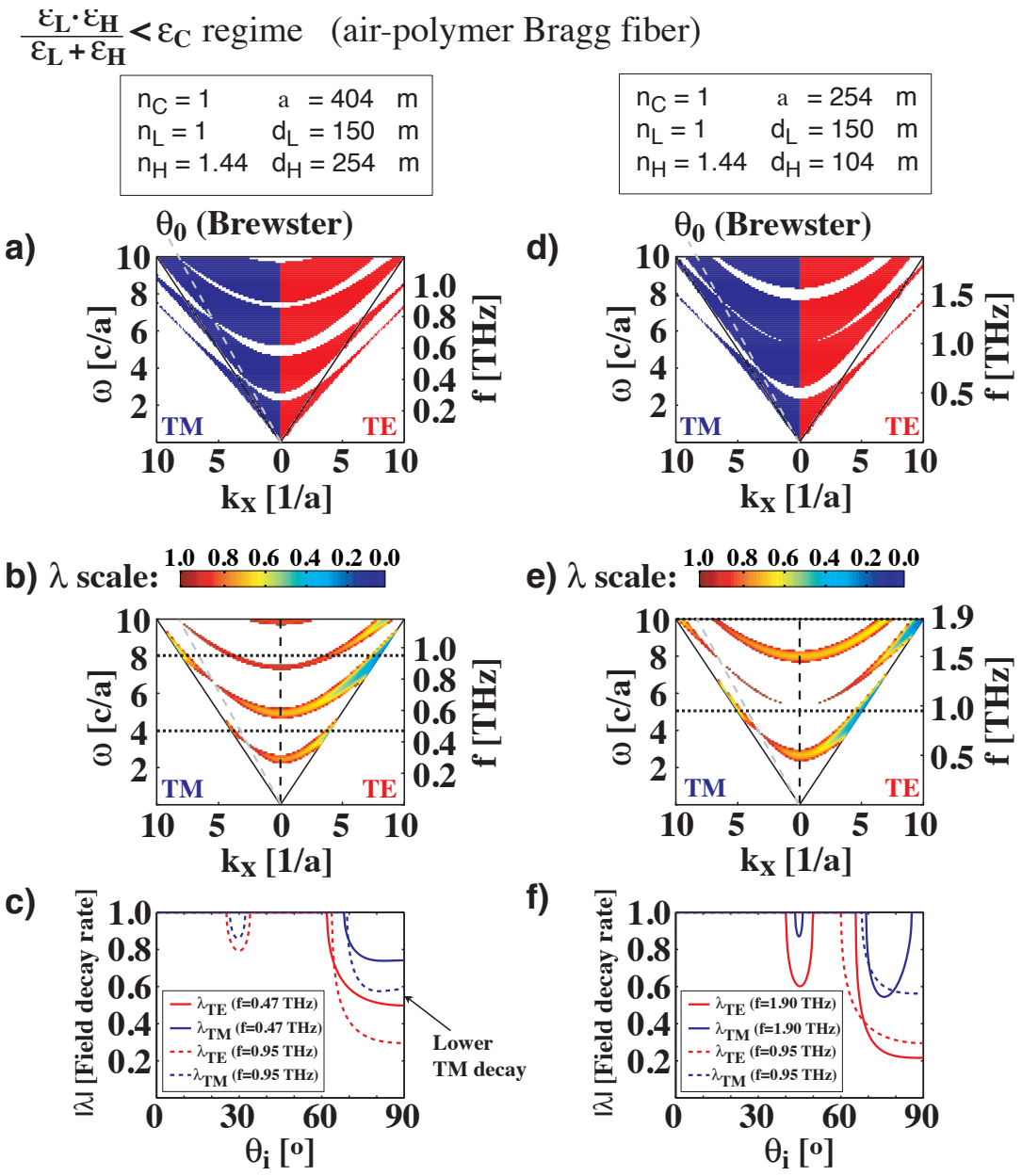

Figure 4.18 Band diagrams and field decay rates of air-polymer planar Bragg reflectors where $\epsilon_L = \epsilon_C$ ($\frac{\epsilon_L \epsilon_H}{\epsilon_L + \epsilon_H} < \epsilon_C$). First column uses parameters of experimental Bragg fiber, second column uses a quarter-wave design at $f = 0.50$ THz and $\theta_i = 0$. First row presents the band diagram of the reflectors. Second row presents λ-diagrams of the field decay rates within the bandgap regions. Third row presents cuts of the λ-diagrams at constant frequencies.

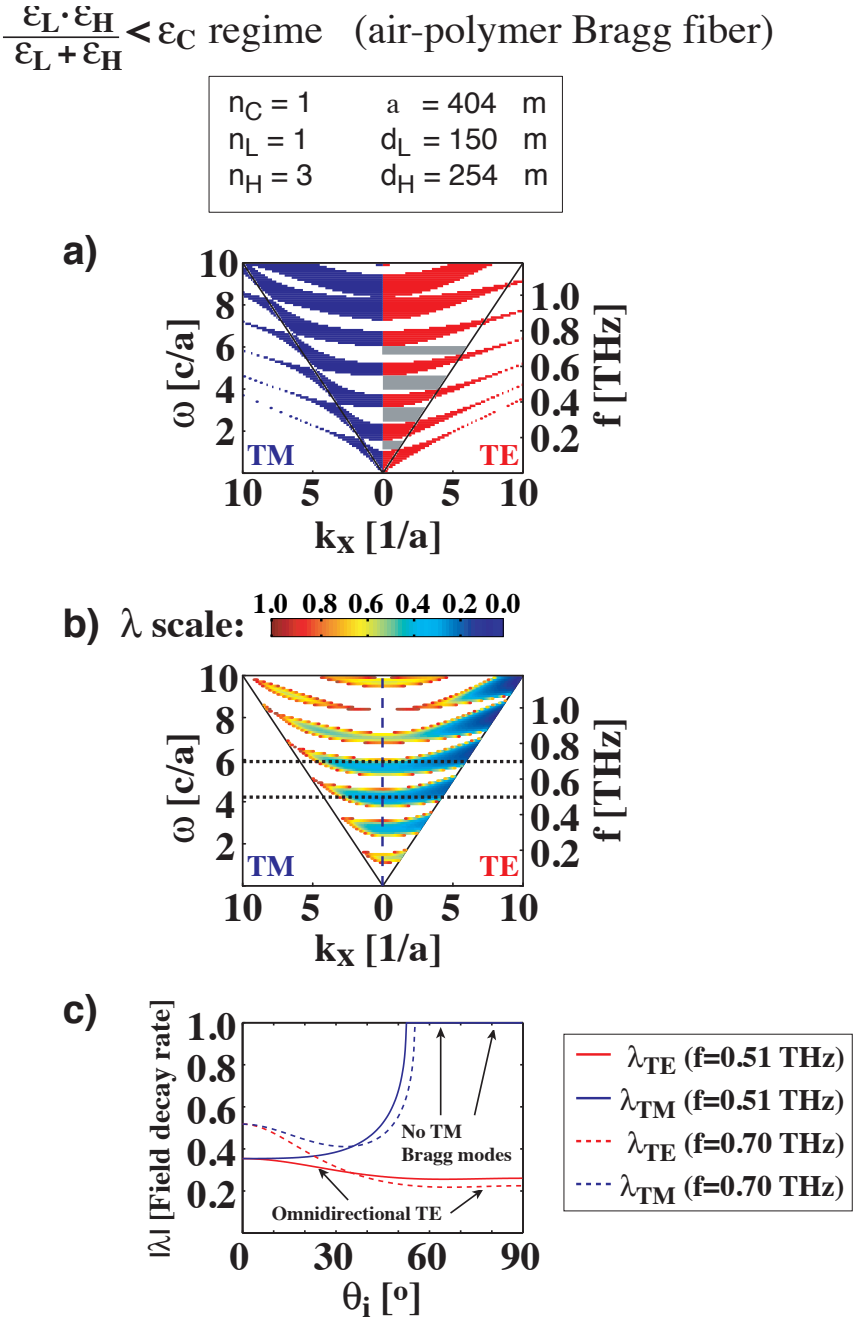

Figure 4.19 Band diagrams and field decay rates of a high-index contrast air-polymer planar Bragg reflector where $\epsilon_L = \epsilon_C$ ($\frac{\epsilon_L \epsilon_H}{\epsilon_L + \epsilon_H} < \epsilon_C$). a) Band diagram of the reflector. b) λ-diagram of the field decay rates within the bandgap regions. c) Cuts of the λ-diagram at constant frequencies.

Brewster angle to the light line *increases* the TM loss substantially at grazing angles of incidence. At low frequencies the TM polarization actually falls within the admittance bands of the multilayer and no guided TM Bragg modes can exist[2]. The TM modes are effectively filtered out by the Brewster angle phenomenon. On the other hand, the TE polarization exhibits very large bandgaps (larger than those of Fig. 4.17.d)) and these are regions of omnidirectional TE reflection, as indicated by the gray regions. Furthermore, the values of λ_{TE} are extremely low and relatively flat as a function of incidence angle (indicating that the bending loss should be low). Such characteristics make this design an interesting candidate for a truly single-mode TE_{01} Bragg fiber. The absence of TM modes would significantly reduce the losses of such a fiber, provided a suitable source is found to excite the azimuthally polarized TE_{01} mode.

4.2.6 Summary of THz Bragg fiber results

In summary, we have fabricated and measured two very different types of Bragg fibers. The first used air for the low index layers whereas the second used a doped polymer compound for the high index layers. The doped-polymer Bragg fiber was shown to operate in a $\frac{\epsilon_L \epsilon_H}{\epsilon_L + \epsilon_H} > \epsilon_C$ regime where the high index contrast leads to omnidirectional reflection. However the HE_{11} losses of this TE_{01} fundamental mode fiber are high due to material absorption and as a result the transmission was low with no clear bandgaps. On the other hand, the air-polymer Bragg fiber was shown to operate in a $\frac{\epsilon_L \epsilon_H}{\epsilon_L + \epsilon_H} < \epsilon_C$ regime. With $\epsilon_L = \epsilon_C$ and a low index contrast, it was shown that the losses of the TM polarization can be lowered such that a low loss HE_{11} mode can occur. Bandgap guidance can be seen in the transmission however coupling needs to be optimized to reduce multimode excitation.

Improvements to the Bragg fibers presented in this chapter include using foam for the low refractive index layers of the air-polymer Bragg fibers in order to increase mechanical stability. Furthermore, the quadratic absorption loss makes TiO_2 a questionable dopant for the doped-polymer Bragg fibers. Crystalline high-resistivity silicon [127] is an interesting alternative with $n_{Si} = 3.418$ and $\alpha_{Si} < 0.05$ cm^{-1} for frequencies ranging from 0 to 2 THz. The crystalline silicon could be ground into micro-particles using standard milling techniques and incorporated as dopant into

[2]No *TM Bragg* reflections exist but a TM mode can be guided by other guidance mechanisms, as will be explained in the next chapter.

PE. It is worth noting that the highest refractive index that could be achieved by a Si compound is lower than that of a TiO_2 compound, however doping with Si would actually *decrease* the absorption loss of the compound yielding an absorption loss lower than that of the pure polymer[3].

4.3 Discussion on hollow-core waveguides

Recent developments in THz waveguides have lead to the demonstration of straight waveguide losses sufficiently low to start being useful ($\alpha \sim 0.01$ cm^{-1}). However, to truly be practical a waveguide should have low bending losses and this factor will ultimately be the discriminant between different waveguiding strategies. An intuitive understanding of the bending losses for the waveguides presented in this chapter can be gained by considering that, from a ray-optic perspective within large core waveguides, bending will result in a decrease of the incidence angle of a ray. The ARR tubes were shown to be efficient at grazing angles of incidence, but considering the strong angle dependence of the single-layer reflectivity it is obvious that the bending losses will be quite high (≥ 0.05 cm^{-1}) at smaller incidence angles. As for the Bragg fibers, it is easy to understand that the multiple reflections within the multilayer will help reduce the angle dependence of the waveguide wall reflectivity. The field decay rates plotted in Figs. 4.17.c) and 4.18.c) offer insights into the bending loss. In Fig. 4.17.c) it is clear from the omnidirectionality of the reflection that the doped-polymer Bragg fiber will guide *some* light no matter what the bending radius. Furthermore, the relative flatness of the curves in the $60 - 90°$ range indicates that the bending loss will not be pronounced. In the case of the air-polymer Bragg fiber (Fig. 4.18.c)), it was shown that lower HE mode loss was achieved by lowering the TM polarization loss, but the tradeoff is foregoing the omnidirectional reflection. Thus, although the field decay rates are relatively flat for incidence angles in the $\theta_{i,\text{straight}} \sim 75 - 90°$ range, the bending losses of air-polymer Bragg fibers are expected to rise sharply once a critical bending radius inducing incidence angles $\theta_{i,\text{bend}} \leq 70°$ (Fig. 4.18.c)) is reached. Although the actual critical incidence angle for high bending losses is polarization and frequency dependent, a rough estimate using $\theta_{i,\text{straight}} = 80°$ and $\theta_{i,\text{bend}} \leq 70°$ in equation (F.3) yields a high bending loss for $R_{\text{bend}} \leq 6$ cm.

It is clear from the transmission results that coupling in multimode waveguides is

[3]The idea of doping with Si is explored more thoroughly in section 5.1.

a critical issue. The experimental coupling conditions were not optimal and resulted in multiple modes being excited at the onset. The presence of multiple modes leads to modal interference in the transmission which is highly sensitive to coupling conditions. This not only makes cutback measurements impractical but is also detrimental to waveguiding applications. It is worth stressing that even in the case where coupling is optimized at the input, such that only one mode is excited, any perturbations to the multimode waveguide (diameter fluctuations, bending, etc.) can couple light into the lossier higher order modes [141]. Therefore it is worth studying the optimization of the design in the limit of a single-mode regime. In this respect, an interesting design was proposed in Fig. 4.19. The $\epsilon_L = \epsilon_C$ and high index contrast design offers a very low loss single TE_{01} mode fiber. Coupling to lossier TM modes from fiber perturbations would be frustrated due to the attenuation of the TM modes by the Brewster phenomenon, and bending losses would be very low due to the omnidirectionality of the TE reflection and the flatness of the incidence angle dependence. Certain important technological challenges remain for the implementation of such a fiber, notably the use of foam instead of powder particles for the low-index layers to increase the mechanical stability of the fiber, and the development of an azimuthally polarized source for efficient coupling to the TE_{01} mode.

Chapter 5

Future prospects for dielectric waveguides

In the last two chapters we have explored two fundamentally different approaches for reducing the absorption loss in dielectric THz waveguides. Many different types of waveguides were studied but each has its own shortcomings, whether it be fabrication difficulties, the small transmission bandwidths for which propagation loss is sufficiently low, or prohibitively high bending losses ($\alpha_{\text{bent guide}} \gg \alpha_{\text{straight guide}}$).

Many ideas remain to be tested to address these issues, but certain theoretical considerations can already provide some insight. In this chapter, we discuss a wide range of topics for the future prospects of THz waveguides. The first section discusses better doping materials to improve THz Bragg fibers. The second section evaluates Bragg fiber bending losses. The third section proposes methods to increase coupling to the lower loss TE_{01} mode of Bragg fibers and debates whether single-mode Bragg fibers are feasible. The fourth section discusses Attenuated Total Internal Reflection (ATIR) waveguides and gives clues suggesting that PVDF copolymers are the ideal material for this type of waveguide. Finally, in the last section we theoretically investigate the design of a Total Internal Reflection (TIR) foam fiber. This waveguide offers the possibility of a truly flexible, low propagation loss, low bending loss fiber that would also solve the water vapor exposure problem by completely encapsulating the THz radiation.

5.1 Polymer doping

In chapter 4 we saw an example of a polymer composite where a high index dopant was mixed into a polymer host to create a high refractive index composite material. However, the use of TiO_2 powder was a poor choice. Although a considerable increase in the refractive index was achieved, the absorption loss was also increased to

prohibitively high levels ($\alpha_{\text{composite}} > 10$ cm^{-1} for $f > 1$ THz). Moreover, the high volume fractions of powder that were required substantially modified the thermo-mechanical properties of the polymer and made processing difficult. A more suitable high index dopant needs to be found.

In a similar respect, the use of foam was proposed as a low-index material. For instance, foam could replace the powder spacers in the air/polymer Bragg fiber of chapter 4, thereby increasing the mechanical stability of that fiber. It should be noted that foam can be treated as a composite material where a polymer is doped with air inclusions. The effective material parameters of a foam remains an open question that needs to be investigated.

We thus seek to explore different doping schemes and to determine the effective material parameters that can be expected. From a theoretical standpoint, the material properties of composite materials can be estimated using effective medium approximations. Among the multiple models that exist we shall consider the following [142]:

Bruggeman (Cube Root):
$$\frac{\epsilon_d - \epsilon_c}{\epsilon_d - \epsilon_h} = (1 - f_V) \cdot \sqrt[3]{\frac{\epsilon_c}{\epsilon_h}} \tag{5.1}$$

Bruggeman (Standard):
$$(1 - f_V) \cdot \frac{\epsilon_h - \epsilon_c}{\epsilon_h + 2\epsilon_c} + (f_V) \cdot \frac{\epsilon_d - \epsilon_c}{\epsilon_d + 2\epsilon_c} = 0 \tag{5.2}$$

Maxwell-Garnett:
$$\frac{\epsilon_c - \epsilon_h}{\epsilon_c + 2\epsilon_h} = (f_V) \cdot \frac{\epsilon_d - \epsilon_h}{\epsilon_d + 2\epsilon_h} \tag{5.3}$$

Eyraud :
$$\epsilon_c = (1 - f_V) \cdot \frac{f_V \epsilon_h A^2 + (1 - f_V)\epsilon_d}{[1 + f_V(A - 1)]^2} + (f_V) \cdot \frac{f_V \epsilon_h + (1 - f_V)\epsilon_d B^2}{[f_V + (1 - f_V)B]^2}, \tag{5.4}$$
$$A = \frac{3\epsilon_d}{\epsilon_h + 2\epsilon_d}, \quad B = \frac{3\epsilon_h}{\epsilon_d + 2\epsilon_h}.$$

Linear :
$$\sqrt{\epsilon_c} = (f_V) \cdot \sqrt{\epsilon_d} + (1 - f_V) \cdot \sqrt{\epsilon_h} \tag{5.5}$$

where ϵ_d, ϵ_h, and ϵ_c are the permittivities of the dopant, the host, and the composite, respectively. The amount of dopant incorporated into the host is given by the volume fraction f_V.

Note that the name Bruggeman appears twice. In the literature, the Bruggeman model is generally considered to be equation (5.2) [143, 144, 145], however sometimes equation (5.1) is referred to as the Bruggeman model [146]. In his book [142], Eyraud attributes equation (5.1) to Bruggeman and equation (5.2) to Landauer. To avoid confusion, in this thesis we shall refer to equation (5.2) as the Bruggeman model and

equation (5.1) as the Cube Root formula.

The different effective medium models have different underlying assumptions the most common being the assumption of spherical inclusions within the host material. It should be noted that Maxwell-Garnett is one of the most popular models but that it is only considered valid for small volume fractions. It should also be noted that the Linear model is linear in refractive index not in permittivity. Furthermore, equation (5.2) is the only model to correctly predict a percolation threshold for metal inclusions within a dielectric host. Indeed, at a certain threshold volume fraction the metal inclusions that fill the space begin to touch each other and the composite material quickly transitions from a dielectric to a metallic behavior. Finally, we remark that the little known Eyraud model is an attempt to generalize the effective medium approximation to high volume fractions. It considers small inclusions of material 1 within material 2 when f_V is small, and small inclusions of material 2 within material 1 when f_V is large. Despite its formidable appearance, the Eyraud model is a simple model based on the additivity of electrostatic energy [142].

Although effective medium approximations are generally only applied to the refractive index we also calculate the effective absorption loss. The material parameters are related to the real and imaginary permittivities as follows,

$$\tilde{\epsilon} = \epsilon_{\mathrm{Re}} - i\epsilon_{\mathrm{Im}} \tag{5.6}$$

$$\epsilon_{\mathrm{Re}} = n^2 - \kappa^2 \tag{5.7}$$

$$\epsilon_{\mathrm{Im}} = 2n\kappa \tag{5.8}$$

$$\alpha = 2\left(\frac{2\pi f}{c}\right)\kappa, \tag{5.9}$$

where for simplicity we assume $f = 1$ THz. We then calculate the real (n) and imaginary (κ) parts of the the composite refractive index separately. We begin by substituting the complex permittivities $\tilde{\epsilon}$ in equations (5.1)-(5.5). We then set $\kappa = 0$ to calculate n_c and $n = 0$ to calculate κ_c. From κ_c we calculate α_c.

5.1.1 Porosity (doping with air)

We begin by exploring the effective material properties of a polymer foam. As host material we consider a generic material that has the following refractive index and absorption loss: $n_{\mathrm{host}} = 1.5$, $\alpha_{\mathrm{host}} = 0.2$ cm^{-1}. Poly(ethylene) would be such a

candidate. As dopant we consider dry air with $n_{\text{dopant}} = 1.0$ and $\alpha_{\text{dopant}} = 0.0$ cm^{-1}.

Using equations (5.1)-(5.5) we calculate the effective refractive index and effective absorption loss at $f = 1$ THz for a host polymer doped with air bubbles, predicting what could be obtained with a PE foam. Fig. 5.1 presents the results for different concentrations of air bubbles (here Porosity $\equiv f_V$). Figs. 5.1.c) and 5.1.d) zoom in on the region of interest where the porosity is high.

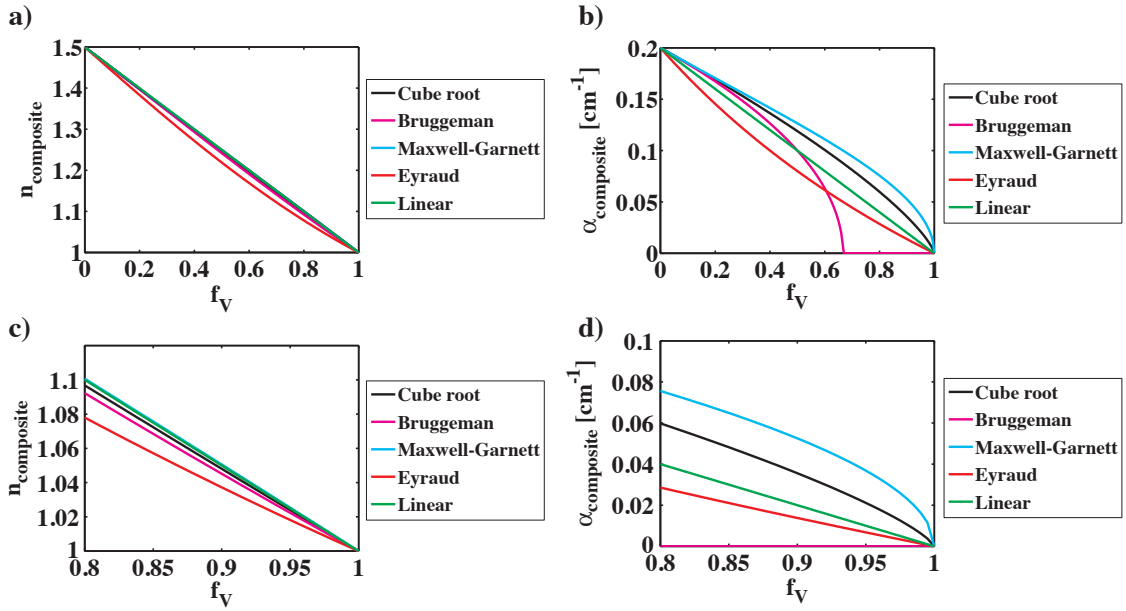

Figure 5.1 Comparison of the effective medium approximations of for the THz material properties of a polymer foam. f_V is the volume fraction of air within a material having $n_{\text{host}} = 1.5$, $\alpha_{\text{host}} = 0.2$ cm^{-1}. Calculations are done at $f = 1$ THz.

In terms of refractive index all the models predict very similar behavior with the refractive index decreasing from the pure polymer index to that of air almost linearly. In terms of absorption loss the differences between the models are more pronounced. We note that the Bruggeman model incorrectly predicts a percolation threshold when the air bubbles fill more than two thirds of the space. Among the other models it is unclear which prediction is more accurate, yet the Maxwell-Garnett curve can be considered as an upper limit and the Eyraud curve can be considered as a lower limit. It can be seen that, for sufficiently high porosities, the bulk absorption loss can be reduced by a factor of ten or more.

To get a sense of what can be achieved in terms of porosity let us consider a

typical poly(styrene) (PS) foam. The material properties of PS foam have already been studied using THz-TDS [147]. From the reported effective refractive index of the foam, $n_{\text{PS foam}} \approx 1.02$, and the THz refractive index reported for bulk PS [148], $n_{\text{PS}} = 1.59$, we can estimate the porosity of the foam. Assuming the linear model for the effective medium approximation we have,

$$f_V = \frac{n_c - n_h}{n_d - n_h} = \frac{1.02 - 1.59}{1.0 - 1.59} \approx 0.966 \tag{5.10}$$

Thus styrofoams with a porosity of 96% are routinely obtained.

In terms of absorption loss the comparison is more difficult. Zhao *et al.* did not present a direct comparison to the bulk loss of pure PS. From the reported spectra it can only be stated that $\alpha_{\text{PS foam}} \leq 0.5$ cm^{-1} when $f < 2$ THz [147]. A value of $\alpha_{\text{PS foam}} \leq 0.2$ cm^{-1} can be estimated at $f = 0.75$ THz. This can be compared to the bulk loss of pure PS reported to be $\alpha_{\text{PS}} = 1.75$ cm^{-1} at $f = 0.75$ THz [148]. So we are indeed close to a factor of ten reduction of absorption loss in the foam. Finally, it was also reported that the choice of foaming agent was important since the use of a chloro-fluoro-carbon gas (HCFC 142b) added additional peaks to the absorption spectrum of the foam whereas the use of CO_2 gas did not [147].

In section 4.2.5, a new design was proposed for a more efficient air-polymer Bragg fiber. We now investigate the design in more detail. We shall consider two geometries. The first is a high index contrast air-polymer fiber with $n_H = 3.0$ and $n_L = 1.0$. The initial aim of this design was to lower the TM field decay rate, but the calculations of section 4.2.5 actually predicted frequency regions where no TM reflections should exist. This results from the multilayer Brewster angle (equation (4.23)) nearing grazing incidence angles when $\epsilon_L = \epsilon_C$. With foam for the low index layer we can actually take this design one step further. As a second geometry we consider $n_H = 3.0$ and $n_L = 1.0606$, such that the Brewster angle tends towards a 90° grazing incidence angle. Fig. 5.2 presents the band diagrams and λ-diagrams of this grazing Brewster angle design. The closing points of the TM bandgaps occur at the Brewster angle and they are seen to lie on the light-line (incidence angle of 90°). As a result we expect a maximum attenuation of the TM modes in a Bragg fiber using such a Bragg reflector. The Brewster angle filtering of the TM modes of a Bragg fiber was first proposed by Bassett *et al.*, but here we shall consider the full frequency propagation loss spectrum instead of a single frequency [149]. For the low index foam of our foam-polymer Bragg

fiber we assume that the dopant is air and that the host material is identical to the high index layers, i.e. $n_{\text{host}} = 3.0$, $\alpha_{\text{host}} = 1.0$ cm^{-1}. The Cube Root formula is used, as it gives values contained within the limits of the other effective medium models, and a foam porosity of 96.875% yields the desired $n_L = 1.0606$. For simplicity all material parameters are assumed to be frequency independent.

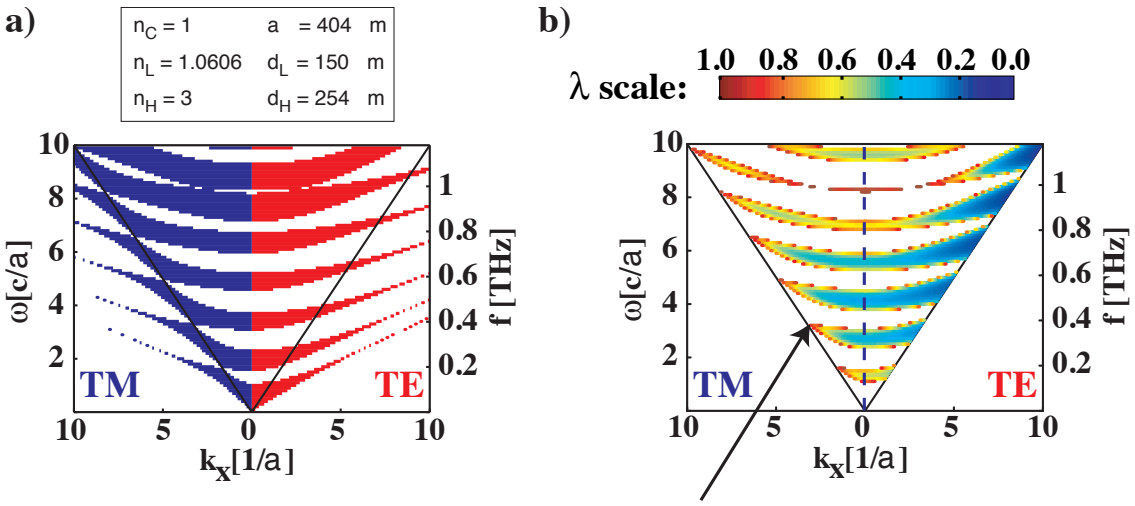

Figure 5.2 Band diagrams and field decay rates of a *high-index contrast* foam-polymer planar Bragg reflector where $\frac{\epsilon_L \epsilon_H}{\epsilon_L + \epsilon_H} < \epsilon_c$ and ϵ_L is chosen such that the Brewster angle falls on the light-line. a) Band diagram of the reflector. b) λ-diagram of the field decay rates within the bandgap regions.

Contrary to the planar Bragg reflector simulations discussed above, Fig. 5.3 presents the exact transfer matrix simulations of Bragg fibers using the above-mentionned Bragg reflector designs. Both fibers have an inner diameter of 6.73 mm and a reflector of 5 bilayers consisting of 254 μm high-index layers and 150 μm low-index layers. In others words, we use the same geometry as the air-polymer Bragg fiber that was fabricated experimentally, but we investigate the transmission properties that would result from increasing the index of the high-index layers and replacing the air layers with foam.

Fig. 5.3.a) presents the propagation losses of the TE_{01}, HE_{11}, TM_{01}, and TE_{02} modes of the *high index contrast* air-polymer Bragg fiber. Comparing to Fig. 4.14.a), we see that the new design has more transmission peaks (because of the higher n_H value) and that at low frequencies there is more than one order of magnitude dif-

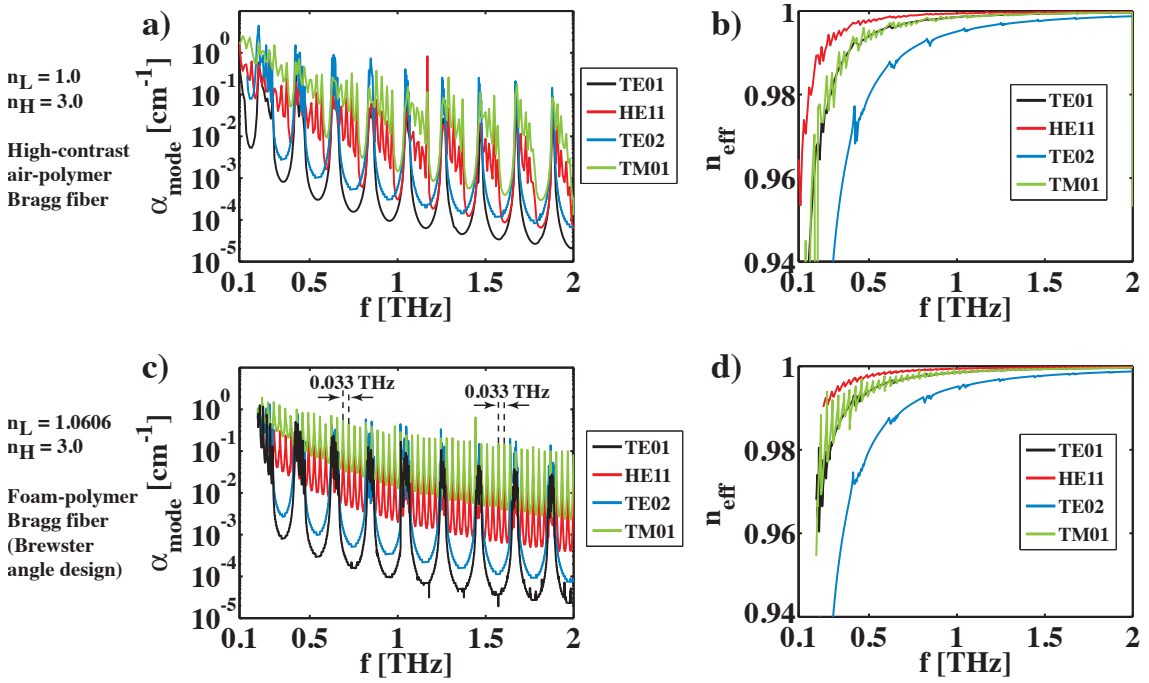

Figure 5.3 Theoretical modeling of the propagation losses of high index contrast air-polymer and foam-polymer Bragg fibers. The indices and layer thicknesses are given on the left-hand side. Both fibers have $n_H = 3$, but we compare air layers ($n_L = 1.0$ in the first row) to foam layers ($n_L = 1.0606$ in the second row) because the later design brings the Bragg reflector Brewster angle onto the light-line. Simulations using the transfer matrix method also assumed $d_{\text{core}} = 6730$ μm and 5 bilayers. a),c) Power propagation loss, b),d) Modal refractive index. There is an excellent agreement with the predictions of planar Bragg reflector simulations.

ference between the loss of the TE_{01} and HE_{11} modes. Comparing Fig. 5.3.a) to Fig. 4.19.b), we see that there is a good correspondence between the planar Bragg reflector prediction and the actual Bragg fiber transmission. The bandgaps of the TE_{01} mode are much wider and yield lower losses than those of the TM_{01} mode. Moreover, due to the curvature of the bands and the proximity of the Brewster angle to the light-line, the TM_{01} bandgaps are narrower and the minima occur at higher frequencies than those of the TE_{01} mode. Note that the HE_{11} mode is not severely attenuated compared to the TE modes. Instead, the higher index contrast has merely narrowed the HE_{11} bandgap windows compared to the experimental low-index contrast air-polymer Bragg fiber. We expect a higher attenuation when the Brewster angle is pushed onto the light line.

Fig. 5.3.c) presents the propagation losses of the grazing Brewster angle foam-polymer Bragg fiber. The loss curves present an interesting and unexpected result. From the planar reflector simulations we had predicted *no TM modes*, and yet a TM_{01} is still clearly present. Upon closer examination we see that there are indeed no TM Bragg reflections, since there are no bandgaps for the TM modes. However, there is still a TM_{01} mode because the Bragg fiber guides by *anti-resonant reflection* in that case. Indeed, at the Brewster angle the TM polarization is completely transmitted through the Bragg reflector and reflections only occur at first and last interfaces, i.e. the core/cladding and cladding/ambient-medium interfaces. Thus for the TM polarization the Bragg fiber cladding acts as a Fabry-Perot resonator with the periodic frequency response of an ARR tube. The formula for the frequency period (Δf) of anti-resonant reflection can be adapted to the case of a TM polarized ray propagating through a multilayer Bragg stack (see Appendix E),

$$\Delta f = \frac{c}{N_{\text{bilayer}} \cdot 2 \cdot (d_{\text{H}} \cdot n_{\text{H}} \cdot \cos\theta_{\text{H}} + d_{\text{L}} \cdot n_{\text{L}} \cdot \cos\theta_{\text{L}})}, \tag{5.11}$$

$$\theta_{\text{H}} = \text{asin}\left(\frac{n_{\text{air}} \sin\theta_1}{n_{\text{H}}}\right), \tag{5.12}$$

$$\theta_{\text{L}} = \text{asin}\left(\frac{n_{\text{air}} \sin\theta_1}{n_{\text{L}}}\right). \tag{5.13}$$

where d_{H} and d_{L} are the thicknesses of the high and low index layers, n_{H} and n_{L} are the refractive indices of the high and low index layers, c is the speed of light, and θ_1 is the incidence angle. A high and low refractive index layer form a bi-layer. N_{bilayer} is the number of bi-layers repeating in multilayer Bragg reflector. Substituting $n_{\text{H}} = 3.0$, $n_{\text{L}} = 1.0606$, $d_{\text{H}} = 254$ μm, $d_{\text{L}} = 150$ μm, $\theta_1 = 85°$, and $N_{\text{bilayer}} = 6$ into equation (5.11) yields $\Delta f = 0.034$ THz, which is in pretty good agreement with the value 0.033 THz measured in Fig. 5.3.c). Interestingly, the guidance mechanism of the HE_{11} mode is also anti-resonant reflection and the loss of the HE_{11} mode is seen to be more than one order of magnitude higher than that of the TE_{01} mode *at all frequencies*. These fiber designs will be further discussed in the next sections when we consider bending losses and mode filtering.

5.1.2 Doping with Si

In Fig. 4.10 it was seen that doping with TiO_2 particles gave unsatisfactorily high absorption losses. One alternative, proposed in section 4.2.6, is doping with ground high-resistivity crystalline silicon particles. We now investigate this option by calculating the effective material parameters. For the polymer host we assume $n_{\text{host}} = 1.5$ and $\alpha_{\text{host}} = 0.2$ cm^{-1}. For the material parameters of the dopant we assume frequency independent values of $n_{\text{Si}} = 3.418$ and $\alpha_{\text{Si}} = 0.05$ cm^{-1} [127]. This is a reasonable approximation because $\alpha_{\text{Si}} \leq 0.05$ cm^{-1} for $f \leq 2$ THz.

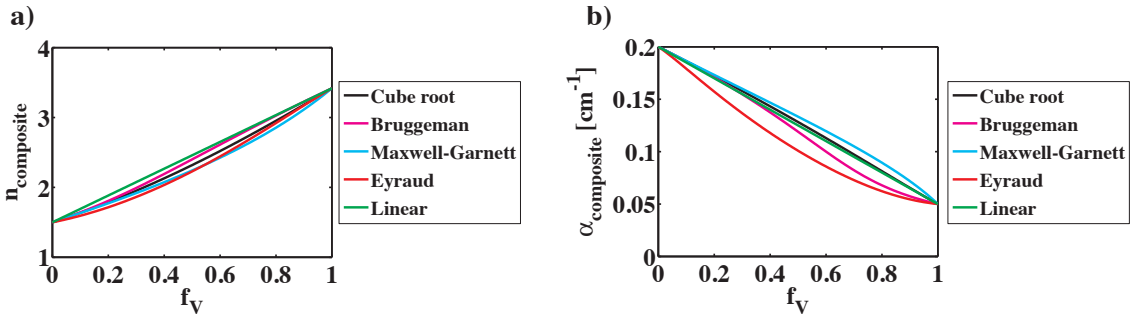

Figure 5.4 Comparison of the effective medium approximations of for the THz material properties of a Si/polymer composite. f_V is the volume fraction of Si particles ($n_{Si} = 3.418$, $\alpha_{Si} = 0.05$ cm^{-1}) within a material having $n_{\text{host}} = 1.5$, $\alpha_{\text{host}} = 0.2$ cm^{-1}. Calculations are done at $f = 1$ THz.

The different effective medium approximations are compared in Fig. 5.4. In this case, the refractive index is seen to increase while the absorption loss actually *decreases* with higher doping concentrations. From the literature on composite materials, volume fractions on the order of $f_V = 0.5 \sim 0.6$ can be considered as an experimental upper limit on the doping concentration [117]. This is due to the fact that when doping concentrations increase it becomes increasingly difficult to mix the dopant homogeneously and to prevent the agglomeration of particles. Although the absorption is seen to decrease in Si/polymer composites, the increase in refractive index is limited. At $f_V = 0.5$, the Si/polymer composite exhibits a mere $n_{\text{Si/polymer}} \sim 2.4$. This is not sufficiently high to be useful, especially considering that it is probably the maximum value that could be achieved experimentally.

5.1.3 Doping with metal

Ideally we could dope with a very high refractive index material such that a small volume fraction of dopant would be sufficient to yield an appreciable increase in the composite material refractive index. An interesting possibility is using a metal. Metals have very high refractive indices, but they also have very high material absorption. For instance, copper has $n_{\mathrm{Cu}} \sim 620$, $\kappa_{\mathrm{Cu}} \sim 990$, and $\alpha_{\mathrm{Cu}} \sim 6.4 \times 10^5$ cm^{-1} at $f = 1$ THz [150]. Nonetheless, it is well known that the refractive index of metal-dielectric composites increases rapidly as the volume fraction of metal particles approaches the percolation limit and this has been exploited to tailor material dielectric constants at microwave frequencies [151]. As metal particles are added to a dielectric host, the particles form clusters and these clusters grow in size as the volume fraction increases. At the percolation threshold ($f_V \sim 1/3$), the clusters begin to connect and there is an exponential increase in the conductivity. Thus the composite material transitions from a dielectric to a metallic behavior. The interesting regime is just before the percolation threshold where there is a rapid increase in refractive index but the composite material is still in a dielectric regime.

To study the potential of metal-insulator composites we consider the example of Cu particles doping a polymer. Once again we use a host polymer having $n_{\mathrm{host}} = 1.5$, $\alpha_{\mathrm{host}} = 0.2$ cm^{-1}. For the Cu particles we use the THz material parameters of Cu given by the Drude model [150]. Fig. 5.5 presents material parameters calculated at $f = 1$ THz with the different effective medium models. Note that in this case the Bruggeman model is the only model to correctly predict the percolation threshold that occurs around $f_V \sim 1/3$. Thus it is the only model that could be considered valid over the entire range of volume fractions. Moreover, the metallic behavior can clearly be seen above the percolation threshold as both the refractive index and the absorption loss increase considerably.

Figs. 5.5.c) and 5.5.d) present the interesting region that is on the cusp of the percolation threshold. If the Bruggeman model can be trusted, we see that a volume fraction as low as 25% gives $n_{\mathrm{eff}} \sim 3$, whereas $n_{\mathrm{eff}} \to 5$ as the volume fraction approaches 30%. The important point is that below the percolation threshold the absorption loss is expected to remain low and we can easily achieve $\alpha_{\mathrm{eff}} \leq 0.5$ cm^{-1}.

Such values are very promising for the high index material of a Bragg fiber. Moreover, the lower volume fractions should help the composite material to retain the thermo-mechanical properties of the pure polymer host. One can easily imagine a

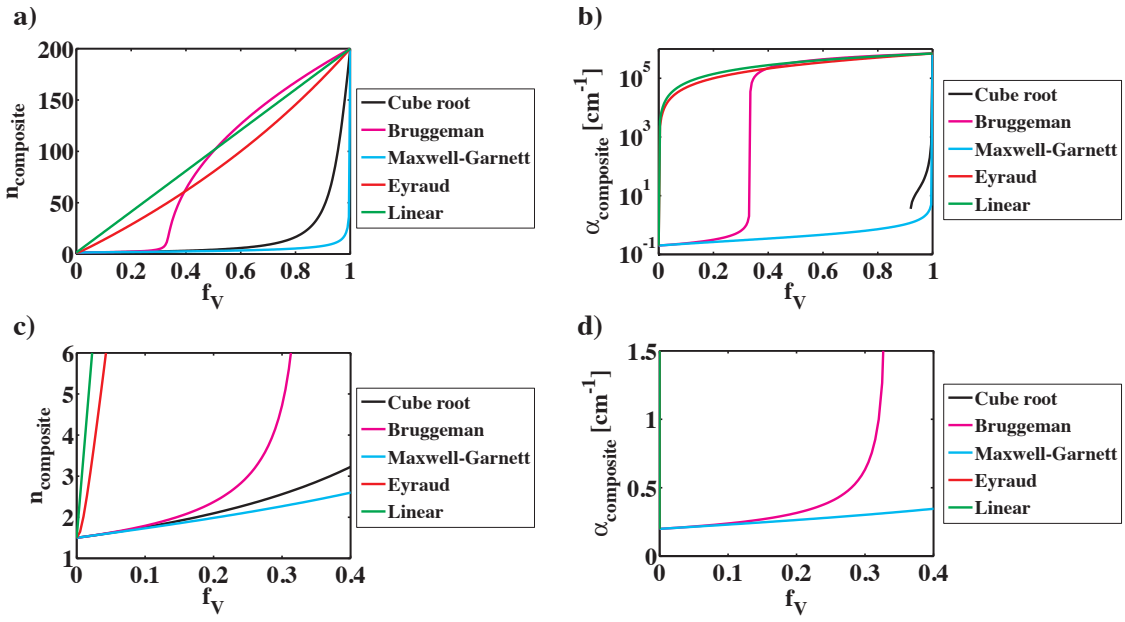

Figure 5.5 Comparison of the effective medium approximations of for the THz material properties of a Cu/polymer composite. f_V is the volume fraction of Cu particles within a material having $n_{\text{host}} = 1.5$, $\alpha_{\text{host}} = 0.2$ cm^{-1}. The THz material parameters of Cu are given by the Drude model [150]. Calculations are done at $f = 1$ THz.

Bragg fiber consisting of low-index pure PE and high-index Cu/PE layers. We therefore calculate the modal parameters of such a Bragg fiber using the transfer matrix method. For the simulations we consider a composite material with $f_V = 0.25$. We also consider a hollow-core diameter of 6630 μm, as well as 6 bilayers consisting of 100 μm low-index PE layers and 64 μm high-index Cu/PE layers. A thickness of 64 μm was chosen in order to have a normal-incidence quarter-wave thickness at $f = 0.5$ THz. The material parameters of the pure PE layers are assumed to be the frequency independent values of the host polymer given above. However, the material parameters of the composite are calculated at each frequency because the Drude model fit of the Cu parameters is highly frequency dependent [150].

Fig. 5.6.a) presents the propagation losses of the TE_{01}, HE_{11}, and TM_{01} modes. Comparing to Fig. 4.14.d), we see that the lower loss of the high-index layers does not inhibit the Bragg reflections like the TiO_2 doping did. Even at high frequencies the bandgaps of the HE_{11} mode remain clear. Furthermore, the propagation losses of the modes are very low. In fact the TE_{01} mode losses of this fiber are the lowest among

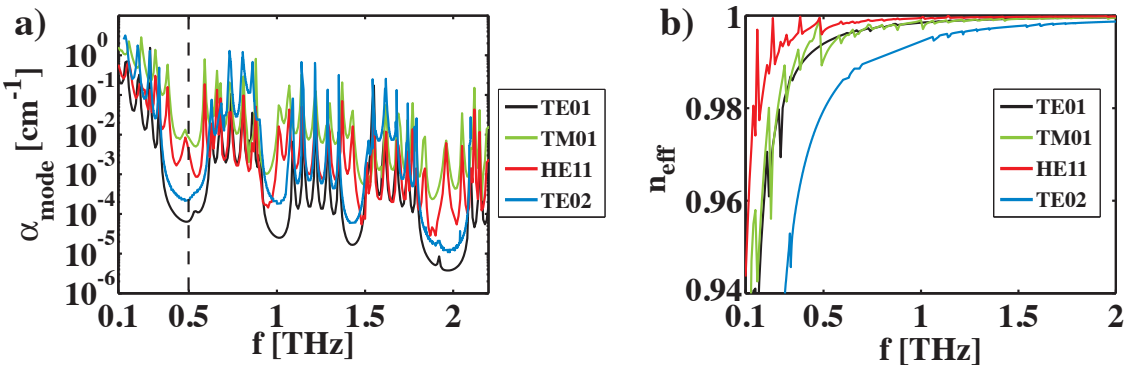

Figure 5.6 Theoretical modeling of the propagation losses of a Cu/polymer Bragg fiber with 64 μm high-index Cu/PE composite layers and 100 μm low-index pure PE layers. Simulations using the transfer matrix method also assumed $d_{\text{core}} = 6630$ μm and 6 bilayers. a) Power propagation loss, b) Modal refractive index.

all the Bragg fibers presented in this thesis and are on the order of 10^{-4} cm^{-1} within the bandgaps. Recall from Fig. 4.17 that for such large refractive index contrasts an omnidirectional reflection was predicted for both TE and TM modes in the first low-frequency bandgap.

5.2 Bragg fiber bending loss

In the previous section, we explored better designs for reducing the propagation loss in Bragg fibers. Once low propagation losses are achieved, the next challenge becomes lowering bending losses to acceptable levels. This raises fundamental questions, such as: "How high is the bending loss?" and "How does the bending loss affect fiber transmission?" In order to answer these questions, we consider a simple calculation based on a Ray-Optic method, which is outlined in appendix F. From *a priori* knowledge of the effective modal propagation indices[1], the Ray-Optic method can accurately calculate the magnitude of the straight fiber propagation loss of a hollow-core fiber. It stands to reason that the extension of the ray-optic method should give an accurate estimate of the propagation losses in a bent fiber.

We now consider the bending loss of Bragg fibers in both of the operating regimes defined in chapter 4. The losses of straight and bent fibers are presented side-by-

[1] n_{eff} of each mode is taken from the transfer matrix simulations.

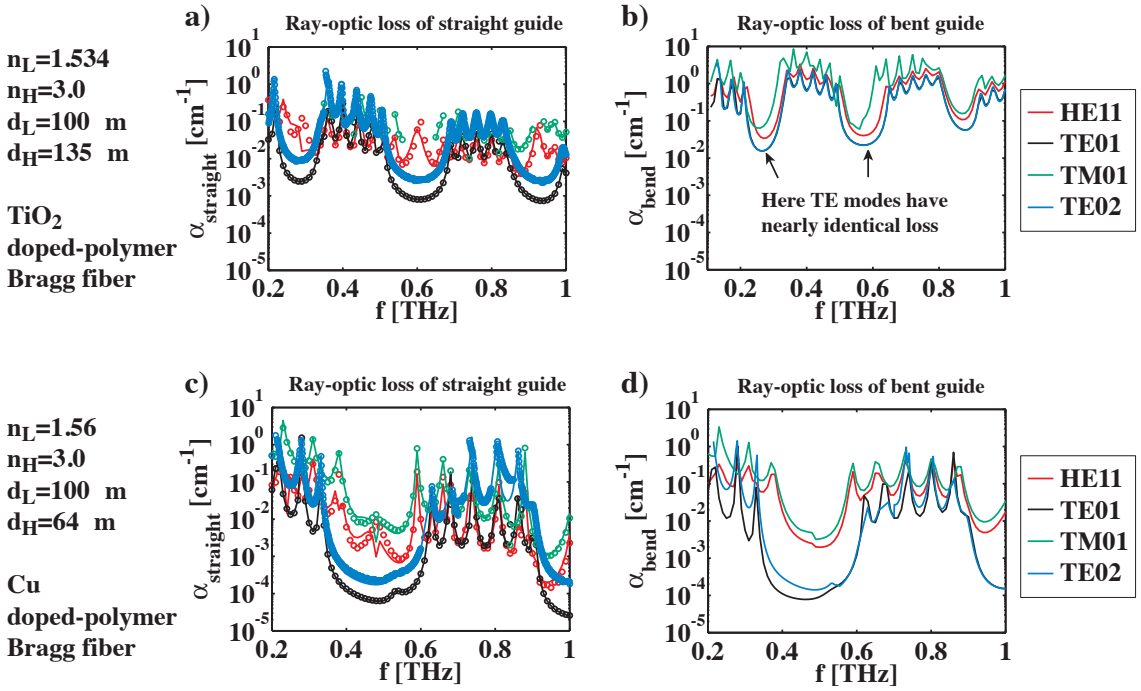

Figure 5.7 Ray-optic estimation of the straight and bent fiber propagation losses of doped-polymer Bragg fibers ($\frac{\epsilon_L \epsilon_H}{\epsilon_L+\epsilon_H} > \epsilon_c$ regime). First row: TiO_2-doped Bragg fiber. Second row: Cu/PE doped Bragg fiber. First column: Straight fiber propagation losses. Second column: Bent fiber propagation losses. Ray-optic calculations (solid lines) are compared to the exact transfer matrix calculations (open circles). Note that we consider $R_{\text{bend}} = 20$ cm.

side for a direct comparison of the effect of bending. A bending radius of 20 cm is considered in all cases. Fig. 5.7 presents the ray-optic calculations for the $\frac{\epsilon_L \epsilon_H}{\epsilon_L+\epsilon_H} > \epsilon_c$ regime (doped-polymer Bragg fibers). The first row presents the results of the TiO_2-doped Bragg fiber, whereas the second row presents the results of the Cu/PE Bragg fiber. To validate the calculations, the values of the straight fiber propagation losses calculated with the ray-optic method (solid lines) are compared to the exact values calculated with the transfer matrix method (open circles). The results are nearly identical and some of the small differences are actually attributable to errors in the determination of n_{mode} not α_{straight}.

In the first row of Fig. 5.7 it is seen that the TiO_2-doped Bragg fiber experiences high propagation loss and that all the modes have a similarly high bending loss. More interestingly, the Cu/PE Bragg fiber shown in the second row appears insensitive to

bending despite a reduction of the incidence angle of the modal ray (not shown). This is a testimony to the flatness of the TE and TM reflectivities and field decay rates with respect to incidence angle. Note that while the TE modes have different straight fiber propagation losses, they have nearly identical bending losses. This is due to an effect illustrated in appendix F. Bending homogenizes the incidence angles of the different modes (see Fig. F.2.d)) and therefore the bending losses for modes of the same family are similar. In other words, TE modes all have rays experiencing identical TE reflections and differences in bending losses result from differences in path length, however similar incidence angles will yield similar bending losses. In Fig. 5.7.d), larger differences between the bending losses of TE modes at low frequencies arise due to the transition to a non-whispering-gallery-mode regime (see appendix F).

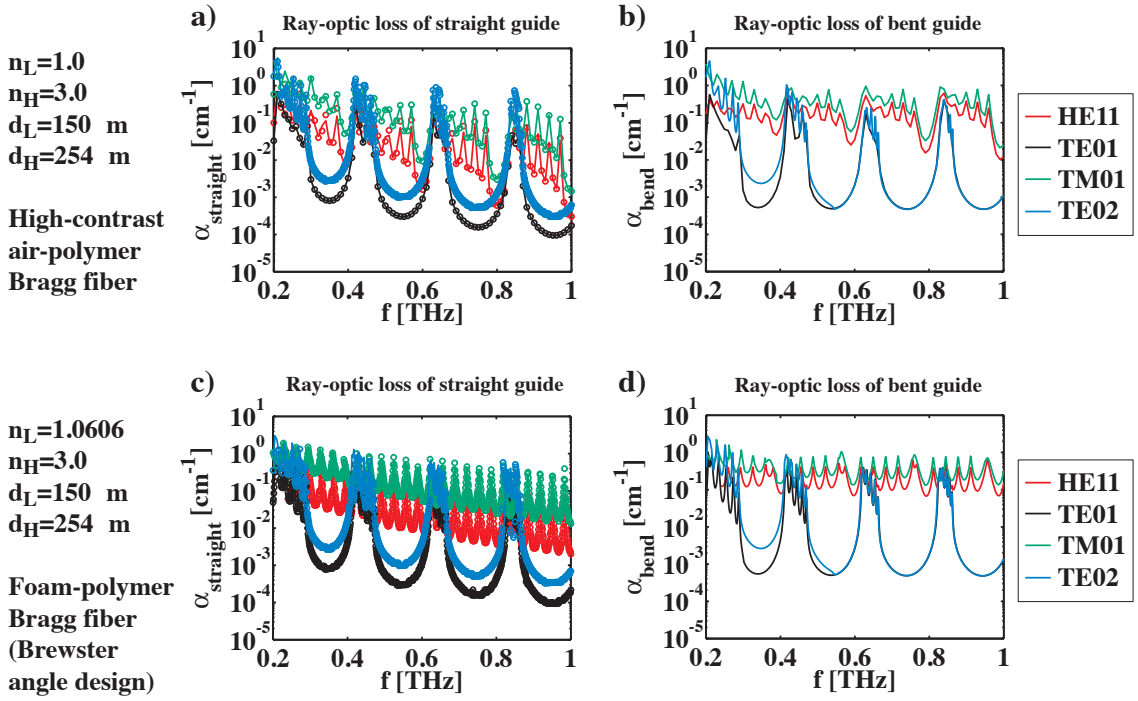

Figure 5.8 Ray-optic estimation of the straight and bent fiber propagation losses of doped-polymer Bragg fibers ($\frac{\epsilon_L \epsilon_H}{\epsilon_L+\epsilon_H} < \epsilon_c$ regime). First row: high index contrast air-polymer Bragg fiber. Second row: high-index contrast foam-polymer Bragg fiber. First column: Straight fiber propagation losses. Second column: Bent fiber propagation losses. Ray-optic calculations (solid lines) are compared to the exact transfer matrix calculations (open circles).

Fig. 5.8 presents the ray-optic calculations for the $\frac{\epsilon_L \epsilon_H}{\epsilon_L+\epsilon_H} < \epsilon_c$ regime (air-polymer

and foam-polymer Bragg fibers). The first row presents the results of the high index contrast air-polymer Bragg fiber, whereas the second row presents the results of the high index contrast foam Bragg fiber with a grazing Brewster angle design. In this second operating regime the bending losses of the TE modes are seen to be much lower than those of the TM modes. For the air-polymer Bragg fiber, the TM and HE mode bandgaps in both the straight and bent fibers are seen to offer narrow bands of lowered loss. However, in the case of the foam-polymer fiber the anti-resonant reflection waveguiding mechanism is seen to yield orders of magnitude higher loss for the TM and HE modes. This is due to the strong incidence angle dependence of the Fabry-Perot anti-resonant reflection, as can be seen in appendix F. An important note is that contrary to the $1/f^2$ scaling of the ARR straight fiber loss minima, the bending induces high losses with minima that remain at a constant level at all frequencies.

We shall later see that bending could be used as a mode filtering technique to eliminate the TM and HE modes. However, a more thorough study in terms of bending radius would be required to more justly evaluate the filtering possibilities. It would also be interesting to compare the ray-optic method to more accurate bending loss calculations using either finite-difference time-domain (FDTD) or coupled-mode methods.

5.3 Single-mode Bragg fiber

One of the major problems that was faced in chapter 4 was the coupling difficulties arising from the highly multimode regime of large core waveguides. A single-mode regime would greatly facilitate input and output coupling, as well as prevent modal interference. In this section, we examine the feasibility of a single-mode THz Bragg fiber.

5.3.1 Single-mode regime versus absorption

The obvious method to achieve a single-mode regime is to reduce the core diameter until only one mode is supported. Of course, a reduction in core size implies an increase in the propagation loss. From a ray-optic perspective, the cladding reflections occur more often and, from a modal perspective, the mode fields penetrate farther into the lossy cladding. To understand the extent of the absorption increase we examine

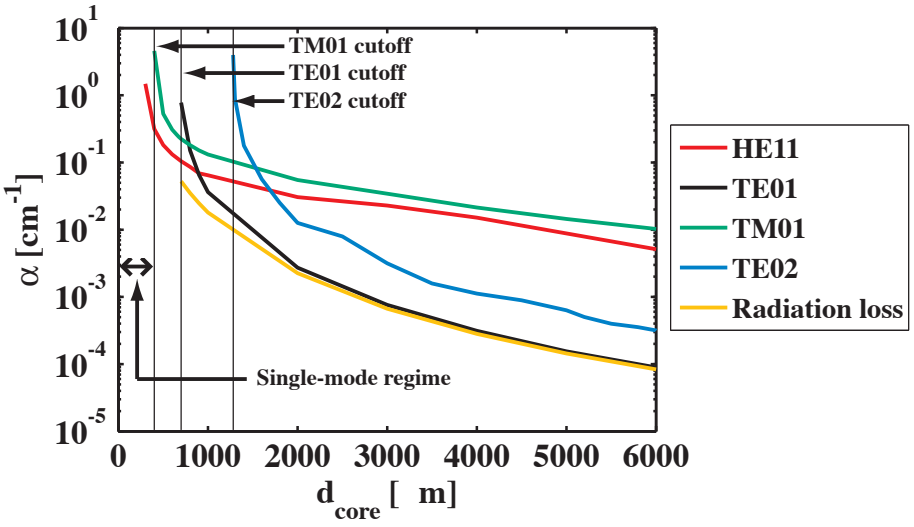

Figure 5.9 Variation of modal propagation loss as a function of THz Bragg fiber core diameter. The Cu/PE Bragg fiber presented in Fig. 5.6 is considered at the frequency $f = 0.5$ THz. Vertical black lines indicate the approximate cutoff points of the TE_{01}, TM_{01}, and TE_{02} modes. Radiation loss dominates at large core sizes and high absorption loss dominates in the single-HE_{11}-mode regime.

the case of the Cu/PE Bragg fiber that was presented in Fig. 5.6. More specifically we shall consider the TE_{01}, HE_{11}, TM_{01}, and TE_{02} modes at $f = 0.5$ THz (indicated by the dashed line in Fig. 5.6). Fig. 5.9 plots the increase in modal propagation loss as the core diameter decreases.

The radiation loss of Bragg fibers is expected to scale according to $\frac{C}{(d_{\text{core}})^3}$, where C is a constant at a given frequency [24]. From the TE_{01} propagation loss presented in Fig. 5.9 it can be seen that radiation loss is the dominant loss mechanism when the core diameter is large. However, as the core diameter decreases the absorption loss is seen to significantly increase the total propagation loss. The vertical black lines approximately indicate the cutoff diameters[2] of the TE_{01} and TM_{01} modes. An interesting fact is that TE_{01} was the lowest loss mode at large core sizes, but as the core diameter approaches the TE_{01} cutoff diameter it is the HE_{11} mode that becomes the lowest loss mode. At a sufficiently low diameter the TM_{01} mode reaches its cutoff point as well and the fiber enters a single-HE_{11}-mode regime. A similar design was

[2]These values are estimated by finding the diameter where the minimum of the corresponding mode ceases to be present in the Transfer Matrix Method optimization function.

proposed by Xu *et al.* for a single-HE_{11}-mode Bragg fiber at telecom wavelengths ($\lambda = 1.55$ μm) [152]. However, such an approach is impractical at THz frequencies because the propagation loss increases to prohibitively high levels ($\alpha_{\text{mode}} > 0.3$ cm^{-1} in the single-mode regime). In other words, the modal propagation loss approaches the bulk absorption loss of the Bragg fiber materials. A foam/polymer Bragg fiber could reduce the cladding absorption but small core Bragg fibers also become increasingly difficult to fabricate. Therefore, Fig. 5.9 demonstrates that a *truly* single-mode THz Bragg fiber is not realistically feasible.

5.3.2 Effectively single-TE_{01}-mode fiber

Another interesting possibility is an *effectively* single-mode regime. The idea is to exploit differences in the losses of different modes to carry out mode filtering such that all modes except one are eliminated. In this regime, the waveguide effectively guides only a single mode. Although optimization of coupling can maximize the amount of power coupled into the lowest loss mode, this maximum is generally not 100% efficiency and some residual power will be coupled into higher order modes due to the multi-mode nature of the waveguide. All the modes of a Bragg fiber are lossy and higher order modes generally have higher propagation losses in either straight or bent waveguides. Therefore, by propagating over a sufficiently long distance these unwanted modes can be eliminated whilst retaining the lowest loss mode. Although we sacrifice some power in the mode filtering process, the effectively single-mode regime is advantageous because it eliminates the undesirable multi-mode interference effects that were discussed in chapter 4.

To evaluate the effectively single-mode regimes (ESMR) of the Bragg fibers presented in this thesis we shall rely on the definition given by Basset *et al.* [149]. Let us consider $L_{20\text{ dB}}$ as the attenuation length over which the modal power is attenuated by 20 dB, i.e. when 1% of the power remains. Let us consider $L_{40\text{ dB}}$ as the attenuation length over which the modal power is attenuated by 40 dB, i.e. when 0.01% of the power remains. By definition we have,

$$L_{20\text{ dB}}\ [\text{cm}] = \frac{20\text{ dB}}{(10\log_{10}(\exp(1))) \cdot \alpha_{\text{mode}}\ [\text{cm}^{-1}]} \tag{5.14}$$

$$L_{40\text{ dB}}\ [\text{cm}] = 2 \cdot L_{20\text{ dB}} \tag{5.15}$$

where the factor $(10\log_{10}(\exp(1)))$ converts the propagation losses to dB/cm. The effectively single-mode regime is defined by a fiber that is longer than $L_{40\text{ dB}}$ of the second lowest loss mode but shorter than $L_{20\text{ dB}}$ of the lowest loss mode,

$$(L_{20\text{ dB}})_{\text{lowest loss mode}} \geq (L_{\text{fiber}})_{\text{ESMR}} \geq (L_{40\text{ dB}})_{\text{second lowest loss mode}}. \tag{5.16}$$

Thus there exists a range of fiber lengths for which the second lowest loss mode is completely attenuated (along with all higher loss modes) whereas the lowest loss mode is not. Note that we shall compare the attenuation of all the modes irrespective of their polarization profiles (HE_{11} is linearly polarized whereas TE_{01} is azimuthally polarized) because fiber perturbations such as macro-bending, micro-bending, scattering, etc. can couple power from one mode to another even if their polarizations are different [141].

The attenuation lengths and ESMRs of the doped-polymer Bragg fibers are presented in Fig. 5.10. Consider for example the TiO_2 doped-polymer Bragg fiber in the first row of Fig. 5.10. An effectively single-mode regime (between the gold line and the solid black curve) is seen to occur in the first bandgap ($f \sim 0.3$ THz) for fiber lengths longer than 10 m, imposed by the dashed blue $L_{40\text{ dB}}$ curve of the TE_{02} mode, and shorter than the limit imposed by the solid black $L_{20\text{ dB}}$ curve of the TE_{01} mode. Thus an 10.5 m fiber would be an effectively single-TE_{01}-mode fiber at $f = 0.3$ THz. Bending in this case does not yield a useful differentiation of the mode losses.

Consider now the Cu/polymer Bragg fiber in the second row of Fig. 5.10. Whereas the TE_{01} mode loss was shown to be extremely low in the Cu/polymer Bragg fiber, the TE_{02} mode *also* has a very low loss. As a result, an ESMR does exist (Fig. 5.10.c)) but a fiber length of more than 100 m is required, which is much longer than current THz waveguides. Therefore it is not sufficient to have a low loss for the lowest loss mode; the loss of the second lowest loss mode must be as high as possible to reduce the fiber length needed for modal filtering. More importantly, we see from Fig. 5.10 that the small contrast between the losses of the TE_{01} and TE_{02} modes leads to very narrow bandwidth frequency regions and very limited fiber lengths for the existence of ESMRs. A much higher loss contrast would be preferable to reduce the constraints on transmission bandwidth and fiber length.

If we now consider the TM and HE modes, we can see in Fig. 5.10.d) that the generally higher bending losses of the TM and HE modes can significantly reduce

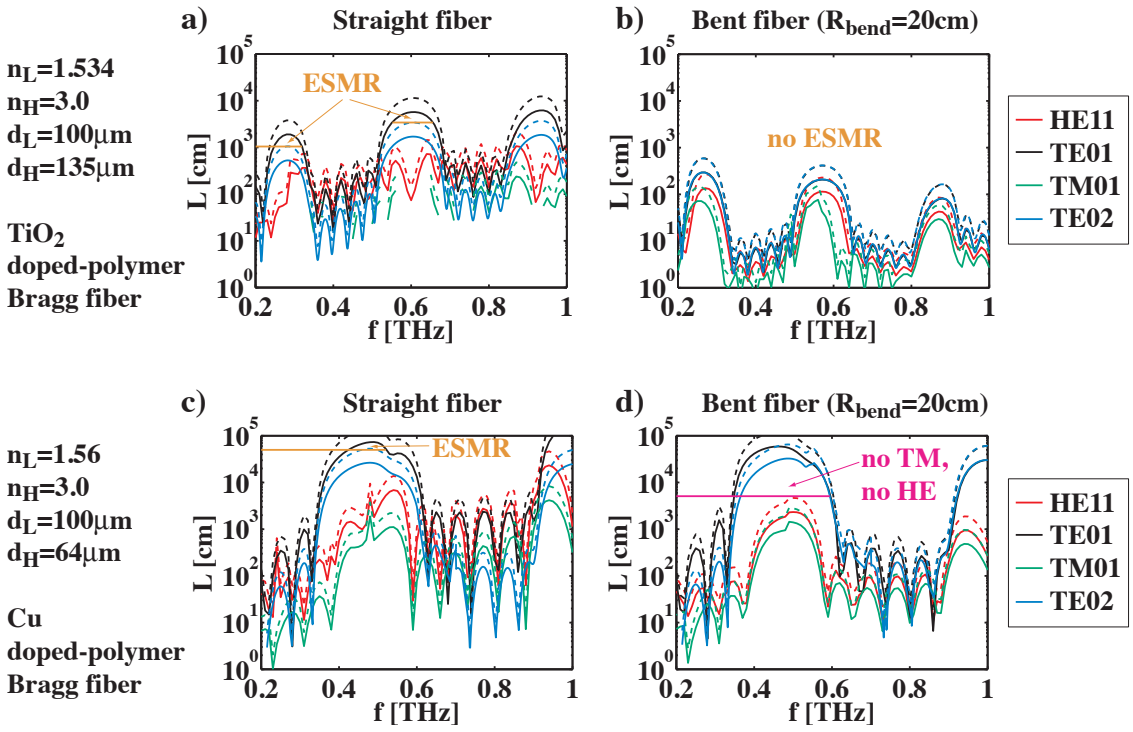

Figure 5.10 Effectively single-mode regimes (ESMRs) of doped-polymer THz Bragg fibers. The fiber length L is plotted as a function of frequency. $L_{20\ \mathrm{dB}}$ and $L_{40\ \mathrm{dB}}$ attenuation lengths of each mode are represented by solid and dashed curves, respectively. First row: TiO_2-doped Bragg fiber. Second row: Cu/PE doped Bragg fiber. First column: Straight fiber absorption lengths. Second column: Bent fiber absorption lengths. Data are taken from Fig. 5.7. ESMRs exist for fiber lengths between gold and black lines. Pink line indicates a minimum fiber length required for the elimination of TM and HE modes.

the length of fiber required to filter out the TM and HE modes. The pink line in Fig. 5.10 represents a minimum fiber length for the complete elimination of TM and HE modes. For instance, a 50 m fiber is seen to completely eliminate the TM and HE modes in Fig. 5.10.d). We also note that the generally lower loss of the HE modes means that the pink line is limited by the red dashed curve of the HE_{11} loss. Ideally, this pink HE mode elimination limit would occur at the lowest fiber length possible.

Before discussing the design of an effectively single TE_{01} mode fiber, let us consider the results for the other THz Bragg fiber designs that were previously studied. Fig. 5.11 presents the attenuation lengths and ESMRs of the air-polymer and foam-

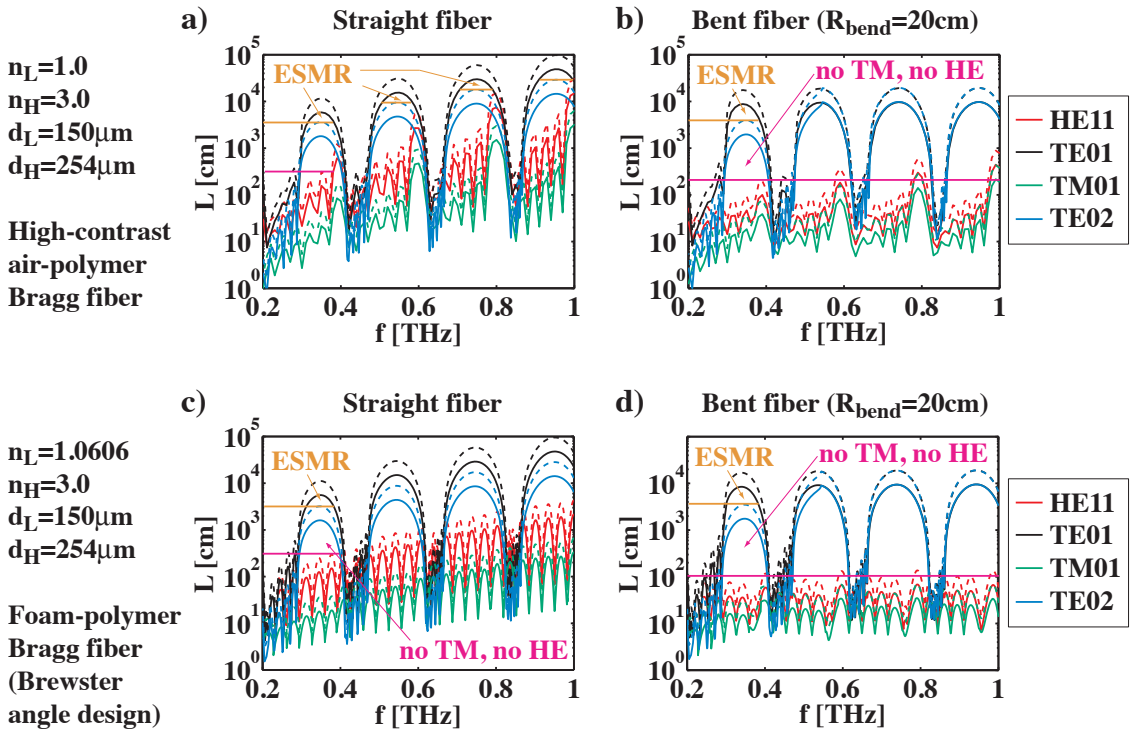

Figure 5.11 Effectively single-mode regimes (ESMRs) of high-index contrast air-polymer and foam-polymer THz Bragg fibers. The fiber length L is plotted as a function of frequency. $L_{20\ \mathrm{dB}}$ and $L_{40\ \mathrm{dB}}$ attenuation lengths of each mode are represented by solid and dashed curves, respectively. First row: air-polymer Bragg fiber. Second row: foam-polymer Bragg fiber. First column: Straight fiber absorption lengths. Second column: Bent fiber absorption lengths. Data are taken from Fig. 5.8. ESMRs exist for fiber lengths between gold and black lines. Pink line indicates a minimum fiber length required for the elimination of TM and HE modes.

polymer Bragg fibers. Effectively single-mode regimes are seen to exist, but once again the presence of the TE_{02} mode is seen to be detrimental. The ESMRs occur at shorter fiber lengths (∼30 m straight fiber length at $f = 0.3$ THz) than for doped-polymer Bragg fibers, however the bandwidths are still limited to frequency bands narrower than the fiber bandgaps. Moreover, Fig. 5.11.a) illustrates another problem in addition to the limited bandwidth of the ESMRs. One important problem with differential loss filtering is that ESMRs of high frequency bandgaps occur at longer straight fiber lengths than ESMRs of low frequency bandgaps. Consequently, the lower frequency bandgaps will incur greater loss if a fiber length is chosen such that

a higher frequency bandgap yields an ESMR. Consider for example the first bandgap ($f \sim 0.3$ THz) of Fig. 5.11.a), which will cease to be transmitted when the third bandgap ($f \sim 0.75$ THz) enters the ESMR because a fiber length of 200 m is longer than the TE_{01} $L_{40\ \mathrm{dB}}$ curve at $f = 0.3$ THz. The point is that not all bandgaps can be in an effectively single-mode regime at the same time if we rely solely on straight fiber propagation loss filtering. Propagation loss in a bent fiber appears to eliminate the $1/f^2$ scaling behavior of the radiation loss, thereby permitting multiple bandgaps to reach an ESMR simultaneously.

In section 4.2.5 we saw that the Brewster angle phenomenon could be used to increase the loss of the TM and HE modes. Bassett *et al.* were the first to propose using this mechanism and predicted that the length of fiber required to achieve an ESMR would correspondingly be reduced [149]. Both the air-polymer Bragg fiber and the foam-polymer Bragg fiber have a Brewster angle close to grazing incidence angles and, indeed, the results of Fig. 5.11 indicate that the fiber length required for the elimination of TM and HE modes has been substantially reduced when compared to the doped-polymer Bragg fibers. In Fig. 5.11.d) the high bending losses are seen to eliminate the TM and HE modes at all frequencies with a fiber length of 1 m. The main difference between the foam-polymer Brewster design and the air-polymer design is that the increased TM and HE losses eliminates the small HE mode peaks on the high frequency side of the bandgaps. For instance, the peak at $f = 0.8$ THz in the air-polymer Bragg fiber is no longer as pronounced in the foam-polymer Bragg fiber. This slightly reduces the pink HE mode elimination limit.

However, in order to truly reap the benefits of the Brewster angle design we need to eliminate the higher order TE modes. These modes are present in all the Bragg fiber designs considered so far because the core diameters (∼6 mm) are much larger than the cutoff diameter of the TE_{02} mode (see Fig. 5.9). The only way to increase the loss of the higher order TE modes is to reduce the core diameter until we approach the cutoff point of the TE_{02} mode[3]. The downside however is that the loss of the TE_{01} mode will increase too. For instance at $d_{\mathrm{core}} = 1200$ μm the TE_{02} mode ceases to be guided but the TE_{01} loss has increased to 0.02 cm^{-1}, which is at the limit of practicality. Therefore, to design a fiber with an effectively single TE_{01} mode regime, more simulations at lower core diameters are required in order to find the optimum diameter to balance the effects of eliminating TE_{02} without incurring too high a TE_{01}

[3]Bassett *et al.* did not emphasize this critical point in their paper [149].

loss ($d_{\text{core}} = 1800$ μm in Fig. 5.9 appears to be a good candidate). Note that reducing the core size will also substantially increase the TM and HE mode losses.

Considering the difficulties associated with the fabrication of THz Bragg fibers, we note finally that a shorter minimum fiber length for achieving an ESMR is very important and that the Brewster angle phenomenon could be of fundamental importance to make the effectively single-mode regime practical.

5.3.3 Coupling to TE_{01} mode

In the previous subsection, it was seen that with the proper fiber length all but the TE_{01} mode could be eliminated. Even in a multi-mode regime, the TE_{01} mode generally offers orders of magnitude lower propagation loss and lower bending loss than the HE_{11} mode; but there remains the question of properly coupling light into the TE_{01} mode of a Bragg fiber. The problem stems from the fact that the TE_{01} mode is azimuthally polarized whereas typical THz sources are linearly polarized. The polarization mismatch yields negligible coupling. An increase in the coupling efficiency requires a THz source with an azimuthally polarized beam.

One such source that has recently been demonstrated is a photo-conductive antenna with a special electrode design [97]. This antenna emits an azimuthally polarized beam in the far field. However, such a design is unconventional and is not readily available.

Another interesting possibility that has been demonstrated recently is a mode conversion technique that relies upon a four-quadrant approximation of the desired polarization profile. The principle is illustrated in Figs. 5.12.a)-5.12.c). Consider a linearly polarized beam that is separated into four quadrants. The linear polarizations in each quadrant can be individually rotated to approximate the radial polarization of a TM mode or the azimuthal polarization of a TE mode. Such an approximation yields a pseudo-TE-mode that would greatly enhance the coupling to the true TE mode of a Bragg fiber. These polariation rotations have been demonstrated at visible wavelengths using either a nematic liquid-crystal spatial light modulator [153] or a collage of four half-wave plates [154].

In principle, one can imagine generating a pseudo-TE-mode THz beam from the optical rectification of a pseudo-TE-mode visible-wavelength fs pulse. Each quadrant would have a linearly polarized beam undergoing optical rectification with a different

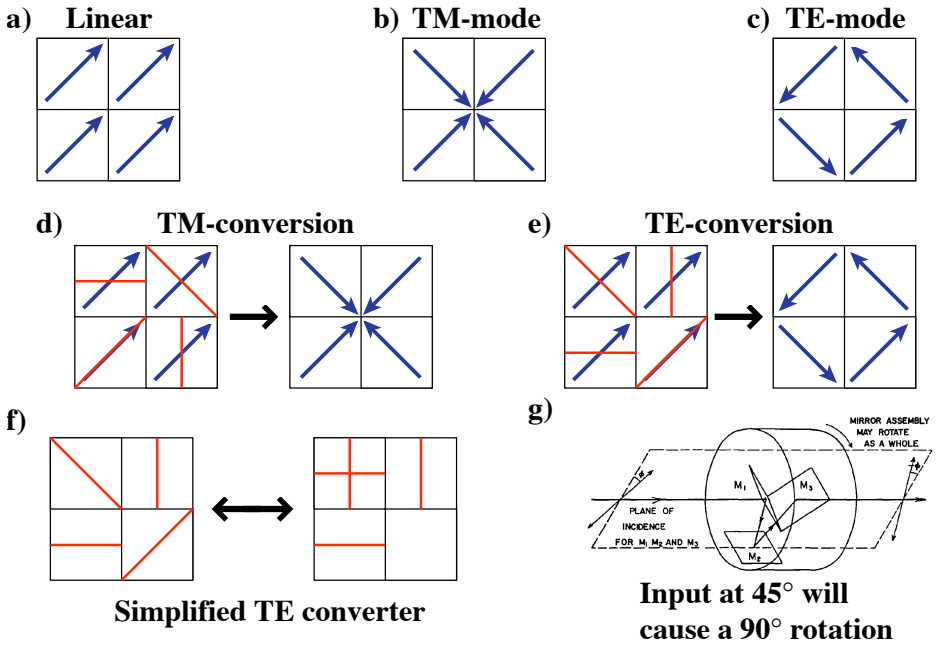

Figure 5.12 Pseudo-TE-mode from a four-quadrant TE mode convertor. Four-quadrant approximations to linear (a), radial (b), and azimuthally (c) polarized beams, respectively. d) Pseudo-TM convertor. e) Pseudo-TE convertor. Red lines indicate axes of mirror symmetry. f) Design simplification using 0,1, or 2 reflections of 90°. g) 90° reflections can be achieved using three mirror assemblies (adapted from [155]).

azimuthal orientation. Although a single $\chi^{(2)}$ crystal placed after a four-quadrant collage of half-wave plates would generate THz radiation via optical rectification, the generation efficiency would not be maximized. For optical rectification of a 800 nm fs pulse, a zincblende crystal cut along the (111) plane is generally used. The THz generation efficiency of zincblende crystals has a well known cosinusoidal dependence on the crystal orientation angle [93]. The period of the angle dependence is 120° due to the 3-fold symmetry of the (111) plane. Therefore, to maximize the efficiency, the four-quadrant optical rectification scheme would require not only a collage of four half-wave plates but also a collage of four carefully oriented zincblende crystals. Nevertheless this is a promising scheme for generating a THz pseudo-TE-mode since the device is passive and the alignment of components is fairly simple[4].

[4]The alignment complexity has been transfered to the fabrication of a collage of precisely oriented crystals.

A final possibility would be a mode convertor to directly convert a linearly polarized THz beam into a pseudo-TE-mode. The waveplate approach is impractical at THz frequencies in part because a waveplate cannot be half-wave over a decade of frequencies. In this case, a more suitable approach to the four-quadrant technique relies on the polarization rotation of mirror assemblies [155, 156, 157]. Figs. 5.12.d) and 5.12.e) present the axes of mirror symmetry required for TM and TE mode conversion. Such mirror symmetries are equivalent to a 90° or 180° polarization rotation. The design of a four-quadrant mode converter can be further simplified (Fig. 5.12.f)) by relying solely on the application of 0, 1, or 2 rotations of 90°. Fig. 5.12.g) illustrates a three-mirror polarization rotation device [155] where a 90° polarization rotation can be achieved if the input linear polarization makes a 45° angle with respect to the reflection plane of the mirrors. This is a broadband equivalent to a half-wave plate and is actually more efficient in the far-infrared than in the near-infrared due to the higher metallic mirror reflectivities.

An example of a mode converter design is given in Fig. 5.13. The mode converter is fabricated by a simple juxtaposition of the basic building blocks schematized in Fig. 5.13.a). These building blocks can easily be machined from blocks of aluminum where the reflective surfaces are polished to increase reflectivity. Blocks A and B yield polarization rotations of 0° and 90°, respectively. These blocks are placed in series to achieve either 0, 1, or 2 polarization rotations of 90°. Blocks C and D are roof mirror delay lines that are necessary to compensate the delay incurred in Block B. By placing delay blocks after the polarization rotation blocks (Fig. 5.13.b)) the optical paths lengths can be equalized to allow proper time-domain measurements of the pseudo-TE-mode. Block 1 (Fig. 5.13.c)) is a four-quadrant assembly made by a collage of the basic building blocks. The blocks can either be glued or screwed together. Block 2 (Fig. 5.13.d)) is identical to Block 1 except that it is rotated 90° counterclockwise. The final mode converter is obtained by placing Blocks 1 and 2 in series. Note that the device is a monolithic collage that allows easy alignement. Furthermore, a second convertor can be used in the same orientation to convert a pseudo-TE-mode back to a linearly polarized mode.

By using this polarization convertor in conjunction with an axicon lens, to obtain a "doughnut"-shaped power distribution from a gaussian power distribution, we effectively obtain a TE_{01}-mode convertor. It is hoped that this design will encourage other THz researchers to explore TE_{01}-based THz waveguides.

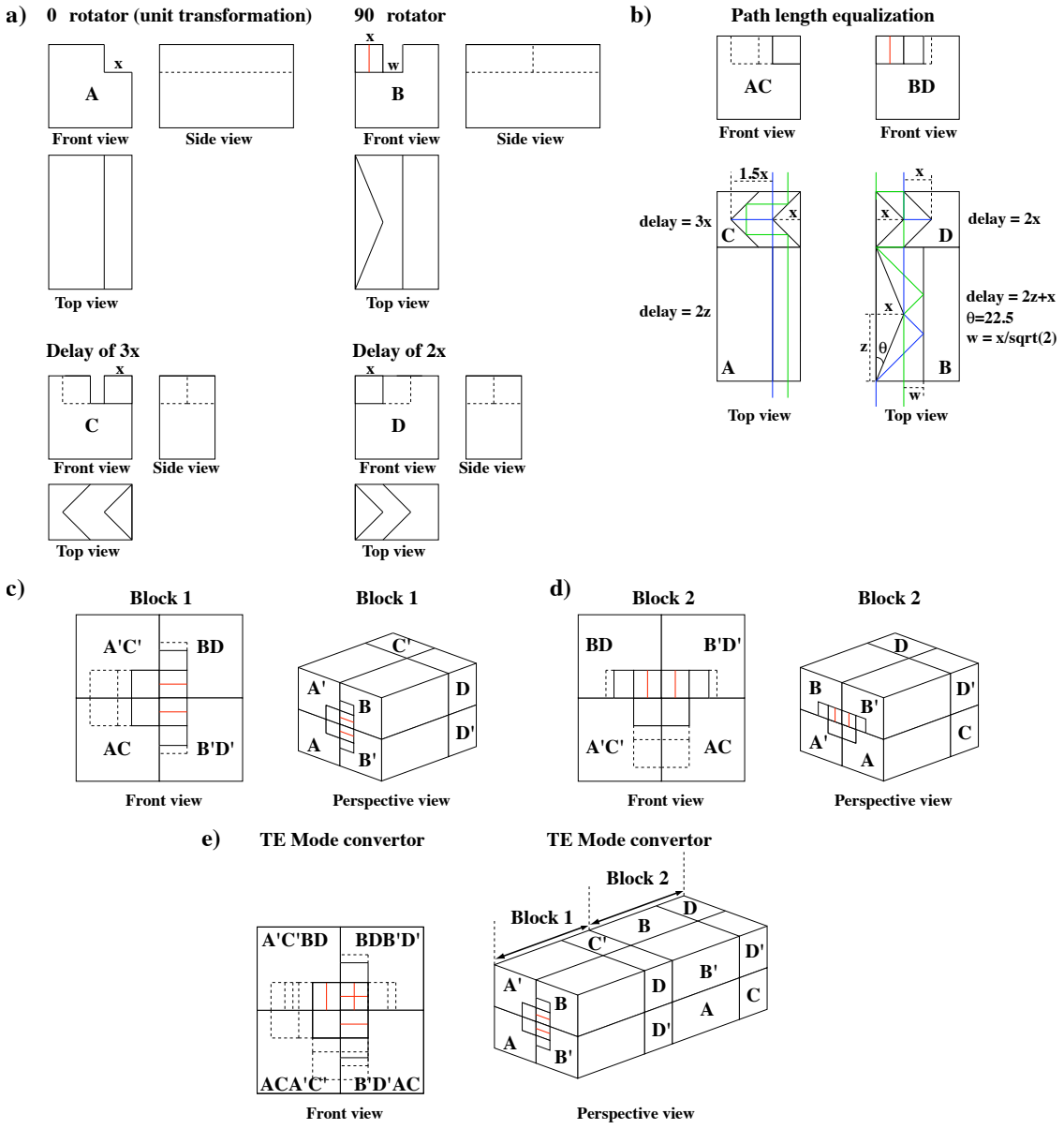

Figure 5.13 Simple TE-mode convertor design based on a four-quadrant assembly of mirrors. Mode-convertor is made from an assembly of blocks. a) Schematics of the building blocks. b) Delay lines (Blocks C and D) are added to equalize path lengths. c)-d) Collage of elementary blocks form Blocks 1 and 2. Block 2 corresponds to Block 1 rotated 90°. e) Mode convertor consists of Blocks 1 and 2 placed in series.

5.4 $n_{\text{clad}} < 1$ waveguides

Attenuated Total Internal Reflection (ATIR) is another waveguiding mechanism that is very interesting but that has not received much attention due to the difficulty in finding suitable materials. Nevertheless, Hidaka *et al.* demonstrated a THz ATIR waveguide made of PVDF that had low propagation loss ($\alpha \sim 0.017$ cm^{-1}) and a low bending loss ($\alpha_{\text{bend}} \sim 0.023$ cm^{-1} at a bending radius of 35 cm) [72]. The main problem with this waveguide is that the PVDF required electrical poling to induce the proper crystal phase for the ATIR regime. It would be very interesting to find suitable materials that do not require electrical poling. This would greatly facilitate the fabrication of such waveguides since simple tubes could be fabricated by polymer extrusion. Such materials would also enable the fabrication of more complicated Bragg fibers, where the ATIR and Bragg reflection mechanisms complement each other to extend the transmission bandwidth of the fiber [77].

In this section we describe the ATIR mechanism in more detail, explain the problem with PVDF, and propose the use of PVDF copolymers to achieve an ATIR regime without electrical poling.

5.4.1 Waveguiding principle

In certain materials, anomalous dispersion (decrease of the refractive index) on the high frequency side of an absorption peak can lead to a frequency region where $n_{\text{material}} < 1$. This anomalous dispersion regime is illustrated in Fig. 5.14.a). Curiously, a tube of such material guides light within the air core by total internal reflection, because the refractive index of air is *higher* than the cladding refractive index in the anomalous dispersion regime ($n_{\text{clad}} < 1$). The reflection is attenuated because the frequency region where $n_{\text{material}} < 1$ is in the vicinity of a strong absorption peak. Waveguides relying on this principle are often called ATIR waveguides, but the term $n_{\text{clad}} < 1$ waveguides would be more descriptive.

Two important points need to be highlighted. Firstly, the material loss in the anomalous dispersion regime is fairly high due to the strong absorption peak that is close to the frequency range of interest. As a result, an $n_{\text{clad}} < 1$ waveguide has a lower propagation loss if the field penetration into the cladding is limited. An increase in the fraction of power guided in the air core requires either an increase in the index contrast (Fig. 5.14.b)) or an increase in the core diameter. Of course, the

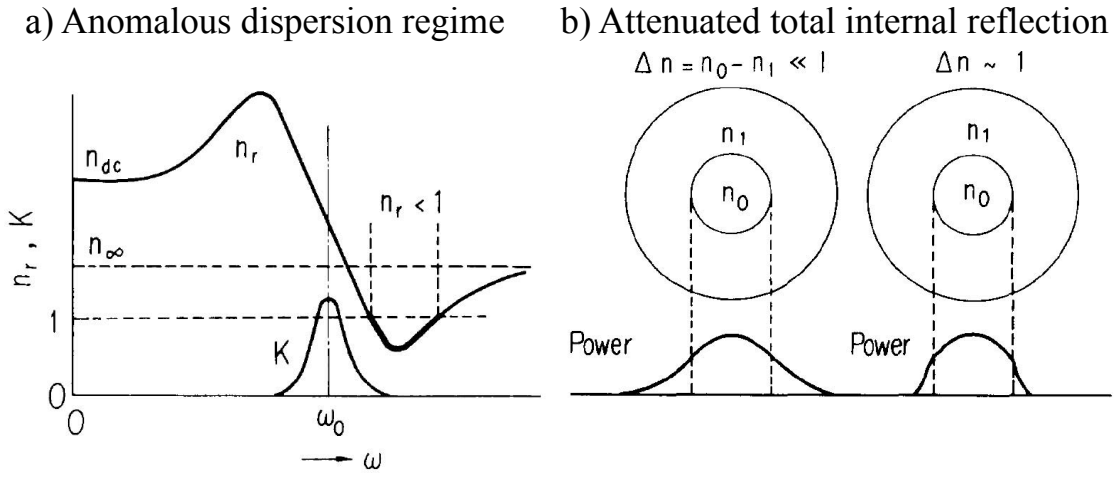

Figure 5.14 Operating principle of an Attenuated Total Internal Reflection (ATIR) waveguide. a) On the high frequency side of an absorption peak, anomalous dispersion can create a frequency window where $n_r < 1$ (adapted from [158]). b) A hollow-core tube of such a material becomes a Total Internal Reflection waveguide with the air core having the higher index in the anomalous dispersion regime. Transmission is attenuated by the high absorption loss in the cladding so a higher index contrast lowers the loss (adapted from [29]).

index contrast is material dependent and an increase in the core size increases the number of guided modes. Secondly, the bandwidth of the $n_{\text{clad}} < 1$ frequency region is limited and material dependent. In the case of poled PVDF the $n_{\text{clad}} < 1$ region extends roughly from 1 to 2 THz [72].

ATIR waveguides were first developed for guiding CO_2 laser radiation ($\lambda = 10\ \mu$m) [29, 159, 160, 161]. Oxide glasses provided the anomalous dispersion regime and it is interesting to note that doping of germanate glasses with metallic oxides was shown to shift the frequency range of anomalous dispersion [158]. So modification of a material that already has an anomalous dispersion regime can help tune the frequency region of interest.

5.4.2 PVDF and copolymers

The only material that is claimed to have an anomalous dispersion regime at THz frequencies is poled PVDF [72]. Electrical poling consists in applying large electric fields to a sample in order to create or orient electric dipoles [162, 163]. The sample is

simultaneously heated to increase the mobility of the atoms. Many kV are typically applied over a distance of a few microns to create sufficiently high fields. Consequently, the difficulty in creating and maintaining high electric fields makes electrical poling a difficult process. To understand why the poling is necessary in the case of PVDF we must first consider the nature of the PVDF polymer.

Poly(vinylidene fluoride) is a polymer made by the repetition of the vinylidene fluoride monomer $(-CH_2 - CF_2-)$. In other words, two hydrogen atoms are linked to one carbon atom and two fluoride atoms are linked to the next carbon atom, and these chemical bonds keep alternating along the carbon backbone of the polymer chain. It is the electric dipole of the highly polar $C-F$ bonds which confer to poled PVDF its interesting properties such as ferroelectricity, piezoelectricity, and pyroelectricity [164].

Moreover, PVDF is a semi-crystalline polymer. The long molecular chains of the polymer can locally align themselves and pack together to form small crystallites that are separated by amorphous regions. PVDF is a particularly complex polymer because it can form *four* different crystal phases under different processing conditions [164], such as stretching, high temperature annealing, high pressure quenching, and poling. The lattice unit cells of the different crystal phases are illustrated in Fig. 5.15.a). Without outside influence the molten polymer will tend to crystallize in the anti-polar α-phase upon cooling.

In the β-phase (Fig. 5.15.b)), the polymer chains are in the all-trans conformation, i.e. all the fluoride atoms are on the same side of a chain. It is this conformation that leads to the tightest packing of the chains and to the highest alignment of the C–F bonds. The β-phase thus has a net electrical dipole and its dipole is the strongest among the different crystal phases. It should therefore be stressed that the β-phase is required for all the applications of PVDF. A considerable amount of papers can be found in the literature concerning the processing of PVDF into its β-phase. Stretching displaces the polymer chains and helps align them along the stretching axis (Fig. 5.15.c)). This favors the formation of crystallites. Both stretching and poling were found to induce the formation of β-phase crystals, but it is the combination of both that actually yields the highest amount of β-phase crystals [166, 167]. Therefore electrical poling is a necessary step to induce a useful amount of β-phase in PVDF.

Let us now consider the THz anomalous dispersion regime of PVDF. A fit to the dielectric data is given by Hidaka *et al.* [72], but the reference that they cite for the

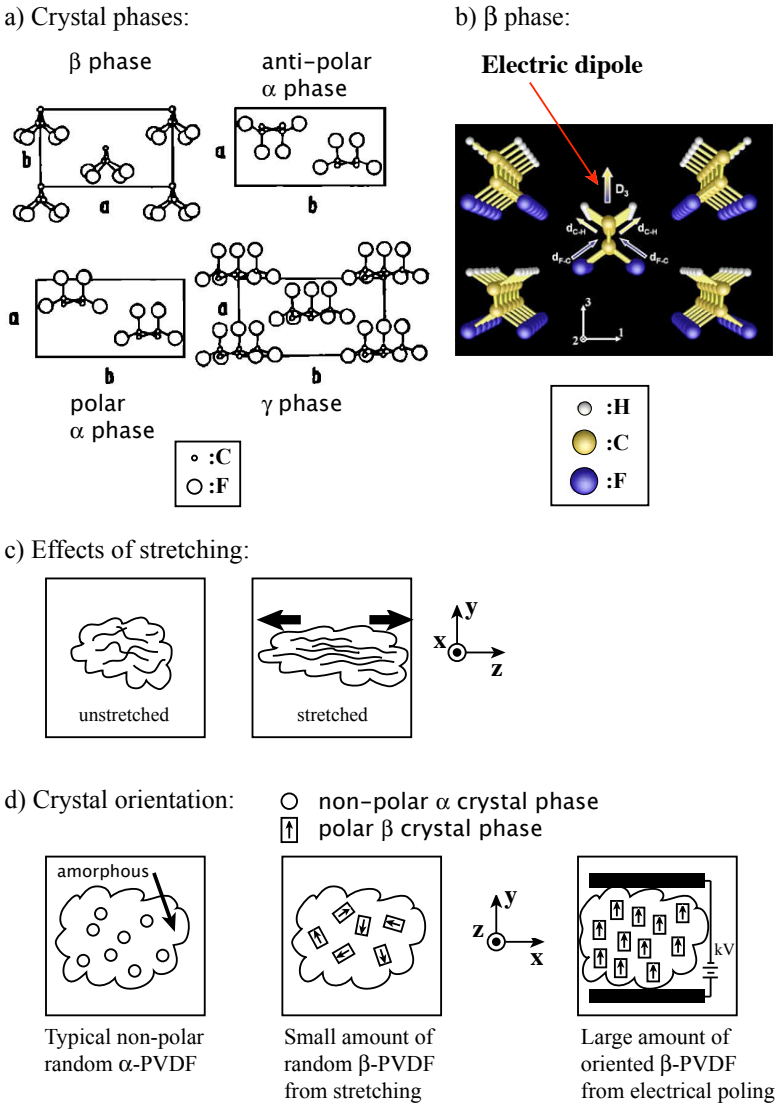

Figure 5.15 Crystal phases and polarizations of the semi-crystlline polymer PVDF. a) 4 crystal phases are formed under different conditions. (Adapted from [164]). b) The polar β crystal phase has the highest alignment of the polar C-F bonds (dipoles). (Adapted from [165]). c) Stretching aligns the polymer chains along the elongation axis and favors the formation of the β phase. d) Stretching transforms the non-polar α phase into randomly orientated β crystals, but electrical poling favors chain rotation and aligns the β crystals.

dielectric data does not actually contain a direct measurement of the THz refractive index. Moreover, we recall that the anomalous dispersion regime is in the vicinity of an absorption peak. Even if we assume the fit of the dielectric data to be valid,

the exact nature of the absorption peak remains somewhat nebulous. The absorption peak is likely due to a lattice vibration, but which crystal phase and which vibration? Due to the anisotropy of the PVDF crystals, we expect a different refractive index depending on the orientation of THz electric field polarization with respect to the crystal axes. So there is also a question of macro-alignment of the crystallites within a polycrystalline PVDF sample which is not properly addressed in Ref. [72].

It is clear that the β-phase is involved because α-phase PVDF does not have an anomalous dispersion regime (see Fig. 3.4.b)). However, it is not clear whether the orientation of the β-phase crystallites is important. Consider for instance the crystal orientations schematized in Fig. 5.15.d). Stretching induces a β-phase with the long axis of the crystallites aligned along the stretching direction but with the crystal dipoles randomly orientated in the transverse plane. On the contrary, electrical poling forces the alignment of the β-phase crystallites in the transverse plane. From the data of Hidaka's paper, it is unclear which orientation is sufficient for the anomalous dispersion regime and whether a complicated *radial poling* procedure [168] is a prerequisite for an ATIR tube waveguide. Moreover P(VDF-TrFE) copolymers[5] also have a β-phase and they are known to *automatically* form β-phase crystals upon cooling if the TrFE content is high enough [169]. It should be stressed that a β-phase naturally arises in copolymers without electrical poling. Therefore knowing whether the β-phases of copolymers also have THz anomalous dispersion regimes and knowing which crystal alignment is necessary and sufficient for ATIR is of primary importance for polymer ATIR waveguides.

Some answers to these questions can be found in a little known but detailed paper by Petzelt *et al.* [170]. In their paper, they present a detailed analysis of far-infrared FTIR transmission measurements through PVDF and P(VDF-TrFE) films. Unfortunately, the FTIR measurements imply that the THz refractive index cannot be determined directly. Nevertheless, the data clearly demonstrate absorption peaks and elucidates the polarization dependent behavior. The most important results of Petzelt's paper are reproduced in Fig. 5.16 for clarity.

Copolymers of different concentrations were studied with the VDF/TrFE ratio given in percent. Thus the '100/0' sample corresponds to pure PVDF and the '60/40' sample has 60% VDF and 40% TrFE. All of their samples were prepared by stretching films and some samples were additionally poled. Thus all of the samples had β-phase

[5]Poly(vinylidene fluoride - trifluoroethylene) coplymer, $-CH_2-CF_2-CHF-CF_2-$

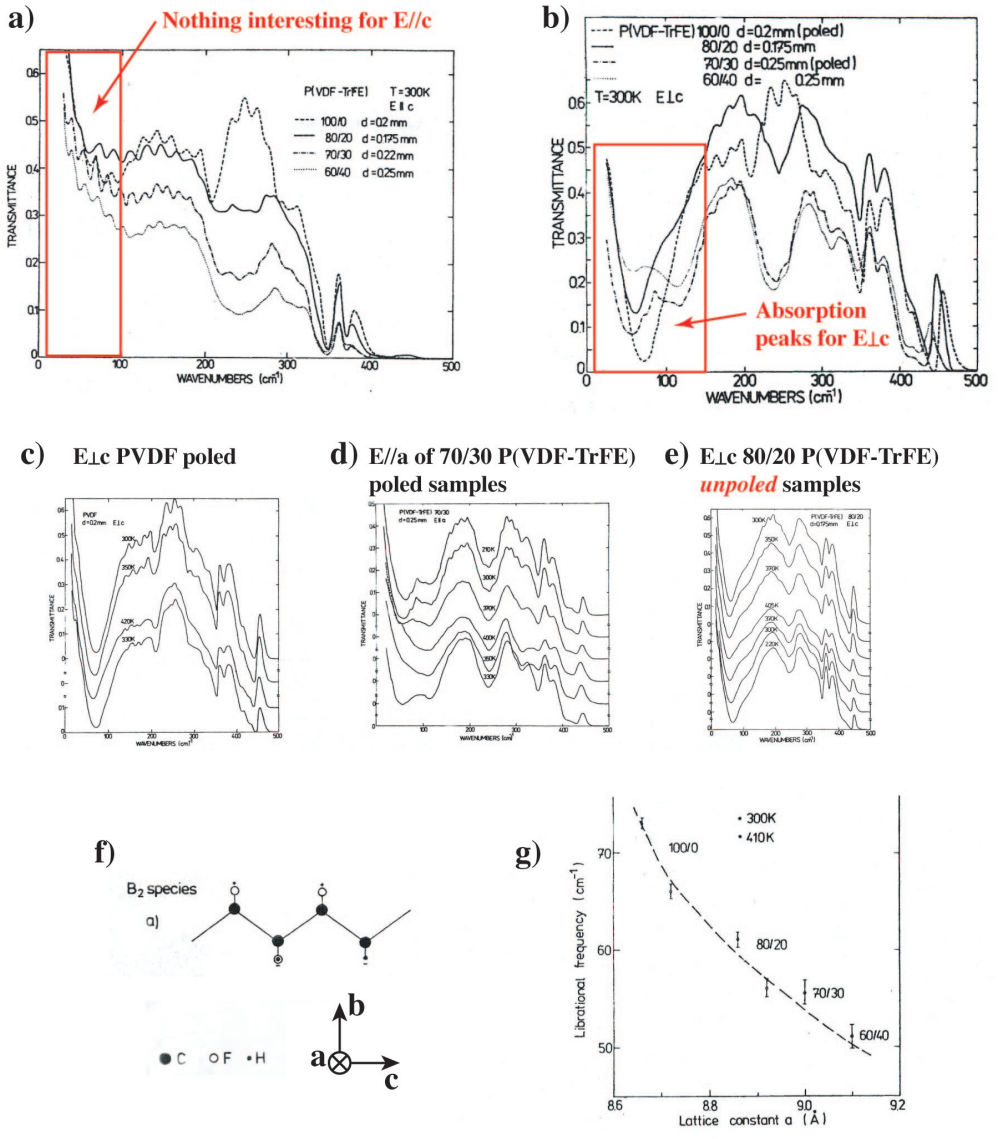

Figure 5.16 THz FTIR data of P(VDF) and P(VDF-TrFE) copolymers reproduced from a paper by Petzelt [170]. Transmission spectra through stretched copolymer films are shown for incident polarizations parallel (a) or perpendicular (b) to the c-axis of the β-phase crystals. Spectra are clearly attributed to poled PVDF (c), poled copolymer (d), and *unpoled* copolymer (e) samples. Absorption peaks are attributed to lattice vibrations perpendicular to the c-axis of the polymer chains (f). Finally, in addition to avoiding electrical poling, copolymers are shown to tune the peak absorption frequency and presumably tune the $n < 1$ frequency bands.

crystals with the long axis of the crystallites, the c axis, oriented along the stretching direction within the plane of the film. Note that the c-axis also points along the length of the polymer chains. Transmission through the films was measured with the electric field polarization of the incident light either parallel or perpendicular to the c-axis. We seek to identify absorption peaks that are determined by dips in the transmission. The frequency range of interest is 0 to 3 THz which corresponds to wavenumbers of 0 to 100 cm^{-1}. Fig. 5.16.a) indicates an absence of absorption peaks below 100 cm^{-1} for $E//c$. On the contrary, Fig. 5.16.b) indicates very interesting absorption peaks below 100 cm^{-1} for $E \perp c$.

Many facts can be deduced from Fig. 5.16.b). Firstly, we note that the measured PVDF sample was poled. Secondly, we note that *all* the copolymers have absorption peaks similar to that of poled PVDF, which is understandable considering the similarities in molecular and crystal structure compared to pure PVDF. Thirdly, it is reasonable to assume that the copolymer absorption peaks also induce an anomalous dispersion regime where $n < 1$ considering the behavior of poled PVDF. Fourthly, this data also confirms that the absorption peak stems from the β-phase because the PVDF needed to be poled. Further proof of this is found in Fig. 5.16.c) where heating the poled PVDF film to a temperature of 420 K did not affect the absorption peak. Thermal vibrations are known to destroy the alignment of the electric dipoles within poled samples [163]. However, 420 K is below the melting point of the polymer and the thermal vibrations will lead to rotations of the electric dipoles around the c-axis of the crystals without changing the crystal phase. Furthermore, it is seen that poling of copolymers can definitely result in absorption peaks (5.16.d)), but this is not strictly necessary as *unpoled* samples have also shown the characteristic absorption peaks (5.16.e)).

Petzelt's paper also studies the nature of this absorption peak and attributes it to a lattice vibration perpendicular to the polymer chain, which is illustrated in 5.16.f). From a simple mass-spring harmonic oscillator model it is easy to understand that heavier atoms along the polymer chain will lead to vibrations at lower resonance frequencies. Hence, we would expect the absorption peak to occur at lower frequencies as the TrFE content increases in the copolymers, due to the fluorine atoms being heavier than the hydrogen atoms. This is clearly demonstrated in Fig. 5.16.g), where the librational frequencies of the copolymers are indicated. Therefore, P(VDF-TrFE) copolymers offer not only the possibility of $n < 1$ frequency bands without electrical

poling, but the position of the bands can actually be tuned to lower frequencies by adjusting the TrFE concentration of the copolymer. Note that similar frequency shifting can be expected with the even heavier chlorine atoms of P(VDF-TrFE-CTFE) ter-polymers[6] [171].

From these results, we conclude that the only requirements for an ATIR waveguide are a copolymer with a sufficiently high TrFE concentration to automatically crystallize in the β-phase, and for the c-axis of the copolymer chains to be aligned along the length of the waveguide. This can be achieved by stretching the waveguide along its length, as stretching aligns the polymer chains along the stretching axis. This stretching should naturally occur in the drawing or extrusion of copolymer tubes.

Finally, we note that the absorption peak of PVDF was measured at 73 cm^{-1}, which is comparable to the 70 cm^{-1} value predicted for the lattice vibration in β-phase PVDF [170]. However, both of these frequencies are higher than the value reported in Hidaka's paper. Therefore proper THz-TDS measurements of PVDF and its copolymers are required to make a direct measurement of the THz refractive index of these materials. Such measurements would: *i)* clarify once and for all the different reports in the literature, *ii)* catalogue the $n < 1$ frequency bands of the different copolymers, and *iii)* give more precise models of the dielectric function for more accurate simulations of THz ATIR waveguides.

5.5 TIR Foam fibers

In this final section we consider simple step-index fibers that guide by total internal reflection (TIR). In the search for broadband *single-mode* waveguides that have low bending losses, TIR fibers are hard to beat. The only obstacle for the implementation of TIR fibers is material absorption loss. We have seen many techniques for reducing the propagation loss of waveguides, but in this case we truly require a low absorption loss bulk material. An interesting candidate material is polymer foam. As seen in section 5.1.1, doping with air can significantly reduce the absorption loss and can also tailor the refractive index.

We therefore theoretically investigate the design of Total Internal Reflection foam fibers, where the core and cladding materials consist of foams with different porosities.

[6] Poly(vinylidene-fluoride - trifluorethylene - chlorotrifluoroethylene) terpolymer, $-CH_2-CF_2-CHF-CF_2-CClF-CF_2-$

We begin by examining how certain design parameters such as core index, index contrast, and core diameter affect the mode confinement. We then consider simulations results of propagation loss, dispersion, and bending loss as a function of these parameters. The transmission bandwidth of the fiber is then defined in terms of bending loss and the single-mode regime. Finally, we discuss encapsulation of the foam fiber for mechanical stability and the elimination of water vapor absorption, and conclude with a discussion on feasibility.

5.5.1 Foam fiber design considerations

The simplest total internal reflection waveguide is a two-layer step-index fiber, which has a high index core surrounded by a lower index cladding. It is well known that the two-layer step-index waveguiding problem can be solved analytically in terms of the normalized frequency V [114, 115]. By definition,

$$V = \left(\frac{\pi}{c}\right) f \cdot d_{\text{core}} \sqrt{n_{\text{core}}^2 - n_{\text{clad}}^2}, \tag{5.17}$$

where c is the speed of light, f is the frequency, n_{clad} is the refractive index of the cladding, d_{core} is the core diameter, and n_{core} is the refractive index of the core. For the fundamental mode, the effective propagation index n_{eff} and the fraction of power in the core η_{core} are functions that rapidly increase with V and saturate asymptotically to some limit at large V values [115].

Fig. 5.17 presents the power distribution of the fundamental mode to illustrate how the mode confinement is affected by the various fiber parameters. The level of mode confinement within the core, quantified by the fraction of modal power within the core $\eta_{\text{core}} = P_{\text{core}}/P_{\text{mode}}$, will help give an intuitive understanding of absorption and bending losses.

Since we are studying foam fibers with very low material indices, an obvious first question is how the mode confinement is affected by the index contrast and the core index. It is well known that a small index contrast is sufficient for waveguiding. For instance, $\Delta n = n_{\text{core}} - n_{\text{clad}} = 4.5 \times 10^{-3}$ for the standard SMF28$^{\text{TM}}$ telecommunications fiber. However, it is less obvious how the core index affects waveguiding. Fig. 5.17.a) illustrates how the mode confinement decreases as the index contrast decreases, but what is perhaps less intuitive is that the same index contrast gives similar confinement levels even if the core index decreases. Compare, for instance, the dashed

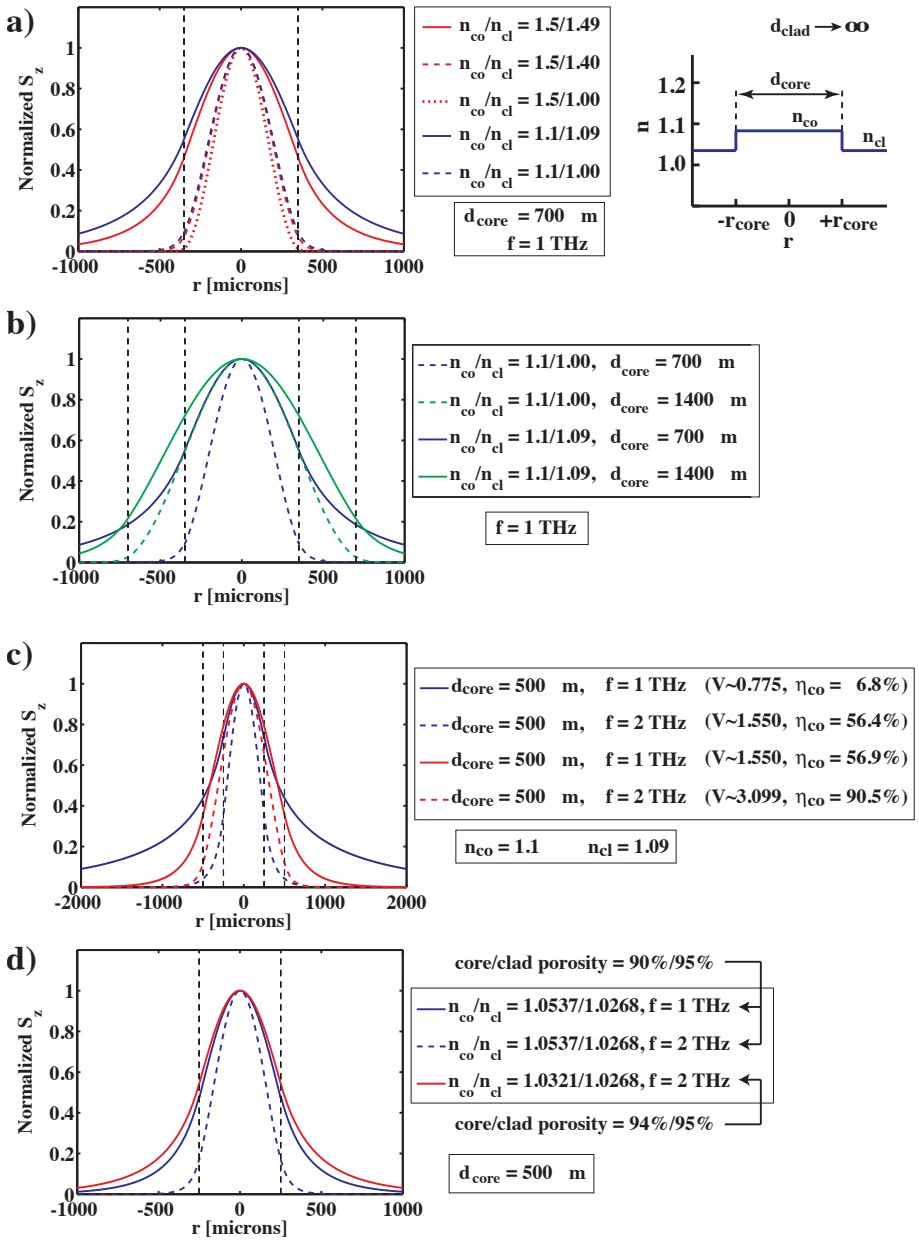

Figure 5.17 Comparison of the fundamental mode power distributions of two-layer step-index fibers for which various design parameters are varied: such as core index, index contrast, and core diameter. a) Index contrast is more important for confinement than core index. Schematization of two-layer step-index profile is shown on the right. b) Increasing core size increases the fraction of power in the core. c) Similar normalized frequency (V) values give similar fractions of power within the core (η_{co}). d) Lowering the index contrast is equivalent to lowering the core diameter.

lines and solid lines in Fig. 5.17.a). Thus, the index contrast is more important than the actual core index for assuring a certain level of confinement.

Another important question is how big the fiber should be to efficiently guide light at a certain frequency. In Fig. 5.17.b) we consider different fiber geometries that guide light at 1 THz. An increase of the core diameter is seen to increase the relative fraction of power in the core, regardless of what the index contrast is. Furthermore, an increase in frequency, in Fig. 5.17.c), is seen to increase the fraction of power in the core for a fixed core diameter. Such observations are consistent with the V parameter solutions. An increase in either index contrast, frequency, or core diameter will increase the value of V and thus increase the value of η_{core}. Moreover, it is not surprising to see that similar V values give similar fractions of power within the core even if the diameters are different. In Fig. 5.17.c) for instance, a level of confinement (η_{core}) similar to the dashed blue curve can be achieved at a lower frequency if the core diameter is increased (such that V remains constant). It will later be seen that such an effect is important for mitigating the effects of bending loss.

Finally, Fig. 5.17.d) indicates that a similar equalization of the V values can be achieved by changing the core and cladding refractive indices instead of changing the fiber diameter. A confinement level similar to the solid red curve can be achieved at a lower frequency by increasing the index contrast.

The next sections will more clearly illustrate how the index contrast, core index, and core diameter affect the fundamental mode properties such as propagation loss, dispersion, and bending loss.

5.5.2 Propagation loss and dispersion calculations

The transfer matrix method was once again used to carry out exact vectorial simulations of the fiber modes. Since we seek to design a single-mode fiber we limit our interest to the fundamental mode, but we consider different fiber geometries to investigate the potential of foam fibers. Given that the material regions are assumed to be polymer foams, the effective material parameters of the air doped polymer were calculated using the Cubic Root formula (5.1), as in section 5.1.1. The following material parameters were considered for the host material and dopant, respectively: $n_{\text{host}} = 1.5$, $\alpha_{\text{host}} = 0.2$ cm^{-1}, $n_{\text{dopant}} = 1.0$, and $\alpha_{\text{dopant}} = 0.0$ cm^{-1}. Note that different porosities of the same type of foam are considered for the core and cladding

regions. Moreover, the porosity of the foam gives a more intuitive description than the actual effective refractive index value, thus the different fiber designs are labelled according to the porosity of the core (P_{co}) and cladding (P_{cl}).

Table 5.1 Effective material parameters of a polymer foams of different porosity, calculated using the Cubic Root effective medium model.

Porosity [%]	n_{eff}	α_{eff} [cm^{-1}]
0	1.5000	0.200
80	1.1083	0.060
90	1.0537	0.036
94	1.0321	0.024
95	1.0267	0.021
100	1.0000	0.000

Three different index contrasts are considered with core/clad porosity ratios of 80%/90%, 90%/95%, and 94%/95%. The refractive indices and absorption losses of the corresponding foams are calculated using the Cubic Root effective medium model and are given in table 5.1. In order to simplify the subsequent calculations it is assumed that the foam material parameters are frequency independent. The different designs therefore consider a reduction in the index contrast and an increase in the core porosity. Furthermore, for each index contrast different core diameters are considered and the variation of the mode properties with respect to frequency are calculated.

We begin by considering the propagation losses. Fig. 5.18 presents the propagation loss α_{mode} and the fraction of power in the core η_{core} for fibers of different geometries. Each column corresponds to a different index contrast and the legend to the core diameters is given in the bottom right corner. In all cases, α_{mode} (first row) and η_{core} (second row) are seen to tend towards an asymptotic value as the frequency increases. The fraction of power in the core tends towards 1.0, i.e. total confinement within the core, and as an obvious consequence the propagation loss tends towards the absorption loss of the core (compare to the values of table 5.1).

Furthermore, we intuitively expect $\alpha_{\text{mode}} = \eta_{\text{core}}\alpha_{\text{core}} + \eta_{\text{clad}}\alpha_{\text{clad}}$, where η_j and α_j are respectively the fractions of power and the attenuation coefficients. Since $\eta_{\text{core}} + \eta_{\text{clad}} = 1$, the above formula reduces to $\alpha_{\text{mode}} = A\eta_{\text{core}} + B$, where A and B are constants. Indeed, if we plot α_{mode} (Fig. 5.18.b)) as a function of η_{core} (Fig. 5.18.e))

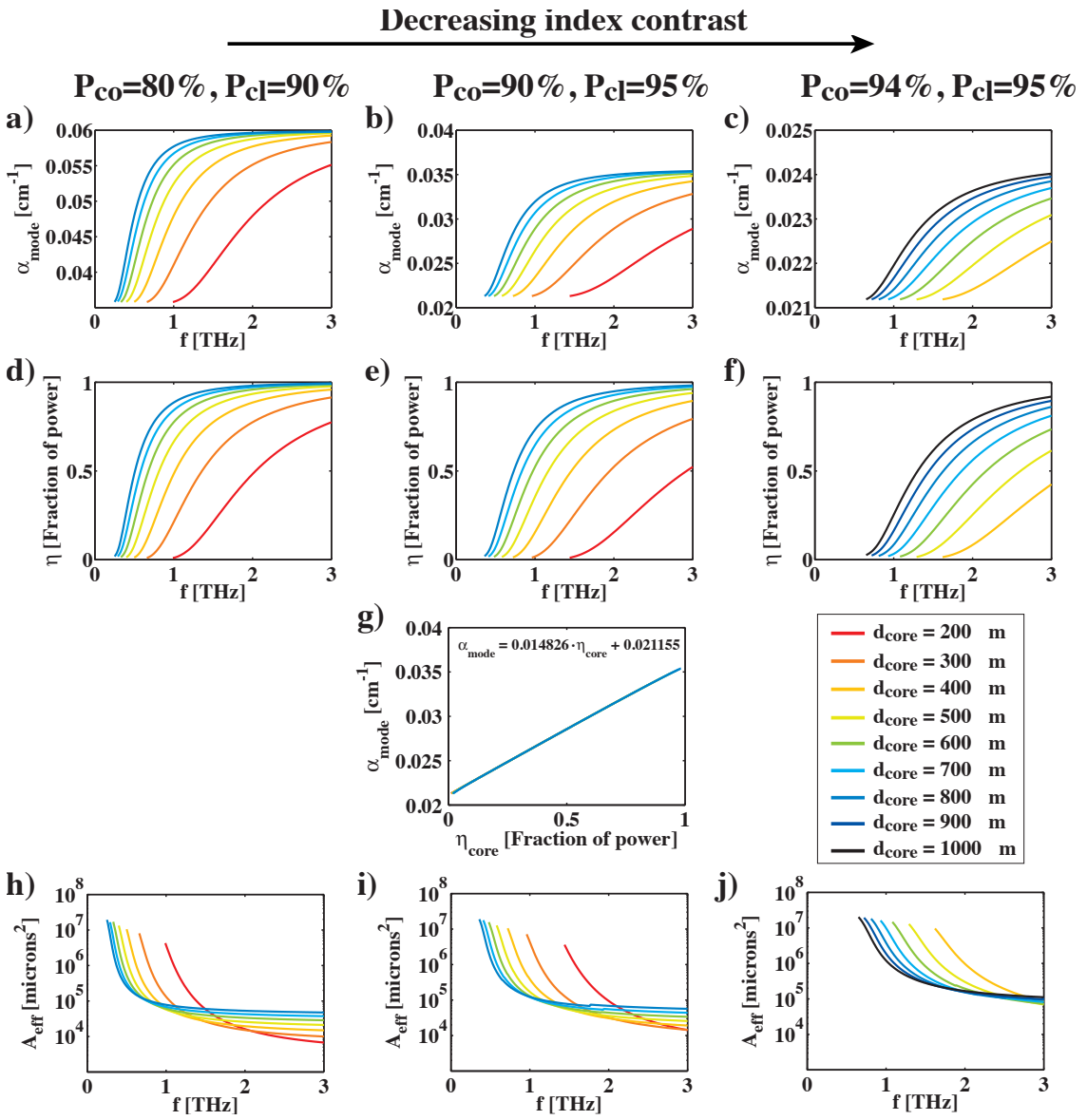

Figure 5.18 Variation of the propagation loss, the fraction of power in the core, and the effective modal area of the fundamental mode for foam fibers of different geometries. Each column corresponds to the index contrast labelled at the top. First row: power propagation loss α_{mode}. Second row: fraction of power in the core η_{core}. Third row: α_{mode} is shown to be proportional to η_{core}. Fourth row: area of mode A_{eff}. The legend indicates the core diameters.

we obtain a straight line confirming this intuitive model (Fig. 5.18.g)). Therefore the modal attenuation is dominated by absorption loss and greatly affected by changes

in the fraction of power guided in the lossier core. In Fig. 5.18 a decrease in the core diameter is seen to decrease η_{core} and, at a constant frequency and core diameter, a decrease in the index contrast is also seen to decrease η_{core}. Such observations are consistent with the changes in power distribution illustrated in the previous section. Similarly to the case of the subwavelength porous fibers studied in chapter 3, we conclude that decreasing the core diameter or the index contrast are alternative methods to decreasing the attenuation loss. However, such a reduction is achieved at the expense of lower mode confinement, which means that the bending loss will be higher.

The final row presents the effective area A_{eff} of the fundamental mode, calculated according to the general equation [172]

$$A_{\text{eff}} = \frac{\left[\int_0^\infty S_z(r) r dr\right]^2}{\int_0^\infty [S_z(r)]^2 r dr}, \tag{5.18}$$

where S_z is the z-component of the Poynting vector. In Fig. 5.18 the effective area is plotted on a logarithmic scale, with large evanescent modes at low frequencies and small highly confined modes at high frequencies. This is true independently of index contrast, but the higher the index contrast the higher the confinement at *low* frequencies. This remark will be important for bending losses.

It should also be noted that in the case of subwavelength fibers we were in the $\eta_{\text{core}} \to 0$ limit with large evanescent modes. As we will see in the next section, we are actually more interested in the $\eta_{\text{core}} \to 1$ limit in order to reduce the bending loss. Consequently, we can use $\alpha_{\text{mode}} \leq \alpha_{\text{core}}$ as a design limit. Instead of choosing the core diameter and index contrast to reduce the propagation losses, we accept α_{core} as a design rule for α_{mode} and choose the core diameter and index contrast to minimize the bending losses instead. Therefore we conclude that core porosity should be made as high as possible to reduce the absorption loss. An additional constraint is that the cladding porosity remain higher. For reasons of mechanical stability an air cladding should be avoided so a lower index (higher porosity) foam is required for the cladding.

Let us now consider the effective propagation index n_{eff} of the fundamental mode. The first row of Fig. 5.19 plots the effective indices for the various foam fiber geometries. It can be seen that n_{eff} has the same frequency dependence as α_{eff}. At the low frequency limit the propagation indices of the large evanescent modes tend towards the index value of the cladding foam, whereas in the high frequency limit the highly

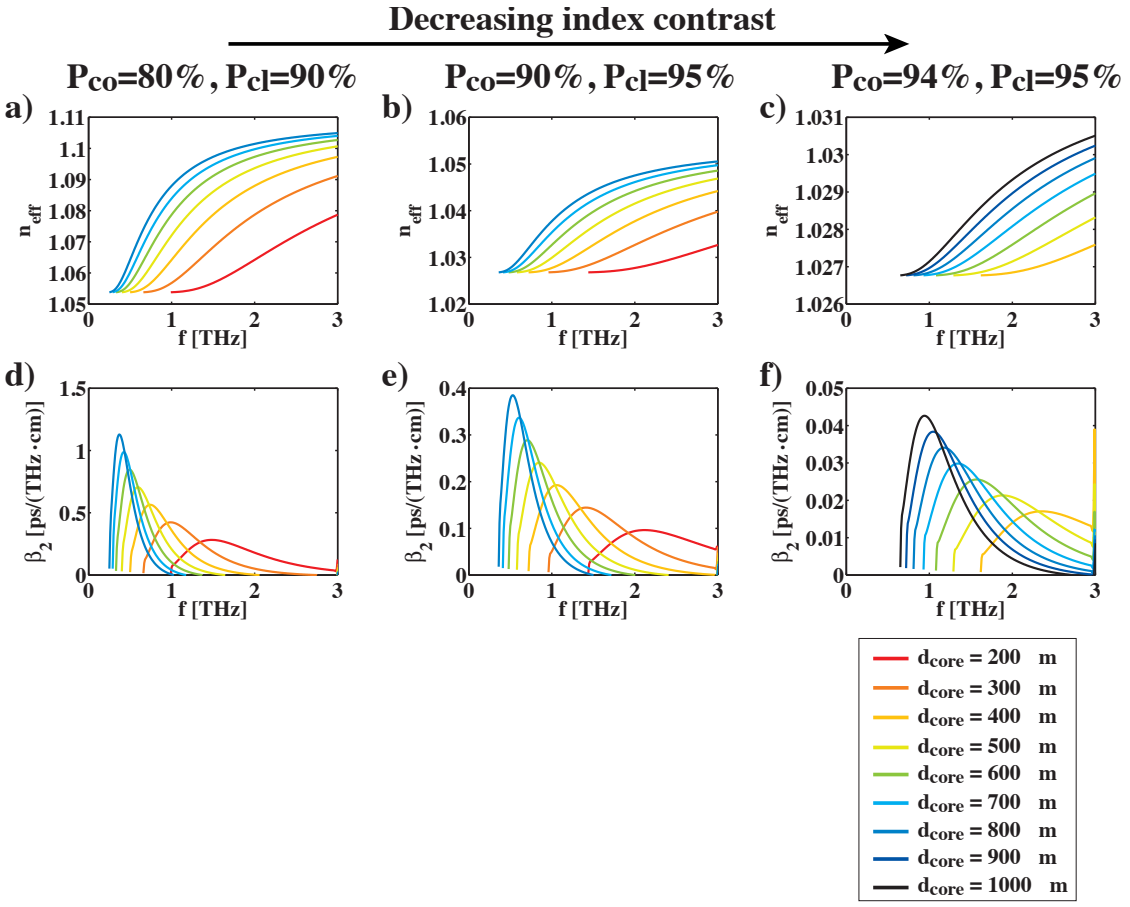

Figure 5.19 Variation of the effective index and β_2 dispersion parameter for foam fibers of different geometry. Each column corresponds to the index contrast labelled at the top. First row: n_{eff}. Second row: β_2 dispersion parameter. The legend of core diameters is given in the bottom right corner.

confined modes have values that tend towards the core index. Of greater concern is the dispersion accumulated by the propagation of short THz pulses within the fiber. The dispersion parameter $\beta_2 = (1/2\pi c)(f \cdot \partial^2 n_{\text{eff}}/\partial f^2 + 2 \cdot \partial n_{\text{eff}}/\partial f)$ is plotted in the second row of Fig. 5.19. A higher dispersion is expected in the transition regions where the effective index is rapidly increasing as a function of frequency. From Fig. 5.19 it can be seen that a higher index contrast leads to a larger variation in the propagation index and a larger dispersion value. It should be noted that values ≤ 0.05 ps·THz/cm are negligibly small (0.05 ps·THz/cm $\ll 1.0$ ps·THz/cm $= (\beta_2)_{\text{limit}}$, see section 3.4.3).

5.5.3 Bending loss calculations

Beyond propagation losses, large bending losses are one of the greatest factors limiting the practical use of THz waveguides. To evaluate the bending losses of the foam fibers we use the standard bending loss formula for fibers of arbitrary index profile [173, 174]. Nielsen et al. showed that the formula could be greatly simplified in the $R_{\text{bend}} \gg r_{\text{core}}$ limit [175], where R_{bend} is the bending radius of the fiber about a point and r_{core} is the radius of the fiber core. In the case of THz fibers $R_{\text{bend}} \gg r_{\text{core}}$ is an excellent approximation since $r_{\text{core}} \leq 0.3$ cm and $R_{\text{bend}} \geq 10$ cm. After simplifications, the power[7] bending loss α_{bend} is given by the following formula [111]:

$$\alpha_{\text{bend}} \approx \frac{1}{4}\sqrt{\frac{2\pi}{3}}\frac{1}{A_{\text{eff}}}\frac{1}{\beta_{\text{eff}}} \cdot F\left(\frac{2}{3} \cdot R_{\text{bend}} \cdot \frac{\left[\beta_{\text{eff}}^2 - \beta_{\text{clad}}^2\right]^3}{\beta_{\text{eff}}^2}\right), \tag{5.19}$$

$$F(x) = x^{-1/2} \cdot \exp(-x), \tag{5.20}$$

where A_{eff} is the effective area given by equation (5.18), $\beta_{\text{eff}} = n_{\text{eff}} \cdot 2\pi/\lambda$ is the effective propagation constant of the mode, and $\beta_{\text{clad}} = n_{\text{clad}} \cdot 2\pi/\lambda$.

The first row of Fig. 5.20 presents the bending loss as function frequency for the different fiber geometries. In this case the bending radius is fixed at 20 cm. As expected, the modes are less confined in the core at lower frequencies and the bending loss increases because it is easier for the mode to radiate from the fiber. Furthermore, increasing the core diameter increases the fraction of power in the core and therefore increases the confinement level at lower frequencies. The result is a shifting of the bending loss curves to lower frequencies because the high frequency components are better confined and have lower bending losses. However, we note that all the curves exhibit a local minimum on the low frequency side before the bending losses increase unabatedly; see for instance Fig. 5.20.c). Note that some curves are incomplete due to numerical calculation difficulties at low frequencies, but the presence of the minima is clear. This minimum results from the fact that as the frequency decreases there is a certain frequency range where A_{eff} is increasing more rapidly than the $F(x)$ function, thereby temporarily decreasing the bending loss. In any case, such minima

[7] Note that references [173], [175], and [111] define α_{bend} as an *amplitude* attenuation coefficient; whereas reference [174] defines α_{bend} as a *power* attenuation coefficient, hence the factor 4 in the denominator instead of 8. Here we write α_{bend} as power attenuation for a direct comparison the power propagation loss of straight fibers.

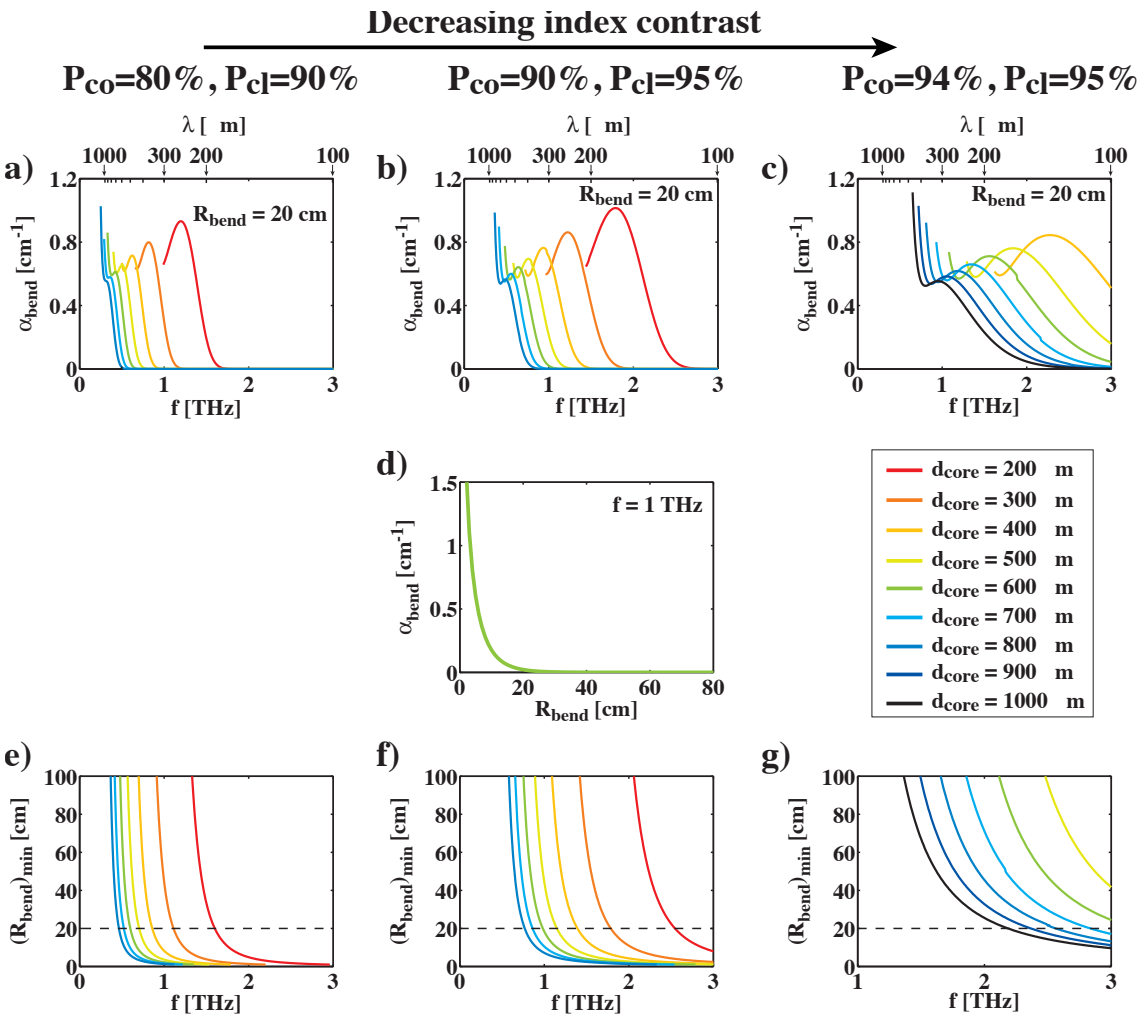

Figure 5.20 Bending loss calculations of foam fibers. Each column corresponds to the index contrast labelled at the top and the legend of core diameters is given in the second row. First row: Bending loss as a function of frequency ($R_{\text{bend}} = 20$ cm). Second row: Bending loss as a function of bending radius. Third row: Minimum bending radius to insure that $\alpha_{\text{bend}} \leq \alpha_{\text{mode}}$. A fixed minimum bending radius (dashed line) defines a lower frequency limit for a given core size.

are uninteresting because all bending loss values are seen to be much greater than the propagation losses; compare α_{bend} to the straight fiber propagation loss values (α_{mode}) in Fig. 5.18.

We wish to find the conditions for an acceptable bending loss. Despite the frequency dependence, the bending loss depends even more strongly on the bending radius. Since x is proportional to R_{bend}, the $F(x)$ function implies that the bending loss

increases exponentially as the bending radius decreases, as illustrated in Fig. 5.20.d). Instead of thinking in terms of bending loss, a more useful design parameter is a critical bending radius R^*. From the above considerations it is natural to define the critical bending radius as a minimum, $R^* \equiv (R_{\text{bend}})_{min}$, with larger bending radii yielding lower bending losses. Consequently, the critical bending radius defines some arbitrary limit for the maximum bending loss $(\alpha_{\text{bend}})_{max}$. A natural choice for this limit, for obvious practical reasons, is that the maximum bending loss should be equal to the straight fiber propagation loss. We therefore define $(R_{\text{bend}})_{min}$ as the minimum permissible bending radius such that $\alpha_{\text{bend}} \leq \alpha_{\text{mode}}$ if $R_{\text{bend}} \geq (R_{\text{bend}})_{min}$. Using the frequency dependent α_{mode} values of Fig. 5.18, we calculate $(R_{\text{bend}})_{min}$ by finding the R_{bend} value that equalizes the bent and straight fiber propagation losses.

The third row of Fig. 5.20 plots $(R_{\text{bend}})_{min}$ as a function of frequency for the different fiber geometries. These curves can be used as *design laws* for determining the useful bandwidth of the fiber. As an example let us consider a practical value of $(R_{\text{bend}})_{min} = 20$ cm, such that we can bend the fiber up to a bending radius of 20 cm with negligible bending loss. Let us consider the $d_{\text{core}} = 200$ μm curve of Fig. 5.20.e). The design law $(R_{\text{bend}})_{min} = 20$ cm defines an intersection point (between the dashed black line and the solid red line) and this intersection point defines a *lower* frequency limit for permissible bending loss. In this example, $f_{\text{min}} = 1.6$ THz. Fig. 5.20.a) illustrates the frequency dependence of the bending loss at $R_{\text{bend}} = 20$ cm as it can be seen that the bending loss becomes prohibitively large below 1.6 THz and negligibly small above. The lower frequency limit can also be understood from Fig. 5.20.e) since frequencies <1.6 THz would require a larger bending radius to have a permissibly low bending loss. From the results of Fig. 5.20 we conclude that increasing the core size and increasing the index contrast reduces the low frequency limit because the modes become more confined at low frequencies and the onset of bending loss is postponed.

5.5.4 Transmission bandwidth

On one hand, we saw in the previous section that $(R_{\text{bend}})_{min}$ sets a lower frequency limit (f_{min}) to the useful bandwidth of the fiber. On the other hand, the upper frequency limit is given by the single-mode regime limit. It is well known that in the case of two-layer step-index fibers the cutoff point of the second guided mode, where the second mode ceases to be guided, is determined by $V \sim 2.404$ [114, 115], where V

is the normalized frequency defined by equation (5.17). Rearranging terms we obtain the upper frequency limit,

$$f_{\max} = \frac{V_{\text{cutoff}}}{(\frac{\pi}{c}) \cdot d_{\text{core}} \sqrt{n_{\text{core}}^2 - n_{\text{clad}}^2}} = \frac{2.404}{(\frac{\pi}{c}) \cdot d_{\text{core}} \sqrt{n_{\text{core}}^2 - n_{\text{clad}}^2}}. \tag{5.21}$$

These two limits, $f_{\min}$ and $f_{\max}$, define the useful transmission bandwidth in which the fiber transmits a single mode and can be bent up to $R_{\text{bend}} = 20$ cm with negligible bending loss.

Table 5.2 Transmission bandwidth of various foam fibers. d_{core}, P_{co}, and P_{cl} are respectively the core diameter, core porosity, and cladding porosity of the foam fiber. $f_{\min}$ is defined by $(R_{\text{bend}})_{min} = 20$ cm and $f_{\max}$ is given by equation (5.21).

	P_{co} = 80%, P_{cl} = 90%		P_{co} = 90%, P_{cl} = 95%		P_{co} = 94%, P_{cl} = 95%	
d_{core} [μm]	f_{min} [THz]	f_{max} [THz]	f_{min} [THz]	f_{max} [THz]	f_{min} [THz]	f_{max} [THz]
200	1.599	3.344	2.546	4.847	--	--
300	1.111	2.229	1.786	3.231	--	--
400	0.859	1.672	1.392	2.423	4.389	5.455
500	0.705	1.338	1.149	1.939	3.689	4.364
600	0.600	1.115	0.983	1.616	3.199	3.637
700	0.523	0.955	0.861	1.385	2.836	3.117
800	0.465	0.836	0.769	1.212	2.561	2.728
900	--	--	--	--	2.366	2.425
1000	--	--	--	--	2.186	2.182

The bandwidth limits of the different fiber geometries are reported in table 5.2 but the tendencies can more easily be visualized in Fig. 5.21. The transmission bandwidth becomes narrower and shifts to lower frequencies when the core diameter is increased. Furthermore, increasing the index contrast is also seen to shift the transmission windows to lower frequencies. What is less intuitive, when comparing Figs. 5.21.b) and 5.21.c), is that increasing the core porosity (decreasing the core index) leads to a significant narrowing of the transmission bandwidth in fibers of same diameter.

It should be noted that the upper frequency limit is a strict requirement. We could extend the bandwidth upwards by accepting a second mode, as illustrated by the squares in Fig. 5.21, but a single-mode regime facilitates input coupling and eliminates the perturbative excitation of higher order modes as well as the multi-mode interference effects. The lower frequency limit is less stringent because $(R_{\text{bend}})_{min} = 20$ cm was an arbitrary choice. The fiber *will* guide at lower frequencies, but the permissible

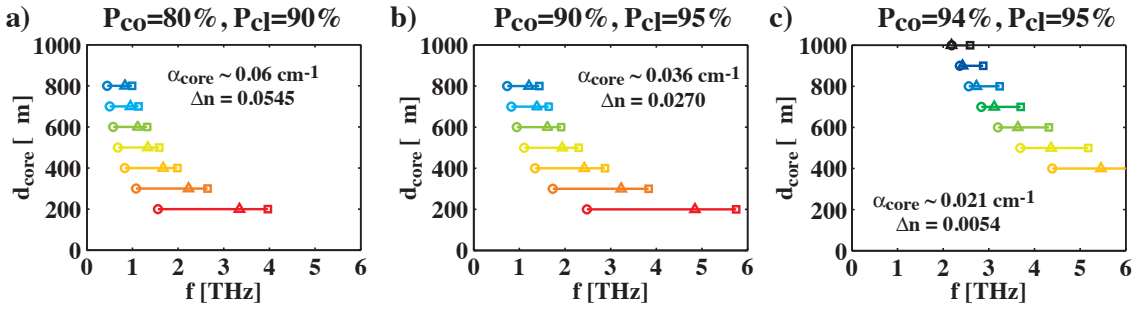

Figure 5.21 Transmission bandwidth of various foam fibers. Circles represent $f_{\min}$ defined by $(R_{\text{bend}})_{min} = 20$ cm. Triangles represent the second mode cutoff point defined by equation (5.21) with $V_{\text{cutoff}} = 2.404$. Squares represent the third mode cutoff point defined by equation (5.21) with $V_{\text{cutoff}} = 2.853$.

bending radii for low bending losses will be larger.

5.5.5 Comment on subwavelength fiber bending loss

We pause momentarily to comment on the bending losses of subwavelength fibers. The foam fiber design may appear similar to the subwavelength fiber designs of chapter 3 but the operating regimes are fundamentally different. To further illustrate this difference we use equation (5.19) to calculate and quantify the bending loss of non-porous subwavelength fibers.

Fig. 5.22.b) presents the straight fiber propagation loss calculated for non-porous subwavelength fibers of different diameters. The core material is assumed to have $n_{\text{core}} = 1.56$ and $\alpha_{\text{core}} = 0.2$ cm^{-1}, which is a reasonable approximation of the material parameters of PE at the frequencies of interest ($f < 0.3$ THz). We now wish to calculate the bending loss at the main fiber transmission frequency. The peak transmission frequency can be approximated in the following manner. Experimentally we found that the fibers have losses around $\alpha_{\text{mode}} \sim 0.02$ cm^{-1}, so if we consider only absorption loss we can state empirically that the fibers guide with $\eta_{\text{core}} \sim 0.10$, because $\alpha_{\text{core}} = 0.2$ cm^{-1}, $\alpha_{\text{clad}} = 0$ cm^{-1}, and $\alpha_{\text{mode}} = \eta_{\text{core}}\alpha_{\text{core}} + \eta_{\text{clad}}\alpha_{\text{clad}}$. We note that $\eta_{\text{core}} \sim 0.10$ corresponds to $V \sim 1.1$ [115], which in turn defines a maximum transmission frequency for a fixed core diameter. For example, $V = 1.1$ yields $f \sim 0.11$ THz for a 800 μm fiber and $f \sim 0.22$ THz for a 400 μm fiber. These frequencies are fairly consistent with the peak transmission frequencies observed in chapter 3 and are used

for the bending loss calculation. Fig. 5.22.c) plots the bending loss as a function of bending radius for the different fiber core diameters and estimated transmission frequencies. As expected, the large evanescent modes suffer from high bending losses and a bending radius on the order of meters (a nearly straight fiber) is required for negligible bending loss.

The $\eta_{\text{core}} \rightarrow 1$ regime of foam fibers significantly reduces the bending losses, permitting lower bending radii which are much more attractive for practical waveguiding applications.

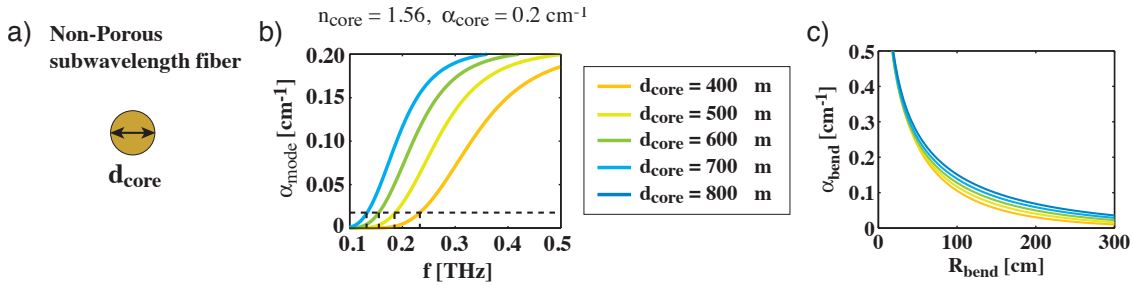

Figure 5.22 Propagation loss in straight and bent non-porous subwavelength fibers. a) Schematization of the geometry. b) Straight fiber propagation loss. c) Bending loss as a function of bending radius, assuming $\eta_{\text{core}} = 0.10$ and $V = 1.1$. A bending radius on the order of meters is required for negligible bending losses.

5.5.6 Encapsulation

For practical reasons it is desirable to encapsulate the foam fiber within a larger solid polymer tube, as illustrated in Fig. 5.23.a). There are two reasons why the addition of an outer polymer tube would be beneficial. Firstly, to facilitate the manipulation of the foam fiber, encapsulation within a solid tube would confer greater mechanical stability. This would allow manipulation and bending of the fiber without squishing or breaking the foam. Secondly, it is the guided mode and not just the foam regions that would be completely encapsulated within the tube. As such, the fiber holder losses and the waveguide cross-talk experienced with subwavelength fibers would be completely eliminated.

In fact, encapsulation of guided mode within the foam regions has an even more fundamental importance. In the case where the foam is formed of *closed cells*, the gas within the cells would be devoid of water vapor. Consequently, guiding within the

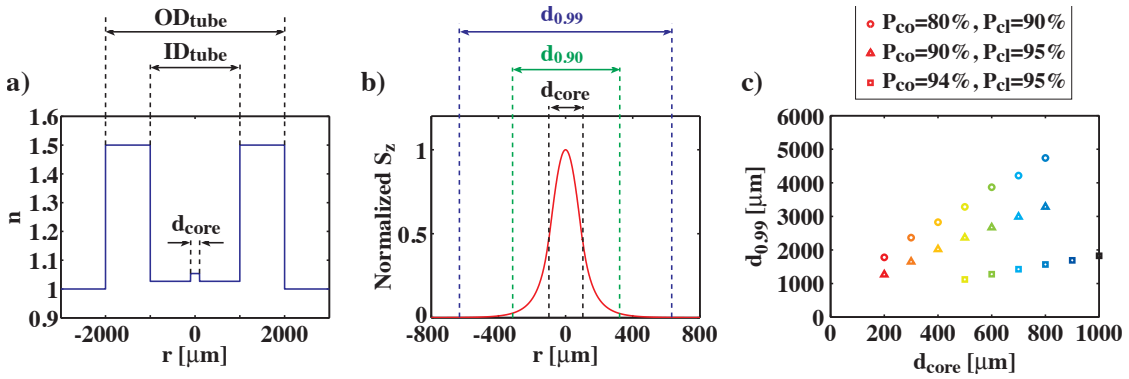

Figure 5.23 Encapsulation of a foam fiber by an outer polymer tube. a) Index profile of a step-index foam fiber encapsulated by an outer polymer tube. ID = Inner Diameter, OD = Outer Diameter. b) Extent of mode is delimited by d_η. $d_{0.90}$ encompasses 90% of the mode power. c) $d_{0.99}$ is plotted for the different foam fiber geometries. A proper design requires $\mathrm{ID_{tube}} \geq d_{0.99}$. Care should be taken in interpreting the results because each point is calculated at a different frequency ($f_{\min}$). Please refer to the text.

foam fiber would eliminate the water vapor absorption problem because the guided THz radiation would never come into contact with water vapor. This makes the foam fiber design very interesting because the water vapor absorption is a serious impediment to the practical application of THz waveguides at frequencies above 1 THz. The solution for other hollow-core waveguides is sealing dry air within the core, but a foam fiber would eliminate the sealing step because the foam would *automatically* be sealed.

Therefore, the remaining requirement is that the guided mode be completely contained within the foam cladding and this can be analyzed by calculating the size of the guided mode. From the typical bell-shaped power distribution of the guided mode (Fig. 5.23.b)) we can see that the size of a mode is an ambiguous notion. A conventional definition is full width at half maximum but here we actually want to evaluate the extent of the tail sections of the mode profile to eliminate all contact with the lossier outer tube material. A more appropriate definition in this case is $d_\eta = 2r_\eta$, which is the diameter that encompasses a certain fraction of power η. For a given

power fraction η, the value of r_η can be found by satisfying the following equation:

$$\eta = \frac{\int_0^{r_\eta} S_z(r) r dr}{\int_0^{\infty} S_z(r) r dr}. \tag{5.22}$$

To avoid contact of the guided mode with the outer encapsulating tube we calculate $d_{0.99}$, the diameter that encompasses 99% of the modal power. Fig. 5.23.c) plots the values of $d_{0.99}$ for the different fiber geometries. Since the mode extent decreases with frequency we consider only the mode size at $f = f_{\min}$, where $f_{\min}$ is the low frequency limit set by permissible bending loss. Care must be taken when comparing the different fiber designs because they are calculated at different frequencies. The lower index contrast fibers have a *more* confined mode because $f_{\min}$ occurs at *higher* frequencies. Smaller core diameter fibers also have smaller $d_{0.99}$ values because $f_{\min}$ occurs at higher frequencies where the mode is more confined. The requirement for the inner diameter of the tube size is $\mathrm{ID}_{\mathrm{tube}} \geq d_{0.99}$. From the results of Fig. 5.23 we conclude that the inner diameter of the encapsulating tube will need to be on the order of a few mm.

5.5.7 Design conclusions

From the preceding results we can make general conclusions about TIR foam fiber design. Firstly, mode confinement is a double edged sword, with more confinement leading to lower bending loss but higher absorption loss. We have seen that to mitigate the effects of bending loss we require a frequency, core diameter, and index contrast such that $\eta_{\mathrm{core}} \to 1$. Consequently, the fiber propagation loss is dominated by absorption and as a general design rule we have considered $\alpha_{\mathrm{mode}} \leq \alpha_{\mathrm{core}}$. We therefore need the lowest possible α_{core} and $P_{\mathrm{co}} \geq 94\%$ would be interesting because $\alpha_{\mathrm{mode}} \leq 0.024$ cm^{-1} would yield an absorption length $L_\alpha \geq 40$ cm. However, we are also limited by the cladding material. For reasons of mechanical stability and encapsulation, we require the cladding to be a foam instead of a dry gas. This is a rather large constraint because the porosity of the cladding foam must necessarily be higher than that of the core, to insure TIR, and would ideally be as different as possible to insure a large enough index contrast. An ideal core/cladding porosity ratio would be 95%/99%.

Secondly, the transmission bandwidth is greatly affected by the core diameter.

The core diameter can be decreased to increase the bandwidth, but the transmission window is shifted to higher frequencies. Guiding a decade of frequencies is difficult and realistically many fibers of different diameter will be required to guide different portions of the THz spectrum. Thirdly, we have seen that encapsulation with an outer polymer tube should be relatively straightforward as a tube diameter of a few mm is sufficient for the inner foam cladding to appear infinite to the THz radiation.

As an aside, we note that the foam fiber could also be operated in the subwavelength fiber regime, where low frequencies have $\eta_{\text{core}} \to 0$. In that case, the foam fiber would be a superior design than the porous subwavelength fibers studied in chapter 3 because encapsulation by an outer tube would greatly facilitate the manipulation of the fiber. Care would have to be taken, however, to insure that outer tube be far enough from the core because $d_{0.99}$ increases considerably at low frequencies.

5.5.8 Discussion on feasibility

Polymer foams are created by mixing a blowing agent into the polymer. Upon heating the blowing agent deteriorates, releasing gas molecules that blow bubbles into the polymer. During the fabrication of a foam fiber preform, it is likely that a gradient of blowing agent would form, resulting in a graded-index foam fiber. In this section we have only considered step-index foam fibers, but it should be stressed that similar results could be obtained with graded-index fibers [115].

A noteworthy fact is that optical fibers drawn with blowing agents are not without precedent. Kominsky *et al.* have fabricated random hole silica fibers by generating bubbles in a powdered silica cladding [176, 177]. Silicon carbide was mixed with silica powder particles to fill the inner cladding of a preform. Upon heating the silicon carbide released CO_2 gas that blew bubbles into the fused glass. Drawing of the fiber stretched the randomly packed bubbles into tubules of random size that were not continuous along the length of the fiber. The geometry that they fabricated was a solid silica core surrounded by a silica foam encapsulated within a larger silica tube. They successfully guided near-infrared light albeit with losses on the order of dB/m. They reported certain fabrication difficulties, notably a tendency for fiber blowout if the concentration of blowing agent was too high. A direct comparison with polymer foams is difficult because the fluid mechanics of glasses are different from that of polymers and the silica foam did not have a porosity as high as what

is commonly achieved with polymer foam. Nevertheless, one would expect that a similar fabrication process could be used with polymers and an important point is that the foam regions in the drawn fiber are expected to have gas tubules instead of spherical gas bubbles.

Another important point is the choice of blowing agent. Zhao *et al.* studied closed cell poly(styrene) foams made with different blowing agents [147]. It was reported that when CO_2 is used as a blowing agent, the small CO_2 gas molecules permeate through the poly(styrene) and are rapidly replaced with air. However, when large 1-chloro-1,1-difluoroethane (HCFC 142b) gas molecules are used as a blowing agent they remain trapped within the polymer for many decades. The down side of HCFC was that it had an absorption peak around ~ 0.5 THz. It should also be remarked that different polymers are expected to have different permeabilities to gas. A proper choice of blowing agent needs to be investigated if the diffusion of water vapor into the closed cells is to be prevented.

Finally, we note that Zhao *et al.* studied poly(styrene) foams with cell sizes ≤ 150 μm [147]. Depending on the actual cell size of the foams within a foam fiber and the expected frequency transmission window, scattering loss simulations would be required to more accurately evaluate the fiber propagation losses.

Chapter 6

CONCLUSION

6.1 Summary of results

In this thesis we have explored a wide variety of dielectric waveguides that rely on many different waveguiding mechanisms to guide THz radiation. We have explored both theoretically and experimentally a large number of waveguide designs with the aim of reducing propagation and bending losses. The different waveguides can be classified into two fundamentally different strategies for reducing the propagation loss: small-core single-mode evanescent-field fibers or large hollow-core multi-mode tubes.

Beyond the design and fabrication of new THz waveguides, the results of this thesis hinged on the proper characterization of the experimental waveguides and this required the development of a novel THz-TDS setup specially adapted for measuring waveguides. By placing mirror assemblies on a translation rail we implemented a versatile THz-TDS setup with a easily adjustable path length capable of accommodating waveguides up to 50 cm in length. With this setup we successfully measured both thin planar samples as well as a variety of THz waveguides, some 40 cm in length.

Our focus was first set on exploring the small-core evanescent-field fiber strategy. Following initial theoretical work in our group, much effort was spent on the fabrication and measurement of evanescent-field *porous* subwavelength fibers. The fabrication of such fibers is a challenge and many novel techniques were devised to properly prepare the preforms and draw the fibers without hole collapse. The first method sealed the holes of an assembly of tubes and lead to fibers of relatively low porosity (25%) due to reduction in hole size during fiber drawing. Development of the novel sacrificial polymer technique enabled complete prevention of hole collapse during the drawing process. Finally, the third method was a combination of preform casting using glass molds and drawing with pressurized air within the holes. This led to fibers of record porosity (86%).

The measurement of these porous fibers began with a collaboration with a group from the university of Sherbrooke. At the time, the only available detector was a frequency integrating liquid-helium-cooled bolometer (powermeter). A novel directional coupler method for measuring the losses of subwavelength fibers was developed whereby an evanescent coupler is formed by bringing a probe fiber in proximity to the sample fiber. By translating the coupling probe fiber along the length of the sample, the propagation loss could be estimated in a non-destructive and repeatable way. Because of the low-pass frequency filtering of the probe fiber and the frequency integration of the detector, the results required careful interpretation and spectral information was limited to the vicinity of 0.2 THz. Subsequent transmission experiments using the adjustable THz-TDS setup enabled the measurement of the full loss spectrum and confirmed the very low propagation loss (< 0.02 cm^{-1} for $f \sim 0.21-0.26$ THz) of the porous subwavelength fibers, among some of the lowest reported losses to date. These measurements further demonstrated that the addition of porosity enables transmission at higher frequencies with a wider transmission window than non-porous subwavelength fibers (full-width-half maximum: $\Delta f_{\text{porous}} = 0.1$ THz, whereas $\Delta f_{\text{non-porous}} = 0.05$ THz).

Much effort was also spent on exploring the hollow-core waveguide strategy with the development of large hollow-core Bragg fibers. Two different methods were proposed and implemented for increasing the refractive index contrast between the layers of the Bragg reflector. The first method consisted of co-rolling a polymer film with powder particles in order to create air layers, leading to an index contrast of $\Delta n = 0.5$ between the polymer and the air. The second method consisted in rolling a bilayer of a TiO_2 doped PE film and a pure PE film. Despite the increased index contrast between the doped and undoped layers ($\Delta n = 1.5$), the overall propagation loss was larger than that of the air-polymer Bragg fiber due to the high absorption loss of the doped films. Although much prior work had been done on planar Bragg reflectors this is the first implementation of a THz Bragg fiber. Unfortunately, in their current implementation the fibers are either too lossy or mechanically unstable.

Finally, many new ideas were proposed for future work on dielectric THz waveguides and initial theoretical investigations were given. For the improvement of THz Bragg fibers, less absorbent dopant materials were considered for doped-polymer Bragg fibers. The effects of bending losses were also investigated as well as the potential for an effectively single-TE_{01}-mode regime. On the other hand, total internal

reflection waveguides were seen to be very promising. PVDF copolymers were proposed as new materials for Attenuated Total Internal Reflection (ATIR) waveguides. Despite the higher cost of the copolymers this solution is very attractive because the formation of a polymer tube is a simpler fabrication process. Finally, we theoretically investigated the design of a Total Internal Reflection (TIR) foam fiber. This waveguide offers the possibility of a truly flexible, low propagation loss, low bending loss fiber that would also solve the water vapor exposure problem by completely encapsulating the THz radiation.

6.2 Limitations to the proposed solutions

6.2.1 Limitations of THz-TDS waveguide setup

There are two major limitations to the implemented THz-TDS setup: a humidity purging problem and the inability of measuring bending losses. Despite many efforts to seal the cage and increase the purging efficiency of the humidity removal, there remains residual traces of water vapor absorption. Although this was not a considerable problem in terms of the resulting source spectrum, the purging time (> 10 hours) and the consumption of dry nitrogen are high. A transition to vacuum pumping should seriously be considered as the purging time would be much faster and, since a low vacuum should be sufficient, it would be a less expensive solution in the long run. It should also be noted that the setup could be *much* more compact since rail #2 turned out to be unnecessary. Reducing the size of the cage should also be considered for alleviating the purging problem. These improvements were not attempted during the course of this thesis because the removal of rail #2 to reduce the size of the cage would require a complete realignment of the THz setup, which is a very time-consuming process.

The second limitation is that free space coupling of the pump laser to the photoconductive antennae requires that the antennae remain static. It would be interesting to have a moveable detector because it would facilitate the measurement of the profile of the THz beam, the profile of the guided modes, and the bending losses of the waveguides. Fiber-coupled antennae would be needed. They are only now starting to become commercially available and they are quite expensive. One complication with fiber-coupled antennae, however, is that the fs-pulse needs to be coupled into

an optical fiber and that dispersion compensation is required to avoid spreading of the pump pulse (THz generation bandwidth is inversely proportional to pump pulse duration) [82].

Further improvements to the setup include decreasing the THz-TDS scan time. One option is using an oscillating delay line [178]. But a simpler option that can give an even greater increase in scan speed is increasing the reference modulation frequency for the lock-in amplifier detection. This can be done by modulating the bias voltage applied to the emitter antenna instead of mechanically chopping the optical pump pulse. This enables a modulation frequency on the order of 30 kHz instead of 300Hz. A higher modulation reference frequency shortens the noise filtering time of the lock-in amplifier and thus reduces the THz-TDS scan time. Perhaps it is even possible to get a high frequency lock-in amplifier and directly use the repetition rate of the laser (80 MHz) as a reference frequency. To our knowledge this has never been demonstrated.

6.2.2 Limitations of THz waveguides

A fundamental point that was only touched upon in this thesis and that is largely unaddressed in the literature [179] is the problem of water vapor absorption and encapsulation. All demonstrations in the literature are made in a laboratory setting with experiments carried out in a controlled environment where the humidity is purged. For real-world applications, it is obvious that waveguides would have to be sealed, such that dry air would be trapped within the waveguide in order to avoid water absorption from humidity in the environment. Note, however, that a demonstration of such waveguide encapsulation has yet to be made. Moreover, sealing a waveguide is not such a trivial task considering the problems we have faced in purging our measurement setup. To address this problem we have proposed an alternative solution whereby closed-cell foams in a foam fiber would automatically isolate the THz radiation from the ambient air without requiring a sealing step.

Furthermore, one of the often cited limitations of certain THz waveguides is dispersion. Spreading of the THz pulse beyond 300 ps (5 cm delay) as a result of dispersion poses a technical problem for the time-domain measurement, because of the maximum delay achievable with certain delay lines and the typically long scan times involved. However, this limitation stems not from the waveguide but from

the use of ultrashort broadband THz pulses for THz-TDS. Other alternatives exist, including CW photomixing and Difference Frequency Generation (DFG) using frequency tunable ns pulsed lasers. In those cases the long THz pulses eliminate the dispersion problem.

Note that the current state of the art yields dielectric waveguides with power absorption coefficients on the order of 0.01 cm^{-1}, i.e. absorption lengths on the order of 1 m or less. This is much lower loss than what was demonstrated 10 years ago but it remains a short working distance. In real-world applications the THz source, or at least the pump laser, needs to be at a certain distance from the sample. With the current impossibility of guiding the THz radiation over large distances, commercial solutions have focused on using an optical fiber link between a pump laser and a THz generation head. When using fs-pulses for THz generation, however, this requires the compensation of dispersion and limits the fiber link to a few meters. Practical solutions in an industrial environment would require a fiber optic link at least an order of magnitude longer, so it is only a question of time before more research on photomixing and DFG gains favor. By avoiding ultrashort pulses, whether in THz waveguides or silica waveguides, the issue of dispersion is avoided altogether.

In the case where THz radiation is generated at a distance from the pump laser, it should be stressed that long THz waveguides are no longer needed. A one meter waveguide could be sufficient provided that the bending losses are sufficiently low. It is therefore believed that bending losses will ultimately be the discriminant between the different THz waveguiding strategies.

Large hollow-core waveguides are currently the leaders in low loss propagation of THz radiation. However, the compromise is entering a highly multi-mode regime that has many drawbacks. Optimization of coupling can favor the excitation of the fundamental mode of these over-moded waveguides, however coupling to lossy higher order modes can nonetheless occur because of subsequent fiber perturbations such as waveguide diameter fluctuations, scattering on defects, and macro-bending. Because a freely bendable waveguide is desired a single-mode regime should therefore be privileged. In this thesis it was seen that evanescent-field fibers are single-mode waveguides with low propagation losses, but that the low confinement of the evanescent mode results in prohibitively high bending losses. In this respect, theoretical simulations predict that single-TE_{01}-mode Bragg fibers and total internal reflection foam fibers are more attractive solutions because of their low bending losses.

6.3 Future research directions

In conclusion, the following three proposals are recommended for future research.

Firstly, the investigations of hollow-core waveguides illustrate the superior waveguiding properties of the TE_{01} mode. Research has shied away from considering TE_{01} mode waveguides because of the difficulty of exciting that mode. However, in the THz regime the advantages of the TE_{01} mode become a necessity and the implementation of such waveguides through the development of new sources and mode convertors for the generation azimuthally polarized TE modes should seriously be considered.

Secondly, P(VDF-TrFE) copolymers warrant investigation because the sheer simplicity of guiding light in a simple polymer tube makes attenuated total internal reflection waveguides an attractive solution.

Thirdly, the development of foam fibers is perhaps the most interesting prospect. The potential of tailoring bulk material properties would enable the design of low loss total internal reflection waveguides. Moreover, in contrast to a porosity stemming from large holes, a foam is a self-supporting porous structure due to the small reticulated walls filling the entire space. Finally, and perhaps most interesting of all, a foam fiber could be a self-sealed waveguide where the THz radiation is completely encapsulated within a waveguide, and where dry gas is automatically sealed within the closed cells of the foam. Such a fiber would solve the problems of low propagation loss, low bending loss, and exposure to water vapor simultaneously.

References

[1] S. Dexheimer, Ed., *Terahertz Spectroscopy: Principles and Applications*. Boca Raton, USA: CRC Press, 2008.

[2] D. Mittleman, *Sensing with Terahertz Radiation*. Heidelberg: Springer, 2002.

[3] M. Nagel, P. Haring Bolivar, M. Brucherseifer, H. Kurz, A. Bosserhoff, and R. Büttner, "Integrated THz technology for label-free genetic diagnostics," *Applied Physics Letters*, vol. 80, no. 1, pp. 154–156, 2002.

[4] Y. Ogawa, S. Hayashi, M. Oikawa, C. Otani, and K. Kawase, "Interference terahertz label-free imaging for protein detection on a membrane," *Optics Express*, vol. 16, no. 26, pp. 22 083–22 089, 2008.

[5] J. Xu, K. W. Plaxco, and S. J. Allen, "Probing the collective vibrational dynamics of a protein in liquid water by terahertz absorption spectroscopy," *Protein Science*, vol. 15, pp. 1175–1181, 2006.

[6] B. Yu, F. Zeng, Y. Yang, Q. Xing, A. Chechin, X. Xin, I. Zeylikovich, and R. R. Alfano, "Torsional Vibrational Modes of Tryptophan Studied by Terahertz Time-Domain Spectroscopy," *Biophysical Journal*, vol. 86, pp. 1649–1654, 2004.

[7] K. Yamamoto, M. Yamaguchi, F. Miyamaru, M. Tani, M. Hangyo, T. Ikeda, A. Matsuchita, K. Koide, M. Tatsuno, and Y. Minami, "Noninvasive Inspection of C-4 Explosive in Mails by Terahertz Time-Domain Spectroscopy," *Japanese Journal of Applied Physics*, vol. 43, no. 3B, pp. L414–L417, 2004.

[8] D. J. Hilton, R. P. Pransankumar, S. A. Trugman, A. J. Taylor, and R. D. Averitt, "On Photo-Induced Phenomena in Complex Materials: Probing Quasiparticle Dynamics using Infrared and Far-Infrared Pulses," *J. Phys. Soc. Jpn.*, vol. 75, p. 011006, 2006.

[9] B. B. Hu and M. C. Nuss, "Imaging with terahertz waves," *Optics Letters*, vol. 20, pp. 1716–1719, 1995.

[10] J. Pearce, H. Choi, D. M. Mittleman, J. White, and D. Zimdars, "Terahertz wide aperture reflection tomography," *Optics Letters*, vol. 30, no. 13, pp. 1653–1655, 2005.

[11] D. M. Mittleman, S. Hunsche, L. Boivin, and M. C. Nuss, "T-ray tomography," *Optics Letters*, vol. 22, no. 12, pp. 904–906, 1997.

[12] S. Hunsche, M. Koch, I. Brener, and M. C. Nuss, "THz near-field imaging," *Optics Communications*, vol. 150, pp. 22–26, 1998.

[13] B. Ferguson, S. Wang, D. Gray, D. Abbot, and X. C. Zhang, "T-ray computed tomography," *Optics Letters*, vol. 27, no. 15, pp. 1312–1314, 2002.

[14] A. Bandyopadhyay, A. Stepanov, B. Schulkin, M. D. Federici, A. Sengupta, D. Gary, J. F. Federici, R. Barat, and Z.-H. Michalopoulou, "Terahertz interferometric and synthetic aperture imaging," *J. Opt. Soc. Am. A*, vol. 23, no. 5, pp. 1168–1178, 2006.

[15] T. Löffler, T. Bauer, K. J. Siebert, H. G. Roskos, A. Fitzgerald, and S. Czasch, "Terahertz dark-field imaging of biomedical tissue," *Optics Express*, vol. 9, no. 12, pp. 616–621, 2001.

[16] C.-M. Chiu, H.-W. Chen, Y.-R. Huang, Y.-J. Hwang, W.-J. Lee, H.-Y. Huang, and C.-K. Sun, "All-terahertz fiber-scanning near-field microscopy," *Optics Letters*, vol. 34, no. 7, pp. 1084–1086, 2009.

[17] N. Karpowicz, H. Zhong, J. Xu, K.-I. Lin, J.-s. Hwang, and X.-C. Zhang, "Comparison between pulsed terahertz time-domain imaging and continuous wave terahertz imaging," *Semicond. Sci. Technol.*, vol. 20, pp. S293–S299, 2005.

[18] N. Krumbholz, T. Hochrein, N. Vieweg, T. Hasek, K. Kretschmer, M. Bastian, M. Mikulics, and M. Koch, "Monitoring polymeric compounding processes inline with THz time-domain spectroscopy," *Polymer Testing*, vol. 28, no. 1, pp. 30–35, 2009. [Online]. Available: http://dx.doi.org/10.1016/j.polymertesting.2008.09.009

[19] J. A. Zeitler, P. F. Taday, D. A. Newnham, M. Pepper, K. C. Gordon, and T. Rades, "Terahertz pulsed spectroscopy and imaging in the pharmaceutical

setting - a review," *Journal of Pharmacy and Pharmacology*, vol. 59, pp. 209–223, 2007.

[20] N. Karpowicz, H. Zhong, C. Zhang, K.-I. Lin, J.-S. Hwang, J. Xu, and X. C. Zhang, "Compact continuous-wave subterahertz system for inspection applications," *Applied Physics Letters*, vol. 86, p. 054105, 2005.

[21] K. Kawase, Y. Ogawa, Y. Watanabe, and H. Inoue, "Non-destructive terahertz imaging of illicit drugs using spectral fingerprints," *Optics Express*, vol. 11, no. 20, pp. 2549–2554, 2003.

[22] T. Kiwa, M. Tonouchi, M. Yamashita, and K. Kawase, "Laser terahertz-emission microscope for inspecting electrical faults in integrated circuits," *Optics Letters*, vol. 28, no. 21, pp. 2058–2060, 2003.

[23] J. A. Harrington, "A Review of IR Transmitting, Hollow Waveguides," *Fiber & Integrated Optics*, vol. 19, no. 3, pp. 211–227, Jul. 2000.

[24] S. G. Johnson, M. Ibanescu, M. Skorobogatiy, O. Weisberg, T. D. Engeness, M. Soljacic, S. A. Jacobs, J. D. Joannopoulos, and Y. Fink, "Low-loss asymptotically single-mode propagation in large-core OmniGuide fibers," *Optics Express*, vol. 9, no. 13, pp. 748–779, 2001.

[25] M. Y. Frankel, S. Gupta, J. A. Valdmanis, and G. A. Mourou, "Terahertz Attenuation and Dispersion Characteristics of Coplanar Transmission Lines," *IEEE Transactions on Microwave Theory and Techniques*, vol. 39, no. 6, pp. 910–916, 1991.

[26] R. W. Mcgowan, G. Gallot, and D. Grischkowsky, "Propagation of ultrawideband short pulses of terahertz radiation through submillimeter-diameter circular waveguides," *Optics Letters*, vol. 24, no. 20, pp. 1431–1433, 1999.

[27] G. Gallot, S. P. Jamison, R. W. Mcgowan, and D. Grischkowsky, "Terahertz waveguides," *J. Opt. Soc. Am. B.*, vol. 17, no. 5, pp. 851–863, 2000.

[28] E. Garmire, T. McMahon, and M. Bass, "Flexible Infrared Waveguides for High-Power Transmission," *IEEE Journal of Quantum Electronics*, vol. QE-16, no. 1, pp. 23–32, 1980.

[29] T. Hidaka, T. Morikawa, and J. Shimada, "Hollow-core oxide-glass cladding fibers for middle-infrared region," *J. Appl. Phys.*, vol. 52, no. 7, pp. 4467–4471, 1981.

[30] M. Miyagi and S. Kawakami, "Design Theory of Dielectric-Coated Circular Metallic Waveguides for Infrared Transmission," *Journal of Lightwave Technology*, vol. LT-2, no. 2, pp. 116–126, 1984.

[31] J. Obrzut and P. F. Goldsmith, "Flexible Circular Waveguides at Millimeter Wavelengths from Metallized Teflon Tubing," *IEEE Transactions on Microwave Theory and Techniques*, vol. 38, no. 3, pp. 324–327, 1990.

[32] T. Ito, Y. Matsuura, M. Miyagi, H. Minamide, and H. Ito, "Flexible terahertz fiber optics with low bend-induced losses," *J. Opt. Soc. Am. B*, vol. 24, no. 5, pp. 1230–1235, 2007.

[33] J. A. Harrington, R. George, P. Pedersen, and E. Mueller, "Hollow polycarbonate waveguides with inner Cu coatings for delivery of terahertz radiation," *Optics Express*, vol. 12, no. 21, pp. 5263–5268, 2004.

[34] B. Bowden, J. A. Harrington, and O. Mitrofanov, "Fabrication of terahertz hollow-glass metallic waveguides with inner dielectric coatings," *J. Appl. Phys.*, vol. 104, p. 093110, 2008.

[35] R. Mendis and D. Grischkowsky, "THz Interconnect With Low-Loss and Low-Group Velocity Dispersion," *IEEE Microwave and Wireless Components Letters*, vol. 11, no. 11, pp. 444–446, 2001.

[36] R. Mendis and D. Grischkowsky, "Undistorted guided-wave propagation of subpicosecond terahertz pulses," *Optics Letters*, vol. 26, no. 11, pp. 846–848, 2001.

[37] S. Coleman and D. Grischkowsky, "Parallel plate THz transmitter," *Applied Physics Letters*, vol. 84, no. 5, pp. 654–656, 2004.

[38] A. Bingham, Y. Zhao, and D. Grischkowsky, "THz parallel plate photonic waveguides," *Appl. Phys. Lett.*, vol. 87, p. 051101, 2005.

[39] A. L. Bingham and D. Grischkowsky, "High-Q, one-dimensional terahertz photonic waveguides," *Appl. Phys. Lett.*, vol. 90, p. 091105, 2007.

[40] Z. Jian, J. Pearce, and D. M. Mittleman, "Two-dimensional photonic crystal slabs in parallel-plate metal waveguides studied with terahertz time-domain spectroscopy," *Semicond. Sci. Technol.*, vol. 20, no. 7, pp. S300–S306, 2005.

[41] R. Mendis and D. M. Mittleman, "An Ultra Low Loss THz Waveguide," in *CLEO 2008*, 2008, p. CPDA5.

[42] R. Mendis and D. M. Mittleman, "Comparison of the lowest-order transverse-electric (TE1) and transverse-magnetic (TEM) modes of the parallel-plate waveguide for terahertz pulse applications," *Optics Express*, vol. 17, no. 17, pp. 14 839–14 850, 2009.

[43] E. S. Lee, J. S. Jang, S. H. Kim, Y. B. Ji, and T.-i. Jeon, "Propagation of single-mode and multi-mode terahertz radiation through a parallel-plate waveguide," *Journal of the Korean Physical Society*, vol. 53, no. 4, pp. 1891–1896, 2008.

[44] K. Wang and D. M. Mittleman, "Metal wires for terahertz wave guiding," *Nature*, vol. 432, pp. 376–279, 2004.

[45] H. Cao and A. Nahata, "Coupling of terahertz pulses onto a single metal wire waveguide using milled grooves," *Optics Express*, vol. 13, no. 18, pp. 7028–7034, 2005.

[46] Q. Cao and J. Jahns, "Azimuthally polarized surface plasmons as effective terahertz waveguides," *Optics Express*, vol. 13, no. 2, pp. 511–518, 2005.

[47] M. Wächter, M. Nagel, and H. Kurz, "Frequency-dependent characterization of THz Sommerfeld wave propagation on single-wires," *Optics Express*, vol. 13, no. 26, pp. 10 815–10 822, 2005.

[48] T.-I. Jeon, J. Zhang, and D. Grischkowsky, "THz Sommerfeld wave propagation on a single metal wire," *Appl. Phys. Lett.*, vol. 86, pp. 161 904–161 906, 2005.

[49] J. A. Deibel, K. Wang, M. D. Escarra, and D. M. Mittleman, "Enhanced coupling of terahertz radiation to cylindrical wire waveguides," *Optics Express*, vol. 14, no. 1, pp. 279–290, 2006.

[50] V. Astley, J. Scheiman, R. Mendis, and D. M. Mittleman, "Bending and coupling losses in terahertz wire waveguides," *Optics Letters*, vol. 35, no. 4, pp. 553–555, 2010.

[51] M. Mbonye, R. Mendis, and D. M. Mittleman, "A terahertz two-wire waveguide with low bending loss," *Appl. Phys. Lett.*, vol. 95, pp. 233 506–233 508, 2009.

[52] T.-I. Jeon and D. Grischkowsky, "THz Zenneck surface wave (THz surface plasmon) propagation on a metal sheet," *Applied Physics Letters*, vol. 88, p. 061113, 2006. [Online]. Available: http://link.aip.org/link/APPLAB/v88/i6/p061113/s1&Agg=doi

[53] Y.-S. Jin, G.-J. Kim, and S.-G. Jeon, "Terahertz Dielectric Properties of Polymers," *Journal of the Korean Physical Society*, vol. 49, pp. 513–517, 2006.

[54] A. Sengupta, A. Bandyopadhyay, B. F. Bowden, J. A. Harrington, and J. F. Federici, "Characterisation of olefin copolymers using terahertz spectroscopy," *Electronics Letters*, vol. 42, no. 25, 2006.

[55] M. Goto, A. Quema, H. Takahashi, S. Ono, and N. Sarukura, "Teflon Photonic Crystal Fiber as Terahertz Waveguide," *Japanese Journal of Applied Physics*, vol. 43, no. 2B, pp. L317–L319, 2004.

[56] S. P. Jamison, R. W. Mcgowan, and D. Grischkowsky, "Single-mode waveguide propagation and reshaping of sub-ps terahertz pulses in sapphire fibers," *Applied Physics Letters*, vol. 76, no. 15, pp. 1987–1989, 2000.

[57] R. Mendis and D. Grischkowsky, "Plastic ribbon THz waveguides," *Journal of Applied Physics*, vol. 88, no. 7, pp. 4449–4451, 2000.

[58] L.-J. Chen, H.-W. Chen, T.-F. Kao, J.-Y. Lu, and C.-K. Sun, "Low-loss subwavelength plastic fiber for terahertz waveguiding," *Optics Letters*, vol. 31, no. 3, pp. 308–310, 2006.

[59] H.-W. Chen, Y.-T. Li, C.-L. Pan, J.-L. Kuo, J.-Y. Lu, L.-J. Chen, and C.-K. Sun, "Investigation on spectral loss characteristics of subwavelength terahertz fibers," *Optics Letters*, vol. 32, no. 9, pp. 1017–1019, 2007.

[60] M. Nagel, A. Marchewka, and H. Kurz, "Low-index discontinuity terahertz waveguides," *Optics Express*, vol. 14, no. 21, pp. 9944–9954, 2006.

[61] A. Dupuis, J.-F. Allard, D. Morris, K. Stoeffler, C. Dubois, and M. Skorobogatiy, "Fabrication and THz loss measurements of porous subwavelength fibers using a directional coupler method," *Optics Express*, vol. 17, pp. 8012–8028, 2009.

[62] A. Dupuis, A. Mazhorova, F. Desevedavy, M. Roze, and M. Skorobogatiy, "Spectral characterization of porous dielectric subwavelength THz fibers fabricated using a microstructured molding technique," *Optics Express*, vol. 18, pp. 13 813–13 828, 2010.

[63] J.-Y. Lu, C.-C. Kuo, C.-M. Chiu, H.-W. Chen, Y.-J. Hwang, C.-L. Pan, and C.-K. Sun, "THz interferometric imaging using subwavelength plastic fiber based THz endoscopes," *Optics Express*, vol. 16, no. 4, pp. 2494–2501, 2008.

[64] J.-Y. Lu, C.-M. Chiu, C.-C. Kuo, C.-H. Lai, H.-C. Chang, Y.-J. Hwang, C.-L. Pan, and C.-K. Sun, "Terahertz scanning imaging with a subwavelength plastic fiber," *Appl. Phys. Lett.*, vol. 92, p. 084102, 2008.

[65] M. Cho, J. Kim, H. Park, Y. Han, K. Moon, E. Jung, and H. Han, "Highly birefringent terahertz polarization maintaining plastic photonic crystal fibers," *Optics Express*, vol. 16, no. 1, pp. 7–12, 2008.

[66] H. Han, H. Park, M. Cho, and J. Kim, "Terahertz pulse propagation in a plastic photonic crystal fiber," *Applied Physics Letters*, vol. 80, no. 15, pp. 2634–2636, 2002.

[67] H. Park, M. Cho, J. Kim, and H. Han, "Terahertz pulse transmission in plastic photonic crystal fibres," *Phys. Med. Biol.*, vol. 43, pp. 3765–3769, 2002.

[68] C. S. Ponseca, R. Pobre, E. Estacio, N. Sarukura, A. Argyros, M. C. J. Large, and M. A. V. Eijkelenborg, "Transmission of terahertz radiation using a microstructured polymer optical fiber," *Optics Letters*, vol. 33, no. 9, pp. 902–904, 2008.

[69] K. Nielsen, H. K. Rasmussen, A. J. L. Adam, P. C. Planken, O. Bang, and P. U. Jepsen, "Bendable, low-loss Topas fibers for the terahertz frequency range," *Optics Express*, vol. 17, no. 10, pp. 8845–8854, 2009.

[70] Y. F. Geng, X. L. Tan, P. Wang, and J. Q. Yao, "Transmission loss and dispersion in plastic terahertz photonic band-gap fibers," *Appl. Phys. B.*, vol. 91, pp. 333–336, 2008.

[71] G. Ren, Y. Gong, P. Shum, X. Yu, and J. Hu, "Polarization Maintaining Air-Core Bandgap Fibers for Terahertz Wave Guiding," *IEEE Journal of Quantum Electronics*, vol. 45, no. 5, pp. 506–513, 2009.

[72] T. Hidaka, H. Minamide, H. Ito, J.-I. Nishizawa, K. Tamura, and S. Ichikawa, "Ferroelectric PVDF Cladding Terahertz Waveguide," *Journal of Lightwave Technology*, vol. 23, no. 8, pp. 2469–2473, 2005.

[73] C.-H. Lai, Y.-C. Hsueh, H.-W. Chen, Y.-J. Huang, H.-C. Chang, and C.-K. Sun, "Low-index terahertz pipe waveguides," *Optics Letters*, vol. 34, no. 21, pp. 3457–3459, 2009.

[74] C.-H. Lai, B. You, J.-Y. Lu, T.-A. Liu, J.-L. Peng, C.-K. Sun, and H.-C. Chang, "Modal characteristics of antiresonant reflecting pipe waveguides for terahertz waveguiding," *Optics Express*, vol. 18, no. 1, pp. 309–322, 2010.

[75] J.-Y. Lu, C.-P. Yu, H.-C. Chang, H.-W. Chen, Y.-T. Li, C.-L. Pan, and C.-K. Sun, "Terahertz air-core microstructure fiber," *Appl. Phys. Lett.*, vol. 92, p. 064105, 2008.

[76] A. Dupuis, K. Stoeffler, B. Ung, C. Dubois, and M. Skorobogatiy, "THz transmission measurements of hollow-core Bragg fibers," *J. Opt. Soc. Am. B (Submitted)*, 2010.

[77] M. Skorobogatiy and A. Dupuis, "Ferroelectric all-polymer hollow Bragg fibers for terahertz guidance," *Appl. Phys. Lett.*, vol. 90, p. 113514, 2007.

[78] R.-J. Yu, B. Zhang, Y.-Q. Zhang, C.-Q. Wu, Z.-G. Tian, and X.-Z. Bai, "Proposal for Ultralow Loss Hollow-Core Plastic Bragg Fiber With Cobweb-Structured Cladding for Terahertz Waveguiding," *Photonics Technology Letters*, vol. 19, no. 12, pp. 910–912, 2007.

[79] M. Miyagi and S. Nishida, "A Proposal of Low-Loss Leaky Waveguide for Submillimeter Waves Transmission," *IEEE Transactions on Microwave Theory and Techniques*, vol. MIT-28, no. 4, pp. 398–401, 1980.

[80] G. W. Chantry, *Submillimetre spectroscopy.* London, England: Academic Press, 1971.

[81] D. K. Lambert and P. L. Richards, "Martin-Puplett interferometer: an analysis," *Applied Optics*, vol. 17, no. 10, pp. 1595–1602, 1978.

[82] M. Hoffmann, "Novel Techniques in THz-Time-Domain-Spectroscopy," Ph.D. dissertation, Albert-Ludwigs-Universität, Freiburg, 2006.

[83] K. Sakai, Ed., *Terahertz Optoelectronics.* Berlin, Germany: Springer-Verlag, 2005.

[84] M. Tonouchi, "Cutting-edge terahertz technology," *Nature Photonics*, vol. 1, pp. 97–105, 2007.

[85] J. M. Chamberlain, "Where optics meets electronics : recent progress in decreasing the terahertz gap," *Phil. Trans. R Soc. Lond. A*, vol. 362, pp. 199–213, 2004.

[86] J. R. Morris and Y. R. Shen, "Theory of far-infrared generation by optical mixing," *Physical Review A*, vol. 15, no. 3, pp. 1143–1156, 1977.

[87] J. Hebling, A. Stepanov, G. Almasi, B. Bartal, and J. Kuhl, "Tunable THz pulse generation by optical rectification of ultrashort laser pulses with tilted pulse fronts," *Applied Physics B: Lasers and Optics*, vol. 78, no. 5, pp. 593–599, Mar. 2004. [Online]. Available: http://www.springerlink.com/openurl.asp?genre=article&id=doi:10.1007/s00340-004-1469-7

[88] A. G. Stepanov, J. Kuhl, I. Kozma, E. Riedle, G. Almási, and J. Hebling, "Scaling up the energy of THz pulses created by optical rectification." *Optics Express*, vol. 13, no. 15, pp. 5762–5768, Jul. 2005. [Online]. Available: http://www.ncbi.nlm.nih.gov/pubmed/19498579

[89] R. W. Boyd, *Nonlinear Optics.* San Diego, USA: Academic Press, 1992.

[90] Y. J. Ding and I. B. Zotova, "Second-order nonlinear optical materials for efficient generation and amplification of temporally-coherent and narrow-linewidth terahertz waves," *Optical and Quantum Electronics*, vol. 32, pp. 531–552, 2000.

[91] F. G. Sun, W. Ji, and X.-C. Zhang, "Two-photon absorption induced saturation of THz radiation in ZnTe," *Conference on Lasers and Electro-Optics, OSA Technichal Digest*, pp. 479–480, 2000.

[92] H. Zhong, N. Karpowicz, and X.-C. Zhang, "Terahertz emission profile from laser-induced air plasma," *Applied Physics Letters*, vol. 88, p. 261103, 2006. [Online]. Available: http://link.aip.org/link/APPLAB/v88/i26/p261103/s1&Agg=doi

[93] X. Mu, Y. J. Ding, and Y. B. Zotova, "Transition from photocurrent surge to resonant optical rectification for terahertz generation in p-InAs." *Optics letters*, vol. 32, no. 22, pp. 3321–3323, Nov. 2007. [Online]. Available: http://www.ncbi.nlm.nih.gov/pubmed/18026294

[94] G. Gallot and D. Grischkowsky, "Electro-optic detection of terahertz radiation," *J. Opt. Soc. Am. B*, vol. 16, no. 8, pp. 1204–1212, Aug. 1999. [Online]. Available: http://www.opticsinfobase.org/abstract.cfm?URI=josab-16-8-1204

[95] L. Duvillaret, F. Garet, J.-F. Roux, and J.-L. Coutaz, "Analytical Modeling and Optimization of Terahertz Time-Domain Spectroscopy Experiments Using Photoswitches as Antennas," *IEEE Journal on Selected Topics in Quantum Electronics*, vol. 7, no. 4, pp. 615–623, 2001.

[96] D. H. Auston, K. P. Chueng, and P. R. Smith, "Picosecond photoconducting Hertzian dipoles," *Appl. Phys. Lett.*, vol. 45, pp. 284–286, 1984.

[97] S. Winnerl, B. Zimmermann, F. Peter, H. Schneider, and M. Helm, "Terahertz Bessel-Gauss beams of radial and azimuthal polarization from microstructured photoconductive antennas," *Optics Express*, vol. 17, no. 3, pp. 1571–1576, 2009.

[98] P. A. Temple, "An introduction to phase-sensitive amplifiers: An inexpensive student instrument," *American Journal of Physics*, vol. 43, no. 9, pp. 801–807, 1975.

[99] Wikipedia, "Taxicab geometry," *(Retrieved 05/10/2010)*. [Online]. Available: http://en.wikipedia.org/wiki/Taxicab_geometry

[100] Y. H. Lee, "Alignment of an off-axis parabolic mirror with two parallel He-Ne laser beams," *Optical Engineering*, vol. 31, no. 11, pp. 2287–2292, 1992.

[101] D. E. Gray, Ed., *American Institute of Physics Handbook*. New York, USA: McGraw-Hill, 1972.

[102] A. E. Siegman, *Lasers*. Sausalito, USA: University Science Books, 1986, ch. 17, p. 1283.

[103] M. T. Reiten, S. A. Harmon, and R. A. Cheville, "Terahertz beam propagation measured through three-dimensional amplitude profile determination," *J. Opt. Soc. Am. B*, vol. 20, no. 10, pp. 2215–2225, 2003.

[104] M. Van Exter, C. Fattinger, and D. Grischkowsky, "Terahertz time-domain spectroscopy of water vapor," *Optics Letters*, vol. 14, no. 20, pp. 1128–1130, 1989.

[105] F. Blanchard, L. Razzari, H. C. Bandulet, G. Sharma, R. Morandotti, J. C. Kieffer, T. Ozaki, M. Reid, H. F. Tiedje, H. K. Haugen, and F. A. Hegmann, "Generation of 1.5 microJ single-cycle terahertz pulses by optical rectification from a large aperture ZnTe crystal." *Optics Express*, vol. 15, no. 20, pp. 13 212–13 220, Oct. 2007. [Online]. Available: http://www.ncbi.nlm.nih.gov/pubmed/19550589

[106] T. Taniuchi and H. Nakanishi, "Continuously tunable terahertz-wave generation in GaP crystal by collinear difference frequency mixing," *Electronics Letters*, vol. 40, no. 5, 2004.

[107] J.-I. Nishizawa, K. Suto, T. Sasaki, T. Tanabe, and T. Kimura, "Spectral measurement of terahertz vibrations of biomolecules using a GaP terahertz-wave generator with automatic scanning control," *Journal of Physics D: Applied Physics*, vol. 36, pp. 2958–2961, Dec. 2003. [Online]. Available: http://stacks.iop.org/0022-3727/36/i=23/a=015?key=crossref.0c1de813e6494ea08b3407f141b64eef

[108] A. Bartels, A. Thoma, C. Janke, T. Dekorsy, A. Dreyhaupt, S. Winnerl, and M. Helm, "High-resolution THz spectrometer with kHz scan rates," *Optics Express*, vol. 14, no. 1, p. 430, 2006. [Online]. Available: http://www.opticsexpress.org/abstract.cfm?URI=OPEX-14-1-430

[109] R. Guo, K. Akiyama, H. Minamide, and H. Ito, "Frequency-agile terahertz-wave spectrometer for high-resolution gas sensing," *Applied Physics Letters*, vol. 90, no. 12, p. 121127, 2007. [Online]. Available: http://link.aip.org/link/APPLAB/v90/i12/p121127/s1&Agg=doi

[110] C. Zhao, M. Wu, D. Fan, and S. Wen, "Field enhancement and power distribution characteristics of subwavelength-diameter terahertz hollow optical fiber," *Optics Communitions*, vol. 281, pp. 1129–1133, 2008.

[111] A. Hassani, A. Dupuis, and M. Skorobogatiy, "Low loss porous terahertz fibers containing multiple subwavelength holes," *Applied Physics Letters*, vol. 92, p. 071101, 2008.

[112] A. Hassani, A. Dupuis, and M. Skorobogatiy, "Porous polymer fibers for low-loss Terahertz guiding," *Optics Express*, vol. 16, no. 9, pp. 6340–6351, 2008.

[113] S. Atakaramians, S. A. V, B. M. Fischer, D. Abbott, and T. M. Monro, "Porous fibers : a novel approach to low loss THz waveguides," *Optics Express*, vol. 16, no. 12, pp. 8845–8854, 2008.

[114] A. W. Snyder and J. D. Love, *Optical Waveguide Theory*. New York: Chapman and Hall, 1983.

[115] J. Bures, *Guided Optics*. Weinheim, Germany: Wiley-VCH, 2009.

[116] J. C. Knight, "Photonic crystal fibres," *Nature*, vol. 424, pp. 847–851, 2003.

[117] C. Jansen, S. Member, F. Neubauer, J. Helbig, D. M. Mittleman, and M. Koch, "Flexible Bragg reflectors for the terahertz regime composed of polymeric compounds," in *IRMMW*, 2007, pp. A–TjKh–NN4N.

[118] A. Boudrioua and J. C. Loulergue, "New approach for loss measurements in optical planar waveguides," *Optics Communications*, vol. 137, pp. 37–40, 1997.

[119] Wikipedia, "Fisherman's Knot," *(Retrieved 23/08/2010)*. [Online]. Available: http://en.wikipedia.org/wiki/Fisherman's_knot

[120] S. Atakaramians, S. A. V, H. Ebendorff-Heidepriem, M. Nagel, B. M. Fischer, D. Abbott, and T. M. Monro, "THz porous fibers : design, fabrication and experimental characterization," *Optics Express*, vol. 17, no. 16, pp. 14 053–14 062, 2009.

[121] S. Guo, S. Albin, and R. S. Rogowski, "Comparative analysis of Bragg fibers," *Optics Express*, vol. 12, no. 1, 2004.

[122] M. Sumetsky, "How thin can a microfiber be and still guide light?" *Optics Letters*, vol. 31, no. 7, pp. 870–872, Apr. 2006. [Online]. Available: http://www.ncbi.nlm.nih.gov/pubmed/16599195

[123] M. Sumetsky, "How thin can a microfiber be and still guide light? Errata," *Optics Letters*, vol. 31, no. 24, pp. 3577–3576, Jan. 2006. [Online]. Available: http://www.ncbi.nlm.nih.gov/pubmed/21151432

[124] B. You, T.-a. Liu, J.-l. Peng, C.-l. Pan, and J.-y. Lu, "A terahertz plastic wire based evanescent field sensor for high sensitivity liquid detection," *Optics Express*, vol. 17, no. 23, pp. 20 675–20 683, 2009.

[125] G. P. Agrawal, *Nonlinear Fiber Optics*, 3rd ed. San Diego, USA: Academic Press, 2001.

[126] E. Pone, C. Dubois, N. Guo, Y. Gao, A. Dupuis, F. Boismenu, S. Lacroix, and M. Skorobogatiy, "Drawing of the hollow all-polymer Bragg fibers," *Optics Express*, vol. 14, no. 13, pp. 5838–5852, 2006.

[127] D. Grischkowsky, S. Keiding, M. V. Exter, and C. Fattinger, "Far-infrared time-domain spectroscopy with terahertz beams of dielectrics and semiconductors," *J. Opt. Soc. Am. B*, vol. 7, no. 10, pp. 2006–2015, 2006.

[128] M. A. Duguay, Y. Kokubun, T. L. Koch, and L. Pfeiffer, "Antiresonant reflecting optical waveguides in SiO-Si multilayer structures," *Applied Physics Letters*, vol. 49, pp. 13–15, 1986.

[129] H. A. Haus, *Waves and Fields in Optoelectronics*. Englewood Cliffs, New Jersey: Prentice-Hall, 1984.

[130] D. Turchinovich, A. Kammoun, P. Knobloch, T. Dobbertin, and M. Koch, "Flexible all-plastic mirrors for the THz range," *Appl. Phys. A*, vol. 74, pp. 291–293, 2002.

[131] W. Withayachumnankul, B. M. Fischer, and D. Abbott, "Quarter-wavelength multilayer interference filter for terahertz waves," *Optics Communications*, vol. 281, pp. 2374–2379, 2008.

[132] Y. Han, M. Cho, H. Park, K. Moon, E. Jung, and H. Han, "Terahertz Time-domain Spectroscopy of Ultra-high Reflectance Photonic Crystal Mirrors," *Journal of the Korean Physical Society*, vol. 55, no. 2, pp. 508–511, 2009.

[133] C. Jansen, S. Wietzke, V. Astley, D. M. Mittleman, and M. Koch, "Fully Flexible Terahertz Bragg Reflectors Based on Titania Loaded Polymers," in *CLEO*, vol. 2, 2008, p. CTuN1.

[134] S.-Z. Lo and T. E. Murphy, "Nanoporous silicon multilayers for terahertz filtering," *Optics Letters*, vol. 34, no. 19, pp. 2921–2923, 2009.

[135] P. Yeh, A. Yariv, and E. Marom, "Theory of Bragg fiber," *Journal of the Optical Society of America*, vol. 68, no. 9, pp. 1196–1201, Sep. 1978. [Online]. Available: http://www.opticsinfobase.org/abstract.cfm?URI=josa-68-9-1196

[136] S. Wietzke, C. Jansen, F. Rutz, D. M. Mittleman, and M. Koch, "Determination of additive content in polymeric compounds with terahertz time-domain spectroscopy," *Polymer Testing*, vol. 26, pp. 614–618, 2007.

[137] M. Skorobogatiy and J. Yang, *Fundamentals of photonic crystal guiding*. New York, USA: Cambridge University Press, 2009.

[138] Y. Xu, R. K. Lee, and A. Yariv, "Asymptotic analysis of Bragg fibers," *Optics Letters*, vol. 25, no. 24, pp. 1756–1758, 2000.

[139] P. Yeh, A. Yariv, and C.-S. Hong, "Electromagnetic propagation in periodic stratified media. I. General theory," *J. Opt. Soc. Am.*, vol. 67, no. 4, pp. 423–438, 1977.

[140] M. Miyagi and S. Nishida, "Transmission characteristics of dielectric tube leaky waveguide," *IEEE transactions on Microwave Theory and Techniques*, vol. 28, no. 6, pp. 536–541, 1980.

[141] M. Skorobogatiy, K. Saitoh, and M. Koshiba, "Full-vectorial coupled mode theory for the evaluation of macro-bending loss in multimode fibers: application to the hollow-core photonic bandgap fibers," *Optics Express*, vol. 16, no. 19, pp. 14 945–14 953, 2008.

[142] L. Eyraud, *Diélectriques, solides anisotropes et ferroélectricité*. Paris, France: Gauthier-Villars, 1967.

[143] H. T. Feng, R. H. Zhuo, J. T. Chen, D. Yan, J. J. Feng, H. J. Li, S. Cheng, Z. G. Wu, J. Wang, and P. X. Yan, "Synthesis, Characterization, and Microwave Absorption Property of the SnO2 Nanowire/Paraffin Composites," *Nanoscale Res. Lett.*, 2009.

[144] M. Wu, X. Yao, J. Zhai, and L. Zhang, "Determination of microwave complex permittivity of particulate materials," *Meas. Sci. Technol.*, vol. 12, pp. 1932–1937, 2001.

[145] M. E. Achour, M. E. L. Malhi, J. L. Miane, F. Carmona, and F. Lahjomri, "Microwave Properties of Carbon Black-Epoxy Resin Composites and Their Simulation by Means of Mixture Laws," *Journal of Applied Polymer Science*, vol. 73, pp. 969–973, 1999.

[146] M. Scheller, S. Wietzke, C. Jansen, and M. Koch, "Modelling heterogeneous dielectric mixtures in the terahertz regime: a quasi-static effective medium theory," *J. Phys. D: Appl. Phys.*, vol. 42, p. 065415, 2009.

[147] G. Zhao, M. T. Mors, T. Wenckebach, and P. C. M. Planken, "Terahertz dielectric properties of polystyrene foam," *Journal of the Optical Society of America B*, vol. 19, no. 6, pp. 1476–1479, Jun. 2002. [Online]. Available: http://www.opticsinfobase.org/abstract.cfm?URI=josab-19-6-1476

[148] R. Piesiewicz, C. Jansen, S. Wietzke, D. Mittleman, M. Koch, and T. Kürner, "Properties of Building and Plastic Materials in the THz Range," *International Journal of Infrared and Millimeter Waves*, vol. 28, pp. 363–371,

Mar. 2007. [Online]. Available: http://www.springerlink.com/index/10.1007/s10762-007-9217-9

[149] I. Bassett and A. Argyros, "Elimination of polarization degeneracy in round waveguides." *Optics Express*, vol. 10, no. 23, pp. 1342–1346, Nov. 2002. [Online]. Available: http://www.ncbi.nlm.nih.gov/pubmed/19451997

[150] M. A. Ordal, R. J. Bell, R. W. Alexander, L. L. Long, and M. R. Querry, "Optical properties of fourteen metals in the infrared and far infrared: Al, Co, Cu, Au, Fe, Pb, Mo, Ni, Pd, Pt, Ag, Ti, V, and W." *Applied optics*, vol. 24, no. 24, pp. 4493–4499, Dec. 1985. [Online]. Available: http://www.ncbi.nlm.nih.gov/pubmed/18224235

[151] D. T. Zimmerman, J. D. Cardellino, K. T. Cravener, K. R. Feather, N. M. Miskovsky, and G. J. Weisel, "Microwave absorption in percolating metal-insulator composites," *Applied Physics Letters*, vol. 93, no. 21, p. 214103, 2008. [Online]. Available: http://link.aip.org/link/APPLAB/v93/i21/p214103/s1&Agg=doi

[152] G. Xu, W. Zhang, Y. Huang, and J. Peng, "Loss Characteristics of Single-HE11-Mode Bragg Fiber," *Journal of Lightwave Technology*, vol. 25, no. 1, pp. 359–366, 2007.

[153] M. Bashkansky, D. Park, and F. K. Fatemi, "Azimuthally and radially polarized light with a nematic SLM." *Optics Express*, vol. 18, no. 1, pp. 212–217, Jan. 2010. [Online]. Available: http://www.ncbi.nlm.nih.gov/pubmed/20173841

[154] H. Dehez, M. Piché, and Y. De Koninck, "Enhanced resolution in two-photon imaging using a TM01 laser beam at a dielectric interface," *Optics Letters*, vol. 34, no. 23, pp. 3601–3603, 2009.

[155] L. H. Johnston, "Broadband polarization rotator for the infrared," *Applied Optics*, vol. 16, no. 4, pp. 1082–1084, 1977.

[156] C. E. Greninger, "Reflective device for polarization rotation," *Applied Optics*, vol. 27, no. 4, pp. 774–776, 1988.

[157] E. J. Galvez and P. M. Koch, "Use of four mirrors to rotate linear polarization but preserve input-output collinearity. II." *J. Opt. Soc. Am. A*, vol. 14, no. 12, pp. 3410–3414, 1997.

[158] T. Hidaka, K. Kumada, J. Shimada, and T. Morikawa, "GeO(2)-ZnO-K(2)O glass as the cladding material of 940-cm^{-1} CO_2 laser-light transmitting hollow-core waveguide," *J. Appl. Phys.*, vol. 53, no. 8, pp. 5484–5490, 1982.

[159] T. Hidaka, "Loss calculations of the hollow-core, oxide-glass-cladding, middle-infrared optical waveguides," pp. 93–97, 1982.

[160] J. a. Harrington and C. C. Gregory, "Hollow sapphire fibers for the delivery of CO(2) laser energy." *Optics letters*, vol. 15, no. 10, pp. 541–543, May 1990. [Online]. Available: http://www.ncbi.nlm.nih.gov/pubmed/19768001

[161] C. C. Gregory and J. A. Harrington, "Attenuation, model, and polarization properties of n $<$ 1, hollow dielectric waveguides," *Applied Optics*, vol. 32, no. 27, pp. 5302–5309, 1993.

[162] T. Furukawa and G. E. Johnson, "Measurements of ferroelectric switching characteristics in polyvinylidene fluoride," *Appl. Phys. Lett.*, vol. 38, no. 12, pp. 1027–1029, 1981.

[163] F. Kajzar, K.-S. Lee, and A. K.-Y. Jen, "Polymeric Materials and their Orientation Techniques for Second-Order Nonlinear Optics," *Advances in Polymer Science*, vol. 161, p. 85, 2003.

[164] G. M. Sessler, "Piezoelectricity in polyvinylidenefluoride," *J. Acoust. Soc. Am.*, vol. 70, no. 6, pp. 1596–1608, 1981.

[165] S. M. Nakhmanson, M. Buongiorno Nardelli, and J. Bernholc, "Collective polarization effects in beta-polyvinylidene fluoride and its copolymers with tri- and tetrafluoroethylene," *Physical Review B*, vol. 72, p. 115210, 2005.

[166] T. Kaura, R. Nath, and M. M. Perlman, "Simultaneous stretching and corona poling of PVDF films," *J. Phys. D: Appl. Phys.*, vol. 24, pp. 1848–1852, 1991.

[167] A. Kumar and M. Perlman, "Simultaneous stretching and corona poling of PVDF and P(VDF-TriFE) films," *J. Phys. D: Appl. Phys.*, vol. 26, pp. 469–473, 1993.

[168] R. Kashyap and P. Pantelis, "Optical fibre absorption loss measurement using a pyro-electric poly(vinylidene fluoride) tube," *J. Phys. D: Appl. Phys.*, vol. 18, pp. 1709–1721, 1985.

[169] M. Imai, T. Shimizu, Y. Ohtsuka, and A. Odajima, "An electric-field sensitive fiber with coaxial electrodes for optical phase modulation," *Journal of Lightwave Technology*, vol. LT-5, no. 7, pp. 926–931, 1987.

[170] J. Petzelt, J. F. Legrand, S. Pacesova, S. Kamba, G. V. Kozlov, and A. A. Volkov, "Far infrared and Submillimetre Studies of the Ferroelectric Phase Transition in (VF2-F3E) Copolymers," *Phase Transitions*, vol. 12, pp. 305–336, 1988.

[171] C. Ang and Z. Yu, "'Dielectric relaxor' behavior of electroactive fluorinated polymers," *Applied Physics Letters*, vol. 86, p. 262903, 2005.

[172] N. A. Mortensen, "Effective area of photonic crystal fibers," *Optics Express*, vol. 10, no. 7, pp. 341–348, 2002.

[173] J.-I. Sakai and T. Kimura, "Bending loss of propagation modes in arbitrary-index profile optical fibers," *Applied Optics*, vol. 17, no. 10, pp. 1499–1506, 1978.

[174] J.-I. Sakai, "Simplified bending loss formula for single-mode optical fibers," *Applied Optics*, vol. 18, no. 7, pp. 951–952, 1979.

[175] M. D. Nielsen, N. A. Mortensen, M. Albertsen, J. R. Folkenberg, A. Bjarklev, and D. Bonacinni, "Predicting macrobending loss for large-mode area photonic crystal fibers," *Optics Express*, vol. 12, no. 8, pp. 1775–1779, 2004.

[176] D. Kominsky, G. Pickrell, and R. Stolen, "Generation of random-hole optical fiber," *Optics Letters*, vol. 28, no. 16, pp. 1409–1411, 2003.

[177] G. Pickrell, D. Kominsky, R. Stolen, F. Ellis, J. Kim, A. Safaai-Jazi, and A. Wang, "Microstructural Analysis of Random Hole Optical Fibers," *IEEE Photonics Technology Letters*, vol. 16, no. 2, pp. 491–493, 2004.

[178] Y.-S. Jin, S.-G. Jeon, G.-J. Kim, J.-I. Kim, and C.-H. Shon, "Fast scanning of a pulsed terahertz signal using an oscillating optical delay line," *Review*

of Scientific Instruments, vol. 78, p. 023101, 2007. [Online]. Available: http://link.aip.org/link/RSINAK/v78/i2/p023101/s1&Agg=doi

[179] T. Hidaka, A. Ishikawa, J.-I. Kojou, T. Ikari, Y.-I. Ishikawa, H. Minamide, A. Kudoh, J.-I. Nishizawa, and H. Ito, "Adaptive optics instrumentation in submillimeter/terahertz spectroscopy with a flexible polyvinylidene fluoride cladding hollow waveguide." *The Review of scientific instruments*, vol. 78, no. 8, p. 086109, Aug. 2007. [Online]. Available: http://www.ncbi.nlm.nih.gov/pubmed/17764369

[180] L. Duvillaret, F. Garet, and J.-L. Coutaz, "A Reliable Method for Extraction of Material Parameters in Terahertz Time-Domain Spectroscopy," *IEEE Journal of Selectrd Topics in Quantum Electronics*, vol. 2, no. 3, pp. 739–746, 1996.

[181] L. Duvillaret, F. Garet, and J.-L. Coutaz, "Highly precise determination of optical constants and sample thickness in terahertz time-domain spectroscopy," *Applied Optics*, vol. 38, no. 2, pp. 409–415, 1999.

[182] R. Wilk, I. Pupeza, R. Cernat, and M. Koch, "Highly Accurate THz Time-Domain Spectroscopy of Multilayer Structures," *IEEE Journal of Selected Topics in Quantum Electronics*, vol. 14, no. 2, pp. 392–398, 2008. [Online]. Available: http://ieeexplore.ieee.org/lpdocs/epic03/wrapper.htm?arnumber=4481136

[183] C.-P. Yu and H.-C. Chang, "Yee-mesh-based finite difference eigenmode solver with PML absorbing boundary conditions for optical waveguides and photonic crystal fibers," *Optics Express*, vol. 12, no. 25, pp. 6165–6177, Dec. 2004.

Appendix A

Proof of large hollow-core waveguide propagation loss scaling law

In this appendix we demonstrate the $\alpha \sim \frac{1}{f^2 d_{\text{core}}^3}$ scaling law of large hollow-core multi-mode waveguides (satisfying $d_{\text{core}} \gg \lambda$, where λ is the wavelength of guided light). Here we give a simplified demonstration based on the ray-optic perspective, however a more rigorous derivation using Maxwell's equations and mode analysis yields the same result [30]. Consider the generic waveguide schematized in Fig. A.1. Two interfaces delimit a core region of size d_{core}, and an optical ray with an incidence angle θ_1 reflects off the waveguide interfaces. The power reflectivity of a single reflection is R.

The power propagation loss is defined in the following manner,

$$\frac{P(L)}{P(0)} \equiv e^{-\alpha L}, \tag{A.1}$$

where L is the length of the waveguide. By defining L_1 as the distance between two consecutive reflections (see Fig. A.1) and $N = \frac{L}{L_1}$ as the number of reflections along the length of the waveguide, we can relate the power loss to the reflections on the waveguide interfaces,

$$\begin{aligned} e^{-\alpha L} &= R^N = R^{\frac{L}{L_1}}, \\ \alpha &= \frac{-\ln(R)}{L_1}. \end{aligned} \tag{A.2}$$

This very general loss formula (equation (A.2)) is the basic starting point, but in order to complete the proof we need to obtain some intermediate results.

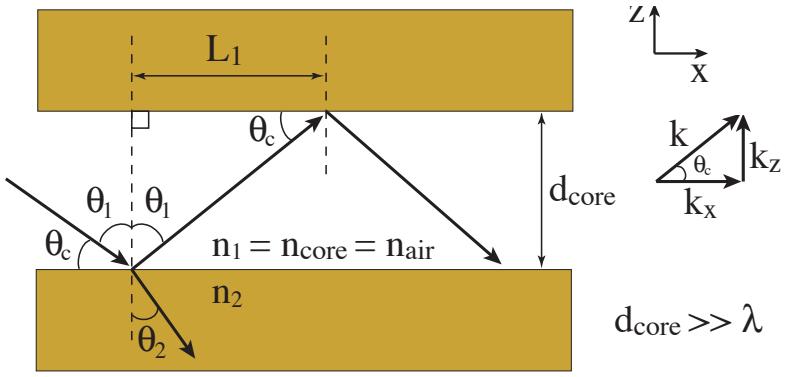

Figure A.1 Schematization of a large hollow-core waveguide, defining the geometric variables needed for the scaling law proof.

A.1 Grazing incidence

Upon solving Maxwell's equations and imposing the continuity conditions of the geometry given in Fig. A.1, we obtain [137] a very general condition for a stationary wave in the transverse direction,

$$k_z \cdot d_{\text{core}} = p\pi, \tag{A.3}$$

where p is an integer and k_z is the transverse propagation constant within the core.

From Fig. A.1 we have,

$$\sin\theta_c = \frac{k_z}{k} \tag{A.4}$$

$$k_z = \sin\theta_c \left(\frac{2\pi n_{\text{core}}}{\lambda}\right). \tag{A.5}$$

Substituting equation (A.5) into equation (A.3) and assuming $p = 1$ we obtain,

$$\sin\theta_c \left(\frac{2\pi n_{\text{core}}}{\lambda}\right) \cdot d_{\text{core}} = p\pi,$$

$$\sin\theta_c = \frac{\lambda}{2n_{\text{core}} \cdot d_{\text{core}}}. \tag{A.6}$$

The rest of the proof relies on the assumption that for large core waveguides the

following condition is satisfied,

$$d_{\text{core}} \gg \lambda. \tag{A.7}$$

Using condition (A.7) on equation (A.6) we obtain

$$\sin\theta_c \approx \theta_c = \frac{\lambda}{2n_{\text{core}} \cdot d_{\text{core}}}. \tag{A.8}$$

Since θ_c and θ_1 are complimentary angles ($\theta_c + \theta_1 = \frac{\pi}{2}$ in Fig. A.1), we note that

$$\sin\theta_c = \cos\theta_1 = \frac{\lambda}{2n_{\text{core}} \cdot d_{\text{core}}}. \tag{A.9}$$

Finally, we also note that $\cos\theta_1 \to 0$ implies $\theta_1 \to \frac{\pi}{2}$, in other words the rays have grazing incidence angles.

A.2 Geometrical argument

We now determine the distance L_1 between reflections. From Fig. A.1 we have

$$\tan\theta_1 = \frac{d_{\text{core}}}{L_1} = \frac{1}{\tan\theta_c}. \tag{A.10}$$

The grazing incidence condition $\theta_1 \to \frac{\pi}{2}$ is equivalent to $\theta_c \to 0$. Using this condition and substituting equation (A.8) in (A.10) yields,

$$\begin{aligned} \tan\theta_c = \frac{d_{\text{core}}}{L_1}, \qquad & \tan\theta_c \approx \theta_c, \\ \theta_c \sim \frac{d_{\text{core}}}{L_1} \sim \frac{\lambda}{2n_{\text{core}} \cdot d_{\text{core}}}, & \\ L_1 \sim \frac{2n_{\text{core}} \cdot d_{\text{core}}^2}{\lambda}. & \end{aligned} \tag{A.11}$$

A.3 Grazing reflectivity

Notice that so far we have assumed nothing about the nature of the waveguide material. Without loss of generality we consider the Fresnel power reflection coefficient

for the TE polarization,

$$R = \left(\frac{n_1 \cos\theta_1 - n_2 \cos\theta_2}{n_1 \cos\theta_1 - n_2 \cos\theta_2} \right)^2, \tag{A.12}$$

where $n_1 = n_{\text{core}}$ is the core material and n_2 is the waveguide material. Notice that we still make *no assumptions about the waveguide material* because n_2 could correspond to a metal or a dielectric, as pointed out by Miyagi and Kawakami [30]. Let us remark that despite considering only a single TE reflection, similar expressions can be obtained for other polarizations [30] (TM, HE) and for multiple reflections in Fabry-Perot and Bragg reflectors [137].

We now develop the reflectivity formula under the grazing incidence condition $\cos\theta_1 \to 0$. Keeping only first order terms we obtain,

$$R = \left[(n_1 \cos\theta_1)^2 - 2(n_1 \cos\theta_1)(n_2 \cos\theta_2) + (n_2 \cos\theta_2)^2 \right] \frac{1}{\left[n_2 \cos\theta_2 \right]^2} \left[1 + \frac{n_1 \cos\theta_1}{n_2 \cos\theta_2} \right]^2,$$

$$R \approx \left[1 - \frac{2n_1 \cos\theta_1}{n_2 \cos\theta_2} \right] \left[1 + \frac{2n_1 \cos\theta_1}{n_2 \cos\theta_2} \right], \qquad (1+\epsilon)^2 \approx 1 + 2 \cdot \epsilon$$

$$= 1 - \frac{4n_1 \cos\theta_1}{n_2 \cos\theta_2} \tag{A.13}$$

$$\equiv 1 - T, \tag{A.14}$$

where the last line stems from power conservation ($R+T = 1$ if we neglect absorption). Thus,

$$T \sim \frac{4n_1 \cos\theta_1}{n_2 \cos\theta_2} \sim \left(\frac{4n_1}{\sqrt{n_2^2 - n_1^2}} \right) \cos\theta_1, \tag{A.15}$$

where we have used the following expression obtained with Snell's law ($n_1 \sin\theta_1 = n_2 \sin\theta_2$) and $\sin\theta_1 \to 1$

$$n_2 \cos\theta_2 = n_2 \sqrt{1 - \sin^2\theta_2} = \sqrt{n_2^2 - n_2^2 \sin^2\theta_2} = \sqrt{n_2^2 - n_1^2 \sin^2\theta_1} \approx \sqrt{n_2^2 - n_1^2}.$$

Note that at grazing incidence angles, $R \to 1$ and $T \ll 1$. Finally, substituting equation (A.9) in (A.15) gives

$$T \sim \left(\frac{4n_1}{\sqrt{n_2^2 - n_1^2}} \right) \frac{\lambda}{2n_{\text{core}} \cdot d_{\text{core}}}. \tag{A.16}$$

A.4 Final power loss scaling law

Under the condition of grazing incidence angles we have $R \to 1$ and $T \ll 1$. Using $\ln(1-x) \approx -x$ when $x \ll 1$, equation (A.2) becomes,

$$\alpha = \frac{-\ln(R)}{L_1} = \frac{-\ln(1-T)}{L_1}$$
$$\alpha \approx +\frac{T}{L_1} \tag{A.17}$$

To complete the proof, we neglect material dispersion ($n_2 = \text{const}$) and substitute equations (A.11) and (A.16) into the previous expression, yielding

$$\alpha \sim \frac{T}{L_1} \sim \left(\frac{4n_1}{\sqrt{n_2^2 - n_1^2}} \frac{\lambda}{2n_{\text{core}} \cdot d_{\text{core}}} \right) \left(\frac{\lambda}{2n_{\text{core}} \cdot d_{\text{core}}^2} \right)$$
$$\alpha \sim \text{const.} \cdot \frac{\lambda^2}{d_{\text{core}}^3}, \qquad \text{and since } \lambda = \frac{c}{f}, \tag{A.18}$$
$$\alpha \sim \text{const.} \cdot \frac{1}{f^2 \cdot d_{\text{core}}^3} \quad \square \tag{A.19}$$

Alternative proofs can be found in the literature [30, 137]. More importantly, this scaling law has been confirmed both in simulations and in experiments for a wide range of large core ($d_{\text{core}} \gg \lambda$) waveguides [23, 24, 42], both metallic and dielectric in nature.

Appendix B

Calculation of the optical parameters from a THz-TDS transmission spectrum

The determination of material parameters by THz spectroscopy is of fundamental importance for research. The advantage of Time-Domain Spectroscopy (TDS) is that a simultaneous measurement of the amplitude and the phase of the complex transmission spectrum allows for reconstruction of both the absorption loss (α) and the refractive index (n), respectively. The simplest method is to measure transmission through a thin planar film although certain high loss materials such as liquids require reflection measurements. Many different calculation methods have been developed, with differing degrees of sophistication [180, 181, 182].

Let us consider the simplest model for transmission. The sample consists of two interfaces separated by the thickness of the sample (L). It is assumed that the thickness is known. The incident light will have partial reflection and transmission at both interfaces. In fact, there will always be multiple reflections at the interfaces of the planar sample. Since the THz signal is a pulse these reflections will lead to multiple pulse echoes (pulses have arrival times that are odd multiples of the time it takes to traverse the optical thickness of the sample, $\frac{nL}{c}$, $\frac{3nL}{c}$, $\frac{5nL}{c}$, ...). If the echoes are well separated in time, i.e. the echo 1 does not overlap with echo 0 ($\frac{3nL}{c}$ >Echo duration), then we can neglect Fabry-Perot interference effects. In the case where Fabry-Perot effects can be neglected, we have a Fresnel transmission coefficient at both interfaces and a single-pass transmission through the sample incurring a phase delay and some

absorption. The complex *amplitude* spectrum $\tilde{T}$ can therefore be written as [180]:

$$\widetilde{E}_{\text{sample}} = \widetilde{E}_{\text{ref}}(\omega)\frac{4n}{(n+1)^2}\cdot e^{-\frac{\alpha}{2}L}\cdot e^{i(n-1)\frac{\omega L}{c}} \tag{B.1}$$

$$\widetilde{T}(\omega) = \frac{\widetilde{E}_{\text{sample}}(\omega)}{\widetilde{E}_{\text{ref}}(\omega)} = \frac{4n}{(n+1)^2}\cdot e^{-\frac{\alpha}{2}L}\cdot e^{i(n-1)\frac{\omega L}{c}}, \tag{B.2}$$

where c is the speed of light, $\omega = 2\pi f$ is the angular frequency, n is the refractive index of the sample, α is the *power* absorption coefficient of the sample, and $\widetilde{E}_{\text{ref}}(\omega)$ is the spectrum of the source including all losses and phase delays before and after the sample. The $e^{i(n-1)\frac{\omega L}{c}}$ phase term stems from the fact that the sample replaces air when it is in place. Experimentally, $\widetilde{E}_{\text{sample}}$ is the signal measured with the sample in place and $\widetilde{E}_{\text{ref}}$ is the signal measured without the sample. By dividing the complex spectra we obtain the complex amplitude transmission coefficient.

Taking the imaginary and real parts of equation (B.2) it is straightforward to extract the material parameters:

$$n = 1 + \frac{c}{\omega L}\text{angle}\left(\widetilde{T}\right) \tag{B.3}$$

$$\alpha = -\frac{2}{L}\ln\left[\frac{(n+1)^2}{4n}\text{abs}\left(\widetilde{T}\right)\right] \tag{B.4}$$

An example of the calculation is given in Fig. B.1 for a relatively thick PE slab.

In the case where the samples are thin and the echo pulses overlap, artificial ringing oscillations will occur in the reconstruction parameters if equations (B.3) and (B.4) are used; see for example Fig. 4.10. This results from Fabry-Perot effects which must be taken into account. However, the calculations become considerably more complicated when Fabry-Perot effects are included because analytical solutions are no longer available. Instead, the material parameters must be found through an optimization procedure [180]. Moreover, the largest error in the material parameter calculation is generally the error on the sample thickness. More sophisticated calculations also optimize the sample thickness to get the most accurate material parameter reconstruction [181, 182].

Finally, we note that waveguide parameter estimation can be done in a similar manner. The spectrum at the output of the waveguide is normalized with respect to the spectrum at the input (measured without the waveguide). Instead of fresnel coefficients we consider input and output amplitude coupling coefficients (C_{in}, C_{out}).

Assuming only one mode is propagating equation (B.2) becomes,

$$\widetilde{T}(\omega, L_{\mathrm{w}}) = \frac{\widetilde{E}_{\mathrm{waveguide}}(\omega)}{\widetilde{E}_{\mathrm{reference}}(\omega)} = C_{\mathrm{in}} \cdot C_{\mathrm{out}} \cdot e^{-\frac{\alpha L_{\mathrm{w}}}{2}} e^{i(n_{\mathrm{eff}}-1)(\frac{\omega}{c})L_{\mathrm{w}}}, \tag{B.5}$$

where n_{eff} is the effective propagation index of the mode, α_{w} is the power propagation loss of the mode, and L_{w} is the length of the waveguide.

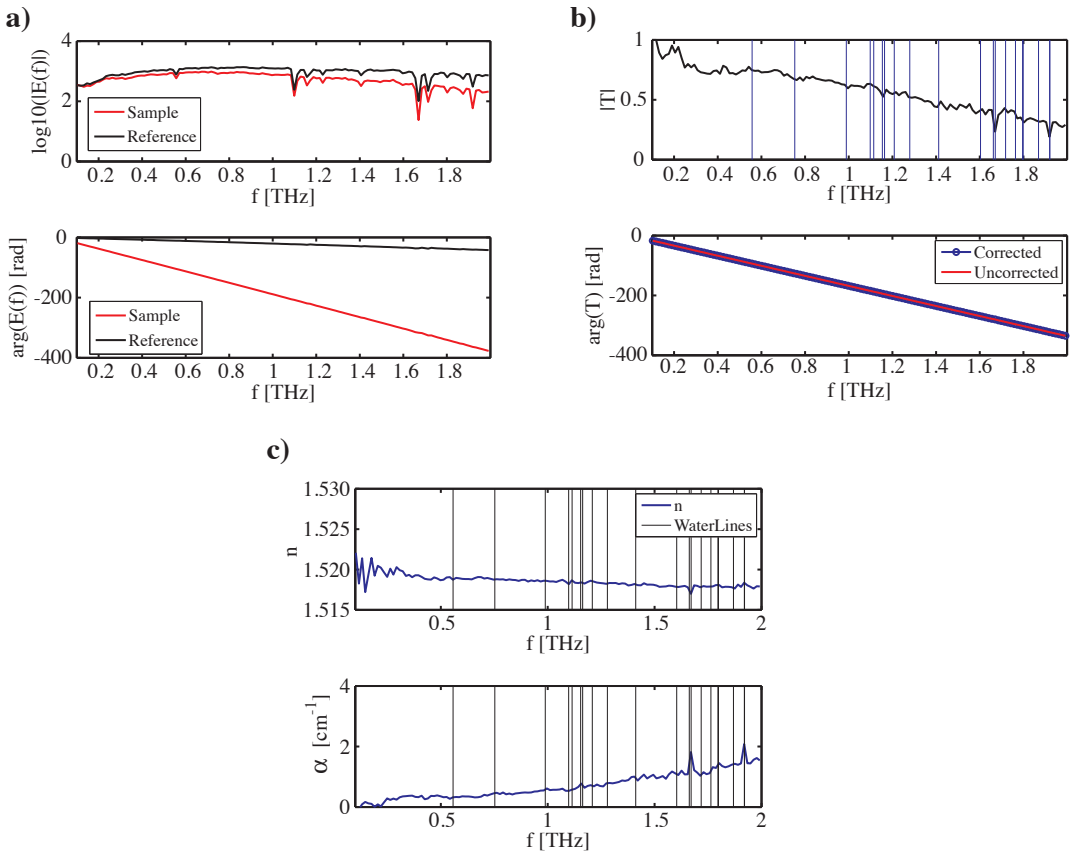

Figure B.1 Example of the calculation of material parameters from the complex transmission spectrum measured with THz-TDS. The sample is a 1.55 cm thick slab of PE. a) Complex spectra measured with (red) and without (black) the sample. b) Normalization with respect to the reference spectrum gives the complex transmission coefficient. c) n is calculated from the phase using equation (B.3), α is calculated from the amplitude using n and equation (B.4).

Appendix C

Transfer Matrix waveguide simulations

In the case of a circularly symmetric geometry the waveguide mode parameters (n_{eff}, α_{mode}) can be calculated using exact vectorial simulations in a transfer matrix formalism. The calculation procedure is detailed in the literature [135, 121] and summarized as follows.

From a given arbitrary circularly symmetric step-index profile we seek to find the proper mode parameters than give modal fields which respect Maxwell's equations. It is well known that in a cylindrical layer of uniform refractive index the field components of a guided mode (E_z, E_ϕ, H_z, H_ϕ) which satisfy the Maxwell equations can be expressed as a linear combination of Bessel functions [114, 115]. In a matrix formalism this can be written as,

$$\begin{bmatrix} E_z \\ H_\phi \\ H_z \\ E_\phi \end{bmatrix} = \begin{bmatrix} J_m(k_i r) & Y_m(k_i r) & 0 & 0 \\ \frac{i\omega\epsilon_i}{k_i} J'_m(k_i r) & \frac{i\omega\epsilon_i}{k_i} Y'_m(k_i r) & \frac{-m\beta}{k_i^2 r} J_m(k_i r) & \frac{-m\beta}{k_i^2 r} Y_m(k_i r) \\ 0 & 0 & J_m(k_i r) & Y_m(k_i r) \\ \frac{-m\beta}{k_i^2 r} J_m(k_i r) & \frac{-m\beta}{k_i^2 r} Y_m(k_i r) & \frac{-i\omega\mu_i}{k_i} J'_m(k_i r) & \frac{-i\omega\mu_i}{k_i} Y'_m(k_i r) \end{bmatrix} \begin{bmatrix} A \\ B \\ C \\ D \end{bmatrix} \tag{C.1}$$

where J, and Y are Bessel functions of the first and second kind, ϵ_i and μ_i are the permittivity and permeability of the current layer, and the prime denotes a derivative with respect to r, the radial coordinate. m is the azimuthal mode number used for labeling the modes, such as TE_{mn} or HE_{mn}. $k_i = \sqrt{(\frac{2\pi f}{c} n_i)^2 - (\frac{2\pi f}{c} n_{\text{eff}})^2}$, where n_i is the refractive index of the current layer and n_{eff} is the refractive index of the mode. $\beta = \frac{2\pi f}{c} n_{\text{eff}}$ is the propagation constant of the mode and f is the simulation frequency. Finally, A, B, C, D are the coefficients which must be determined for the fields of a mode to be physically realizable.

In a more general form, the propagation loss and radiation loss can be included by considering a complex valued refractive index $\widetilde{n} = n_{\text{eff}} - i\alpha_{\text{mode}} \frac{c}{4\pi f}$. Consequently, the Bessel functions have complex arguments and are generalized to Hankel functions.

Therefore, equation (C.1) becomes [121],

$$\begin{bmatrix} E_z \\ H_\phi \\ H_z \\ E_\phi \end{bmatrix} = \begin{bmatrix} H_m^I(k_i r) & H_m^{II}(k_i r) & 0 & 0 \\ \frac{i\omega\epsilon_i}{k_i} H_m'^I(k_i r) & \frac{i\omega\epsilon_i}{k_i} H_m'^{II}(k_i r) & \frac{-m\beta}{k_i^2 r} H_m^I(k_i r) & \frac{-m\beta}{k_i^2 r} H_m^{II}(k_i r) \\ 0 & 0 & H_m^I(k_i r) & H_m^{II}(k_i r) \\ \frac{-m\beta}{k_i^2 r} H_m^I(k_i r) & \frac{-m\beta}{k_i^2 r} H_m^{II}(k_i r) & \frac{-i\omega\mu_i}{k_i} H_m'^I(k_i r) & \frac{-i\omega\mu_i}{k_i} H_m'^I(k_i r) \end{bmatrix} \begin{bmatrix} A \\ B \\ C \\ D \end{bmatrix}. \quad \text{(C.2)}$$

where $H^I = J + iY$ and $H^{II} = J - iY$ are respectively the Hankel functions of the first and second kind.

The transfer matrix method hinges on relating the fields of one layer (layer i) to the fields of the next (layer $i+1$),

$$\begin{bmatrix} A_i \\ B_i \\ C_i \\ D_i \end{bmatrix} = T_i \begin{bmatrix} A_{i+1} \\ B_{i+1} \\ C_{i+1} \\ D_{i+1} \end{bmatrix}. \quad \text{(C.3)}$$

The elements of the transfer matrix T_i are found by imposing continuity of the fields and their derivatives at the interfaces [135]. The expressions for the elements of T_i are considerably longer to enumerate so the interested reader should refer to the literature [135, 121]. The fields of a valid mode must be continuous across *all* interfaces, therefore we seek the mode parameters that satisfy the matrix equation

$$\begin{bmatrix} A_1 \\ B_1 \\ C_1 \\ D_1 \end{bmatrix} = T_{\text{total}} \begin{bmatrix} A_N \\ B_N \\ C_N \\ D_N \end{bmatrix}, \quad \text{(C.4)}$$

where

$$T_{\text{total}} = T_1 T_2 ... T_{\text{N}-2} T_{\text{N}-1}, \quad \text{(C.5)}$$

is the product of the transfer matrices of all the layers. The nontrivial solutions to this equation are given by

$$\det\left(T_{\text{total}}\right) = 0. \quad \text{(C.6)}$$

Nontrivial, indeed. There are no analytical solutions to equation (C.6), therefore the mode parameters (n_{eff}, α_{mode}) must be found numerically. Although we could search for the roots of $\det(T_{\text{total}})$ it is generally simpler to cast the problem in terms of finding the minima of an optimization function. We therefore use $|\det(T_{\text{total}})|^2$ to define a function with minima and take the logarithm because $|\det(T_{\text{total}})|^2$ rapidly varies on a scale of many orders of magnitude. The optimization function is therefore defined in the following manner,

$$F(n_{\text{eff}}, \alpha) = \log_{10}\left(|\det(T_{\text{total}})|^2\right). \tag{C.7}$$

The $F(n_{\text{eff}}, \alpha)$ function will only tend towards $-\infty$ ($\det(T_{\text{total}}) = 0$) if the values of n_{eff} and α are *exactly* those of the mode. More generally, a coarse sampling of the $F(n_{\text{eff}}, \alpha)$ function will yield minima in the vicinity of the mode solutions. In the case of large core waveguides multiple modes may be guided and this will result in multiple minima. As an example, let us consider a Bragg fiber with $n_{\text{core}} = n_{\text{L}} = 1.0$, $n_{\text{H}} = 3.0$, $d_{\text{core}} = 6.73$ mm, $d_{\text{L}} = 150$ μm, $d_{\text{H}} = 254$ μm, and 5 bilayers. The waveguide is a large hollow-core tube and consequently the effective propagation indices n_{eff} will lie between 0.0 and 1.0. Fig. C.1 illustrates the optimization function at a frequency of 2 THz. Although the function could also be plotted in terms of the real and imaginary parts of the propagation constant β, plotting in terms of n_{eff} and α makes it easier to track changes as a function of frequency. Note that α is on a log scale because it often varies by many orders of magnitude as the frequency changes. In Fig. C.1.a) is can be seen that dozens (if not hundreds) of modes can be guided at 2 THz. The modes with the highest n_{eff} values are the lowest order modes. Looking for the minimum with the highest n_{eff} we see that there are actually two *nearly degenerate* TE and TM modes leading to two proximate minima. Note that a similar degeneracy is observed with HE and EH modes. Differentiating between modes of different order (say TE_{01} and TE_{02}) is easy, but differentiating between the nearly degenerate modes of a given order (say TE_{01} and TM_{01}) often leads to errors in the mode searching algorithm.

A simple search algorithm is a steepest descent algorithm where small steps are taken in the (n_{eff},α)-plane such that the current point descends to the closest minimum. The algorithm is initialized by a given starting point $(n_{\text{eff}}, \alpha)_{\text{start}}$. By virtue of continuity of the mode parameter functions, the mode solutions at subsequent frequency steps are found by using the previous frequency step solution as a starting

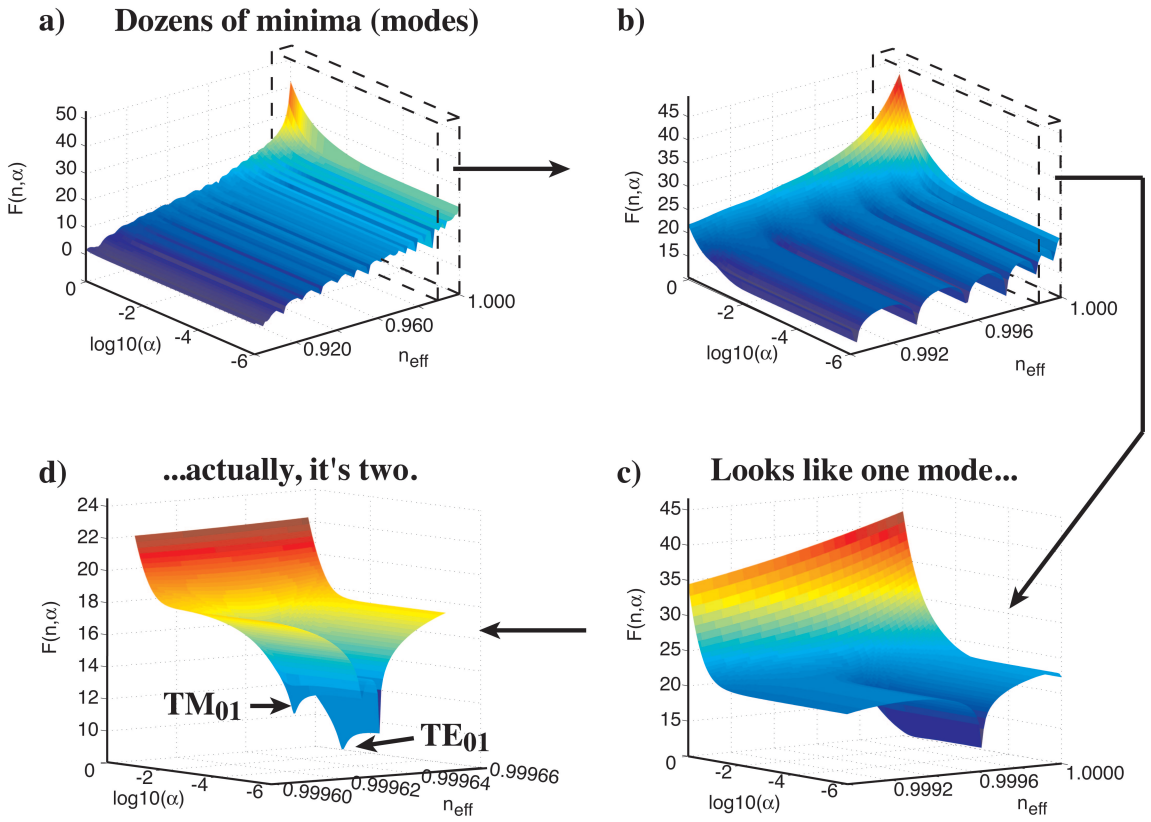

Figure C.1 Illustration of the modes (minima) of the optimization function of the Transfer Matrix Method. Here we consider a high index contrast air-polymer Bragg fiber, with $n_{\text{core}} = n_{\text{L}} = 1.0$, $n_{\text{H}} = 3.0$, $d_{\text{core}} = 6.73$ mm, $d_{\text{L}} = 150$ μm, $d_{\text{H}} = 254$ μm, and 5 bilayers. The calculation is made at $f = 2$ THz as it can be seen that many modes (minima) are supported. It should be stressed that the TE and TM modes give nearly degenerate solutions and that the proximity of the minima often leads to errors in the minima searching algorithm.

point. This simple method works generally well provided that the stepsizes are sufficiently small, however nearly discontinuous variations in the n_{eff} curves can cause problems. Figs. C.2 and C.3 illustrate the mode searching algorithm and the various problems that are encountered. The starting points are highlighted by white squares. In Figs. C.2.a) and C.2.b) starting points close to the sought after minima are seen to converge easily to the correct solutions. However, we see that in Fig. C.2.c) a "discontinuous" jump in the position of the TM_{01} minimum causes the search algorithm to converge on the wrong mode. This failure is more clearly illustrated in Fig. C.3.a) where the TM_{01} mode is seen to erroneously converge onto the TE_{01} min-

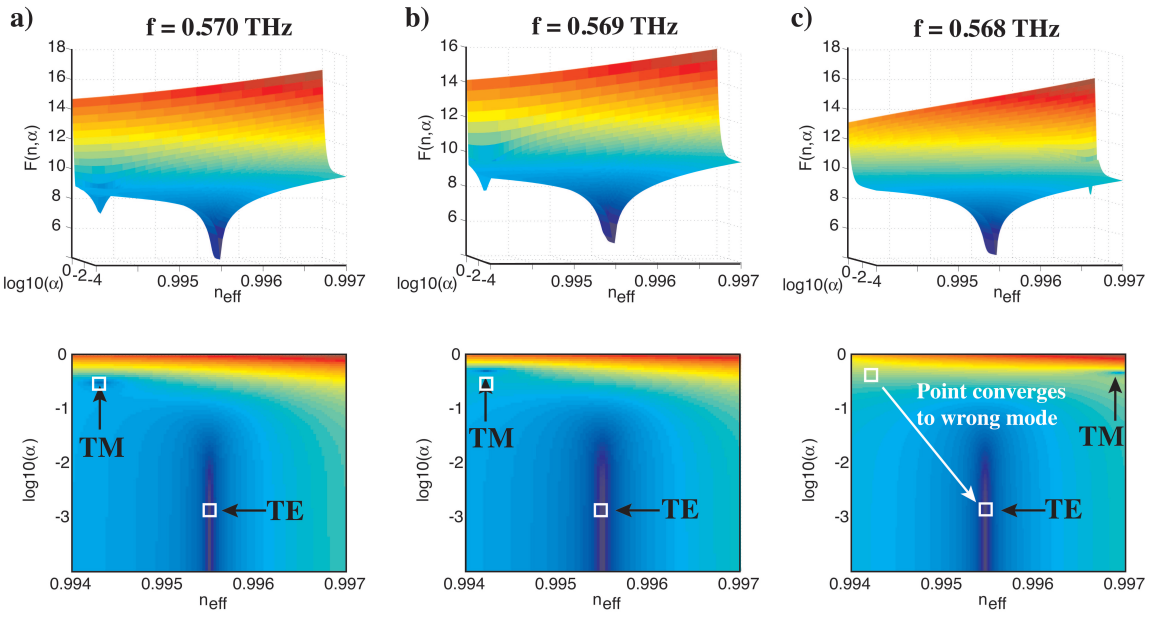

Figure C.2 Illustration of the steepest descent algorithm and the "discontinuous" jump in n_{eff} values of a mode. Starting points of the steepest descent algorithm are highlighted by squares. a), b) Algorithm converges properly to the desired minima. c) Sharp change in the position of the minimum makes the search algorithm converge on the wrong mode.

imum. Moreover, errors can also occur when the modes are nearly degenerate. Too large a step size in the (n_{eff},α)-plane can also cause the algorithm to step from one mode minimum onto the next; see Figs. C.3.c) and C.3.c).

Unfortunately, this means that the search algorithm must be repeatedly reset with new starting points (Fig. C.3.b)) and this makes the calculations long and arduous. Other methods such as a brute force search on evenly sampled grid within the (n_{eff},α)-plane have also been attempted, but they suffer from longer execution times and are also prone to different types of errors. In fact, such frustrations could be completely avoided in the case of TE and TM modes. The code that we use was implemented with the 4x4 matrices of equation (C.2), however, when $m = 0$ the TE and TM equations are decoupled and the equations can be written *separately* [121]. Rewriting the code to separate the TE and TM equations means that the modes can be solved separately, which would eliminate the problems associated with quasi-degenerate solutions.

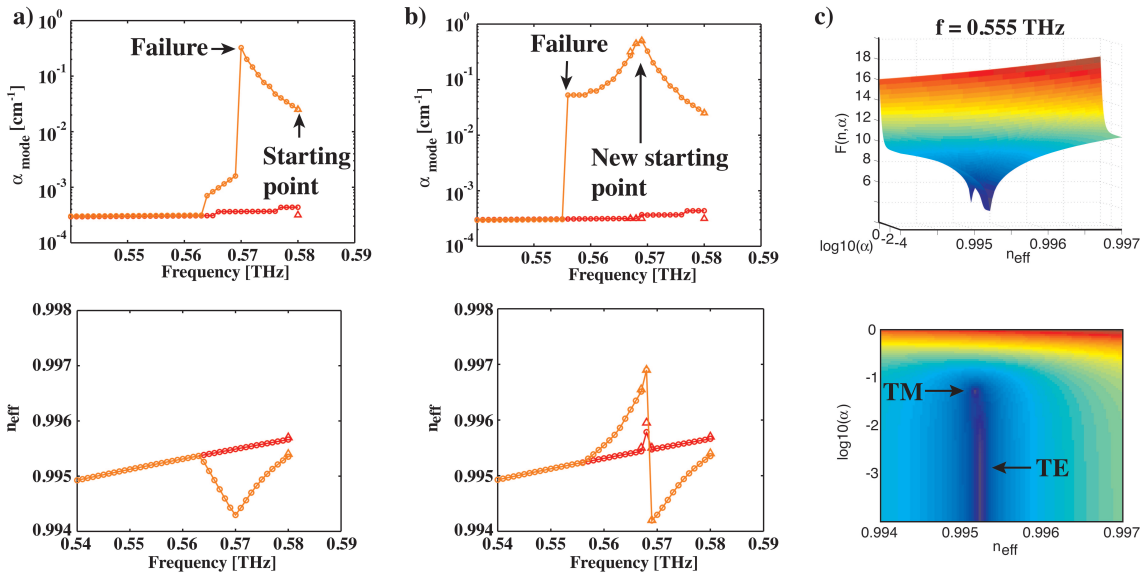

Figure C.3 Illustration of failures in the steepest descent algorithm arising from "discontinuous" jumps in the position of a minimum and from a step size that is too large in the (n_{eff},α)-plane. a) Failure in finding the TM_{01} because of the discontinuous jump in the position of the minimum, as illustrated in Figs. C.2.b) and C.2.c). b) Failure in finding TM_{01} because the algorithm took a "large" step in the (n_{eff},α)-plane and fell into the TE_{01} minimum. c) Proximity of the nearly degenerate TE_{01} and TM_{01} modes causes problems with the search algorithm.

Appendix D

COMSOL waveguide simulations

In the absence of circular symmetry the waveguide mode solutions were calculated using Finite Element simulations. The commercial COMSOL Multiphysics finite element package was used. Fortunately, Matlab is used as a scripting language to program finite element simulations and this greatly facilitates the interface. However, no examples are given for solving for the eigenmodes of waveguides and many (if not all) of the obscure programming details are poorly explained (or completely absent) in the documentation. One helpful tool is that the history of commands executed in the program can (mostly) be translated into script commands when the work environment is saved as a Matlab file. So by trial and error a proper script was written to calculate the guided modes of a waveguide with arbitrary geometry.

The calculation starts by drawing the fiber geometry (Fig. D.1.a)). Note that the fiber must be surrounded by a Perfectly Matched Layer (PML) in order to filter out spurious solutions. The different regions of the geometry correspond to subdomains which are numbered randomly by COMSOL. A tricky subsequent step is the procedure for assigning different physical properties to the different subdomains. Once the geometry is prepared it is automatically meshed with finite elements (Fig. D.1.b)) and the eigenmode problem for finding the modal parameters is solved. Once the mode is found at a given frequency, various post-processing steps can be carried out such as plotting the power distribution of the mode (Fig. D.1.c)). The process is repeated at each frequency and the mode parameters ($n_{\mathrm{mode}}(f)$, $\alpha_{\mathrm{mode}}(f)$) can be saved in file.

Many of the details for carrying out such calculations are poorly explained in the COMSOL documentation so an annotated script detailing a waveguide calculation example will be made available on the website of our group: `http://www.photonics.phys.polymtl.ca/`.

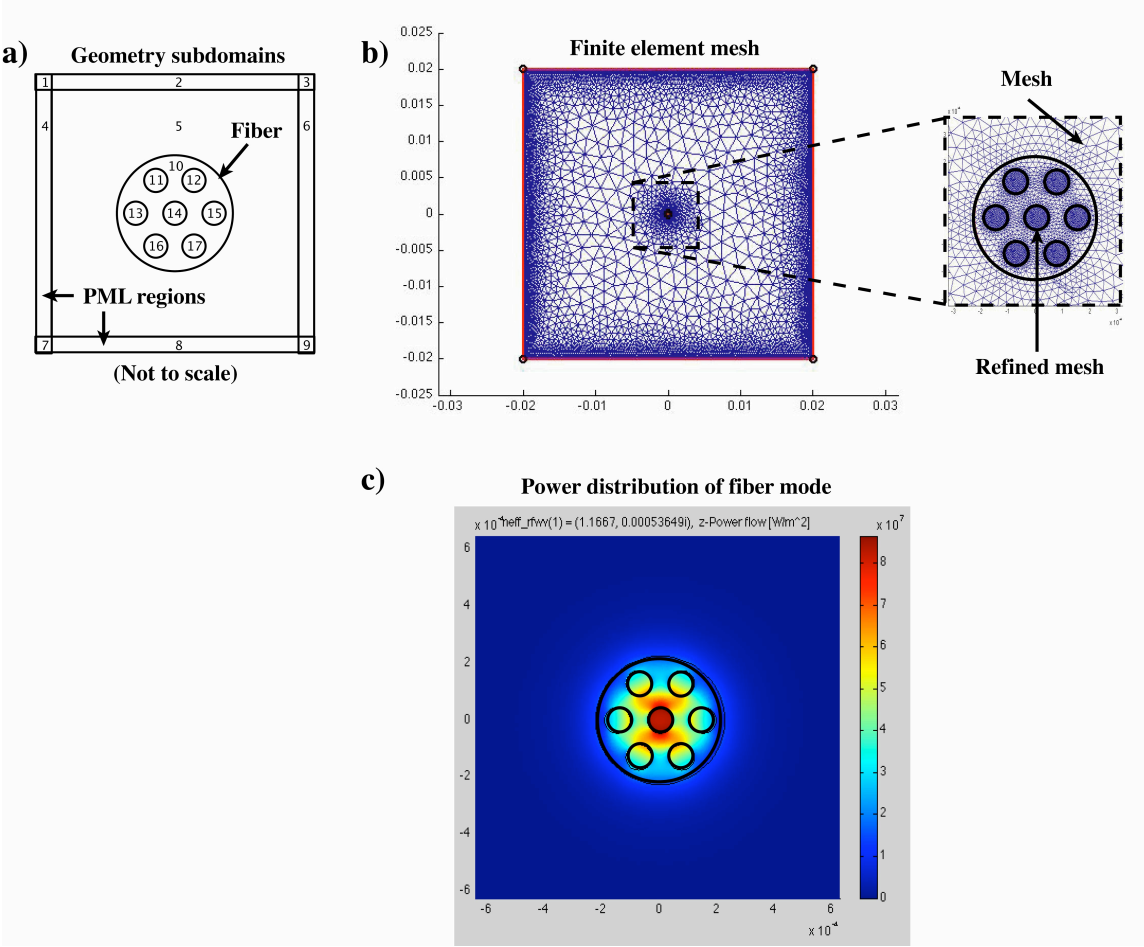

Figure D.1 Example of a finite element calculation of a waveguide mode using COMSOL. a) The fiber geometry is drawn and surrounded with a Perfectly-Matched Layer. The different subdomains are numbered and attributed different physical properties. b) The geometry is meshed with finite elements and the eigenmode problem is solved to find the mode parameters. c) Post-processing such as plotting the power distribution of the mode can then be carried out.

Appendix E

Proof of the formulae for the frequency periods of anti-resonant reflections

Here we demonstrate the equations relating the frequency period of anti-resonant reflection to the thicknesses and refractive indices of the reflector layers. We begin with the simple case of a single-layer (Fabry-Perot) reflector, and then generalize the equation to 2 layers (one bi-layer) and N bi-layers.

E.1 Single-layer reflector

Let us consider the schematization of a single-layer reflector shown in Fig. E.1.a). The refractive index is n_{wall} and the thickness t_{wall}. From the right angle triangles we have,

$$\frac{t_{\text{wall}}}{x} = \cos(\theta_2), \tag{E.1}$$

$$\frac{z}{x} = \sin(\theta_2), \tag{E.2}$$

$$\frac{y}{2z} = \sin(\theta_1). \tag{E.3}$$

The accumulated difference in optical distance between the rays A and B is

$$\Delta d = 2 \cdot n_{\text{wall}} \cdot x - n_{\text{air}} \cdot y. \tag{E.4}$$

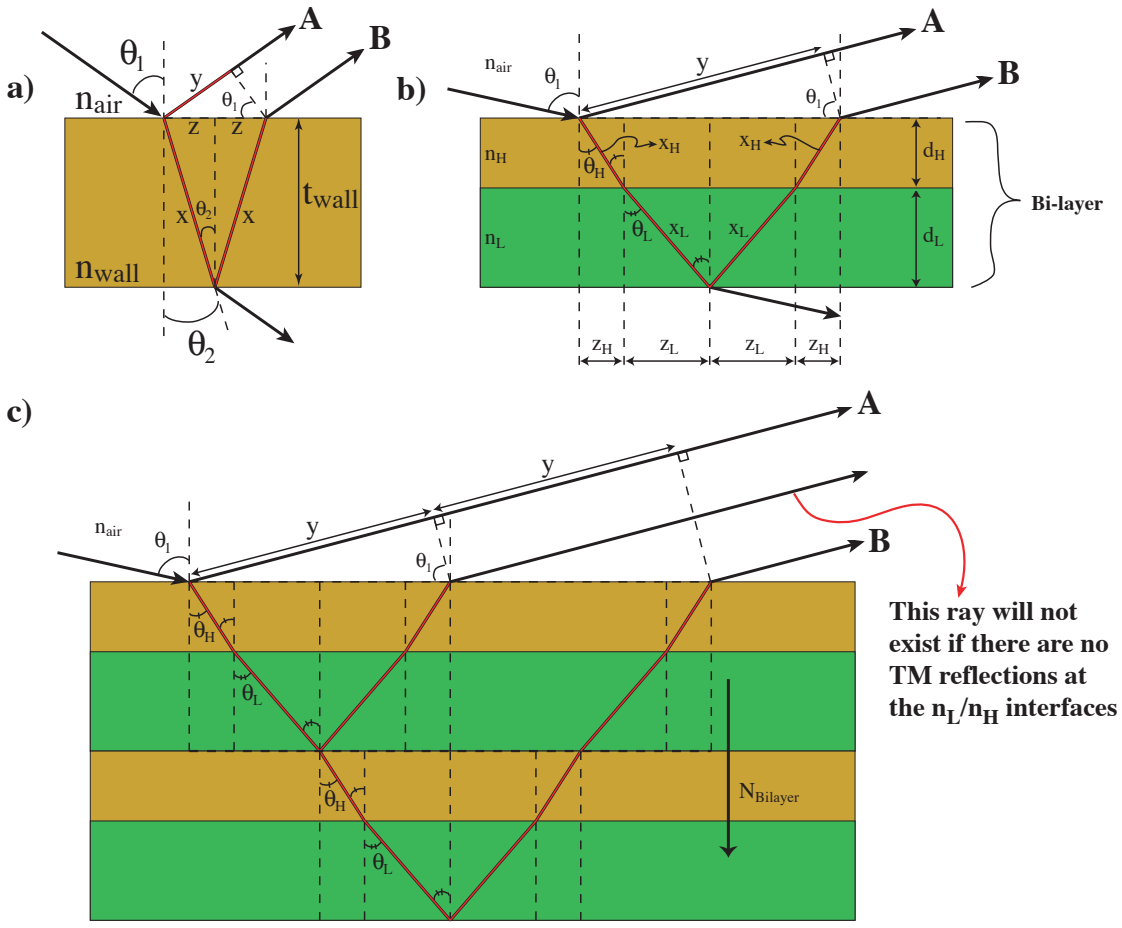

Figure E.1 Schematization of the geometries for single-layer (Fabry-Perot) or multiple-layer (Bragg) reflectors. These geometries are used to calculate the frequency period of anti-resonant reflection. a) Single-layer reflector, b) Bi-layer reflector, c) Periodic bi-layer (Bragg) reflector.

With $n_{\text{air}} = 1$ and by substituting equations (E.3) and (E.2) we have,

$$\begin{aligned}\Delta d &= 2 \cdot n_{\text{wall}} \cdot x - y, \\ &= 2 \cdot n_{\text{wall}} \cdot x - 2 \cdot (x \sin\theta_2) \cdot \sin\theta_1 \\ &= 2 \cdot x \cdot [n_{\text{wall}} - \sin\theta_2 \cdot \sin\theta_1] \,. \end{aligned} \tag{E.5}$$

We now substitute Snell Law,

$$n_{\text{air}} \sin\theta_1 = n_{\text{wall}} \sin\theta_2, \tag{E.6}$$

into equation (E.5),

$$\begin{aligned}
\Delta d &= 2 \cdot \left(\frac{t_{\text{wall}}}{\cos\theta_2} \right) \cdot \left[n_{\text{wall}} - \sin\theta_2 \cdot \frac{n_{\text{wall}} \sin\theta_2}{n_{\text{air}}} \right], \\
&= 2 \cdot \left(\frac{t_{\text{wall}}}{\cos\theta_2} \right) \cdot \left[n_{\text{wall}} - n_{\text{wall}} \sin^2\theta_2 \right], \\
&= 2 \cdot \left(\frac{t_{\text{wall}} \cdot n_{\text{wall}}}{\cos\theta_2} \right) \cdot \left[1 - \sin^2\theta_2 \right], \\
&= 2 \cdot \left(\frac{t_{\text{wall}} \cdot n_{\text{wall}}}{\cos\theta_2} \right) \cdot \cos^2\theta_2, \\
\Delta d &= 2 \cdot t_{\text{wall}} \cdot n_{\text{wall}} \cdot \cos\theta_2. \qquad \text{(E.7)}
\end{aligned}$$

First, we remark that the time delay between rays A and B is

$$\Delta\tau = \frac{\Delta d}{c} = \frac{2 \cdot t_{\text{wall}} \cdot n_{\text{wall}} \cdot \cos\theta_2}{c}. \qquad \text{(E.8)}$$

The phase difference between the two rays is

$$\delta = k \cdot \Delta d = \frac{2\pi f}{c} \cdot \Delta d. \qquad \text{(E.9)}$$

The resonance frequencies f_m are those that satisfy $\delta = m2\pi$, thus,

$$\begin{aligned}
\delta = m2\pi &= \frac{2\pi f_m}{c} \cdot \Delta d \\
f_m &= \frac{mc}{\Delta d}. \qquad \text{(E.10)}
\end{aligned}$$

Finally, the frequency period of the anti-resonant reflections is given by,

$$\Delta f = f_{m+1} - f_m = \frac{c}{2 \cdot t_{\text{wall}} \cdot n_{\text{wall}} \cdot \cos\theta_2}. \quad \square \qquad \text{(E.11)}$$

Which is the same equation as (4.4) given that $\cos\theta_2 = \frac{n_{\text{air}}}{n_{\text{wall}}} \sqrt{(\frac{n_{\text{wall}}}{n_{\text{air}}})^2 - 1}$ when $\theta_1 \to \pi/2$.

E.2 Bilayer reflector

A similar argument can be constructed for the case of the bilayer reflector schematized in Fig. E.1.b). From the right angle triangles we now have,

$$\frac{d_{\mathrm{H}}}{x_{\mathrm{H}}} = \cos\theta_{\mathrm{H}}, \qquad \frac{d_{\mathrm{H}}}{x_{\mathrm{H}}} = \cos\theta_{\mathrm{H}} \tag{E.12}$$

$$\frac{z_{\mathrm{H}}}{x_{\mathrm{H}}} = \sin\theta_{\mathrm{H}}, \qquad \frac{z_{\mathrm{H}}}{x_{\mathrm{H}}} = \sin\theta_{\mathrm{H}} \tag{E.13}$$

$$\frac{y}{2\cdot(z_{\mathrm{L}}+z_{\mathrm{L}})} = \sin(\theta_1). \tag{E.14}$$

From Snell's Law we have,

$$n_{\mathrm{air}}\sin\theta_1 = n_{\mathrm{H}}\sin\theta_{\mathrm{H}} = n_{\mathrm{L}}\sin\theta_{\mathrm{L}}. \tag{E.15}$$

Note that θ_{H} and θ_{L} can be calculated from Snell's law:

$$\theta_{\mathrm{H}} = \mathrm{asin}\left(\frac{n_{\mathrm{air}}\sin\theta_1}{n_{\mathrm{H}}}\right), \tag{E.16}$$

$$\theta_{\mathrm{L}} = \mathrm{asin}\left(\frac{n_{\mathrm{air}}\sin\theta_1}{n_{\mathrm{L}}}\right). \tag{E.17}$$

The difference in optical distance between the two rays yields,

$$\begin{aligned}
\Delta d &= 2\cdot(n_{\mathrm{H}}x_{\mathrm{H}} + n_{\mathrm{L}}x_{\mathrm{L}}) - y \\
&= 2\cdot(n_{\mathrm{H}}x_{\mathrm{H}} + n_{\mathrm{L}}x_{\mathrm{L}}) - 2\cdot(x_{\mathrm{H}}\sin\theta_{\mathrm{H}} + x_{\mathrm{L}}\sin\theta_{\mathrm{L}})\cdot\sin\theta_1 \\
&= 2\cdot x_{\mathrm{H}}\cdot(n_{\mathrm{H}} - \sin\theta_{\mathrm{H}}\sin\theta_1) + 2\cdot x_{\mathrm{L}}\cdot(n_{\mathrm{L}} - \sin\theta_{\mathrm{L}}\sin\theta_1) \\
&= 2\cdot x_{\mathrm{H}}\cdot(n_{\mathrm{H}} - n_{\mathrm{H}}\sin^2\theta_{\mathrm{H}}) + 2\cdot x_{\mathrm{L}}\cdot(n_{\mathrm{L}} - n_{\mathrm{L}}\sin^2\theta_{\mathrm{L}}) \\
&= 2\cdot\frac{d_{\mathrm{H}}}{\cos\theta_{\mathrm{H}}}\cdot n_{\mathrm{H}}\cdot\cos^2\theta_{\mathrm{H}} + 2\cdot\frac{d_{\mathrm{L}}}{\cos\theta_{\mathrm{L}}}\cdot n_{\mathrm{L}}\cdot\cos^2\theta_{\mathrm{L}} \\
\Delta d &= 2\cdot(d_{\mathrm{H}}\cdot n_{\mathrm{H}}\cdot\cos\theta_{\mathrm{H}} + d_{\mathrm{L}}\cdot n_{\mathrm{L}}\cdot\cos\theta_{\mathrm{L}})
\end{aligned} \tag{E.18}$$

The resonant frequencies are still given by $f_m = \frac{mc}{\Delta d}$, such that the frequency period becomes

$$\Delta f = f_{m+1} - f_m = \frac{c}{2\cdot(d_{\mathrm{H}}\cdot n_{\mathrm{H}}\cdot\cos\theta_{\mathrm{H}} + d_{\mathrm{L}}\cdot n_{\mathrm{L}}\cdot\cos\theta_{\mathrm{L}})}. \quad \square \tag{E.19}$$

E.3 N bilayer (Bragg) reflector

Finally, we consider the case of a Bragg reflector consisting of alternating high and low refractive index layers. The geometry is schematized is Fig. E.1.c). We are interested in finding the frequency period of anti-resonant reflections (ARR) through the Bragg reflector. In section 5.1.1 we considered the design of a very special Bragg reflector where the thicknesses $(d_{\mathrm{H}}, d_{\mathrm{L}})$ and refractive indices $(n_{\mathrm{H}}, n_{\mathrm{L}})$ of the layers were chosen such that the Brewster angle of the TM polarization occurs *within* the Bragg reflector when the incidence angle is at grazing angles ($\theta_1 \to 90°$). Thus, in this particular reflector there are no TM reflections at the intermediate $n_{\mathrm{H}}/n_{\mathrm{L}}$ interfaces. A TM ray will therefore traverse the entire Bragg reflector and reflections will only occur at the air interfaces. Anti-resonant reflections can occur by interference between the rays reflected at the top and bottom air interfaces. This situation is analog to the simple single-layer Fabry-Perot reflector with the major difference that refraction within the Bragg multilayer is changing the optical path length.

To calculate the frequency period of the anti-resonant reflections, we exploit the previous result concerning the bi-layer. For simplicity, we consider the Bragg reflector to be a periodic array of bi-layers. The number of bi-layers in the Bragg reflector is given by N_{bilayer}. Fig. E.1.c) illustrates the case $N_{\mathrm{bilayer}} = 2$. By examining this figure it is easy to understand that adding more bi-layers increases the optical path length such that the total difference between the optical distances of rays A and B is $\Delta d_{\mathrm{total}} = N_{\mathrm{bilayer}} \Delta d_{\mathrm{bilayer}}$. Consequently, the frequency period becomes,

$$\Delta f = \frac{c}{N_{\mathrm{bilayer}} \cdot 2 \cdot (d_{\mathrm{H}} \cdot n_{\mathrm{H}} \cdot \cos\theta_{\mathrm{H}} + d_{\mathrm{L}} \cdot n_{\mathrm{L}} \cdot \cos\theta_{\mathrm{L}})}. \quad \square \tag{E.20}$$

Appendix F

Bending loss estimation using a ray-optic method

In their paper on anti-resonant reflection (ARR) waveguides, Lai *et al.* demonstrated that the transmission loss could be calculated from a simple ray-optic model provided that $n_{\text{eff}}(f)$ is known *a priori* [74]. The model is applicable to any multi-mode waveguide provided that the core size (d_{core}) is large enough for the ray-optic approximation to be valid. One could arbitrarily define the limit of applicability to be $d_{\text{core}} > 10\lambda$, where λ is the guided wavelength. Consider the straight waveguide section in Fig. F.1.a). The ray-optic model estimates the power propagation loss α_{straight} by considering the incidence angle dependence of the power reflectivity of core-cladding interface ($R_{\text{wall}}(\theta)$) and the average distance between the reflections of a ray ($d_{\text{core}} \tan(\theta)$):

$$\alpha_{\text{straight}} = \frac{\ln(\ R_{\text{wall}}(\theta, f)\ )}{d_{\text{core}} \tan(\theta)}, \tag{F.1}$$

$$\theta(f) = \arcsin\left(\frac{n_{\text{eff}}(f)}{n_{\text{core}}}\right), \tag{F.2}$$

where $\theta(f)$ is the frequency dependent incidence angle determined by $n_{\text{eff}}(f)$. This simple model was shown to give the same results as Finite-Difference Frequency-Domain (FDFD) simulations [74, 183]. It should be stressed, however, that the *a priori* knowledge of $n_{\text{eff}}(f)$ is required.

We wish to extend this simple model to estimate the bending loss of waveguides. A simple ray-optic model of bending loss was elaborated by Hidaka *et al.* in their paper on hollow-core PVDF tubes [72], however they assumed that the initial ray exiting the straight waveguide and entering the bent waveguide had an frequency independent incidence angle of 90°. As a result, the ray propagated through the bend as a Whispering-Gallery-Mode (WGM), i.e. reflecting only on the outer wall of the

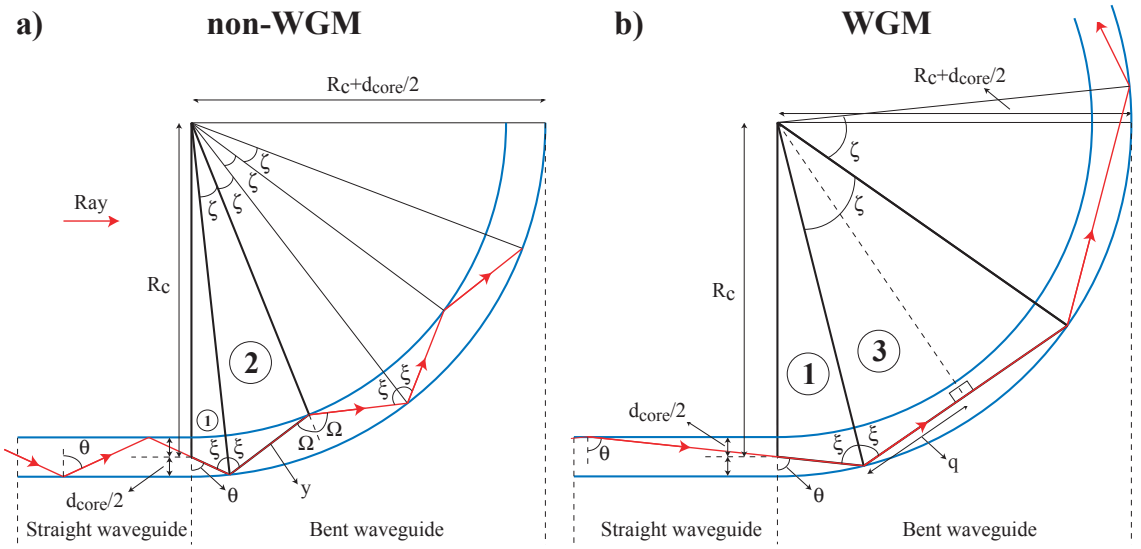

Figure F.1 Ray-optic model of bending loss in large core multimode waveguides. a) Schematization of non-Whispering-Gallery-Mode (non-WGM), b) Schematization of Whispering-Gallery-Mode (WGM).

waveguide (consider $\theta = 90°$ in Fig. F.1.b). This simple model can easily be extended to any incidence angle and the loss can be estimated for both WGM and non-WGM regimes (i.e. reflections on both outer and inner walls of the waveguide).

The two possible bending loss regimes are illustrated in Fig. F.1. Note that a WGM has reflections on the outer wall only and will thus have a smaller bending loss. In this model, it is assumed that $n_{\text{eff}}(f)$ is known such that the frequency dependent incidence angle of a ray within a straight waveguide ($\theta(f)$) can be calculated using equation (F.2). We wish to express the bending loss in the same form as equation (F.1), in other words as a propagation loss within the bent waveguide instead of the total loss after the bend. It is easy to see that the bending will induce a change in the incidence angle and that the average distance between the reflections will change. The bending loss can be determined in the following manner. Let the radius of curvature (R_c) be the distance between the center of a waveguide of core diameter d and the center of rotation of the bend. We shall consider that the ray entering the bent waveguide emanates from the core center with an incidence angle $\theta(f)$ taken from

the straight waveguide. From triangle 1 in Fig. F.1 we have,

$$\frac{\sin(\pi-\theta)}{R_c+d/2}=\frac{\sin(\xi)}{R_c}\quad\Rightarrow\quad\sin(\xi)=\Big(\frac{R_c}{R_c+d/2}\Big)\sin(\theta),\tag{F.3}$$

where ξ is the new incidence angle for the reflection on the outer wall. From triangle 2 we have,

$$\frac{\sin(\xi)}{R_c-d/2}=\frac{\sin(\pi-\Omega)}{R_c+d/2}\quad\Rightarrow\quad\sin(\Omega)=\Big(\frac{R_c+d/2}{R_c-d/2}\Big)\sin(\xi),\tag{F.4}$$

where Ω is the new incidence angle for the reflection on the inner wall, if such a reflection occurs. Substituting (F.3) in (F.4) we obtain the minimum incidence angle for the existence of a whispering-gallery mode:

$$\begin{aligned}&\sin(\Omega)=\Big(\frac{R_c+d/2}{R_c-d/2}\Big)\sin(\xi)=\Big(\frac{R_c}{R_c-d/2}\Big)\sin(\theta),\\&\sin(\Omega)\le 1,\\&\theta_{\min}=\arcsin(\frac{R_c-d/2}{R_c}).\\&\quad\text{if }\ \theta>\theta_{\min}\quad\text{WGM regime}\\&\quad\text{if }\ \theta\le\theta_{\min}\quad\text{non}-\text{WGM regime}\end{aligned}\tag{F.5}$$

Furthermore, the distance between reflections for the non-WGM regime can be obtained by considering triangle 2:

$$\pi-\Omega+\xi+\zeta=\pi\quad\Rightarrow\quad\zeta=\Omega-\xi,\tag{F.6}$$

$$\frac{\sin(\zeta)}{y}=\frac{\sin(\Omega-\xi)}{y}=\frac{\sin(\xi)}{R_c-d/2}=\frac{\sin(\pi-\Omega)}{R_c+d/2}.\tag{F.7}$$

Re-arranging (F.7) and then substituting (F.4) we obtain,

$$\begin{aligned}\frac{y}{R_c - d/2} &= \frac{\sin(\Omega - \xi)}{\sin(\xi)} \\ &= \frac{1}{\sin(\xi)}\Big[\sin(\Omega)\cos(\xi) - \cos(\Omega)\sin(\xi)\Big] \\ &= \frac{1}{\sin(\xi)}\Big[\Big\{\Big(\frac{R_c + d/2}{R_c - d/2}\Big)\sin(\xi)\Big\}\cos(\xi) - \cos(\Omega)\sin(\xi)\Big] \\ y &= (R_c + d/2)\cos(\xi) - (R_c - d/2)\cos(\Omega). \end{aligned} \tag{F.8}$$

The distance between reflections for the WGM regime ($2q$) can be determined by considering triangle 3 in Fig. F.1.b):

$$q = (R_c + d/2)\cos(\xi) \tag{F.9}$$

Finally, the bending loss can be written as

$$\alpha_{\text{bend}} = \frac{-\ln(\, R_{\text{wall}}(\theta = \xi, f)\,)}{2q}, \qquad \text{WGM regime} \tag{F.10}$$

$$\alpha_{\text{bend}} = \frac{-\ln(\, R_{\text{wall}}(\theta = \xi, f) R_{\text{wall}}(\theta = \Omega, f)\,)}{2y}, \quad \text{non} - \text{WGM regime.} \tag{F.11}$$

As an example, let us consider an ARR tube consisting of a 7.66 mm core diameter PTFE tube having a wall thickness of 300 μm. $R_{\text{wall}}(\theta, f)$ is considered to be the Fabry-Perot reflectivity of the tube wall and $\theta(f)$ is calculated using the effective index of propagation $n_{\text{eff}}(f)$ that was obtained from a prior transfer matrix calculation. R_{TE} and R_{TM} are the reflectivities for the TE and TM modes and the loss of the HE modes are defined as,

$$\alpha_{HE} \equiv \frac{\alpha_{TE} + \alpha_{TM}}{2} \quad \Rightarrow \quad R_{HE} \equiv \sqrt{R_{TE}}\sqrt{R_{TM}}. \tag{F.12}$$

To illustrate the calculation procedure we consider the example of an ARR polymer tube ($n_{\text{wall}} = n_{\text{PTFE}} = 1.44$, $n_{\text{core}} = 1.0$, $d_{\text{core}} = 7.66$ mm). The calculation steps are presented in Fig. F.2. We begin with the effective indices of the different waveguide modes (Fig. F.2.a)) that were calculated using the transfer matrix method. The incidence angle of the modal ray in the straight waveguide, $\theta(f)$, is calculated using equation (F.2). Note that the incidence angle increases with frequency and

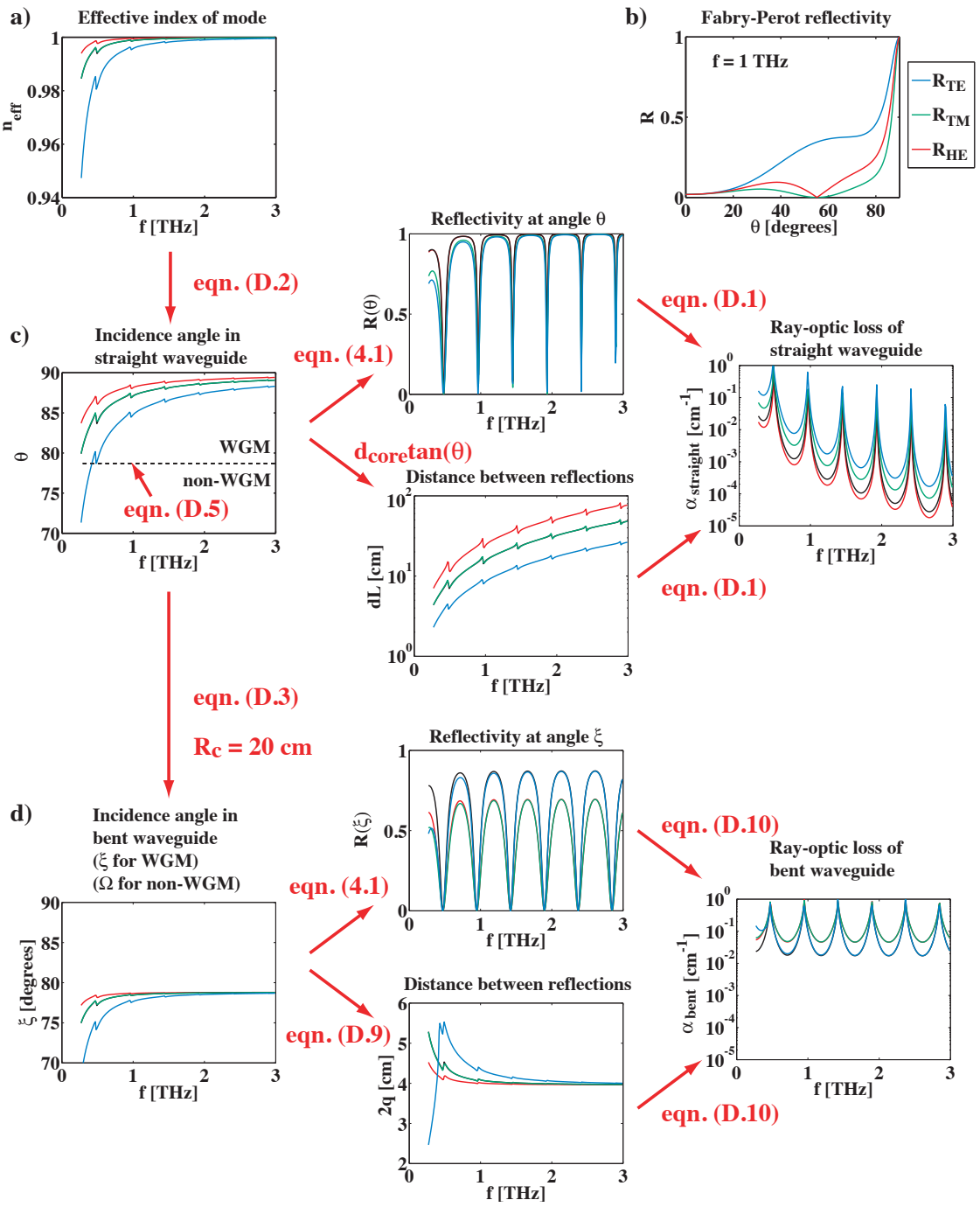

Figure F.2 Example of the ray-optic calculations of straight and bent waveguide propagation losses. The calculation procedure is presented as a flow chart with the necessary equations highlighted in red.

that the values tend towards grazing incidence at high frequency ($\theta \rightarrow 90°$). From the incidence angle it is straightforward to calculate the average distance between reflections ($d_{\text{core}} \tan(\theta)$). Furthermore, the crux of the method relies on the calculation of the wall reflectivity. In this case, the wall reflectivity corresponds to that of a Fabry-Perot interferometer and is calculated using equation (4.1). Contrary to equation (4.2), the single-interface reflectivities must now be written as a function of incidence angle [74]. Moreover, the TE and TM reflectivities have different expressions [74]. Fig. F.2.b) plots the TE and TM Fabry-Perot reflectivities as a function of incidence angle. Although the $R(\theta, f)$ reflectivities are seen to decrease sharply when the incidence decreases from 90° to 60°, the dominant feature is the strong periodic frequency behavior. From the reflectivity and the distance between reflections we calculate the propagation loss using equation (F.1). The high loss resonances are seen to originate from the zeroing of the reflectivity and the loss slowly decreases as the frequency increases because the distance between reflections increases when the incidence angle becomes larger (i.e. when the frequency increases).

We now consider the bending loss of the tube waveguide when it is bent with a bending radius $R_c = 20$ cm. The straight waveguide incidence angles must be compared to the WGM limit angle to see whether the ray in the bent waveguide will be in a WGM or non-WGM regime. The limit is calculated using equation (F.5) and plotted in Fig. F.2.c) as a dashed line. Without loss of generality we limit this example to the WGM regime since only a small portion of the blue curve is below the dashed line. The bending induces a reduction in the incidence angles and the incidence angles of the bent waveguide, ξ, are calculated using equation (F.3). Note that bending homogenizes the incidence angles in addition to reducing them. In other words, the difference between the angles of different modes is smaller in the bent waveguide and the values tend towards the same incidence angle at high frequencies. The reflectivities at the new incidence angles are calculated and the distance between reflection is calculated with equation (F.9). The propagation losses of the bent waveguide are subsequently calculated using equation (F.10). The similarity in the bending losses of the different modes stems from the similitude of the incidence angles ξ. The main difference between the TE, TM, and HE modes stems from differences in the reflectivities. Bending is seen to increase the loss by many orders of magnitude.

Finally, Fig. F.3 validates the ray-optic calculation by comparing the calculated straight waveguide propagation losses (solid lines) to the exact values calculated using

the transfer matrix method (open circles). In this case, the ray-optic method is seen to slightly underestimate the loss. However, in the case of Bragg fibers (see chapter 5), the ray-optic and transfer matrix method calculations give nearly identical results. This is consistent with the results of Lai *et al.* [74]. It would be interesting to compare the bent waveguide propagation loss calculation to more accurate simulations using Finite-Difference Frequency-Domain or coupled-mode calculations in order to validate the ray-optic estimate.

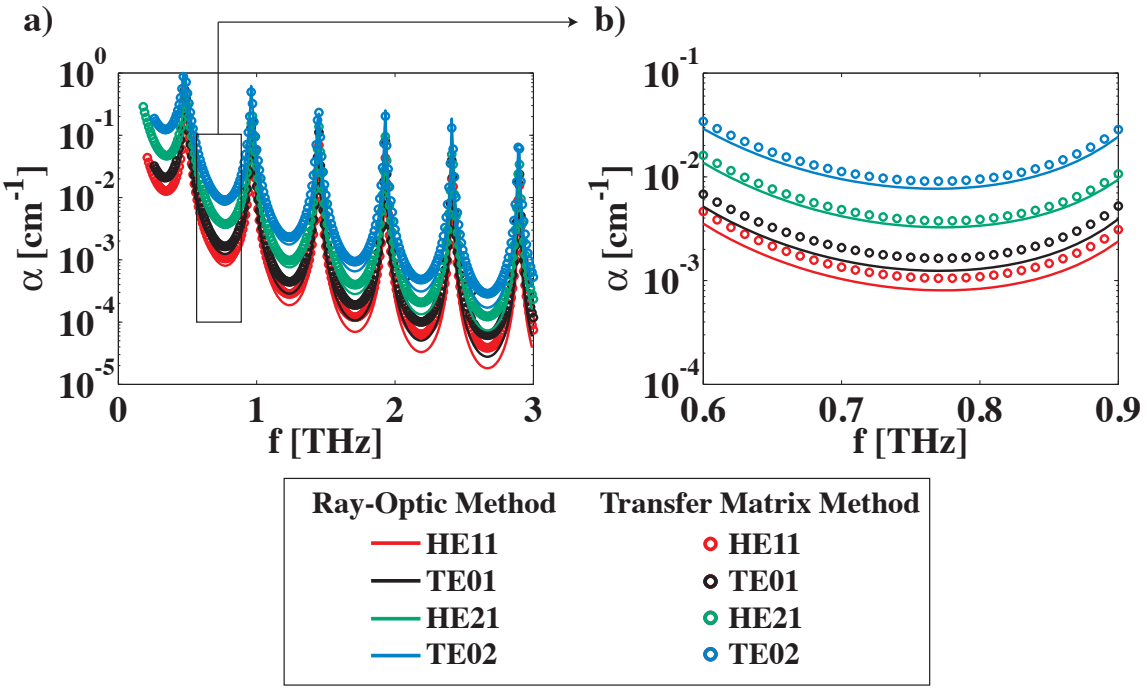

Figure F.3 Comparison between the straight waveguide propagation losses calculated using the ray-optic method (solid lines) and the exact transfer matrix method (open circles).